UNIVERSITY OF SOUTHAMPTON

FACULTY OF ENGINEERING, SCIENCE & MATHEMATICS

School of Engineering Sciences

Micromechanical studies and modelling of toughness in high strength aluminium alloys

by

Thilo Frank Morgeneyer

Thesis for the degree of Doctor of Philosophy

April 2008

UNIVERSITY OF SOUTHAMPTON

ABSTRACT

FACULTY OF ENGINEERING, SCIENCE & MATHEMATICS
SCHOOL OF ENGINEERING SCIENCES

Doctor of Philosophy

Micromechanical studies and modelling of toughness in high strength aluminium alloys

by Thilo Frank Morgeneyer

In this thesis the influence of microstructure on fracture toughness is investigated for two different medium/high strength Al-alloys for aerospace application. In weldable AA6156 (Al-Mg-Si-Cu) alloy sheet, the quench sensitivity in toughness is assessed via enhanced Kahn tear tests. Toughness was seen to be reduced for both 60°C water quenched and air cooled materials *cf.* 20˚C water quench material. Fractography via scanning electron microscopy (SEM) and synchrotron radiation computed tomography (SRCT), as well as Differential Scanning Calorimetry (DSC) and Transmission Electron Microscopy (TEM) studies, have clarified the mechanisms of the quench sensitivity with respect to toughness. Both the coverage of grain boundary decoration and precipitate free zone (PFZ) width increase with reduced quench rates. The failure morphology of the air cooled material appears consistent with classical intergranular ductile failure. Coarse voiding and shear decohesion was prevalent in 20°C water quenched material (depending on local triaxiality), whilst the 60°C water quenched material showed a mixture of transgranular and intergranular fracture modes. The experimental toughness trends are compared to models in the literature and a simple new model is suggested.
Fracture toughness anisotropy of AA2139 (Al-Cu-Mg), a candidate alloy for age forming, in T351 and T8 conditions has been investigated via mechanical testing of smooth and notched specimens of different geometries, loaded in the rolling direction (L) or in the transverse direction (T). Fracture mechanisms are again investigated via SEM and SRCT. Fracture toughness is seen to be anisotropic for both heat treatment conditions tested, but is substantially reduced for the T8 condition compared to the T351. Contributions to failure behaviour have been identified with: (i) anisotropic initial void shape and growth, (ii) plastic behaviour, including isotropic/kinematic hardening and plastic anisotropy, and (iii) nucleation at a 2^{nd} population of 2^{nd} phase particles leading to coalescence via narrow crack regions. SRCT analysis of arrested cracks revealed alignment of voids in the crack during propagation in the rolling direction, resulting in shorter intervoid ligaments than for crack propagation in the transverse direction. Coalescence through shear decohesion in the crack initiation and propagation region was found indicating the necessity to investigate and account for this mechanism. A model based in part on the Gurson-Tvergaard-Needleman approach is constructed to describe and predict deformation behaviour, crack propagation and, in particular, toughness anisotropy. Model parameters are fitted using microstructural data and data on deformation and crack propagation for a range of small test samples. The model accounts for the material features found in the experimental study and its transferability has been shown by simulating tests of large M(T) samples showing strong fracture toughness anisotropy. A parametric study shows that nucleation of small voids at different strains for different loading directions is crucial for a correct model of toughness anisotropy; the combined effects of kinematic hardening and void growth anisotropy can not fully describe fracture toughness anisotropy.

Contents

List of Figures

List of Tables

Nomenclature

Several fields of science have been involved in this thesis. Some signs may have different meanings in different fields. In order to be close to the nomenclature of the original work the parameters have not been renamed here. When a parameter has different meanings they are given here.

a	crack length in the anisotropy model: factor influencing the yield surface shape
b	Burger's vector length
b^1, b^2	factors influencing the yield surface shape
c	solute concentration
$c_{i=1-6}^{k=1-2}$	constants controlling the anisotropy of the yield surface
d	- diameter of grains (in Hall-Patch relationship) - particle diameter - gb width - distance between sample and detector
d_G	typical grain dimension
d_{PFZ}	full PFZ width
f	volume fraction
$\dot{f}$	void volume fraction change rate
f_c	critical void volume fraction
f_g	void volume fraction linked to growth
f_{GB}	fraction of precipitates on the grain boundary
fi	volume fraction of incoherent particles
$\dot{f}_n$	void nucleation rate
fi	void volume fraction linked to 2nd phase particles
f_0	initial void volume fraction
f_*	effective void volume fraction
h_b	factor for linear hardening law of the boundary
h_g	factor for linear hardening law of the grain
k	a constant
k_1, k_2	parameters for isotropic hardening
l	distance between source and sample
l_n	plastic zone widh
m_1	constant
n	work hardening exponent
n_i	work hardening of the PFZ
n_l	number of precipitates per unit area of grain boundary
$\underline{n}$	normal vector
p	strain
$p_{crit,L}$	critical strain for nucleation in L direction

$p_{crit,T}$	critical strain for nucleation in T direction
p_e	strain at which nucleation ends
p_G	hardening exponent of the grain
p_i	fraction of grain boundary contribution
p_{PFZ}	hardening exponent of the PFZ
p_s	strain at which nucleation starts
q_1, q_2	fitting parameters by Tvergaard and Needleman
r	radius of precipitates
A_f	grain boundary particle coverage
A_n	void nucleation function
A_I	area fraction of intergranular failure
A_T	area fraction of transgranular failure
A_n	strain nucleation function
A_n^1	strain nucleation function for first population of particles
A_n^2	strain nucleation function for second population of particles
A_n^{01}	factor in strain nucleation function for first population of particles
A_n^{02}	factor in strain nucleation function for second population of particles
B_0	initial sheet thickness
B_*	effective scalar stress
$\underline{B}$	stress tensor related to kinematic hardening
$\widetilde{B}_{i=1,2,3}$	eigenvalues of modified stress tensor
C	kinematic hardening constant
D	- diameter - average grain size (Hornbogen model for intergranular failure) - parameter for kinematic hardening - defocusing distance
E	in Hooke's law: Young's modulus in the Beer-Lambert law: energy of incident photons
E_{load}	logarithmic deformation in loading direction
E_p	total energy related to plastic deformation by shear
$E_{p,G}$	energy related to plastic deformation by shear in the grain
$E_{p,PFZ}$	energy related to plastic deformation by shear in the PFZ
$E_{p,crit}$	energy related to plastic deformation by shear where failure starts
E_{prop}	logarithmic deformation in propagation direction
E_S	logarithmic deformation in thickness direction
E_i	energy dissipated in intergranular fracture
E_t	energy dissipated in transgranular fracture
$\underline{\underline{E}}$	fourth order stiffness tensor
G	strain energy release rate
G_{IC}	energy release rate
G_{ICi}	strain energy release rate for intergranular failure
G_{ICt}	strain energy release rate for transgranular failure
H	half GB particle thickness
H_0	initial half unit cell height
J	J integral
K_G	hardening factor of the grain
K_{PFZ}	hardening factor of the PFZ
K_{1C}	fracture toughness
K_{1Ct}	fracture toughness for transgranular failure

K_{1Ci}	fracture toughness for intergranular failure
L	particle length
L_i	empirical constant with the dimension of a length
$\underline{\underline{L}}$	fourth order tensor
M	Taylor factor
N	extent of strain localisation
N_s	number of precipitates per unit area of grain boundaries
$R(p)$	function representing isotropic hardening
R_x	initial void dimension in x –direction
R_z	initial void dimension in z –direction
R_0	-parameter in isotropic hardening law -initial unit cell radius
$S^k_{i=1-3}$	principal values of the modified stress deviator
S_{GB}	slip band spacing
T	temperature
U_{diss}	dissipated energy
W_0	void aspect ratio
W	half PFZ width
W_{SB}	slip band width
X_0	void spacing in crack propagation direction
$\underline{X}$	internal back stress tensor
Z	atomic number
Z_0	void spacing in loading direction
α	– angle between slip plane and crack plane - factor influencing the shape of the yield surface (for anisotropic plasticity)
$\alpha_{i=L,T,S}$	weight factors for anisotropic growth in direction L,T,S respectively
$\underline{\alpha}$	second order tensor of the kinematic hardening state variable
δ	-crack tip opening displacement - multiplicative factor for coalescence
ε	strain
ε_f	fracture strain
ε_{fi}	fracture strain of the PFZ
ε_n	critical strain to nucleate voids
$\underline{\dot{\varepsilon}}$	strain rate tensor
$\underline{\dot{\varepsilon}}_p$	plastic strain rate tensor
$\underline{\dot{\varepsilon}}_e$	elastic strain rate tensor
η	parameter taking into account the stress state of the material
γ	average strain at the crack tip
γ_c	average shear strain
γ_G	shear strain of the grain
γ_{PFZ}	shear strain of the PFZ
γ_{SB}	shear strain in slip band
λ	-particle spacing -X-ray wavelength
μ	-attenuation coefficient -Lode parameter

$\mu_{\dot{p}}$	Lode parameter for strain rate
ρ	density
σ	stress
σ_c	decohesion stress
σ_{decoh}	local decohesion stress
σ_{eq}	von Mises stress
σ_f	- fracture stress - flow stress in the GTN model
σ_G, $\sigma_{y,G}$, σ_g	yield strength of the grain
σ_{GB}	yield strength of the grain boundary
σ_{PFZ}, σ_{yi}	yield strenth of the PFZ
σ_R	stress close to yield strength
σ_y	yield strength
$\sigma_{t=1,2,3}$	principal stresses
$\overline{\sigma}$	anisotropic effective stress
σ_*	effective scalar stress
$\sigma_{0.2\%}$	0.2% proof strength
σ_{kk}	trace of the stress tensor
σ_0	yield stress of the matrix
$\underline{\sigma}$	Cauchy stress tensor
τ	critical resolved shear stress shear stress
τ_G	shear stress of the grain
τ_{PFZ}	shear stress if the PFZ
θ	angle
ν	Poisson's ratio
$\underline{\chi}$	Intermediate back stress tensor
Γ_i	energy to create two free surfaces by intergranular progression
Γ_t	energy to create two free surfaces by transgranular progression
Φ	yield surface
Φ_c	critical angle
CCD	charge-coupled device
CTOD	crack tip opening displacement
CMOD	crack mouth opening displacement
EBSD	electron back scattered diffraction
EDS	energy dispersive spectrometry
ESRF	European Synchrotron Radiation Facility
DSC	differential scanning calorimetry
FE	finite element
FEG-SEM	field emission gun scanning electron microscope
GB	grain boundary
GP	Guinier Preston
GTN	Gurson-Tvergaard-Needleman
LEFM	linear elastic fracture mechanics
L	rolling direction
µCT	micro computed tomography
M(T)	large panel samples

PFZ	precipitate free zone
RT	room temperature
S	short-transverse direction
SEM	scanning electron microscope
SRCT	synchrotron radiation computed tomography
T	transverse direction
TEM	transmission electron microscope
T351	treatment condition : solutionised, cold worked + naturally aged
T8	treatment condition : artificially aged
UIE	unit initiation energy
UTS	ultimate tensile strength
X-ray CT	X-ray computed tomography
2-D	two-dimensional
3-D	three-dimensional

Declaration of Authorship

I, Thilo Frank Morgeneyer declare that the thesis entitled:

Micromechanical studies and modelling of toughness in high strength aluminium alloys

and the work presented in it are both my own, and have been generated by me as the result of my own original research. I confirm that:

- this work was done wholly or mainly while in candidature for a research degree at this University under supervision of Prof. Ian Sinclair and Prof. Marco Starink;
- a part of this PhD, related to the Finite Element modelling has been carried out at Centre des Matériaux de l'Ecole des Mines de Paris with the help of Prof. Jacques Besson
- where any part of this thesis has previously been submitted for a degree or any other qualification at this University or any other institution, this has been clearly stated;
- no part of this thesis has been previously submitted for a degree at this University or any other institution.
- where I have quoted from the work of others, the source is always given. With the exception of such quotations, this thesis is entirely my own work;
- I have acknowledged all main sources of help;
- parts of this work have been published prior to submission and a list of journal publications is given on page xxiv.

Signed: …….

Date: ……

Acknowledgements

There are a number of people to whom I will always be indebted for the help and support they have offered and without whom I could not have done my PhD. My biggest thanks go to Ian Sinclair, Marco Starink and Jacques Besson for their support, guidance, ideas and supervision. They have contributed an enormous amount to my research and personal (also linguistic) development, for which I will always be grateful.

I would like to thank Frédéric Bron, Bernard Bès, and Jean-Christophe Ehrström from Alcan CRV for their technical support and helpful discussion.

I would like to acknowledge Alcan CRV for making this PhD possible with their technical and financial support. The "Association Nationale de la Recherche Technique" is also acknowledged for their financial help.

The work at ESRF could not have been performed without the ID19 beamline staff and in particular the kind help of Jean-Yves Buffière (who performed one very important scan for me after I had already left ESRF), Greg Johnson and Elodie Boller. I would like to thank Andrew Moffat and Pete Wright for scanning some of my samples.

I would like to acknowledge the support of all the staff and students in the Engineering Materials Research Group at the University of Southampton who have aided me along the way. I am especially grateful to the people who have spent time with me (not only) in the office: Nik, Thomas, Andrew, Polly, Toby, Pete, Ian and Stewart. I would also like to acknowledge the help of Shun Cai Wang for helping with the electron scanning microscopy and Nong Gao for the DSC experiments and analysis carried out as part of this research. The secretarial and technical staff (Bob, Gwyneth, Dave and Eric) have also been invaluable.

I would like to thank the Royal Academy of Engineering, the Worshipful Company of Armourers and Brasiers for their financial support in the form of conference attendance awards.

I am very grateful for the support and help of all the staff and students I have met during my time at 'Centre des Matériaux de l'Ecole des Mines de Paris'. In particular I would like to thank Henry Proudhon, Fanck N'Guyen and Kamel Madi who helped me analyse my tomography data. The students in the centre (Ovidi, Manel, Eva, Johann, Melis, Marc, Martin, Matthieu, Guillaume, Nicolas, Edouard and Thibault) are acknowledged for their support, entertainment, language lessons and technical help.

Big thanks go to my family and my friends who supported and encouraged me during this PhD.

Publications

Morgeneyer T.F., Starink, M.J, Sinclair I. *Experimental analysis of toughness in 6156 Al-alloy sheet for aerospace application.* Materials Science Forum, 2006. 519-521: p.1023-1028.

Morgeneyer T.F., Starink M.J., Sinclair I. *Evolution of voids during ductile crack propagation in an aluminium alloy sheet toughness test studied by synchrotron radiation computed tomography*. Acta Materialia, 2008. 56: p. 1671-1679

Morgeneyer T.F., Starink M.J., Wang S.C., Sinclair I. *Quench sensitivity of toughness in an Al alloy: Direct observation and analysis of failure initiation at the precipitate-free zone*, Acta Materialia, 2008, in press, doi:10.1016/j.actamat.2008.02.021

Morgeneyer T.F., Besson J., H. Proudhon, Starink M.J. and Sinclair I., *Analysis of toughness anisotropy in AA2139 Al-alloy sheet; part I: experiments,* article under preparation

Morgeneyer T.F., Besson J., Starink M.J. and Sinclair I. *Analysis of toughness anisotropy in AA2139 Al-alloy sheet; part II: model and simulations*; article under preparation

Chapter 1

Introduction

Air traffic has increased by 96% in the European Economic Area member countries between 1990 and 2003 [1] and is expected to continue increasing worldwide. Whilst air travel has many benefits, it is also, due to fuel combustion, a source of greenhouse gasses such as CO_2. The impact of air travel on climate change may even be disproportional compared to other means of transport as combustion of jet fuel at high altitudes results in additional environmental impact in addition to those of CO_2 [2]. Most industrialised countries intend to reduce emissions of CO_2 to prevent catastrophic effects of global warming. The reduction of aircraft weight via enhancing aerospace materials can clearly contribute to reduction of green house gas emissions.

Due to these environmental concerns and the need of economic efficiency in a competitive air travel industry there is a well established drive within airframe manufacture for better materials to increase the performance of aircraft and reduce manufacture and maintenance costs as well as fuel emissions. With ongoing research effort in Al-based materials for aerospace application there is a driver for increasing the strength, fatigue resistance and toughness of the available alloys. Enhancing these materials is even more important for the aluminium industry as improvements of polymer matrix composites make composites a serious competitor in the aerospace field. Fatigue fracture resistance and fracture toughness are critical design criteria, especially in parts of the aircraft that are typically loaded under tension such as the fuselage and lower wing skins [3].

New airframe production methods are the subject of ongoing work, *e.g.* the attachment of stringers to the aircraft skin via welding instead of riveting [4-8]. Welding is considered to be a superior assembly method as structure weight may be reduced since rivets are no longer needed. The fatigue fracture resistance may also be enhanced through welding as the riveting holes cause stress concentrations and can act as fracture initiation sites.

Additionally, the cost of assembly can be reduced via welding [4]. As such there is interest in deployment of 6XXX series aluminium alloys in airframes, as these alloys are weldable and are currently widely used within the automotive industry [9]. The use of the relatively new technique of friction stir welding is under particular consideration as it has the advantage of joining materials in a solid state which may prevent many metallurgical problems that result from the melting and solidification processes occurring during conventional fusion welding. In this project a AA6156 (Al-Mg-Si-X) alloy sheet is investigated that is designed for fuselage applications. This heat treatable alloy is strengthened through precipitation hardening and has relatively high solute levels. High solute levels are known to cause quench sensitivity and hence the alloy is assessed here in terms of the quench sensitivity of fracture toughness.

A further trend in airframe manufacture is the use of age forming for curved structures which may represent a significant production cost benefit. The final aged structure may also have less residual stresses than structures produced through conventional techniques which may therefore enhance fatigue and stress corrosion resistance [10]. In the age forming process a curved component is formed via a combination of pressure and temperature [11]. The technique is typically used for production of upper wing skins of commercial aircraft, but as lower wing skin alloys lose their damage tolerant properties upon ageing, it is currently not applied for lower wing skins [11]. As such, new age hardenable alloys with superior damage tolerance capability are under development such as the AA2139 (Al-Cu-Mg-X) alloy [12] investigated in this project. This type of heat treatable alloy is of particular interest for fuselage and bottom wing skin applications where high damage tolerance is required. Given the role of toughness in such applications, the experimental assessment of failure mechanisms is clearly of value. In particular, the material considered here is examined in terms of anisotropy of fracture properties.

Following on from recent studies by Bron and co-workers [3, 13-15], a key aim of this thesis is the modelling of toughness results obtained by centre-cracked tension panels M(T) [16] through FE analysis of Kahn tear test results. The toughness testing of large M(T) panels is generally used to obtain stable crack propagation to qualify aluminium alloys [14]. Prediction of M(T) toughness from Kahn test is of considerable interest as the Kahn tear tests are significantly easier to perform than tests with M(T) samples.

With recent developments in Synchroton Radiation Computed Tomography (SRCT) it has become possible to visualise fracture mechanisms in materials at sub-micron scale in 3D dimensions [17]. Several SRCT studies have assessed fracture micromechanisms *e.g.* Qian *et al*. [18] have assessed the growth of voids and their coalescence during fracture via *in-situ* SRCT tests. Maire et al. [19] have assessed the monotonic growth of voids in a model aluminium matrix composite. Also fatigue crack closure phenomena have been assessed in several SRCT studies [20-23]. In the present study this powerful technique is applied to the arrested cracks to further assess in fracture mechanisms of the two alloys.

1.1 Project aims

The broad aim of this project is to better understand the relationship between microstructure and toughness in the two investigated Al alloys. The ductile fracture micromechanisms influencing fracture toughness are to be assessed.

In detail the following aims are to be achieved:

- Investigation of failure mechanisms in an AA6156 (Al-Si-Mg-Cu) alloy. In addition, the influence of quench rates on the fracture toughness and microstructure as, well as fracture micromechansisms, are to be understood.
- Assessment of fracture toughness anisotropy of the AA2139 (Al-Cu-Mg-Ag) alloy and clarification of its physical origins. The toughness as a function of test direction and hardening capacity (naturally and artificially aged condition) are to be investigated.
- Extending the Finite Element (FE) modelling studies of Bron and Besson [3, 13-15] initially applied to 2024 T3 type sheet, to fracture toughness anisotropy in the AA2139 alloy in different heat treatment conditions in order to predict large panel M(T) tests. A full set of experimental data assessing plasticity, fracture behaviour and microstructural features is to be obtained.

1.2 Methodology

The methods utilized to pursue the aims are:

- Assessment of microstructure by field emission gun scanning electron microscopy (FEG-SEM), transmission electron microscopy (TEM), differential scanning

calorimetry (DSC), electron backscatter diffraction (EBSD), energy dispersive spectrometry (EDS), synchrotron radiation computed tomography and optical microscopy

- Kahn tear testing to assess fracture toughness
- Detailed failure analysis by FEG-SEM and SRCT as a function of quench rates (AA6156 alloy) and material orientation (AA2139 alloy).
- Assessment of plastic anisotropy via tests on smooth and notched samples (AA2139 alloy)
- Fracture modelling via “local approach” FE methods

1.3 Thesis structure

This thesis contains eight chapters. Following this introduction, Chapter 2 contains the literature review, which is divided into three main sections: a general background of aluminium alloys and processing, a review of fracture and an overview of the tomography technique. In Chapter 3 details of all the experimental methods used in this thesis and materials details are given. The results of the work carried out in this thesis are then given in three further chapters, drawing closely on four journal papers. Chapter 4 contains a paper presenting the toughness quench sensitivity study of the AA6156 alloy. Chapter 5 contains a paper on the tomography observation of void evolution in a Kahn tear test during crack propagation in the AA2139 alloy. The experimental assessment of plasticity and fracture of the AA2139 alloy as well as a tomography study of damage evolution during crack initiation is given in Section 1 of Chapter 6. The second section of Chapter 6 contains the computational work carried out on the fracture toughness anisotropy of the AA2139 alloy. The conclusions are given in Chapter 7. Possible directions of further results and some initial results for modeling of slant fracture are given in Chapter 8.

1.4 References

1. EEA. *Report number 1/2007. Transport and the environment: on the way to a new common transport policy.*, 2007

2. Olsthoorn, X. *Carbon dioxide emissions from international aviation: 1950-2050.* Journal of Air Transport Management, 2001. 7: p. 87-93.

3. Bron,F. *Déchirure ductile des tôles minces en alliage d'aluminium 2024 pour application aèronautique*. thèse, Ecole des Mines de Paris, 2004.

4. Gallais,C. *Joints soudes par friction malaxage d'alliages d'aluminium de la serie 6XXX: charcterisation et modelisation*. thèse, Institut National Polytechnique de Grenoble, 2005.

5. Lafly, A.L., Dalle Donne, C., Biallas, G., Alléhaux , D. , Marie ,F. *Role of residual stresses on Fatigue Crack Propagation of FSW 6056-T78 aluminium joints under various technologies*. Materials Science Forum, 2006. 519-521: p. 1089-1094.

6. Braun, R., Alfaro Mercado, U., Biallas,G. *Investigation on strength and corrosion behaviour of friction stir welded similar and dissimilar aluminium alloys*. Materials Science Forum, 2006. 519-521: p. 1113-1118.

7. Alléhaux, D. , Marie,F. . *Mechanical and corrosion behaviour of the 2139 aluminium-copper alloy welded by the Friction Stir Welding using the bobbin tool technique*. Materials Science Forum, 2006. 519-521: p. 1131-1138.

8. Warner,T. *Recently-developed aluminium solutions for aerospace applications*. Materials Science Forum, 2006. 519-521: p. 1271-1278.

9. Warner, T.J., Shahani, R.A., Lassince, P., Raynaud,G.M., *Aluminium alloy developments for affordable airframe structures*. Research report of ALCAN, Centre de recherches de Voreppe, 1999

10. Zhu, A.W., Starke,E.A. *Materials aspects of age-forming of Al-xCu alloys*. Journal of Materials Processing Technology, 2001. 117: p. 354-358.

11. Starink, M.J., Sinclair, I., Gao, N., Kamp, N., Gregson, P.J., Pitcher, P.D., Levers, A., Gardiner,S. *Development of new damage tolerant alloys for age-forming*. Materials Science Forum, 2002. 396-402: p. 601-606.

12. Cho, A., Bes,B. *Damage Tolerance Capability of an Al-Cu-Mg-Ag Alloy(2139).* Materials Science Forum, 2006. 519-521: p. 603-608.

13. Bron, F., Besson,J. *A yield function for anisotropic materials Application to aluminum alloys*. International Journal of Plasticity, 2004. 20: p. 937-963.

14. Bron, F., Besson, J., Pineau,A. *Ductile rupture in thin sheets of two grades of 2024 aluminum alloy*. Materials Science and Engineering A, 2004. 380: p. 356-364.

15. Bron, F., Besson,J. *Simulation of the ductile tearing for two grades of 2024 aluminum alloy thin sheets*. Engineering Fracture Mechanics, 2006. 73: p. 1531-1552.

16. ASTM-international, *E 561-98 Standard practice for R-curve determination.* Annual book of ASTM Standads 03.01. 1999.

17. Maire, E., Buffiere, J.-Y., Salvo, L., Blandin, J.J., Ludwig, W., Letang,J.M. *On the application of X-ray microtomography in the field of materials science*. Advanced Engineering Materials, 2001. 3: p. 539-46.

18. Qian, L., Toda, H., Uesugi, K., Kobayashi, T., Ohgaki, T., Kobayashi,M. *Application of synchrotron x-ray microtomography to investigate ductile fracture in Al alloys*. Applied Physics Letters, 2005. 87: p. 241907-241910.

19. Maire, E., Bordreuil, C., Babout, L., Boyer,J.-C. *Damage initiation and growth in metals. Comparison between modelling and tomography experiments*. Journal of the Mechanics and Physics of Solids, 2005. 53: p. 2411-34.

20. Khor, K.H., Buffiere, J.-Y., Ludwig, W., Toda, H., Ubhi, H.S., Gregson, P.J., Sinclair,I. *In situ high resolution synchrotron x-ray tomography of fatigue crack closure micromechanisms*. Synchroton Radiation for Advanced Materials Analysis and Processing Journal of Physics Condensed Matter, 2004. 16: p. 3511-3515.

21. Toda, H., Sinclair, I., Buffiere, J.-Y., Maire, E., Khor, K.H., Gregson, P., Kobayashi,T. *A 3D measurement procedure for internal local crack driving forces via synchrotron X-ray microtomography*. Acta Materialia, 2004. 52: p. 1305-17.

22. Guvenilir, A., Stock,S.R. *High resolution computed tomography and implications for fatigue crack closure modelling*. Fatigue & Fracture of Engineering Materials and Structures, 1998. 21: p. 439-450.

23. Guvenilir, A., Breunig, T.M., Kinney, J.H., Stock,S.R. *Direct observation of crack opening as a function of applied load in the interior of a notched tensile sample of Al-Li 2090*. Acta Materialia, 1997. 45: p. 1977-87.

Chapter 2

Literature review

2.1 Aluminium alloys

Aluminium alloys are used in various areas of industry. Different alloying compositions and material treatments provide materials with a wide variety of physical and mechanical properties. In aerospace applications, as well as in other transportation areas, aluminium is commonly used because of its good specific stiffness and strength combined with its formability, fatigue resistance and toughness.

Wrought aluminium alloys, as commonly used for aerospace engineering, are divided into 8 basic groups depending on their main alloying elements.

First digit	Main alloying elements
1XXX	99.00% minimum aluminium
2XXX	Copper
3XXX	Manganese
4XXX	Silicon
5XXX	Magnesium
6XXX	Magnesium and Silicon
7XXX	Zinc
8XXX	others

Table 2-1:Aluminium alloy series according to main alloying elements (after Ref. [1])

Additionally, aluminium alloys may be further divided into 2 classes: the alloy groups whose strength is essentially independent of heat treatment, identified as non-heat treatable alloys, as opposed to alloys where strength can be enhanced and controlled through heat treatments. The 2XXX, 6XXX and 7XXX alloy series are particularly significant in the latter group [1].

In aerospace applications especially, 2XXX alloys are widely used for applications where high damage tolerance is needed, such as the fuselage and the bottom wing skin structures. 7XXX alloys can generally achieve higher yield strength levels and are commonly used in structures under compression, such as upper wing skins.

6XXX alloys are commonly used for extruded pieces for general engineering purposes and in the automotive industry. However, there has been increasing interest in the use of 6XXX alloys in aerospace applications [2]. A mayor advantage would be the weldability of these alloys, potentially supporting advanced manufacturing concepts such as welded skin stringer structures [3, 4].

Wrought aluminium alloys are often distinguished from cast aluminium alloys. Wrought aluminium alloys are initially produced in cast ingot or billet form but are then worked by processes such as rolling, extruding, forging, drawing. The material is then identified as "semi finished" [5]. As such, the detrimental cast structure is broken down in the resultant products (i.e. plate, sheet, bar *etc.*).

2.1.1 Standard nomenclature: alloy and temper

The International Alloy Designation System for wrought products is generally used to describe wrought aluminium alloy in terms of 4-digit codes [1]. As Table 2-1 suggests, the first digit mostly refers to the main alloying elements. The second digit gives information of the material purity. To summarize the condition of a given alloy, temper designations are used. The temper designation is given by a letter and additional number after the 4-digit alloy code. Table 2-2 shows various different designations for common commercial conditions.

letter	condition	digit	process
F	As fabricated		
O	Annealed		
H	Strain hardened	1	Strain hardened only
		2	Strain hardened and partially annealed
		3	Strain hardened and stabilized
		4	Strain hardened and lacquered or painted
W	Solution treated		
T	Thermally treated to produce stable tempers other than F, O, H	1	Annealed and natural ageing
		2	Annealed, cold worked and naturally aged
		3	Solutionized cold worked and naturally aged
		4	Solutionized and naturally aged
		5	Annealed and artificially aged
		6	Solutionized and artificially aged
		7	Solutionized and over aged
		8	Solutionized cold worked and artificially aged
		9	Solutionized cold worked and artificially aged
		10	Annealed, cold worked and artificially aged
	(additional specifications concerning stress relief)	T_51	Stress relieved by stretching
		T_52	Stress relieved by compression
		T_53	Stress relieved thermally
		T_54	Stress relieved by cold forging

Table 2-2: Temper designations for aluminium alloys (after Ref. [1])

2.1.2 Homogenization

Homogenization is performed on alloys before ingots are in semi-finished form. This process step has several objectives. One is to reduce the effects of microsegregation during casting. The other aim is to remove non-equilibrium, low melting point eutectics that may cause cracking during subsequent process steps [6]. In addition, controlled precipitation of excess concentrations of elements that are dissolved during solidification may be achieved [1].

2.1.3 Second phase particles in aluminium alloys

Wrought, heat treatable aluminium alloys generally contain three main groups of second phase particles. The groups are commonly termed coarse intermetallics, dispersoids and fine precipitates.

2.1.3.1 Coarse intermetallics

Coarse intermetallic particles (also called constituent particles), consist of two main groups. The first one comprises iron and silicon containing phases which are virtually insoluble. The second group consists of soluble compounds of the major alloying elements. Intermetallics generally do not have a useful function in an alloy but are often detrimental to fracture properties. Common commercial alloys for structural applications all contain coarse intermetallic particles due to the high cost of their complete removal [1].

Coarse particles predominantly form during ingot solidification. The aim of homogenization is to dissolve the soluble constituents. During the secondary working of cast ingots coarse particles are generally fractured and become aligned in the working direction. The typical size of such particles after deformation processing is ~1-10 μm.

2.1.3.2 Dispersoid particles

Dispersoids have a typical size of 0.05 to 0.5μm and form during the homogenization of ingots by solid state precipitation of compounds containing elements which have modest solubility, typically Zr, Mn or Cr [1]. Dispersoids retard recrystallization and grain growth so that grain structure can be controlled by the amount of disperoids present in an alloy and appropriate choice of thermo-mechanical treatment. It is not entirely clear whether dispersoids improve fracture toughness or whether they are detrimental to it. On the one hand they are thought to have a positive influence on fracture toughness as dispersoid

particles limit recrystallization which is believed to be detrimental to it. On the other they may nucleate voids and void sheets which is detrimental to fracture toughness [7].

2.1.3.3 Precipitates and precipitation hardening

Fine precipitates are formed during the age hardening of heat treatable alloys. They may be exceptionally fine and their size, in terms of their smallest dimension, is typically up to 0.05 μm. In many heat treatable alloys the first stage of precipitation is the formation of so-called Guinier Preston (GP) zones which are solute rich clusters of atoms that keep the structure of the host matrix. GP zones are finely dispersed in the matrix [1]. The amount of GP zones which can appear can depend strongly on the presence of excess vacancies in the lattice. In some alloys the intermediate precipitates (precipitates forming before the stable equilibrium phase) nucleate at the sites of stable GP zones.

In general terms, the requirements for precipitation strengthening are:

- Alloying elements must have a substantial solubility in aluminium at high temperatures, which then decreases with decreasing temperature.
- After quenching (which is the cooling from the solutionising temperature) a Supersaturated Solid Solution (SSSS) must form.
- During the ageing process finely dispersed precipitates must form.

The thermal treatments applied to heat treatable aluminium alloys for age hardening are the following treatment:

Solutionizing:

The soluble phases are generally dissolved during heat treatment stage but the material does not melt. The solutionising temperature depends on the material, the piece size and desired properties of the material, the time depends mostly on the piece size.

Quenching:

The material is quickly cooled from the solutionising temperature to a much lower temperature. A supersaturated Al rich phase is produced by fast quenching. If the quench rates are too slow, solute can precipitate during the quench and the material properties will be compromised. Solute which precipitates during a slow quench can no longer contribute to solid solution strengthening of the material. In addition, vacancies can be lost during a

slow quench, reducing nucleation rates. Different alloys are differently sensitive to quench rates. Quench factor analysis is a commonly used technique to assess and quantify the "loss" of solute during the quenching [8, 9].

Ageing:

During the ageing process, precipitation of solute occurs either at room temperature (natural ageing) or at higher temperatures (artificial ageing). The hardness and strength of a typical aluminium alloy increases with ageing until it reaches a peak. In the underaged condition, before achieving maximum hardness, precipitates can generally be overcome by dislocation shearing, whilst after the achieving the peak aged state, precipitates exhibit classical Orowan-loop interactions with mobile dislocations (see section 2.1.6.2).

2.1.3.4 Precipitates in 6XXX alloys with and without Cu

Generally the sequence of precipitate formation in Al-Mg-Si 6xxx series alloys is identified as the following [10]:

$$\alpha(SSS) \rightarrow \beta'' \rightarrow \beta' \rightarrow \beta$$

where β'' is the main hardening phase in most of these alloys. β (Mg_2Si) is the stable equilibrium precipitate.

For applications in the automotive industry, Al-Mg-Si-Cu alloys have been widely investigated [11]. Depending on their exact composition these alloys may in fact be classified as 2XXX or 6XXX series. Alloys with a high copper content have different properties from the "classical 6XXX" alloys; hardness is enhanced as well as the precipitation hardening kinetics. These different properties are partly linked to a phase named "Q" forming in the copper containing alloys [10, 11]. The composition of the phase is identified as $Al_5Cu_2Mg_8Si_6$ in Ref.[10], but the exact composition is still unknown. Figure 2-1 shows the section of the aluminium-copper-magnesium-silicon diagram at 775°K, at 1wt%Si, (the silicon content in the AA6156 alloy of interest in this project is slightly lower (~0.8 wt %) than in the diagram).

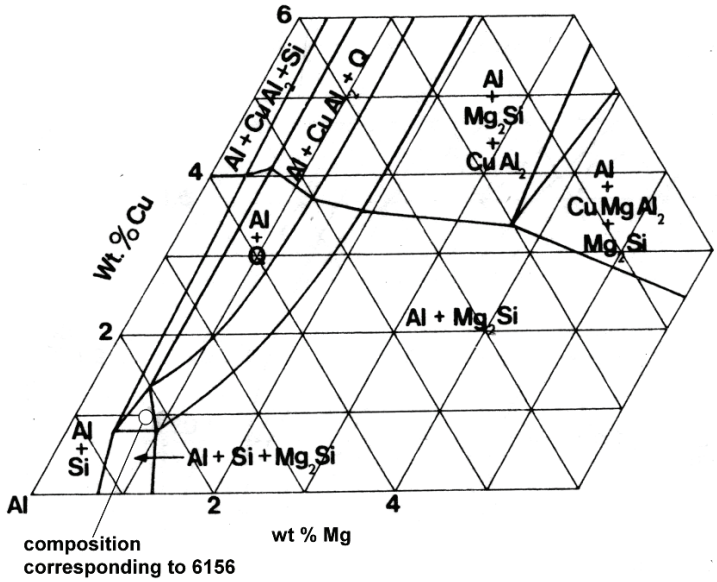

Figure 2-1: Section of the aluminium-copper-magnesium-silicon diagram at 775°K, 1% Si (adapted after Ref. [12])

The composition of the AA6156 can be found in the Al+Q+Mg_2Si field. It can be seen that increasing Cu content promotes the formation of Q phase. The Q phase can be an equilibrium phase. An important metastable precursor phase of the Q phase is Q′ which has the same crystal system and similar composition as Q, but is coherent with the Al matrix along its long axis [11]. The Q′ has a lath morphology and a hexagonal structure and Q′ may also have precursor phases, for example the "L" phase [11]. The formation of a metastable phase with similar features to Q′ in ternary Al-Mg-Si alloys with excess Si compositions has also been stated [11]. In Al-Mg-Si-Cu alloys age hardening may be caused by the precursor phases of Q′ as well as by the β″ phase. In studies of the 6056 alloy [13, 14] it has been stated that in the T6 condition β″ as well as small amounts of a lath shaped phase that is likely to be a precursor phase of the Q phase are present. With overaging (of the 6056 alloy) the amount of the lath shaped precursor phase of Q seems to increase at the expense of the content of β″ [14]. The nomenclature and structure of the precursor phases of Q is not consistent in the literature and confusion exists about the exact precipitation sequence for the Q phase. For the precursor phases of the Q phase the following designations are used in the literature: Q′, λ′, L, B′ [11, 14-16]. In Ref. [17] Esmaeili and co-workers [17] have performed various Differential Scanning Calorimetry (DSC) studies and a literature review for a 6111 Al-0.79%Mg-0.6Si-0.7Cu-0.2Mn alloy that has a composition similar to 6156. The following precipitation sequence for 6111 alloys [17] is given :

$$\alpha(SSS) \rightarrow \beta'' \rightarrow Q' \rightarrow Q$$

The main hardening precipitate of the 6111 alloy in T6 condition is reported to be β″.

According to computational thermodynamics the main stable phase in a 6111 alloy at 600°C is Q with small amount of β also being present [18].

2.1.3.5 Precipitates in 2XXX alloys

There are a variety of common precipitation reactions occurring in Al-Cu-Mg alloys depending on their composition. The following two sequences are often the most important [19]:

$$\alpha_{SS} \rightarrow \text{Cu clusters (GP)} \rightarrow \theta' \rightarrow \theta(Al_2Cu)$$
$$\alpha_{SS} \rightarrow \text{Cu, Mg clusters (GPB)} \rightarrow S'/S(Al_2CuMg)$$

Which sequence is occurring in the specific 2XXX alloy depends particularly on the Cu/Mg ratio. 2XXX alloys with minor additions of silver may exhibit further specific precipitation processes. Instead of θ'' and θ' which normally form on the $\{111\}_\alpha$ plane, the Ω phase may be identified [1, 20], forming as thin plates on the $\{111\}_\alpha$ plane. The phase is very close with respect to its structure to the equilibrium phase θ [21]. Ω phase is identified to improve the mechanical properties. As such it has been identified that alloys hardened by Ω phase have less grain boundary precipitation and, as a result, exhibit enhanced fracture toughness [20]. In Ref. [22] an overview of research on precursors of the Ω has been given. It is not entirely clear what kind of phase can form nuclei for the precipitation of Ω phase. It has been stated [23] that Mg_3Ag could act as nuclei, whilst elsewhere [24, 25] it has been suggested that MgAg clusters promote the formation of Ω phase.

2.1.4 Precipitate free zones

Precipitate free zones (PFZ) are commonly situated around grain boundaries and may appear in all alloys where precipitation reactions occur. There are two common reasons for the formation of precipitate free zones [1]. Firstly, in a small region around the grain boundaries (of the order of 10s of nms) there may be a reduced solute content due to diffusion of the alloying elements to grain boundaries where relatively large equilibrium particles are formed. The second reason for PFZ around grain boundaries may be the

depletion of vacancies, as critical concentration of vacancies is needed for the formation of precipitates.

PFZs may be detrimental for the mechanical properties of a material as well as for corrosion resistance. The yield strength of the PFZ is significantly lower than that of the main matrix. As such, strain concentrations may then occur in PFZs which may result in premature failure, which will especially influence (various measures) of toughness [26].

2.1.5 Quenching, quench sensitivity and quench factor analysis

The aim of quenching is to maintain the solid solution formed during the solutionizing process to a lower temperature (typically to room-temperature). Not only solute atoms are affected by the quench rate but also the amount of vacancies which are necessary for precipitate formation. If during the quenching procedure solute precipitates on grain boundaries, dispersoids or other particles (i.e. heterogeneous precipitation), it is effectively lost for the age hardening of the material [8, 9]. Quench sensitivity is a general term used to describe whether the properties of a material are sensitive to variations in quench rates or not. Generally, the higher the amount of alloying elements the higher is the quench sensitivity of an alloy. At high alloying element contents supersaturation of the matrix can occur which can then lead to faster formation of particles during the cooling. It has been identified that yield strength and ultimate tensile strength are less sensitive to quench sensitivity than fracture toughness which is however often the more critical parameter [9, 27, 28]. In order to achieve the highest strength and the best balance of strength and toughness high quench rates are desirable. Experimental procedures as well as mathematical models [29] have been developed to determine the shift in strength due to different quench rates. However, few models are available for the prediction of the shift in fracture toughness due to quench sensitivity [9]. Rometsch *et al.* [30] developped a model for the prediction of quench sensitivity. It has been applied on experimental hardness data of a 6XXX alloy after application of different quench rates and achieved a good agreement. In Refs. [31, 32] the effect of water and air quench on the tensile behaviour and the fracture in a 6061 alloy have been assessed. Substantial drops in tensile strength and toughness have been identified and attributed to precipitation of coarse phases on the grain boundary along with the creation of a large precipitate free zone (PFZ).

During quenching there is a temperature range where the highest loss of solute can occur when the quench rate is not fast enough. At temperatures near the solutionising

temperature, diffusion rates are high, whereas there is a low degree of supersaturation. At relatively low temperatures (approaching room temperature) there may be a high degree of supersaturation, but diffusion rates are relatively low. At both of these extremes precipitation rates are low and in a temperature vs. time diagram the curve enclosing the critical regime in quench processing therefore has the shape of a 'C', or may be considered to form a "nose" (see Figure 2-2). In this range the degree of supersaturation as well as diffusion rates are high. The average quench rate through the critical area can give a prediction of the solute loss if the quench rates are reasonably constant. If not, property predictions may only be made using quench factor analysis using C curves (see Figure 2-2). In Ref. [33] the potential and assumptions of quench factor analysis are discussed and some improvements are suggested.

In Ref. [9] interrupted quenches (IQ) have been carried out in order to determine the quench sensitivity of strength and toughness in Al-alloys. Interrupted quench is carried out via rapid quench of small samples that are then held at a certain temperature at a certain time. It has been found that single C curve models can predict the shift of strength due to quench near temperatures of maximum quench sensitivity [9], however at high or low temperatures the predictions are less satisfying. It has been pointed out that "multi C curves" can enhance the predictions of strength [34, 35]. Such multi C curve approaches have also been considered in Ref. [9] taking into account different resulting fracture modes.

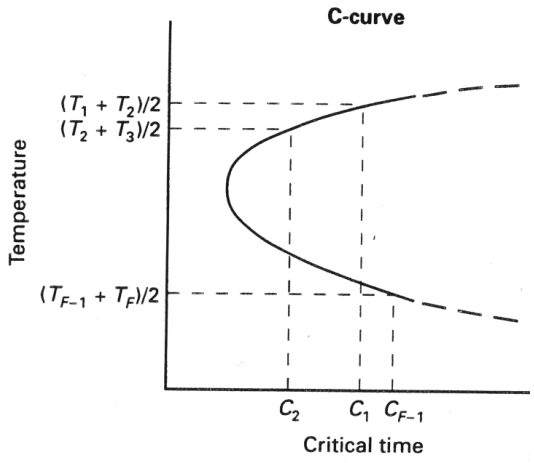

Figure 2-2: Typical C-curve (after Ref.[8])

The most common quench medium is water. Other quench media and procedures are for example air quenching, oil quenching, mist quenching or water spray quenching. Slower

quench rates may on occasion be needed for example for pieces with different thicknesses where a fast quench would lead to very different quench rates within the piece which would cause residual stresses and hence distortion.

Additional attention must be drawn to quench delays, i.e. time elapsing between the moment when a material is taken out of a furnace, and the actual immersion in the quench medium. If this delay is too long, detrimental precipitation effects may again occur.

2.1.6 Strengthening of aluminium alloys

Strength is one of the most important criteria for the choice of a material for an aerospace structure. In aluminium alloys there are 5 main mechanisms which cause strengthening [19]. Solution strengthening, precipitation strengthening, dispersion strengthening and work hardening increase the critical resolved shear stress (CRSS) τ of grains. CRSS of individual grains may then be linked to the macroscopic yield strength of a polycrystal by the following equation [19, 36].

$$\Delta\sigma_y = M\tau \qquad \textbf{(2-1)}$$

Where M is a constant of the order of 2 to 3 [19], reflecting the grain orientation and mechanical compatibility influences.

2.1.6.1 Solid solution strengthening

There are different models for the solid solution strengthening of Al alloys. In Ref. [37] three effects have been taken into account: size effect, modulus effects and short range order effect. The difference in CRSS due to the dissolved elements for the size effect and the short range effect may be given by the following equation :

$$\Delta\tau_{sol} = Ac^{\frac{2}{3}} \qquad \textbf{(2-2)}$$

Where c is the solute concentration. For the size effect A is a function of the shear modulus and the variation of the lattice parameter with alloying, whilst A depends on the alloying element.

For the short range order effect the difference in CRSS is dependent on the concentration c (to the power 1).

2.1.6.2 Precipitation strengthening

Precipitation strengthening is the dominating strengthening mechanism in heat treatable alloys for aerospace applications.

The increase of CRSS due to precipitation strengthening can generally be approximated as [38]:

$$\Delta\tau_{prec} = C_1 f^m r^n \qquad \text{(2-3)}$$

where *f* equals the volume fraction of the precipitates, *r* equals the radius of precipitates and C_1, *m* and *n* are positive constants depending on the particular strengthening mechanism and alloy system considered.

The strength of the material is strongly linked to the size of the precipitates. There are two broad mechanisms by which the dislocations can then interact with precipitates:

- when precipitates are small they may be overcome by shearing
- large precipitates are overcome by by-passing, *i.e*. they are not sheared

2.1.6.3 Dispersion strengthening

The strength of a two phase alloy is governed by the interaction of dislocations and metallurgical obstacles. Those obstacles may be formed by age hardening (see previous section) or by introducing particles. Examples for the addition or formation of particles may be the internal oxidation or powder metallurgical processes such as mechanical alloying [39]. The main advantage of alloys strengthened by powder metallurgical processes is their possible use at elevated temperatures as the particles do not dissolve or coarsen so that strength is preserved [8]. Furthermore these materials can exhibit light weight, appreciable ductility and resistance to stress corrosion cracking. Aluminium alloys strengthened by mechanical alloying commonly contain oxides, oxynitrides and/or carbides in a fine grain aluminium matrix [8].

2.1.6.4 Grain boundary or subgrainboundary strengthening

Grain boundaries are barriers for dislocations. As a result the higher the amount of grain boundaries in the material, i.e. the smaller the grain size, the higher the strength of the material. The yield strength is commonly identified with the grain size according to the Hall-Patch equation [36]:

$$\sigma_y = \sigma_0 + k_y d^{-\frac{1}{2}} \qquad \text{(2-4)}$$

Where d is the average grain diameter, and σ_0 and k_y are constants for a particular material. k_y has been reported to be greater than 0.2 for Mg containing alloys and around 0.15 for non Mg containing alloys [40].

2.1.7 Texture

Texture is identified with the distribution of crystallographic orientation of a given grain structure. For rolled Al alloys one can generally distinguish between rolling texture and recrystallization texture. Rolling textures are introduced by cold work in rolled sheet as plastic deformation or slip happens in certain crystallographic planes and directions[1].

2.2 Fracture

Continuum fracture mechanics approaches to fracture are well established for linear elastic situations where plastic deformation occurs only in a very small region. Theories for elastic-plastic fracture behaviour have also been widely developed. In the case of the Kahn tear tests which are used for the toughness assessment of aluminium alloys in the present project, the material behaviour is highly plastic and failure characterisation must consider this appropriately. In this chapter aspects of Kahn tear testing, ductile fracture, micromechanical models and FE based local approach to fracture (especially the Gurson model) are addressed.

2.2.1 Kahn tear tests

In Ref. [41] it has been indicated that Kahn tear tests may provide valuable quantitative fracture results with a relatively compact simple test methodology. The in-plane test piece dimension are about 35mm x 60mm. Kahn tear tests may provide so called "*R* values" which are a measure of fracture toughness for tough, thin samples with moderate strength. *R* values are commonly determined by large panel M(T) tests (around 1m x 1m test piece size). In [42] an FE model has been suggested to predict M(T) *R* values from Kahn tear test *R*-values and material data, such as stress strain curves for different test directions, porosity and intermetallic content. There is significant interest in obtaining quantitative toughness from Kahn tear test specimen as they are easier to perform and less material consuming than more 'rigorous' large panel M(T) tests. Kahn tear tests are used, in the first instance, to rank materials with respect to notch toughness and resistance to crack propagation [43]. They can provide data for nominal "initiation energy" which can be obtained by integrating the area under the force-displacement curve from the beginning of the curve to the point of maximum force, as well as the "propagation energy", obtained by integrating the area under the force-displacement curve from the point of maximum force to the point of complete fracture [43] (see Figure 2-3).

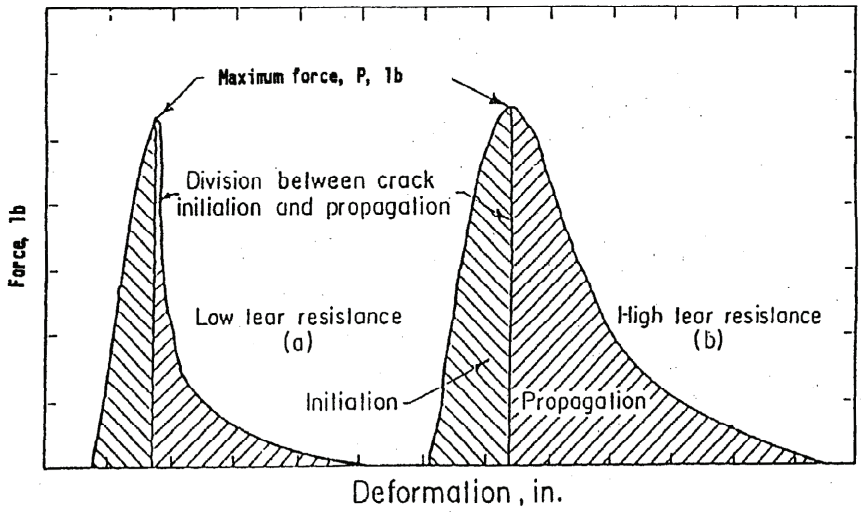

Figure 2-3: Typical force-deformation Kahn tear test curves; distinction between initiation and propagation energy (after Ref.[43])

It has been identified that the initiation energy obtained by Kahn tear tests (of 3mm thickness) is proportional to the square of K_{IC} obtained via compact tension (CT)-tests for a wide range of strengths in AA7xxx thick plate alloys [27]. In Kahn tear tests neither LEFM nor Elastic-Plastic Fracture Mechanics can be readily applied because of the very extensive plastic deformations involved in the fracture of aluminium alloys for aerospace applications. The following equation has been particularly proposed for obtaining R values for Kahn tear tests [42].

$$R = \frac{1}{B_0}\frac{\Delta U_{diss}}{\Delta a}\bigg|_{a=5-15mm} \qquad (2\text{-}5)$$

Where ΔU_{diss} is the change of dissipated energy and Δa is the increase in crack length. The dissipated energy is the total energy minus the elastic energy of the test. B_0 is the initial plate thickness. The values are summed from a crack length of 5mm to a crack length of 15mm (values are chosen to make sure that the crack is out of the mixed stress state-region for this calculation). The unit of R is N/m.

2.2.2 Plane stress/Plane strain and stress triaxiality

Within a notched test specimen under load there are different stress states. To quantify these stress states the stress triaxiality, τ, as defined in equation (2-6) is often used.

$$\tau = \frac{1}{3}\frac{\sigma_{kk}}{\sigma_{eq}} \qquad (2\text{-}6)$$

Where σ_{kk} is the trace of the stress tensor and σ_{eq} is the von Mises stress.

At a deeply embedded crack tip in a sufficiently thick specimen there may be significant stress triaxiality due to elastic constraint in the through-thickness direction and the crack growth direction. The material around the crack particularly tries to contract in the through-thickness direction as high stresses normal to the crack plane are generated but the material is prevented by the presence of the surrounding elastic bulk. High stress triaxiality may be seen to be particularly detrimental to damage evolution [44, 45]. In this situation a particularly high strain gradient and high tensile and hydrostatic stresses are present around the crack tip. In the interior of a thick plate the stress triaxiality near the crack tip may be very high, whilst it is lower at the edges because the stresses in through-thickness direction decrease the closer the material is to the free surface where there can be no stresses in the through-thickness direction (plane stress state). As a crack grows the plastic zone size tends to increase and the stresses in the through-thickness direction may relax more easily and become smaller. In other words the stress state in the mid-thickness may change from high triaxiality to lower triaxiality as the crack grows due to the relaxation of through-thickness stresses by increasing plastic deformation.

The effect of specimen thickness on strain to failure has been investigated numerically on notched plates in [45]. Figure 2-4 shows the strain at fracture of notched samples with different initial thicknesses (B_0) for different distances from the sample mid-thickness. Results for plane stress (PS) and plane strain (PE) computations are also shown. It becomes evident that the thicker the sample and the closer the position to mid-thickness the closer the strain to failure is to a plane strain sample.

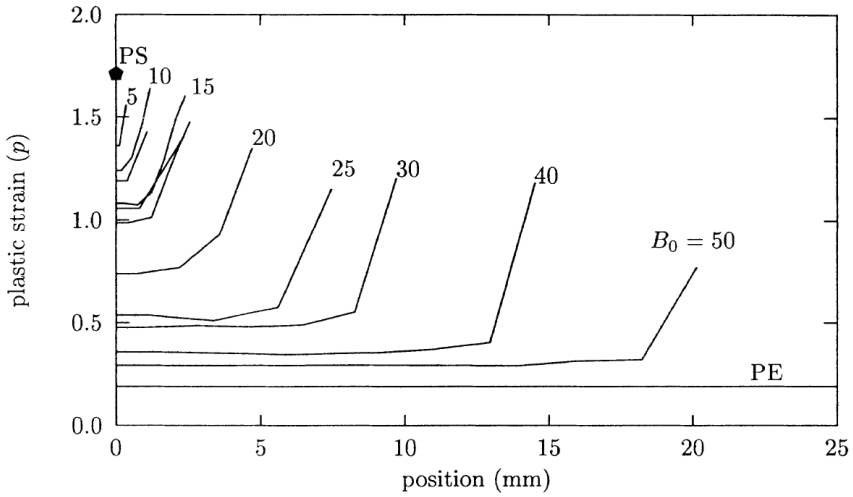

Figure 2-4: Through thickness profiles (at Gauss points) of strain at fracture for various initial plate thicknesses (after [45])

The evolution stress triaxiality in Kahn tear test specimen (also see previous section) during crack initiation and crack propagation has been investigated via a FE analysis in [42]. Figure 2-5(a) shows the evolution of modified stress triaxiality as a function of crack location and COD. The modified stress triaxiality is higher at crack initiation (0mm) than at crack propagation (5mm from the notch) for this 1.6mm thick material. Figure 2-5 (b) shows the logarithmic deformation in 3 directions as a function of the COD. It can be seen that in the propagation region (5mm) the deformation in crack growth direction E_{prop} is close to 0. In other words a situation very close to a plane strain state can be found *with respect to the crack growth direction* in the present configuration. In very thick specimens however (*e.g.* CT specimens) the plane strain direction corresponds to the through-thickness direction.

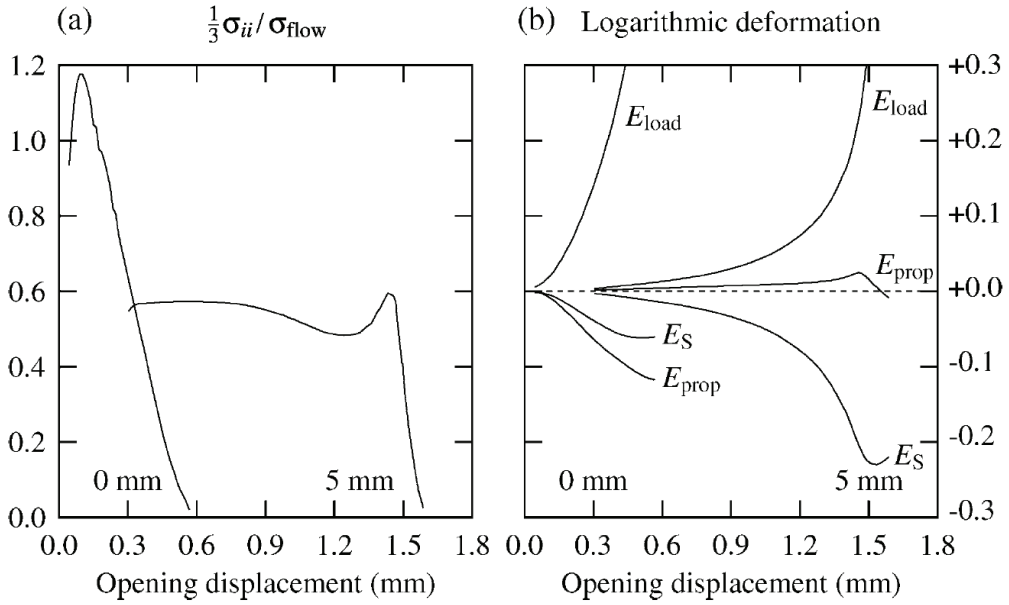

Figure 2-5: 3D Kahn simulation; comparison of the flat triangular fracture zone (0 mm: at the notch root) and the slanted fracture zone (5mm away from the notch root). (a) Stress ratio controlling damage growth in constitutive models and (b) strain state. E_{load}, E_{prop} and E_S stand for the logarithmic deformations in the loading direction, in the propagation direction and in the S direction, respectively. The results are given from the onset of plasticity to rupture (after [42])

2.2.3 Ductile Fracture/ Micromechanical behaviour

As ductile fracture involves mechanics and microstructure it is important to understand the microstructural features and their behaviour with respect to fracture. Aluminium alloys generally fail through ductile fracture. The following stages are then generally associated with the fracture process [46]:

- Nucleation of voids on second phase particles.
- Void growth through plastic deformation.
- Void coalescence to form a complete crack.

It is generally difficult to distinguish between the three different steps, as during crack propagation all the three processes can of course occur simultaneously.

2.2.3.1 Void initiation

Nucleation of voids in Al-alloys is generally linked to cracking of second phase particles or decohesion of the corresponding particle-matrix interface. Commonly the cracking and/or decohesion of particles starts at the largest particles present in a material [47]. Whilst the voids are growing at/around these particles, voids may then start to nucleate at

smaller particles as local stress and strain levels increase. For decohesion of particles from the matrix, the strength of their bond with the matrix may clearly play an important role. For instance, if there is impurity atom segregation around the coarse particles, the stress at which decohesion takes place and voids initiate may be lower [47]. Whether void formation occurs through cracking of a particle may depend on the particle structure size, the strength of the matrix, particle shape and the strength of the matrix-particle bond. In some less prevalent cases, void initiation does not occur at coarse second phase particles. In those cases, grain boundaries, vacancy clusters or slip band intersections can be identified as potential void nucleation sites [47].

Void initiation via particle/matrix decohesion may not only depend on microstructural features but also on the stress state the material is in. At higher levels of stress triaxiality the voids may initiate at lower strains in metals than in a uniaxial stress state [47] .

2.2.3.2 Void growth

After the initiation of voids they may initially be considered to grow independently. Plastic deformation (*i.e.* dislocation motion) is required for void growth to occur. Void growth is known to be promoted by high levels of stress triaxiality, and depends on material properties. Numerous attempts have been made to model void growth. Examples include the work of Ashby [47], who has based his model on dislocation movement, or the continuum mechanics model for void growth suggested by McClintock [47]. Those models have been the basis for further improved models, such as those developed by Gurson [48] and Roussellier [49] (see section 2.2.5).

2.2.3.3 Void coalescence

During void coalescence, initiated voids link up and a crack can grow. There are two main processes for void coalescence which are commonly discerned: the first process only involves one population of particles. Other particles may be present but they do not contribute to the void coalescence. Voids initiate and grow around this one kind of particle (see Figure 2-6 (a) and (b)) until they coalesce through impingement of the formed voids when high strains are achieved in the ligaments between primary voids (see Figure 2-6). Voids link up occurs through necking of the remaining material.

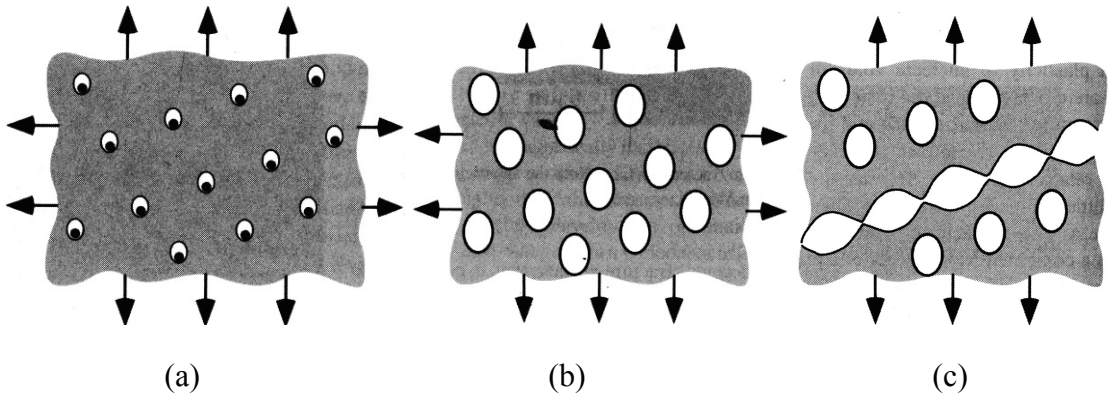

Figure 2-6: (a) initiation, (b) growth and (c)impingement of voids (adapted after Ref. [46])

A common alternative mechanism for void coalescence is when voids first form at one population of particles and subsequently in another population of particles. The second population is generally smaller and better bonded to the host matrix than the first. The voids formed first coalesce with the subsequently formed voids when high strains are achieved in the ligaments between primary voids (see Figure 2-7 and Figure 2-8). In aluminium alloys the coalescence process is often linked to shear decohesion at dispersoid particles, forming void sheets. The sheets act as a rapid coalescence mechanism lowering fracture toughness as strains causing failure are highly localised.

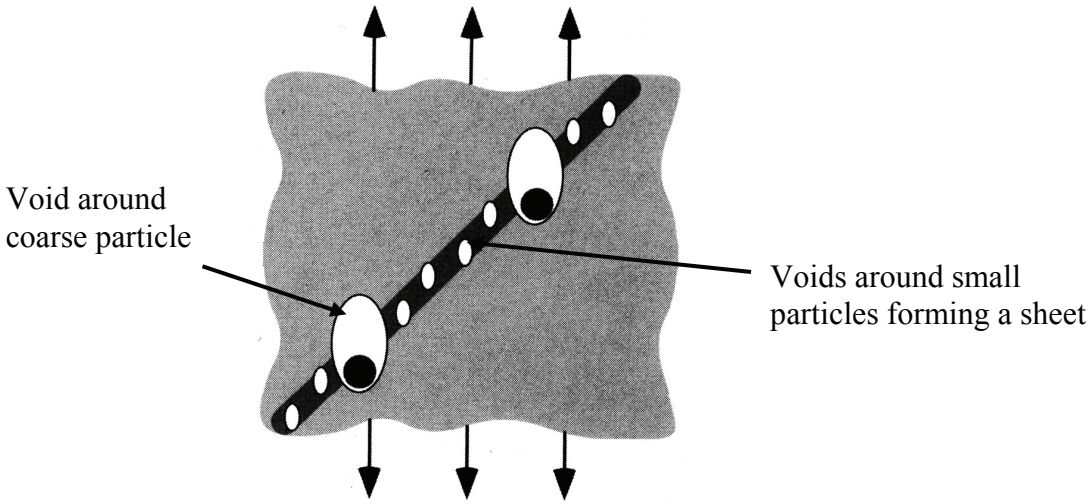

Figure 2-7: Schematic sketch of the void sheet coalescence mechanism (after Ref.[46])

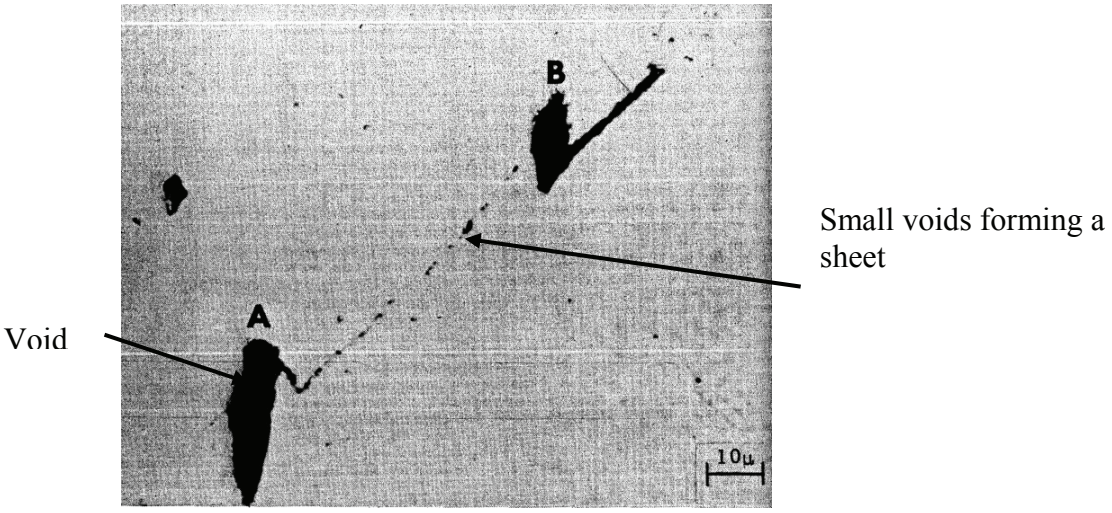

Figure 2-8: Coalescence of two voids by a void sheet mechanism in 4340 steel (after Ref.[47])

2.2.3.4 Slant fracture

Slant fracture is observed in stable tearing tests of many ductile thin sheet materials that are loaded under remote mode I loading conditions [50]. The crack typically starts near the machined notch with a macroscopically flat region normal to the loading direction that is subsequently in the propagation region turning into a slant crack with an angle of ~45° with respect to the loading direction. It has been pointed out that flat fracture corresponds to mode I type crack growth whilst subsequent slant fracture corresponds to a mixed mode I/III type crack growth even though remote loading conditions are mode I for both cases [51]. The phenomenon of slant fracture and the flat to slant fracture transition is still not well understood [51]. As was pointed out in previous sections (see section 2.2.2), fracture initiation in the flat triangular region is dominated by high levels of stress triaxiality [52] that is known to favour void growth [53]. In the slanted region stress triaxiality and the mean stress, $\sigma_{kk}/3$, are smaller so that void growth is less pronounced and void nucleation at a 2nd population of 2nd phase particles , the so-called void sheeting [47], is promoted [42].

In a finite element study [51] the crack propagation of a meshed flat and a slant crack have been investigated. The stress fields ahead of the respective cracks during crack propagation under remote mode I loading have been compared and it was identified that for a slant crack the constraint and the mean stress ahead of the crack are reduced whilst the effective stress is augmented compared to a flat crack. Slant fracture has been found to promote a shearing type of fracture.

Modelling and simulating of the flat to slant transition still reveals to be difficult. Mathur *et al*. [54] have succeeded to simulate the flat to slant transition for dynamic crack growth but a comparison with experiments has not been provided. Besson *et al*. [55] have also modelled the flat to slant transition but the model overestimated the structural response. More recently Xue *et al*. [56, 57] have managed to model slant fracture but the numerical results have not been compared to experiments either. In these studies use was made of a damage accumulation rule and the Lode parameter [58]. It has been identified that at low to intermediate stress triaxiality regimes, stress triaxiality may not be sufficient to predict ductile fracture and the Lode parameter should be used [59]. The Lode parameter μ defined for stresses is shown in the following equation:

$$\mu = \frac{2\sigma_2 - \sigma_1 - \sigma_3}{\sigma_1 - \sigma_3} \qquad \textbf{(2-7)}$$

Where $\sigma_1 \geq \sigma_2 \geq \sigma_3$ are the principal stresses.

The Lode parameter may have values between -1 and 1. In Figure 2-9 the three special cases of generalized tension (μ = -1), generalized shear (μ = 0) and generalized compression (μ = 1) are are shown.

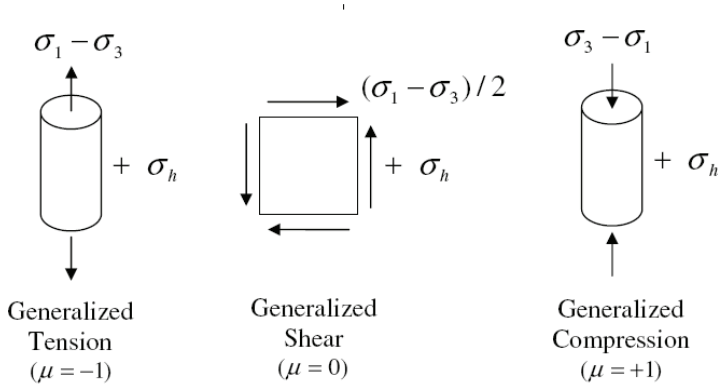

Figure 2-9:Illustration of the Lode parameter μ and the three special cases: generalized tension, shear and compression, respectively after [59]

For shear fracture stress states at a Lode parameter of μ = 0 are particularly relevant.

2.2.3.5 Toughness Anisotropy

One materials issue that is particularly difficult to take account for in predicting toughness performance is the anisotropy of toughness of sheet. During processing, casting as well as thermo-mechanical processing steps such as rolling, anisotropic microstructural features can be introduced.

Possible microstructural sources of toughness anisotropy are numerous that are often all present in engineering alloys.

1. One possible cause is crystallographic textures developed during rolling which will cause the energy dissipated during fracture to depend on the local load level and consequently on the loading direction for anisotropic materials [60-64].

2. The second cause of toughness anisotropy is related to the anisotropic shape and distribution of defects introduced by the material processing [27, 65-70]. Processing may create elongated or flat micro-voids which can either slow down or accelerate damage growth as demonstrated by recent models for ductile damage including the effect of cavity shape [71-74]. Mean defect spacing, which can also depend on the direction, was also shown to affect toughness as it strongly influences the onset of void coalescence [67, 75-79].

3. The third cause of possible toughness anisotropy is initial deformation as sheet materials are often prestrained. Prestrain may cause initial damage, decrease hardening capacity, increase yield stresses and generate internal back stresses (*i.e.* kinematic pre-hardening), all of which can be anisotropic in nature. Such effects can occur for instance in pipeline steels as sheets are deformed to form tubes or in rolled aluminium alloy sheet. This final point has been less investigated than the others but recent results show that prestrain may affect ductility and toughness [63, 80, 81]. All factors linked to prestrain may either decrease or increase toughness but the generation of back stresses appears to have the strongest influence on toughness anisotropy as prestrain induces very little damage and as changes in isotropic hardening will affect all directions in the same way.

2.2.3.6 Intergranular ductile failure

Heat treatable aluminium alloys are well known to be susceptible to intergranular ductile fracture depending on their heat treatment. Grain boundaries (gb) are then the preferred crack path. Three common mechanisms have been reported to be the origin of grain boundary ductile failure [26]:

- Microvoid growth at large gb particles
- Strain localisation in soft, sometimes solute-free, precipitate free zones (PFZ) around the grain boundary.
- The influence of matrix precipitate shear giving rise to inhomogeneous "planar" slip that may apply large stress concentrations to the grain boundary at the blocked ends of slip bands.

The first mechanism is widely reported [26, 82, 83]. The gb particles have been identified to be nucleation sites in grain boundary ductile failure by comparing the distances of the gb particles in the bulk material and the distances of the dimples on the fracture surfaces. There is evidence that large gb particles are more detrimental to fracture toughness than smaller ones [84]. For Al-Li alloys a substantial reduction of toughness was reported for an increasing surface coverage A_f of coarse particles, whilst the matrix yield strength was equivalent. A model has been suggested giving a relationship between toughness (K_c) and grain boundary particle surface coverage A_f [85]:

$$K_c \sim \left(\frac{1}{A_f}\right)^{\frac{1}{2}} \qquad \textbf{(2-8)}$$

Precipitation of secondary phases on the grain boundaries can for example happen during a slow post solutionising quench, when heterogeneous precipitation may take place on high energy interfaces. For overaged alloy conditions coarse grain boundary precipitates may be alternatively attributed to the ageing process [26]. The determination of the exact gb coverage has often proven to be difficult [86].

Where PFZs have a lower yield strength than that of the rest of the matrix (*i.e.* the surrounding grain 'bulk') strain concentration may occur [26] that may contribute to grain boundary failure. The strain localization has for example been identified through TEM

studies where high dislocation densities have been found. Such localization may then promote the growth of voids at grain boundary particles. Grain boundary ductile failure may also occur without the presence of a PFZ but its toughness is expected to be higher than for the presence of a PFZ [26]. Additionally it has been reported that PFZ width may have only a minor influence on fracture toughness [83] as an increase of the PFZ width from 0.1μm to 0.6μm has not shown an effect on the measured toughness. Especially low fracture strain has also been reported for the configurations where grain boundaries are favourably oriented to promote shear in the PFZ [87].

An increase in PFZ width may ultimately be expected to cause a decrease in yield strength and upper tensile strength. However, the influence of such changes is generally reported to be higher on fracture toughness than on flow strength [9]. The properties of the PFZ may be expected to depend on whether it has appeared through solute depletion or vacancy depletion. In the case of solute depletion the PFZ may be very soft with properties close to those of pure aluminium, whilst in the case of vacancy depletion the PFZ is hardened by the presence of alloying elements causing solid solution strengthening. However, as high strength aluminium alloys typically develop considerable precipitation strengthening levels, the PFZ may still be substantially softer than the matrix in both cases.

2.2.4 Modelling of toughness

There have been numerous attempts to model fracture toughness of aluminium alloys. Most of the models try to account for one or more of the following three identified fracture mechanisms:

- Voiding at coarse intermetallic particles that are separated from the matrix via cracking or decohesion
- Transgranular fracture via shear decohesion
- Intergranular fracture

However, it is challenging to account for the various microstructural features as well as stress states that influence the fracture mechanisms, and, as a result, it is virtually impossible to take all factors that influence fracture toughness into account. Each toughness model needs to identify an appropriate fracture criterion. Due to the complexity of the relationship between microstructure, stress state, fracture mode and toughness all models make simplifying assumptions so that they are only valid for certain microstructural configurations. Some models even introduce parameters that have no physical meaning at all. This section includes a non-exhaustive overview of various key contributions to the literature on modelling of fracture toughness.

Early models for fracture toughness that have been developed mainly deal with one fracture mechanism. In the model of Hahn and Rosenfield [88] special attention is drawn to the voiding around coarse intermetallic particles. It is assumed that coarse intermetallic particles fracture at very low strain. The criterion for fracture therefore considers the distance between the fractured particles that needs to be overcome to form a crack. It is assumed that fracture occurs when the distance λ_c between cracked coarse particles equals the extent of the heavily deformed regions ahead of the crack tip, equated with δ, the crack tip opening. The size of the heavily deformed zone ahead of the crack tip will depend on the yield strength σ_{ys} and the Young's modulus E of the material. For this linking-up mechanism the volume fraction of the coarse particles f_c and their average diameter D is taken into account. The model then predicts:

$$K_{ICi} \sim \left[2\sigma_{ys} E \left(\frac{\pi}{6} \right)^{\frac{1}{3}} D \right]^{\frac{1}{2}} f_c^{-\frac{1}{6}} \qquad \textbf{(2-9)}$$

The most obvious contradiction of this model to common experimental experience is that toughness is supposed to rise with the yield strength, which is generally not found to be true. This equation may not however show all the parameters fracture toughness depends on: it has been stated by the same authors [89] that the plane strain fracture toughness may indeed increase with increasing yield strength but decrease with decrease in strain hardening exponent following the equation:

$$K_{IC} \sim n\sqrt{\sigma_y \varepsilon_f} \qquad \textbf{(2-10)}$$

Where *n* is the hardening exponent, σ_y the yield strength and ε_f the critical strain, that depends on the volume fraction of void nucleating particles. Generally, the value of the strain hardening exponent is seen to fall with increasing yield strength so that the influence of an increasing yield strength on toughness is compensated for by the linked decreasing value of strain hardening exponent. Ehrströhm *et al.* [90] have made an attempt to adapt the Hahn and Rosenfield model to cases where the intermetallic particles are clustered by including the work of Mudry [91]. The model has been applied to 6XXX alloys and 7XXX alloys in different conditions. However, the yield strength has been similar for alloys in the same condition with different fractions of intermetallic particles. A good agreement has been found between the developed model and experimental data.

Garrett and Knott [92] have developed an expression for toughness due to transgranular shear decohesion in Al-Cu alloys that has subsequently been refined by Chen and Knott [7]. In this model the critical strain to failure at the crack tip is linked to a critical crack opening displacement (COD). The equation linking the average strain at the crack tip γ to the plastic zone width $l_{(n)}$ and the COD, δ is taken from the work of Hahn and Rosenfield [89]:

$$\gamma = (\delta / 2) / l_{(n)} \qquad \textbf{(2-11)}$$

For the tensile stress acting across the particle/matrix interface when the matrix is deformed, an expression developed by Ashby [93] is used:

$$\sigma_c = A\frac{\gamma_c d}{2b\lambda} \quad \textbf{(2-12)}$$

Where γ_c is the average shear strain, λ is the dispersoid spacing, d the diameter of the dispersoids, b the Burgers vector, and A is a (dimensional) factor of proportionality. Following the work of Hahn and Rosenfield [89] the width the plastic zone $l_{(n)}$ is expressed as a function of the strain hardening exponent n.

$$l_{(n)} \sim \frac{1}{40}n^2 \quad \textbf{(2-13)}$$

Combining those equations toughness is then expressed as a function of yield strength, σ_{ys}, and strain hardening exponent, n as follows:

$$K_{ICi} = Cn\sqrt{\sigma_c \sigma_{ys} \lambda} \quad \textbf{(2-14)}$$

Where σ_c is the decohesion stress, σ_{ys} is the yield stress, λ is the particle spacing n is the strain hardening exponent and C a constant. However, the model is only valid for a constant fraction, distribution and morphology of second phase particles.

Hornbogen [94] has developed a model for toughness exclusively taking into account grain boundary ductile failure and not considering void growth around intermetallic particles or transgranular fracture via shear decohesion. In this model, it is assumed that the deformation in the material only occurs in soft zones around the grain boundary and that the material fractures when a critical local strain is attained in the soft zone. As a result the model may only be valid for cases where the matrix has substantially higher yield strength than the precipitate free zone around the grain boundaries. The relationship for plane strain fracture toughness is derived from the model developed by Hahn and Rosenfield [88]. Hahn and Rosenfield's expression for the bulk plastic properties is applied to the plastic properties of the PFZ:

$$K_{ICi} \sim \left[L_i E \sigma_{yi} n_i^2 \varepsilon_{fi} \frac{d}{D} \right]^{\frac{1}{2}} \quad \textbf{(2-15)}$$

Where L_i is an empirical constant with the dimension of a length, E is the Youngs modulus, σ_{yi} is the yield strength, n_i is the work hardening exponent, ε_{fi} is the

elongation at fracture. *d* is the thickness of the grain boundary PFZ and *D* is the average grain size. Index *i* refers to the soft PFZ.

In equation (2-15), the grain size of the material has an influence on the toughness of the material: the smaller the grain size the higher the fracture toughness. This toughness prediction is in line with experimental results [94]. Hornbogen and Gräf [95] have extended the model developed by Hornbogen in order to account for transgranular fracture and to obtain a multimechanistic model. In the Hornbogen and Gräf model the relationship between the strain at fracture ε_{fi} and the volume fraction of incoherent particles f_i at the grain boundary and the critical strain to nucleate voids ε_n is specified by the proportionality that represents a simplified model for void coalescence [96]:

$$\varepsilon_{fi} \sim \ln\left[\sqrt{\frac{\pi}{f_i}} - \sqrt{\frac{2}{3}} + \varepsilon_n\right] \qquad \textbf{(2-16)}$$

The strain to fracture is considered here as a sum of strain to create voids and strain to grow them to a critical size. In this relationship the strain at fracture decreases with an increasing fraction of incoherent particles which is consistent with experimental findings [85]. The model takes into account the two different fracture mechanisms, transgranular and intergranular failure, by introducing a parameter for the portion of intergranular failure. This parameter depends on the different orientations of the grain boundaries. Initially it is identified that high shear stress promotes intergranular ductile failure. The angle of maximum shear stress with respect to the loading axis is taken to be 45°. If the angle of a grain boundary with respect to the angle of maximum shear stress is larger than a critical angle $\Delta\Phi_c$ it is assumed that transgranular failure occurs.

The fraction of grain boundary contribution to intergranular failure is represented in the introduced parameter *:*

$$p_i = \frac{4\Delta\Phi_c}{\pi} \qquad \textbf{(2-17)}$$

In order to obtain a fracture toughness value for mixed failure modes the toughness value for the different mechanisms are added linearly and weighted in the following manner:

$$K_{IC} = K_{IC_t}(1 - p_i) + K_{IC_i} p_i \qquad \textbf{(2-18)}$$

Where K_{IC_t} is plane strain fracture toughness for transgranular fracture as it has been proposed by Hahn and Rosenfield [88] and K_{ICi} the term for the plane strain fracture toughness for intergranular fracture developed by Hornbogen [94].

Sugamata *et al.* [97] have also made an attempt to formulate a multimechanistic toughness model accounting for several fracture modes. The model takes into account intergranular and transgranular failure. The contributions of the different failure modes are weighted according to the area fraction of the different fracture modes on the fracture surface.

$$K_{IC} = K_{ICt} A_T + K_{ICi} A_i \qquad \textbf{(2-19)}$$

Where K_{ICi} is the fracture toughness of the intergranular fracture derived by Hornbogen [94]. K_{ICt} is the fracture toughness for transgranular fracture developed by Roven [98], A is the area fraction of the different fracture modes on the fracture surface. The model for transgranular fracture has similarities to the model developed by Chen and Knott [7]: it considers shear localisation in a slip band and its corresponding dimensions. This model does however not use the relationship between slip band width and strain hardening exponent (see equation (2-13)) as employed in the model by Chen and Knott [7]. The model for transgranular fracture started from a relationship developed by Hahn and Rosenfield [89] relating the plane strain fracture toughness to the hardening exponent n, the yield strength and the critical strain ε_f, that depends on the volume fraction of void nucleating particles:

$$K_{IC} \sim n\sqrt{\sigma_y \varepsilon_f} \qquad \textbf{(2-20)}$$

An expression for transgranular slip band/shear decohesion fracture has initially been developed by Jata and Starke [99], including the work of Duva *et al*. [100], relating fracture toughness to the slip band spacing S_{GB} and the slip band width W_{SB}.

The crack tip opening displacement is defined:

$$\delta = 2(Nb)\sin\alpha = \frac{0.5K_{ic}^2}{E\sigma_y} \qquad \textbf{(2-21)}$$

Where δ is the COD, N the extent of strain localisation, b the burger's vector, α the angle between the slip planes and the crack plane. The shear in the slip band is defined as:

$$\gamma_{SB} = \frac{Nb}{W_{SB}} \qquad \textbf{(2-22)}$$

A combination of those equations and a simplification of Roven [98] have lead to the final expression for the transgranular plane strain fracture toughness[97].

$$K_{ICt} = \left(\frac{2S_{GB}W_{SB}\sigma_y E}{M\tan(\alpha S_{SB})}\right)^{\frac{1}{2}} \qquad \textbf{(2-23)}$$

Where M is the Taylor factor, S_{GB} the grain boundary spacing and α the angle between the slip planes and the crack plane. It is predicted that for particle shearing the strain localization increases for decreasing slip band width and increasing slip band spacing. It should be noted that the form of such localisation of strain in shear bands is limited to underaged materials in the first instance.

Li and Reynolds [82] carried out intensive TEM studies of grain boundaries in Al-Cu-Mg-Ag alloy and applied the model of Hornbogen and Gräf [95], in combination with the work of Kawabata and Izumi [101], and the work of Embury and Nes [85]. Different ageing treatments were used in order to obtain parameters of grain boundary features such as half-PFZ width W, area fraction of grain boundary precipitates A_f, particle length L and half particle-thickness H and linked to the fracture toughness of the material (see Figure 2-10).

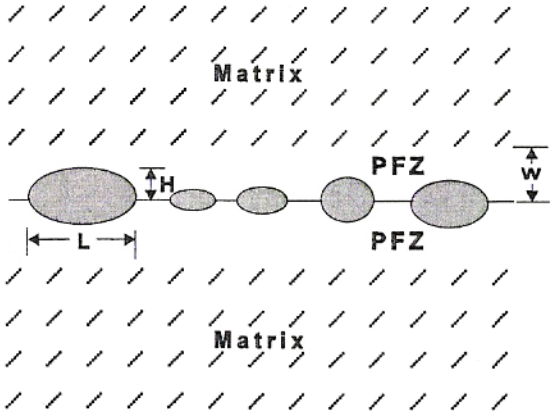

Figure 2-10: Schematic illustration of a grain boundary (after Ref.[82])

The data was successfully related to the Hornbogen and Gräf [95] model using the expression for the critical fracture strain ε_{fi}:

$$\begin{aligned} \varepsilon_{fi} &= k\frac{W}{D^3 N_s} \\ N_S &= n_1^2 \\ D &= (LH)^{\frac{1}{2}} \\ A_f &= \pi(D/2)^2 N_s \end{aligned} \qquad \textbf{(2-24)}$$

Where *k* is a constant related to the interfacial energy between grain-boundary precipitate and the matrix,

n_1 is the number of precipitates per unit length of grain boundary,

N_S number of precipitates of per unit area of grain boundary.

D the mean size of precipitate.

A_f the area fraction of the grain boundary precipitates.

In this study [82] the model proposed by Embury and Nes [85] has also been applied to the data. This model suggests that the plane strain fracture toughness is proportional to $(A_f^{\frac{1}{2}} - 1)^{\frac{1}{2}}$. When comparing the results of this model to the experimental results it appears

that the fit between model and experiment is better for the Hornbogen and Gräf [95] model in combination with the expression for the critical fracture strain suggested by Izumi and Kawagata [101].

Gokhale *et al.* [102] have developed a multimechanistic model for the fracture toughness of a 7XXX alloy. They point out that the stress intensity factors for the contributions of the different fracture mechanisms were not necessarily linearly additive [103] such as is assumed by Hornbogen and Graf [95]. Instead Gokhale *et al*. [102] state that the energy dissipation for a fracture process of more than one micromechanism is linearly additive. Therefore they develop a model based on fracture energies of particle cracking, intergranular failure and transgranular failure. These energies are linked to the area fractions of the different fracture mechanisms on the fracture surface (see equation (2-25)). The contribution of the coarse particles to the total plastic energy dissipation is assumed to be zero as constituent particles crack at very low stresses.

$$G_{IC} = G_{Ici} A_i + G_{Ict} A_t \qquad \textbf{(2-25)}$$

Where G_{Ici} is the energy release rate for intergranular failure and G_{Ict} is the energy release rate for transgranular failure; the area fraction on the fracture surface for intergranular regions is A_i and for transgranular regions A_t. The contribution of the coarse particles to the total plastic energy dissipation is assumed to be zero as constituent particles crack at very low stresses. The relationship between the area fractions on the fracture surface of the different mechanisms is simply given by equation (2-26).

$$A_i + A_t + A_p = 1 \qquad \textbf{(2-26)}$$

In order to be able to predict the fracture toughness of the material without knowing the features of the fracture surface Gokhale *et al.* [102] attempt to link microstructural features to fracture toughness. Special attention is drawn to the orientation of high angle grain boundaries with respect to the fracture surface as it is identified that under plane strain conditions intergranular failure tends to occur at high angle grain boundaries that are oriented in the primary fracture plane. The model describes the influence of recrystallisation with some success and accounts for different fracture mechanisms. However, it does not account for different quenching and ageing conditions of the material which influences the condition of the grain boundaries.

In a recent study Dumont *et al.* [104] have made an attempt to model fracture toughness that accounts for transgranular and intergranular failure. The model has been designed to be valid for a 7XXX alloy with a variety of different microstructures due to different compositions, quenching and ageing treatments. Similar to the model of Gokhale *et al.,* the basic idea of the model is to linearly add dissipation energies for transgranular and intergranular fracture, using:

$$E_{total} = E_i A_i + E_t A_t \qquad \textbf{(2-27)}$$

where E_{total} is the total dissipated energy, E_i is the dissipated energy for intergranular failure and E_t is the dissipated energy for transgranular failure. The area fraction on the fracture surface for intergranular regions is A_i and for transgranular regions A_t. The model used for the derivation of the transgranular fracture is that of Zehnder and Hui [105], which is a simplification of the model developed by Tvergaard and Hutchinson [106]. It describes the critical fracture energy as a function of the plastic properties of the material. Two effects contribute to this energy: the energy to create two free surfaces and the energy dissipated in the plastic zone at the crack tip. The energy to create two free surfaces, Γ_{trans}, is linked to the volume fraction of second phase particles f_v:

$$\Gamma_{trans} \propto f_v^{-\frac{1}{3}} \qquad \textbf{(2-28)}$$

The energy dissipated in the formation of the plastic zone is a product of the size of the plastic zone and the plastic work per unit volume to failure. Equation (2-29) shows the suggested expression for the energy dissipated in transgranular fracture;

$$E_t = \Gamma_{trans}\left\{1+\frac{E}{\pi}(\eta\sigma_y)^{(1-n)/n}\left[\frac{\left(\frac{\sigma_{decoh}}{\eta\sigma_y}-1\right)}{k}\right]^{\frac{1}{n}}\left(\frac{n+\frac{\sigma_{decoh}}{\eta\sigma_y}}{n+1}\right)\right\} \qquad \textbf{(2-29)}$$

where Γ_{trans} is the energy to create two free surfaces by transgranular progression, E is the Young's modulus, η a parameter taking into account the stress state of the material, σ_y

the yield strength, σ_{decoh} the local decohesion stress at which crack propagation occurs, *k* a factor employed in the plasticity law and *n* the hardening exponent.

The model for the intergranular failure accounts for different strain-stress behaviour of the matrix and the soft PFZ around the grain boundaries. For this model the considered shape of the grains is simplified to a rectangle that has two layers: the boundary PFZ and the grain matrix. The stress is proposed to be equal in both layers. The following expression is then derived to describe the energy dissipated in intergranular fracture:

$$E_{\text{int}er} = \frac{E\Gamma_{inter}}{2\pi\sigma_{0.2\%}^2 h_g}\left\{\left[\sigma_b + \frac{h_b}{2}\left(\frac{1}{\sqrt{f_{GB}}} - 1\right)\right]^2 - \sigma_g^2\right\} \qquad \textbf{(2-30)}$$

Where E is the Young's modulus, Γ_{inter} is the energy to create two surfaces by intergranular crack progression, h_g a factor in the linear hardening law for the grain interior, h_b a factor in the linear hardening law for the PFZ, σ_b the yield strength of the PFZ, σ_g the yield strength of the grain interior and f_{GB} the fraction of precipitates on the grain boundary.

Generally the determination of the area fractions of the different fracture modes on the fracture surface demands rupture tests of the material and it is somewhat subjective. As there are no models available to predict the fractions of failure modes [104] Dumont *et al.*[104] have suggested to compare the ratio of the fracture energies $\frac{E_i}{E_t}$ to the experimentally measured distribution of the fracture modes and it has been identified that there is a linear relationship between them. However, some interesting observations could be made, such as the fracture mode becoming fully transgranular before the dissipated energies by transgranular and intergranular fracture are equal. This implies that a crack needs additional energy to deviate to a grain boundary.

In summary, Table 2-3 gives an overview over the models presented and their corresponding features.

Authors/Ref.	Key Equations	Description/Assumptions
Hahn and Rosenfield [88]	$K_{IC} \sim \left[2\sigma_{ys} E \left(\frac{\pi}{6} \right)^{\frac{1}{3}} D \right]^{\frac{1}{2}} f_c^{-\frac{1}{6}}$	• mainly considers influence of coarse particles
Chen and Knott [7]	$K_{ICi} = Cn\sqrt{\sigma_c \sigma_{ys} \lambda}$	• Considers shear decohesion • Critical strain as fracture criterion • Considers bulk tensile properties
Hornbogen [94]	$K_{ICi} \sim \left[L_i E \sigma_{yi} n_i^2 \varepsilon_{fi} \frac{d}{D} \right]^{\frac{1}{2}}$	• Only considers GBDF • Deformation only occurring in soft PFZ • Considers influence of grain sizes
Hornbogen and Graeff [95]	$K_{IC} = K_{ICt} A_T + K_{ICi} A_i$ With the Hahn and Rosenfield [88] expression for transgranular fracture and Hornbogen [94] for intergranular fracture	• Multimechanistic • Takes into account grain boundary orientations • Fracture toughness for different modes presumed to be linearly additive • linear addition of fracture toughness of different modes
Sugamata *et al.* [97]	$K_{IC} = K_{ICt} A_T + K_{ICi} A_i$ With Hornbogen [94] expression for intergranular fracture and Roven [98] for transgranular	• Multimechanistic • Taking into account slip band width and spacing for transgranular failure • linear addition of fracture toughness of different modes
Gokhale *et al.* [102]	$G_{IC} = G_{Ici} A_i + G_{Ict} A_t$	• Multimechanistic • Fracture energies for different mechanisms linearly additive
Li and Reynolds [82]	Uses Hornbogen's [94] toughness expression Critical strain by Kawabata and Izumi [101]	• Only GBDF • Includes GB data from thorough TEM observations
Dumont *et al.* [104]	$E_{total} = E_i A_i + E_t A_t$ Intergranular expression from Embury and Nes, Transgranular expression following Zehnder and Hui [105]	• Multimechanistic • Considers energies • Valid for different quench rates and ageing states and linked microstructures • Linear addition of energies for different modes

Table 2-3: Overview over the different approaches to model fracture toughness

2.2.5 Local approach to fracture

In the last two decades the so called "local approach to fracture" has gained in prominence. Whilst in the "global" approaches one parameter (i.e. *K, J, etc.*) typically describes the material behaviour, the "local approach" accounts for the more specific features and mechanisms of a material. It therefore has advantages *e.g.* in the fields of welding, assembling, thermo-mechanical and non-proportional loading. Additionally, the local approach has the advantage that normally the model parameters only depend on material properties and not on specimen geometries [107]. As a result this may improve the transferability between test specimen and structure. The "local approach" to fracture consists of several steps [108]:

- A detailed experimental analysis of the considered materials and of their specific damage mechanisms
- A "realistic" modelling of these mechanisms
- Implementation of the model into a numerical simulation to predict the behaviour of structural components

In the field of FE modelling of ductile fracture mainly three different types of analyses are reported in the literature [77]: One way to model ductile fracture is to explicitly model voids surrounded by a refined FE mesh. This approach requires a criterion for final failure. The main drawback of this approach is the necessary limitation to a model incorporating only few voids given the long computation times.

In order to model the behaviour of entire structures constitutive models such as the Gurson approach are used (see next section). Initiation and growth of a crack can be modelled using this approach. In these analyses the mesh size is then a crucial parameter and needs to be carefully specified.

Attempts have also been made to model ductile fracture of structures utilising cohesive zone elements. Two characteristic parameters are used in the cohesive zone modelling: a characteristic length and a characteristic stress are set leading to an expression for the work of separation.

2.2.5.1 The Gurson model

In the local approach to ductile fracture, significant attention has been drawn in recent years to the model suggested by Gurson [48] that has later been modified and improved by Tvergaard [109, 110] and Needleman [111]. The Gurson model is in the first instance a model for the growth of voids. It is derived from a model that was previously developed by Rice and Tracey [53] that takes into account an isolated void. Contrary to previous approaches the Gurson model accounts for the hydrostatic component of the stress tensor that may cause macroscopic dilatation and affect plastic yield. It has the effect of introducing a strain softening term. The model represents a simplified porous material by a hollow sphere and introduces a void volume fraction *f*. Voids are assumed to stay spherical during their growth. The material is considered as continuous and homogeneous. A yield surface Φ for the porous material is then given by:

$$\Phi = \frac{\sigma_{eq}^2}{\sigma_0^2} + 2f\cosh\left(\frac{\sigma_{kk}}{\sigma_0}\right) - 1 - f^2 = 0 \qquad \textbf{(2-31)}$$

Where σ_0 is the yield stress of the matrix,

σ_{eq} is the von Mises stress,

σ_{kk} is the trace of the stress tensor and

f is the void volume fraction.

2.2.5.2 Unit cell calculations

In the local approach to fracture unit cell calculations with periodic boundary conditions have been revealed to be a useful tool to validate models and find suitable model parameters. In unit cell calculations an FE model of a simplified microstructure is used in which the voids are represented in a simple repeating array: the easiest way to distribute voids is to generate crystal-like structures, but more sophisticated distributions have also been developed [112]. Typically the results of FE calculations of a sphere in a cylinder where the material surrounding the void is discretised via several elements are generated in terms of the evolution of force *vs*. displacement and displacement *vs.* void volume fraction. These results of void cell calculations can then be used to fit model parameters (see the following sections) by comparing the void cell results to the results of one

element of, for example, a Gurson material with a chosen set of parameters. In an optimisation process varying the relevant parameters may be found to identify optimum values.

2.2.5.3 Extensions of the Gurson model

Attempts have been made to enhance the Gurson model in various aspects. In terms of improved modelling of the plastic flow behaviour of the matrix, the aspects of strain hardening, viscoplasticity, plastic anisotropy and kinematic hardening have been addressed [112]. In the original Gurson model approximations are made in the derivation of the model and the idealisation of the unit cell. For example, void evolution at low triaxiality is not represented correctly and strain hardening at high hardening exponents is not allowed for correctly [112]. In the original Gurson model hollow spheres are considered instead of volumes that can easily fill a considered space when they adjoin each other and the interactions between voids are not realistic for porosity larger than 1% [112].

Void growth modifications

Modifications suggested by Tvergaard [109] particularly address some of the approximations with respect to the unit cell, *i.e.* volume shapes that can easily fill a considered space when they adjoin each other. In order to enhance the Gurson model two fitting parameters (q_1, q_2), influencing the void growth in the model., have been introduced by Tvergaard [109]. These parameters can then be fitted using unit cell calculations. Equation (2-32) shows this modified Gurson potential.

$$\Phi = \frac{\sigma_{eq}^2}{\sigma_f^2} + 2q_1 f \cosh\left(\frac{q_2}{2}\frac{\sigma_{kk}}{\sigma_f}\right) - 1 - q_1^2 f^2 = 0 \qquad \textbf{(2-32)}$$

Via tuning the values of q_2 in particular the influence of stress triaxiality on void growth can be controlled.

In [113] q_1, q_2 have been determined via void cell calculations for different hardening parameters (n) and yield strength/ Young's modulus ratios (σ_0/E). q_1, q_2 also depend on stress triaxiality levels.

A recent modification of the Gurson model in terms of void growth has been suggested by Pardoen [114]. As the Gurson model only describes void growth correctly at elevated stress triaxiality: for this reason it was extended for low stress triaxiality in [114] in order to be able to predict material behaviour *e.g.* in deformation processes at low stress triaxiality. The void shape anisotropy has also been taken into account in this study. However, it is not clear if void growth in situations of low stress triaxiality and high shear deformation should be considered as the main reason for material failure as void nucleation at a 2nd population of 2nd phase particles has been identified to occur at low stress triaxiality [64] as high fracture strains may be reached.

Anisotropic void shape

The assumption made in the Gurson model that voids keep a spherical shape is only true at high values of triaxility. In order to model cases of low triaxiality where voids do not grow spherically or cases with initial non-spherical pores, it is possible to add parameters to the Gurson potential [112]. Gologanu and co-workers [71, 72, 115, 116] however identified an alternative model for such cases (as opposed to an extended Gurson approach) which has been implemented and validated, see Gologanu [116] and Pardoen and Hutchinson [77]. The first approach of Gologanu and co-workers [72] for ellipsoidal voids consists of an overall yield criterion that depends on the porosity and the shape parameter, and of an evolution equation for the porosity and for the void shape, respectively.

Pardoen and Hutchinson [77] have made a computational analysis of the influence of microstructural parameters on J_{IC} fracture toughness. In this work the Gurson-Tvergaard-Needleman (GTN) model [48, 111](and the modifications proposed by Gologanu) have been utilised to predict the (anisotropic) growth of voids. Coalescence has been accounted for using the Thomason model [117]. Especially the influence of initial void shape and void spacing has been studied in a 2D plane strain model accounting for small scale yielding conditions. In these analyses the strain hardening exponent n has been set constant to 0.1 the and the yield stress- Young's modulus ratio (σ_0/E) to 0.003.

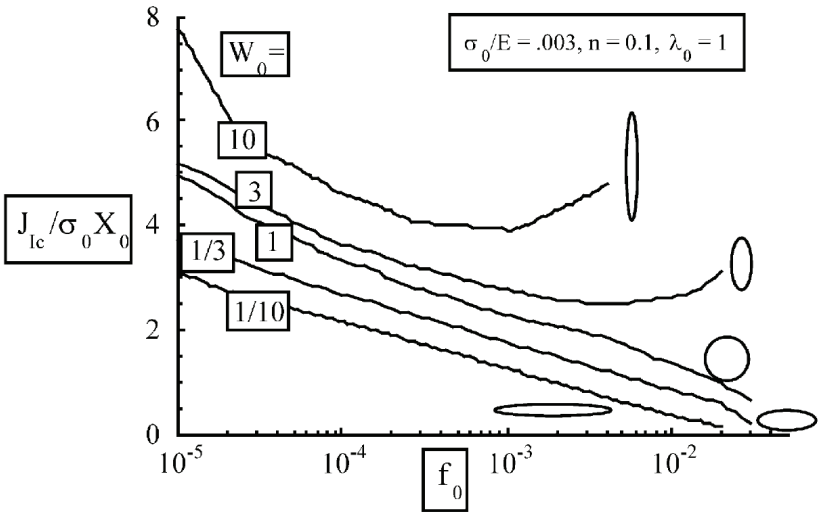

Figure 2-11: Results of FE study of the effect of the initial void shape on the fracture toughness for different initial porosity(after [77]) .

Figure 2-11 shows the normalised plane strain fracture toughness $J_{IC}/\sigma_0 X_0$ as a function of initial void volume fraction f_0 for different void aspect ratios. The void spacing is kept constant in loading and crack growth direction. It becomes evident that at constant void volume fractions the fracture toughness is higher for voids that are elongated in loading direction (prolate voids) than for voids that are flat and penny-shaped in crack growth direction (oblate voids). It should be noted that in the Gologanu model [71, 72] only shapes that are rotation-symmetric are considered. The rotation axis is oriented in the loading direction.

The influence of void arrangement on fracture toughness is carried out considering the void arrangement shown in Figure 2-12. The void arrangement is turned by 90° between Figure 2-12 (a) an (b). The aspect ratio of the voids (W_0) is considered to be 1.

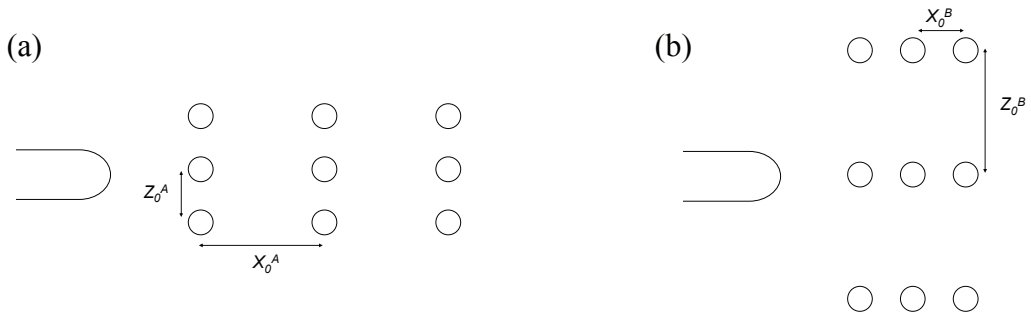

Figure 2-12: Two different crack plane orientations in a material exhibiting initially anisotropic void spacing (after [77]).

The effect of void arrangement on fracture toughness found in this analysis considering the arrangement from Figure 2-12 is shown in Figure 2-13. The ratio of the fracture toughness values for the two directions is plotted as a function of the void volume fraction. In this graph curves for different void spacing ratios (X_0^A / X_0^B) are shown.

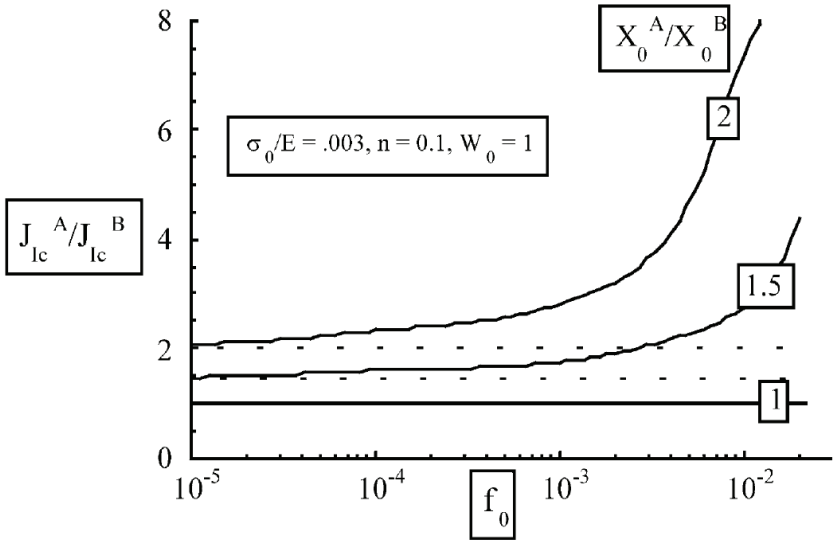

Figure 2-13: Effect of the anisotropic void spacing on the ratio of toughness corresponding to two crack planes oriented at 90° to one another (after [77]).

It can be seen that toughness decreases with increased void spacing and decreases with reduced spacing. The described effects of void spacing and void shape anisotropy on toughness anisotropy will superimpose (either compensate or reinforce) as a function of the encountered configuration [77].

Modelling of void nucleation

As described in Section 2.2.3.1 void nucleation during ductile fracture is typically linked to the cracking of coarse 2nd phase particles to the particle – matrix decohesion. In calculations utilising the Gurson model this effect can be accounted for by adding a void nucleation term to the void growth in the void evolution function (see equation (2-33)).

$$\dot{f} = (1-f)\,trace\,\underset{\sim}{\dot{\varepsilon}}_p + \dot{f}_n \qquad \textbf{(2-33)}$$

In this approach of void nucleation the entire volume of the cracked or debonded intermetallic particle is considered to be a void. Through this way of accounting for void

growth mass is no longer conserved but it can be justified as the cracked particle is no longer contributing to the integrity of the structure.

Nucleation can be considered to be strain or stress dependent. For strain dependent nucleation equation (2-34) is often used. The void nucleation rate is a function of the strain rate and A_n can be any positive function of the state variables.

$$\dot{f}_n = A_n \dot{p} \qquad \textbf{(2-34)}$$

Chu and Needleman [118] have suggested the use of a Gaussian distribution for the nucleation function around a specific strain at which 50% of all particles have nucleated. This approach has been repeatedly used in the literature.

Another frequently used nucleation function is given in equation (2-35), [119],

$$A_n = \frac{f_n}{(p_e - p_s)} \qquad \textbf{(2-35)}$$

Where f_n is the coarse particle volume fraction and p_s is the strain at which nucleation starts and p_e is the strain at which nucleation ends. Using this expression voids nucleate at a constant rate between p_s and p_e .

Modelling of void coalescence

As described in previous sections (see section 2.2.3.3) void nucleation and growth during ductile fracture is followed by void coalescence. Coalescence can occur though void impingement or void sheeting where shear and void nucleation at a 2nd population of smaller particles play a role. Tvergaard and Needleman [111] have suggested a modification of the Gurson model to account for void coalescence in a purely phenomenological way by replacing f with an effective void volume fraction f_* (see equation (2-36)) In which The effect of hydrostatic stress is amplified when a critical void volume fraction f_c is achieved. This description of void coalescence is purely phenomenological. The critical void volume fraction f_c can be obtained via different methods, *e.g* via metallographic analysis or via void cell calculations. The multiplicative

factor δ may depend on various variables such as the stress state, void arrangement and hardening behaviour.

$$f_* \begin{cases} f & for\ f < f_c \\ f_c + \delta(f - f_c) & otherwise \end{cases} \qquad \textbf{(2-36)}$$

The multiplicative factor δ may depend on various variables such as the stress state, void arrangement and hardening behaviour. The critical void volume fraction f_c can be obtained via different methods, *e.g* via metallographic analysis or via void cell calculations. A more sophisticated model for void coalescence has been proposed by Thomason [117]. In this model localisation of plasticity between void is considered using plasticity theory. The model is valid for linking up of voids through void impingement. There is then a competition between the diffuse plastic deformation described by the Gurson model and the localised deformation in the coalescence mechanism that is described by the Thomason model. In approaches that use these two models (such as [77]) the solution of the two models is computed at for every instance during the evolution of fracture and the solution of the model predicting the lower stress is taken into account.

Other attempts to describe coalescence or special cases of coalescence within the framework of the Gurson model have been carried out such as the attempt to model coalescence of voids in columns [79]. However in this study coalescence is only considered for high lateral stresses, a case that is not realistic for propagation in thin sheet materials however.

Nahshon and Hutchinson [120] have suggested a way to account for the influence of shear in the coalescence process is use of the Lode parameter. In this model the void volume fraction is rapidly increasing when the value of the Lode parameter approaches zero which corresponds to a situation of generalized shear. Nahshon and Hutchinson [120] have utilized the modification to study localization at a material point. However, this model has not been used for structural applications as yet.

Fabregue and Pardoen [121] have made an attempt to account for the influence of small voids on the coalescence mechanism. In this approach a hollow sphere surrounded by a material with small voids is investigated and a constitutive model for this case is suggested. However, the relevance of the model is not clear as it has not yet been

identified if nucleation and growth of a 2nd population of 2nd phase particles is triggered via plastic localisation or if nucleation and growth of a 2nd population of 2nd phase particles causes localisation.

Plastic anisotropy

Materials that fail via ductile failure can exhibit plastic anisotropy that may, for example, be linked to the processing history of the material. It is hence useful to account for this plastic anisotropy in the Gurson model to predict material behaviour accurately. This can be done by introducing and anisotropic effective stress $\overline{\sigma}$ instead of the Mises stress σ_{eq} (see equation (2-37))

$$\Phi = \frac{\overline{\sigma}^2}{\sigma_0^2} + 2f\cosh\left(\frac{\sigma_{kk}}{\sigma_0}\right) - 1 - f^2 = 0 \qquad \textbf{(2-37)}$$

Different expressions have been developed for this effective stress, *e.g.* Hill [122], Barlat [123], Karafillis and Boyce [124] and Bron and Besson [52].

Bron and Besson [52] have especially proposed a phenomenological yield function that has been used to describe the anisotropic behavior of aluminium sheet material. In this work the functions given by Barlat *et al.* [123] and Karafillis *et al.* [124] has been extended and a model has been achieved that has numerical advantages compared with previous models. In this model $\overline{\sigma}$ is defined by the following equations.

$$\begin{aligned}
\overline{\sigma} &= (\alpha(\Psi^1)^{\frac{a}{b^1}} + (1-\alpha)(\Psi^2)^{\frac{a}{b^2}})^{\frac{1}{a}} \\
\Psi^1 &= \frac{1}{2}(\left|S_2^1 - S_3^1\right|^{b^1} + \left|S_2^1 - S_3^1\right|^{b^1} + \left|S_2^1 - S_2^1\right|^{b^1}) \\
\Psi^2 &= \frac{3^{b^2}}{2^{b^2}+2}(\left|S_1^2\right|^{b^2} + \left|S_2^2\right|^{b^2} + \left|S_3^2\right|^{b^2})
\end{aligned} \qquad \textbf{(2-38)}$$

Where $S_{i=1-3}^k$ are the principal values of a modified stress deviator that is defined as in equation (2-39).

$$\underset{\sim}{s}^k = \underset{\approx}{L}^k : \underset{\sim}{\sigma} \qquad \textbf{(2-39)}$$

$$\underset{\approx}{L}^{k} = \begin{pmatrix} \left(c_2^k + c_3^k\right)/3 & -c_3^k/3 & -c_2^k/3 & 0 & 0 & 0 \\ -c_3^k/3 & \left(c_3^k + c_1^k\right)/3 & -c_1^k/3 & 0 & 0 & 0 \\ -c_2^k/3 & -c_1^k/3 & \left(c_1^k + c_2^k\right)/3 & 0 & 0 & 0 \\ 0 & 0 & 0 & c_4^k & 0 & 0 \\ 0 & 0 & 0 & 0 & c_5^k & 0 \\ 0 & 0 & 0 & 0 & 0 & c_6^k \end{pmatrix} \quad \textbf{(2-40)}$$

The anisotropy of the yield surface is controlled by $c_{i=1-6}^{k=1-2}$ whilst its shape is controlled by a, b^1, b^2 and α. This yield function includes 16 parameters but only 14 of them are independent.

Kinematic hardening without damage

Materials of industrial use may be prestrained for various reasons. It is thus useful to be able to use kinematic hardening within the Gurson model. Here first the constitutive equations describing kinematic hardening for an elasto-plastic material without damage are presented. The presented model formulation has been proposed by Lemaitre and Chaboche (1990) [125].

The constitutive model for the undamaged materials is based on an additive decomposition of the elastic and plastic strain rates so that:

$$\underline{\dot{\varepsilon}} = \underline{\dot{\varepsilon}}_e + \underline{\dot{\varepsilon}}_p \quad \textbf{(2-41)}$$

where $\underline{\dot{\varepsilon}}$ is the strain tensor and $\underline{\dot{\varepsilon}}_e$ and $\underline{\dot{\varepsilon}}_p$ are the elastic and plastic strain tensors respectively. The Cauchy stress, $\underline{\sigma}$, is computed from the elastic strain tensor using Hooke's law as:

$$\underline{\sigma} = \underline{\underline{E}} : \underline{\varepsilon}_e \quad \textbf{(2-42)}$$

where $\underline{\underline{E}}$ is the fourth order stiffness tensor. Kinematic hardening is represented by an internal back stress $\underline{X}$. The yield surface is expressed as :

$$\Phi = (\underline{\sigma} - \underline{X})_{eq} - R(p) \quad \textbf{(2-43)}$$

Then normality rule is applied so that the plastic strain rate tensor $\underline{\dot{\varepsilon}}_p$ is given by:

$$\dot{\underline{\varepsilon}}_p = \dot{p}\frac{\partial \Phi}{\partial \underline{\sigma}} = \dot{p}\underline{n} \qquad \textbf{(2-44)}$$

The evolution of p is given by the consistency equation: $\Phi = 0$, $\dot{\Phi} = 0$. The evolution of the kinematic hardening variable is assumed to obey a nonlinear rule; it is described by a second order tensor state variable, $\underline{\alpha}$, whose evolution is given by:

$$\dot{\underline{\alpha}} = \dot{\underline{\varepsilon}}_p - \frac{3}{2}\frac{D}{C}\dot{p}\underline{X} = \dot{p}(\underline{n} - \frac{3}{2}\frac{D}{C}\underline{X}) \qquad \textbf{(2-45)}$$

D and C are two material parameters. Finally, the back stress $\underline{X}$ is related to $\underline{\alpha}$ by:

$$\underline{X} = \frac{2}{3}C\underline{\alpha} \qquad \textbf{(2-46)}$$

A more general form could be used in the case of anisotropic materials using fourth order tensors for D and C ([126], [127]).

Figure 2-14 shows the effect of kinematic hardening on the yield surface: When pure kinematic hardening is occurring the yield surface is shifted but its shape remains unchanged.

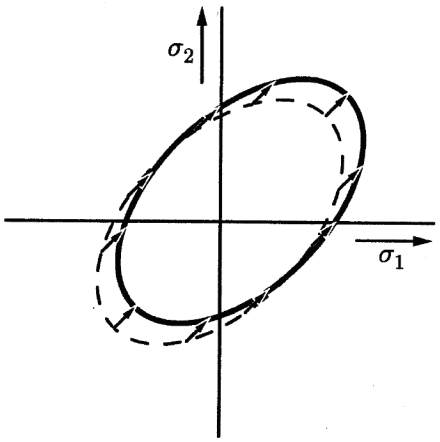

Figure 2-14: Illustration of the shift of the yield surface caused by kinematic hardening

Kinematic hardening linked to the Gurson model

Several attempts have been made in the literature to extend the Gurson model to kinematic hardening ([128-131]). The model presented here is the one suggested by [131].

Damage is represented in this model by a single scalar variable representing the void volume fraction, f. The model is based on the definition of an effective scalar stress, σ_*, which depends on the macroscopic stress tensor and f. σ_* is assumed to be a homogeneous function of degree 1 of $\underline{\sigma}$ so that:

$$\frac{\partial \sigma_*}{\partial \underline{\sigma}} : \underline{\sigma} = \sigma_* \qquad \textbf{(2-47)}$$

In the case of the "standard" GTN model, σ_* is an implicit function of $\underline{\sigma}$ which is obtained by solving the following equation:

$$\Psi\left(\sigma_*, \sigma_{eq}, \sigma_{kk}, f\right) = \frac{\sigma_{eq}^2}{\sigma_*^2} + 2q_1 f_* \cosh\left(\frac{q_2}{2}\frac{\sigma_{kk}}{\sigma_*}\right) - 1 - q_1 f_*^2 = 0 \qquad \textbf{(2-48)}$$

where σ_{eq} is the von Mises stress and σ_{kk} the trace of the stress tensor. q_1 and q_2 are model parameters representing void interaction and f_* is an *ad hoc* function of f introduced to model void coalescence (Tvergaard and Needleman, 1984). If kinematic hardening is to be accounted for it becomes necessary to introduce the $\underline{B} = \underline{\sigma} - \underline{X}$ tensor to define an effective scalar stress B_*. Taking into account plasticity and damage anisotropy, B_* is implicitly defined by:

$$\Psi\left(B_*, B_{eq}, B_{kk}, f\right) = 0 \qquad \textbf{(2-49)}$$

The yield function can then be expressed as:

$$\Phi = B_* - R(p) \qquad \textbf{(2-50)}$$

where the function $R(p)$ still represents isotropic hardening. The plastic strain rate tensor is still given by the normality rule as:

$$\underline{\dot{\varepsilon}}_p = (1-f)\dot{p}\frac{\partial \Phi}{\partial \underline{\sigma}} = (1-f)\dot{p}\frac{\partial \underline{B}_*}{\partial \underline{\sigma}} = (1-f)\dot{p}\underline{n} \qquad \textbf{(2-51)}$$

The $(1 - f)$ factor is introduced in the previous equation so that:

$$\underline{\dot{\varepsilon}}_p : \underline{B} = (1-f)\dot{p}B_* \qquad \textbf{(2-52)}$$

which represents the equality between the macroscopic plastic dissipation (left hand-side) and the microscopic dissipation (right hand-side)[132]. $\dot{p}$ can be calculated for rate independent materials using the consistency condition. For a rate dependent material, $\dot{p}$ is expressed as a function of B_* (e.g. Norton flow). Finally it is necessary to derive equations to obtain the back stress $\underline{X}$. Equation (2-45) is kept to describe the evolution of the kinematic hardening state variable $\underline{\alpha}$.

Note that as the trace of the plastic strain tensor is not equal to zero, the trace of $\underline{\alpha}$ will also be non-zero. However equation (2-46) cannot be used directly to compute the back stress $\underline{X}$ as the macroscopic back stress would not vanish as the material breaks (i.e. for $f_* = 1/q_1$). To solve this problem, one defines an intermediate back stress, $\underline{\chi}$, which can be interpreted as the back stress at the microscopic level. $\underline{\chi}$ is related to $\underline{\alpha}$ using eq. : $\underline{X} = \frac{2}{3}C\underline{\alpha}$ Following Besson and Guillemer-Neel (2003)[131], the actual back is computed such that:

$$\underline{\chi} = \frac{2}{3}X_* \frac{\partial X_*}{\partial \underline{X}} \qquad \textbf{(2-53)}$$

In practice, this equation must be iteratively solved with respect to X.

Applications of the Gurson model and other numerical void growth investigations

Knowing microstructural features of a material, attempts have been made to predict 'global' toughness using the local approach to fracture. For example the local approach has been used to model intergranular ductile failure by considering two zones in the material: the soft PFZ and the material inside the grains [133, 134]. In Ref. [133] growth and coalescence of voids is modelled in both layers via an enhanced Gurson-type model. Account is made of the effects of void aspect ratio and of relative void spacing. Investigations are presented of the effects on ductility of the flow properties of each zone and the relative thickness of the PFZ, along with the particle spacing and volume fraction

within the PFZ. It should be noted that it is not clear if intergranular failure should be considered to be dominated by growth model.

An analysis of multiple voids [135] by Tvergaard and Hutchinson provides a formulation and numerical analysis of a two-dimensional plane strain model with multiple discrete voids located ahead of a pre-existing crack tip. Contrary to the attempts mentioned above the voids as well as the matrix round them are explicitly modeled such as in void cell calculations without using a damage model. At initial void volume fractions that are sufficiently low, initiation and growth is approximately represented by the void by void mechanism where the void growth of each void is independent of the adjacent one. At somewhat higher initial void volume fractions, a transition in behavior occurs, named multiple void growth, whereby many voids ahead of the tip grow at comparable rates and their interaction determines initiation toughness and crack growth resistance. For intermediate void volume fractions a 'hybrid' condition of void-by-void and multiple void coalescence may be encountered.

In a recent study Steglich *et al.* [136] have investigated the anisotropic ductile fracture of hot-rolled 2024 Al plate. The microstructure has been investigated via X-ray micro-tomography and fracture properties have been investigated using round smooth and notched tensile bars. FE studies using a GTN type model and void cell calculations have been carried out in to clarify the origins of fracture anisotropy. Toughness anisotropy has been attributed to the orientation of precipitate free bands and clustered second phase particles. Fracture modes have been found to be intergranular and transgranular. It has been pointed out in this work that in the model the influence of shear has not been accounted for which may however be important for the investigated microstructure and stress state.

2.3 Tomography

Tomography is referred to as the quantitative description of a slice of matter within a bulk object [73]. There are different methods available to perform tomography and they differ in the source of excitation. Possible physical excitation sources are ultrasonics, magnetic field, X- and gamma rays and electric fields. However, nowadays X-rays or gamma rays are the mostly used excitation sources for non-destructive testing as well as materials characterisation. Tomography has been first applied in the 1950's for density characterisation, in medical science in the 1970's, and for industrial applications in the 1980's. In X-ray and gamma-ray tomography different acquisition set-ups are used for transmission tomography, backscattered tomography and emission tomography. In transmission tomography the photons transmitting through the sample are detected whilst for backscattered tomography the backscattered photons are detected. The distinction between Compton and Reyleigh backscattered photons is used for material composition analysis. In emission tomography the photons produced within a material are analysed.

With the availability of micro-computed tomography (μCT) that allows resolution to less than 1μm, numerous studies have been carried out in the field of material science and fracture. It has become possible to acquire data in 3D (as opposed to 2D methods) where images of numerous sections need to be taken in order to get an insight of the 3D morphology of features. As such, characteristic dimensions in a material may be measured fully. Additionally, defects introduced by sample preparation are less prevalent in μCT studies. μCT also allows for *in situ* tests that may provide a detailed insight into the sequence of events of failure processes, *e.g.* studies have been carried out to investigate fatigue cracks and crack closure involving *in situ* loading [137, 138]. Short cracks in Al cast alloys have been investigated via μCT revealing the 3D propagation geometry of the cracks [138, 139]. The growth of voids during ductile fracture in Al-alloys has also been assessed [140] as well as the damage originating from spherical particles in an Al based composite [141].

2.3.1 The principle of X-ray tomography

The principle of X-ray transmission tomography is commonly described by the Beer-Lambert law (equation (2-54)) that gives an expression for the attenuation coefficient μ in the photo-electric regime.

$$\mu(x,y,z) = K\rho\frac{Z^4}{E^3} \qquad \textbf{(2-54)}$$

Where K is a constant, ρ the density and Z the atomic number of the investigated material and E is the energy of the incident photons. Through the Beer-Lambert law the contrast differences in an X-ray radiograph of a heterogeneous material can be explained.

Conventional X-ray computed tomography is typically executed in the following manner: X-rays leaving a source pass through the sample. After leaving the sample the X-rays then arrive at the detector that is composed of a fluorescent screen transforming the X-rays into visible light and a CCD camera that then captures the associated 2D radiograph projection [142]. The information of many radiographs taken at different orientations of the sample is computationally processed so that the local value of the attenuation coefficient is determined at every point of the sample volume [73]. This is commonly based on the "filtered back projection" method [143]. The reconstruction algorithm uses, for reconstruction of any single point, experimental data corresponding to individual rays impinging the point of interest, but coming from different orientations.

2.3.2 Micro-focus tomography

For moderate resolution tomography a "cone beam" system with a classical microfocus X-ray tube as source is commonly used. The resolution is typically in the order of 5-10µm. The maximum resolution in such a system is generally linked to two parameters that are in competition with each other: specifically a compromise needs to be found between X-ray power and the effective "spot size" of the beam emitted from the target material. The X-ray power must be kept at a level where it is strong enough to penetrate the sample, and also to provide short imaging times. However, this is at odds with maintaining a small spot size.

2.3.3 High resolution tomography - synchrotron radiation

In order to go beyond resolutions that are achievable with conventional X-ray tubes, parallel beam synchrotron radiation may be used, exploiting the very high flux of a synchrotron. The best quality images with respect to signal-to-noise ratio can be obtained through this technique. The achievable resolution currently lies under 1 µm and in the case of the synchrotron facility European Synchrotron Radiation Facility (ESRF), imaging is routinely undertaken at a voxel size of 0.7 µm.

The origin of synchrotron radiation is different from the x-ray tubes: the radiation in a synchrotron is generated by ultrarelativistic electrons that are accelerated in a magnetic field and deviated from a straight trajectory. X-rays are emitted in a narrow cone that is situated tangentially to the trajectory of the electrons. Such synchrotron radiation is produced at the European Synchrotron Radiation Facility in Grenoble (see Figure 2-15). The synchrotron mainly consists of a linear accelerator (linac), a circular accelerator (booster synchrotron), and the storage ring. Once the electrons have attained an energy of 6 GeV they are transferred from the booster to the storage ring [144] (see Figure 2-15).

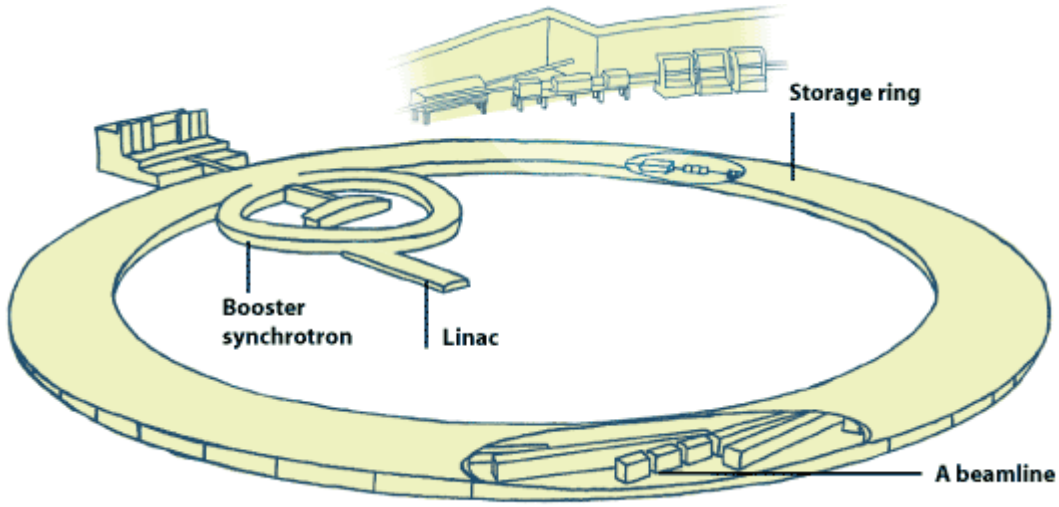

Figure 2-15: Schematic depiction of the ESRF

The electrons are injected in the storage ring in discrete pulses and move inside the ring as bunches. The loss of energy of the electrons during radiation is compensated by a radio-frequency generator/cavity that acts on those bunches. The storage ring of a third generation synchrotron consists of bending magnets, undulators, wigglers and focussing magnets.

- *Bending magnets*

The storage ring consists of straight and curved parts. Bending magnets allow the electron beam to "bend" and to achieve its circular trajectory (Figure 2-16). As it is well known, the so called Lorentz force is exerted on the electrons when they pass through a magnetic field. This force is normal to the speed and magnet field vectors. Through the Lorentz force the electrons are deflected. During this deflection process the electrons emit radiation that is tangential to their trajectory.

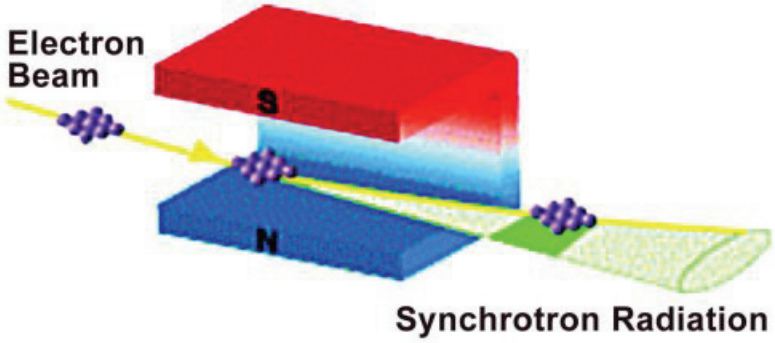

Figure 2-16: Schematic drawing of a bending magnet (after [145])

- *Undulator*

The undulator consists of a set of several magnets that cause an undulated trajectory of the electrons (see Figure 2-17). The aim of this device is to produce an X-ray beam that is more powerful than the one emitted in the bending magnet. The emitted radiation has an enhanced intensity because the radiation emitted by the different bending stages interferes constructively with each other. The undulator is situated between bending magnets and represents a so-called insertion device ("I.D.").

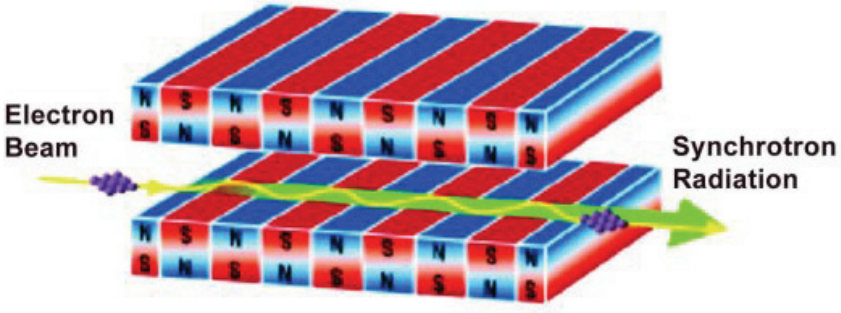

Figure 2-17: Schematic drawing of an undulator (after [145])

- *Wiggler*

The wiggler is an insertion device similar to the undulator. It consists of at least three sets of magnets that make the beam deflect. The difference between an undulator and a wiggler lies in the spectrum of generated radiation that is broader for a wiggler.

- *Focussing magnets*

Focussing magnets are present on the straight lines of the storage ring and have the aim to keep the beam to a well defined size to provide a bright source.

The main asset of 3rd generation synchrotron tomography facility such as the beamline ID 19 at ESRF is that the radiation source is [146]:

- very intense,
- spatially homogeneous,
- parallel
- monochromatic
- coherent

Due to the coherence of the photon source small features under voxel size can be particularly detected via the phase contrast phenomenon (see section 2.3.5).

2.3.4 Artefacts

For quantitative tomography a very accurate map of the attenuation coefficient of every point of the sample volume is crucial. However several artefacts can appear during tomography [73].

- *Beam hardening*

This artefact can be seen as streaks and as cupping in images across sample sections. The origin of the artefact is the use of polychromatic radiation sources and therefore this artefact is less relevant for synchrotron radiation as in a synchrotron the light generally passes through a monochromator before reaching the sample.

- *Detector saturation*

The detector signal needs to be proportional to the photon flux. If this is not the case, which can for example happen at very low or high flux rates, streaks generally appear.

- *Aliasing*

Steep edges in projections lead to high frequencies in the Fourier domain during the processing of the projections which may generate streaks in the end image at the corners of objects.

- *Scattered electrons*

Electrons that are not transmitting through the sample but that are scattered can introduce errors to the radiographic projections.

- *Ill corrected detector*

An ill corrected detector can introduce so called ring artefacts, particularly associated with varying sensitivities of pixels.

- *Spatial distortion of the detector*

Lens distortion can introduce errors when the visible light is projected on the camera CCD.

- *Centering error*

For the reconstruction of the data an accurate knowledge of the exact rotation centre is required which should be accurate to sub-pixel/voxel levels. Therefore inaccuracies in the positioning stage may introduce errors.

2.3.5 Phase contrast

When the coherent radiation of a synchrotron passes through the sample and its constituents, phase differences are introduced due to varying refractive index. On the one hand the resulting Fresnel diffraction may be considered as a nuisance in absorption tomography, but, on the other hand, it allows interfaces in a sample to be emphasized via the so-called “edge detection regime” phase contrast imaging. The phase contrast is the interference of parts of the wavefront after the propagation through a certain distance. A key asset of such phase contrast imaging is that features in the sample can be imaged that can normally not be imaged via absorption, either because the difference in absorption coefficient between two constituents is too small or because the feature to be observed, such as a narrow crack, is too small (i.e sub-voxel). The test set-up for the detection of phase contrast is simple with suitably coherent source such as ID19, as the same set-up as for absorption radiography can be used. The most important parameter for the intensity of

phase contrast is then the distance between the sample and the detector screen, influencing the defocusing distance D (see equation (2-55)) [147].

$$D = \frac{d \times l}{d + l} \qquad \textbf{(2-55)}$$

Where d is the distance between the sample and the detector and l is the distance between the source and the sample. For the beamline ID 19 at ESRF $d << l$ with l=145m, therefore the defocusing distance almost equals the sample-detector distance. The region of the sample that is mainly contributing to the point of image contrast has the radius r_F (see equation (2-56))

$$r_F = \sqrt{\lambda D} \qquad \textbf{(2-56)}$$

Where λ is the X-ray wavelength. If r_F is small compared to the transverse dimensions of the feature length, a, in the sample the images are identified with the "edge-detection regime" and can show phase contrast after application of conventional absorption tomography algorithm. In the "holographic regime", r_F is close to a, and several fringes are present in the projection images. If images in this set-up are taken at different detector-sample distances, further algorithms can be applied to the results that allow quantitative refractive index data to be obtained from the sample.

2.3.6 Gallium wetting

A technique that may be particularly used to highlight grain boundaries in tomography of Al-alloys is gallium wetting [142]. If liquid gallium (Melting point T_m=29.8°C) is brought in contact with aluminium the gallium may penetrate the grain boundaries. The grain boundaries may then be substituted by microscopic layers of Ga (0.1-2µm thickness) [142]. Due to the large difference in X-ray absorption coefficients between gallium and aluminium these thin layers of gallium can be detected via X-ray tomography. However, not all grain boundaries can be highlighted via this technique to the same extent. It has been identified that low angle sub-grain boundaries cannot be seen, along with "special" low energy/ high angle boundaries [148] in conjunction with non-gallium-treated imaging. This approach may provide a valuable technique in micromechanical and microstructural analysis of material behaviour [137, 149].

2.4 References

1. Polmear, I.J., *Light alloys: Metallurgy of the light metals*. Third edition ed. 1995, London New York Sydney Auckland: Arnold.
2. Warner, T.J., Shahani, R.A., Lassince, P., Raynaud,G.M., *Aluminium alloy developments for affordable airframe structures*. Research report of ALCAN, Centre de recherches de Voreppe, 1999
3. Dif, R., Bes, B., Ehstrom, J.C., Sigli, C., Warner, T.J., Lassince, Ph., Ribes,H. *Understanding and modelling the mechanical and corrosion properties of 6056 for aerospace applications*. Materials Science Forum, 2000. 331-337: p. 1613-18.
4. Braun,R. *Investigation on microstructure and corrosion behaviour of 6XXX series aluminium alloys*. Materials Science Forum, 2006. 519-521: p. 735-740.
5. Kaufman, J.G., *Introduction to Aluminium Alloys and Tempers*. 2000, Ohio, USA: ASM international.
6. Robson, J.D., Prangnell,P.B. *Dispersoid precipitation and process modelling in zirconium containing commercial aluminium alloys*. Acta Materialia, 2001. 49: p. 599-613.
7. Chen, C.Q., Knott,J.F. *Effects of dispersoid particles on toughness of high-strength aluminium alloys*. Metal Science, 1981. 15: p. 357-64.
8. ASM, *Aluminium and aluminium alloys*. 1993, OHIO, USA: ASM International.
9. Shuey, R. T. , Tiryakioglu, M., Bray, G. H., Staley,J. T. *Toughness after Interrupted Quench*. Materials Science Forum, 2006. 519-521: p. 1017-1022.
10. Miao, W.F., Laughlin,D.E. *Effects of Cu content and preaging on precipitation characteristics in aluminum alloy 6022*. Metallurgical and Materials Transactions A, 2000. 31A: p. 361-71.
11. Chakrabarti, D. J., Laughlin,D. E. *Phase relations and precipitation in Al-Mg-Si alloys with Cu additions*. Progress in Materials Science, 2004. 49: p. 389-410.
12. Mondolfo, L.F., *Aluminium alloys : Structures and Properties*. 1976, London: Butterworth.
13. Sagalowicz, L., Hug, G., Béchet, D., Sainfort, P., Lepasset,G. *A study of the structural precipitation in the Al-Mg-Si-Cu system*. Proc.4th Int. Conf. on Aluminium Alloys, ICAA4, 1994: p. 636-643.
14. Tanaka, M., Warner,T. *T6 and T78 tempers of AA6065 alloy: a quantitative TEM study*. Material Science Forum, 2000. 331-337: p. 983-8.
15. Chakrabarti, D.J., Cheong, B., Laughlin,D. E. *Precipitation in Al-Mg-Si-Cu alloys and the role of the Q phase and its precursors*. in *Proceedings of the 1998 TMS Annual Meeting, Feb 15-19 1998*. 1998. San Antonio, TX, USA: Minerals, Metals & Materials Soc (TMS), Warrendale, PA, USA.
16. Dumolt, S. D., Laughlin, D. E., Williams,J. C. *Formation of a modified beta prime phase in aluminium alloy 6061*. Scripta Metallurgica, 1984. 18: p. 1347-1350.
17. Esmaeili, S., Wang, X., Lloyd, D.J., Poole,W.J. *On the precipitation-hardening behavior of the Al-Mg-Si-Cu alloy AA6111*. Metallurgical and Materials Transactions A, 2003. 34A: p. 751-63.
18. Ravi, C., Wolverton,C. *Comparison of thermodynamic databases for 3xx and 6xxx aluminum alloys*. Metallurgical and Materials Transactions A: Physical Metallurgy and Materials Science, 2005. 36: p. 2013-2023.
19. Starink, M., Mellor,B., *Advanced Materials I Part III/IV course*. 2004, materials research group, University of Southampton.

20. Cho, A., Bes,B. *Damage Tolerance Capability of an Al-Cu-Mg-Ag Alloy(2139)*. Materials Science Forum, 2006. 519-521: p. 603-608.
21. Zahra, A.-M., Zahra, C.Y., Raviprasad, K., Polmear,I.J. *Effects of minor additions of Mg and Ag on precipitation phenomena in Al-4 mass% Cu*. Philosophical Magazine, 2004. 84: p. 2521-2541.
22. Wang, S.C., Starink,M.J. *Precipitates and intermetallic phases in precipitation hardening Al-Cu-Mg-(Li) alloys*. International Materials Reviews, 2005. 50: p. 193-215.
23. Taylor, J. A., Parker, B. A., Polmear,I. J. *Precipitation in Al-Cu-Mg-Ag casting alloy.* Metal Science, 1978. 12: p. 478-482.
24. Ringer, S. P., Hono, K., Polmear, I. J., Sakurai,T. *Nucleation of precipitates in aged Al---Cu---Mg---(Ag) alloys with high Cu:Mg ratios*. Acta Materialia, 1996. 44: p. 1883-1898.
25. Reich, L., Murayama, M., Starink, M., Hono,K. *Evolution of Omega phase in an Al-Cu-Mg-Ag alloy--a three-dimensional atom probe study*. Acta Materialia, 1998. 46: p. 6053-6062.
26. Vasudevan, A.K., Doherty,R.D. *Grain boundary ductile fracture in precipitation hardened aluminum alloys*. Acta Metallurgica, 1987. 35: p. 1193-1219.
27. Dumont, D., Deschamps, A., Brechet,Y. *On the relationship between microstructure, strength and toughness in AA7050 aluminum alloy*. Materials Science and Engineering A, 2003. 356: p. 326-336.
28. Dorward, R. C., Bouvier,C. *A rationalization of factors affecting strength, ductility and toughness of AA6061-type Al-Mg-Si-(Cu) alloys*. Materials Science and Engineering A, 1998. 254: p. 33-44.
29. Evancho, J. W., Staley,J. T. *Kinetics of precipitation in aluminum alloys during continuous cooling*. Metallurgical Transactions, 1974. 5: p. 43-47.
30. Rometsch, P.A., Wang, S.C., Harriss, A., Gregson, P.J., Starink,M.J. *The effect of homogenizing on the quench sensitivity of 6082*. Materials Science Forum, 2002. 396-402: p. 655-60.
31. Morita, S., Toda, H., Takahashi, A., Hoshiyama, A., Kobayashi, T., Nagashima,H. *Effects of quenching rate on mechanical properties of 6061 aluminum alloy*. Journal of Japan Institute of Light Metals, 2001. 51: p. 307-12.
32. De Haas, M., De Hosson,J.Th.M. *On the effects of thermomechanical processing on failure mode in precipitation-hardened aluminium alloys*. Journal of Materials Science, 2002. 37: p. 5065-5073.
33. Rometsch, P.A., Starink, M.J., Gregson,P.J. *Improvements in quench factor modelling*. Materials Science and Engineering A, 2003. A339: p. 255-64.
34. Tiryakioglu, M., Shuey,R.T. *Multiple C-curves for modeling quench sensitivity of aluminum alloys*. in *Metallurgical Modeling for Aluminum Alloys. Proceedings from Materials Solutions Conference 2003. 1st International Symposium on Metallurgical Modeling for Aluminum Alloys, 13-15 Oct. 2003*. 2003. Pittsburgh, PA, USA: ASM Int.
35. Tiryakioglu, M., Shuey,R.T. *Quench sensitivity of an Al-7wt.%Si-0.6Wt.%Mg alloy: Characterization and modeling*. in *2006 TMS Annual Meeting, Mar 12-16 2006*. 2006. San Antonio, TX, United States: Minerals, Metals and Materials Society, Warrendale, PA 15086, United States.
36. Callister, W.D., *Materials Science and Engineering, an Introduction*. Fifth ed. 1999, New York: John Wiley & Sons, Inc.

37. Gomiero, P., Brechet, Y., Louchet, F., Tourabi, A., Wack,B. *Microstructure and mechanical properties of a 2091 AlLi alloy - II. Mechanical properties: yield stress and work hardening*. Acta Metallurgica et Materialia, 1992. 40: p. 857-861.
38. Sinclair,I. *Fatigue Crack Growth Processes in SiC Particulate Reinforced Commercial Al-Li Alloy, AA8090*. PhD, University of Cambridge, 1990.
39. Cahn, R.W., Haasen, W., Kramer,E.J., *Material science and Technology*. Vol. 6. 1993, Weinheim: VCH Verlagsgesellschaft.
40. Burger, G.B., Gupta, A.K., Jeffrey, P.W., Lloyd,D.J. *Microstructural control of aluminum sheet used in automotive applications*. Materials Characterization, Proceedings of the 27th Annual Convention of the International Metallographic Society, Jul 24-27 1994, 1995. 35: p. 23-39.
41. Bron, F., Besson, J., Pineau,A. *Ductile rupture in thin sheets of two grades of 2024 aluminum alloy*. Materials Science and Engineering A, 2004. 380: p. 356-364.
42. Bron,F. *Déchirure ductile des tôles minces en alliage d'aluminium 2024 pour application aèronautique*. thèse, Ecole des Mines de Paris, 2004.
43. ASTM-international, *Standard Test Method for Tear Testing of Aluminium Alloy Products, Designation B 871 - 01*. 2001: West Conshohocken, USA.
44. Knott,J.F., *Fundamentals of Fracture Mechanics*. 1973, London: Butterworths.
45. Rivalin, F., Besson, J., Pineau, A., Di Fant,M. *Ductile tearing of pipeline-steel wide plates II. Modeling of in-plane crack propagation*. Engineering Fracture Mechanics, 2001. 68: p. 347-364.
46. Anderson, T.L., *Fracture Mechanics*. Third ed. Fundamentals and Applications. 2005, Boca Raton: Taylor & Francis Group.
47. Garrison Jr, W. M., Moody,N. R. *Ductile fracture*. Journal of Physics and Chemistry of Solids, 1987. 48: p. 1035-1074.
48. Gurson, A.L. *Continuum theory of ductile rupture by void nucleation and growth: part 1 yield criteria and flow rules for porous ductile media.* Journal of Engineering Materials and Technology, Transactions of the ASME, 1977. 99 Ser H: p. 2-15.
49. Rousselier, G. *Ductile fracture models and their potential in local approach of fracture*. Nuclear Engineering and Design, 1987. 105: p. 97-111.
50. Lan, W., Deng, X., Sutton, M.A, Cheng,C.S. *Study of slant fracture in ductile materials*. International Journal of Fracture, 2006. 141: p. 469-496.
51. Mahgoub, E., Deng, X., Sutton,M.A. *Three-dimensional stress and deformation fields around flat and slant cracks under remote Mode I loading conditions*. Engineering Fracture Mechanics, 2003. 70: p. 2527-2542.
52. Bron, F., Besson,J. *A yield function for anisotropic materials Application to aluminum alloys*. International Journal of Plasticity, 2004. 20: p. 937-963.
53. Rice, J., Tracey,D. *On ductile enlagement of voids in triaxial stress fields*. Journal of the Mechanics and Physics of Solids, 1969. 17: p. 201-17.
54. Mathur, K. K., Needleman, A., Tvergaard,V. *Three dimensional analysis of dynamic ductile crack growth in a thin plate*. Journal of the Mechanics and Physics of Solids, 1996. 44: p. 439-459.
55. Besson, J., Steglich, D., Brocks,W.B. *Modeling of crack growth in round bars and plane strain specimens*. International Journal of Solids and Structures, 2001. 38: p. 8259-84.
56. Xue,L. *Damage accumulation and fracture initiation in uncracked ductile solids subject to triaxial loading*. International Journal of Solids and Structures, 2007. 44: p. 5163-5181.

57. Xue, L.,T. Wierzbicki. *Ductile fracture initiation and propagation modeling using damage plasticity theory*. Engineering Fracture Mechanics, 2007. 75: p. 3276-3293.
58. Lode,W. *The influence of the intermediate principal stress on yielding and failure of iron, copper and nickel.* Zeitschrift für angewandte Mathematik und Mechanik, 1925: p. 142.
59. Barsoum, I., Faleskog,J. *Rupture mechanisms in combined tension and shear--Experiments*. International Journal of Solids and Structures, 2007. 44: p. 1768-1786.
60. Rivalin, F., Pineau, A., Di Fant, M., Besson,J. *Ductile tearing of pipeline-steel wide plates I. Dynamic and quasi-static experiments*. Engineering Fracture Mechanics, 2001. 68: p. 329-345.
61. Grange, M., Besson, J., Andrieu,E. *An anisotropic Gurson type model to represent the ductile rupture of hydrided Zircaloy-4 sheets*. International Journal of Fracture, 2000. 105: p. 273-93.
62. Brunet, M., Morestin,F. *Experimental and analytical necking studies of anisotropic sheet metals*. Journal of Materials Processing Technology, 2001. 112: p. 214-26.
63. Bron, F., Besson,J. *Simulation of the ductile tearing for two grades of 2024 aluminum alloy thin sheets*. Engineering Fracture Mechanics, 2006. 73: p. 1531-1552.
64. Tanguy, B., Luu, T.T., Perrin, G., Pineau, A., Besson,J. *Plastic and damage behaviour of a high strength X100 pipeline steel: Experiments and modelling*. International Journal of Pressure Vessels and Piping. In Press, Corrected Proof.
65. Son, H.S., Kim,Y.S. *Prediction of forming limits for anisotropic sheets containing prolate ellipsoidal voids*. International Journal of Mechanical Sciences, 2003. 45: p. 1625-1643.
66. Li, H.X., Chen,C.Q. *Mechanism of anisotropy in fracture behaviour and fracture toughness of high strength aluminium alloy plate*. Materials Science and Technology, 1990. 6: p. 850-856.
67. Benzerga, A.A., Besson, J., Pineau,A. *Coalescence-controlled anisotropic ductile fracture*. Journal of Engineering Materials and Technology, Transactions of the ASME, 1999. 121: p. 221-229.
68. Benzerga, A. A., Besson, J., Pineau,A. *Anisotropic ductile fracture: Part I: experiments*. Acta Materialia, 2004. 52: p. 4623-4638.
69. Mir, A.A., Barton, D.C., Andrews, T.D., Church,P. *Anisotropic ductile failure in free machining steel at quasi-static and high strain rates*. International Journal of Fracture, 2005. 133: p. 289-302.
70. Lassance, D., Fabregue, D., Delannay, F., Pardoen,T. *Micromechanics of room and high temperature fracture in 6xxx Al alloys*. Progress in Materials Science, 2007. 52: p. 62-129.
71. Gologanu, M., Leblond, J.-B., Devaux,J. *Approximate models for ductile metals containing nonspherical voids - case of axisymmetric oblate ellipsoidal cavities*. Journal of Engineering Materials and Technology, Transactions of the ASME, 1994. 116: p. 290-297.
72. Gologanu, M., Leblond, J.B., Devaux,J. *Approximate models for ductile metals containing non-spherical voids. Case of axisymmetric prolate ellipsoidal cavities*. Journal of the Mechanics and Physics of Solids, 1993. 41: p. 1723-1754.

73. Peix, G., Duvauchelle, P., Freud,N., *General principles*, in *X-Ray Tomography in Materials Science*, Baruchel, et al., Editors. 2000, Hermes Science Publications: Paris. p. 15-26.
74. Benzerga, A. A., Besson, J., Pineau,A. *Anisotropic ductile fracture: Part II: theory*. Acta Materialia, 2004. 52: p. 4639-4650.
75. Thomason, P.F. *A three-dimensional model for ductile fracture by the growth and coalescence of microvoids*. Acta Metallurgica, 1985. 33: p. 1087-1095.
76. Thomason, P.F. *Three-dimensional models for the plastic limit-loads at incipient failure of the intervoid matrix in ductile porous solids*. Acta Metallurgica, 1985. 33: p. 1079-85.
77. Pardoen, T., Hutchinson,J. W. *Micromechanics-based model for trends in toughness of ductile metals*. Acta Materialia, 2003. 51: p. 133-148.
78. Pardoen, T., Hutchinson,J.W. *Extended model for void growth and coalescence*. Journal of the Mechanics and Physics of Solids, 2000. 48: p. 2467-2512.
79. Gologanu, M., Leblond, J.-B., Devaux,J. *Theoretical models for void coalescence in porous ductile solids. II. Coalescence "in columns"*. International Journal of Solids and Structures, 2001. 38: p. 5595-5604.
80. Enami,K. *The effects of compressive and tensile prestrain on ductile fracture initiation in steels*. Engineering Fracture Mechanics, 2005. 72: p. 1089-1105.
81. Bao, Y., Treitler,R. *Ductile crack formation on notched Al2024-T351 bars under compression-tension loading*. Materials Science and Engineering A, 2004. 384: p. 385-394.
82. Li, B.Q., Reynolds,A.P. *Correlation of grain-boundary precipitates parameters with fracture toughness in an Al-Cu-Mg-Ag alloy subjected to long-term thermal exposure*. Journal of Materials Science, 1998. 33: p. 5849-53.
83. Unwin, P.N.T., Smith,G.C. *The microstructure and mechanical properties of Al-6%Zn-3%Mg*. Journal of the Institute of Metals, 1969. 97: p. 299-310.
84. Embury, J.D. *Plastic flow in dispersion hardened materials*. Metallurgical Transactions A, 1985. 16A: p. 2191-2200.
85. Embury, J. D., Nes,E. *On the tensile fracture of alluminium alloys*. Zeitschrift fuer Metallkunde, 1974. 65: p. 45-55.
86. Steele, D., Evans, D., Nolan, P., Lloyd,D.J. *Quantification of grain boundary precipitation and the influence of quench rate in 6XXX aluminum alloys*. Materials Characterization, 2007. 58: p. 40-45.
87. Lutjering, G., Gysler,A., in *Aluminium Transformation Technologies and Applications*, Pampillo, et al., Editors. 1980, Am. Soc. Metals: Argentina. p. 171.
88. Hahn, G. T., Rosenfield,A. R. *Metallurgical factors affecting fracture toughness of aluminium alloys.* Metallurgical Transactions A, 1975. 6A: p. 653-668.
89. Hahn, G.T., Rosenfield,A.R. ASTM STP 432, 1968: p. 3.
90. Ehrstroem, J.C., Achon, P., Hebert, J.F., Pineau,A. *Microstructural modelling of fracture toughness of Al alloys*. Material Science Forum, 1996. 217-222: p. 1539-44.
91. Mudry,F., Doctoral Thesis, Ecole des Mines de Paris, 1982.
92. Garrett, G.G., Knott,J.F. *The influence of compositional and microstructural variations on the mechanism of static fracture in aluminum alloys*. Metallurgical Transactions A, 1978. 9A: p. 1187-201.
93. Ashby,M.F. *Work hardening of dispersion-hardened crystals*. Philosophic Magazine, 1966. 14: p. 1157.
94. Hornbogen, E. *On the grain size dependance of fracture toughness of precipitation hardened alloys.* Zeitschrift fuer Metallkunde, 1975. 66: p. 511-513.

95. Hornbogen, E., Graef,M. *Fracture toughness of precipitation hardened alloys containing narrow soft zones at grain boundaries*. Acta Metallurgica, 1977. 25: p. 877-81.
96. Brown, L. M., Embury,J. D. *Initiation and growth of voids at second phase particles*. Institute of Metals (London), Monograph and Report Series, 1973. 1: p. 164-169.
97. Sugamata, M., Blankenship, C.P., Jr., Starke,E.A.Jr. *Predicting plane strain fracture toughness of Al-Li-Cu-Mg alloys*. Materials Science and Engineering A, 1993. A163: p. 1-10.
98. Roven,H.J. *A model for fracture toughness predictions in aluminium alloys exhibiting the slip band decohesion mechanism*. Scripta Metallurgica et Materialia, 1992. 26: p. 1383-8.
99. Jata, K. V., Starke,E.A. Jr. *Fatigue crack growth and fracture toughness behaviour of an Al-Li-Cu alloy*. Metallurgical Transactions A, 1986. 17A: p. 1011-1026.
100. Duva, J. M., Daeubler, M. A., Starke, E.A. Jr., Luetjering,G. *Large shearbale particles lead to coarse slip in particle reinforced alloys*. Acta Metallurgica, 1988. 36: p. 585-589.
101. Kawabata, T., Izumi,O. *Ductile fracture in the interior of precipitate free zone in an Al - 6.0% Zn - 2.6% Mg alloy.* Acta Metallurgica, 1976. 24: p. 817-825.
102. Gokhale, A.M., Deshpande, N.U., Denzer, D.K., Liu,J. *Relationship between fracture toughness, fracture path, and microstructure of 7050 aluminum alloy. II. Multiple micromechanisms-based fracture toughness model*. Metallurgical and Materials Transactions A, 1998. 29A: p. 1203-10.
103. Kamat, S.V., Hirth,J.P. *Effect of aging on mixed-mode I/III fracture toughness of 2034 aluminum alloys*. Acta Materialia, 1996. 44: p. 1047-1054.
104. Dumont, D., Deschamps, A., Brechet,Y. *A model for predicting fracture mode and toughness in 7000 series aluminium alloys*. Acta Materialia, 2004. 52: p. 2529-40.
105. Zehnder, A.T., Hui,C.Y. *Simple model relating crack growth resistance to fracture process parameters in elastic-plastic solids*. Scripta Materialia, 2000. 42: p. 1001-1005.
106. Tvergaard, V., Hutchinson,J.W. *Relation between crack growth resistance and fracture process parameters in elastic-plastic solids*. Journal of the Mechanics and Physics of Solids, 1992. 40: p. 1377.
107. Pineau, A., Besson,J., *Introduction*, in *Local approach to fracture*, J. Besson, Editor. 2004, Les Presses de l'Ecole des Mines: Paris.
108. Zaoui, A., *Preface*, in *Local approach to fracture*, J. Besson, Editor. 2004, Les Presses de l'Ecole des Mines: Paris. p. 9-10.
109. Tvergaard, V. *Influence of voids on shear band instabilities under plain strain conditions.* International Journal of Fracture, 1981. 17: p. 389-407.
110. Tvergaard, V. *On localization in ductile materials containing spherical voids*. International Journal of Fracture, 1982. 18: p. 237-52.
111. Tvergaard, V., Needleman,A. *Analysis of the cup-cone fracture in a round tensile bar.* Acta Metallurgica, 1984. 32: p. 157-169.
112. Pardoen, T., Besson,J., *Micromechanics-based constitutive models of ductile fracture*, in *Local approach to fracture*, J. Besson, Editor. 2004, Les Presses de l'Ecole des Mines: Paris. p. 221-264.
113. Faleskog, J., Gao, X., Shih,C. *Cell model for nonlinear fracture analysis - I. Micromechanics calibration*. International Journal of Fracture, 1998. 89: p. 355-373.

114. Pardoen, T. *Numerical simulation of low stress triaxiality ductile fracture*. Computers and Structures, 2006. 84: p. 1641-1650.
115. Gologanu, M., Leblond, J., Devaux,J., *Recent extensions of the Gurson model for porous ductile metals*, in *Continuum micromechanics*, P. Suquet, Editor. 1997, Springer: New York.
116. Gologanu,M. *Etude de quelques problemes de rupture ductile des metaux*. these, Universite Paris 6, 1997.
117. Thomason,P.F., *Ductile Fracture of Metals*. 1990, Oxford: Pergamon Press.
118. Chu, C.C.,A. Needleman. *Void nucleation effects in biaxially stretched sheets*. Transactions of the ASME. Journal of Engineering Materials and Technology, 1980. 102: p. 249-56.
119. Zhang, Z.L., Thaulow, C., Odegard,J. *Complete Gurson model approach for ductile fracture*. Engineering Fracture Mechanics, 2000. 67: p. 155-168.
120. Nahshon, K., Hutchinson,J.W. *Modification of the Gurson Model for shear failure*. European Journal of Mechanics - A/Solids. In Press, Corrected Proof.
121. Fabregue, D., Pardoen,T. *A constitutive model for elastoplastic solids containing primary and secondary voids*. Journal of the Mechanics and Physics of Solids. In Press, Corrected Proof.
122. Hill,R., *The mathematical theory of plasticity*. 1950, Oxford: Clarendon Press.
123. Barlat, F., Lege, D., Brem,J. C. *Six-component yield function for anisotropic materials*. International Journal of Plasticity, 1991. 7: p. 693-712.
124. Karafillis, A.P., Boyce,M.C. *General anisotropic yield criterion using bounds and a transformation weighting tensor*. Journal of the Mechanics and Physics of Solids, 1993. 41: p. 1859-1886.
125. Lemaitre, J., Chaboche,J., *Mechanics of Solid Materials*. 1990, Cambridge: Cambridge University Press.
126. Chaboche,J.-L., *Unified cyclic viscoplastic constitutive equations: development, capabilities, and thermodynamic framework*. 1996, Orlando: Academic Press. 1-68.
127. Chow, C.L., Yang,X.J. *Prediction of forming limit diagram with mixed anisotropic kinematic-isotropic hardening plastic constitutive model based on stress criteria*. Journal of Materials Processing Technology, 2003. 133: p. 304-310.
128. Mear, M.E., Hutchinson,J.W. *Influence of yield surface curvature on flow localization in dilatant plasticity*. Mechanics of Materials, 1985. 4: p. 395-407.
129. Becker, R., Needleman,A. *Effect of yield surface curvature on necking and failure in porous plastic solids*. Journal of Applied Mechanics, Transactions ASME, 1986. 53: p. 491-499.
130. Leblond, J.-B., Perrin, G., Devaux,J. *Improved gurson-type model for hardenable ductile metals*. European Journal of Mechanics, A/Solids, 1995. 14: p. 499.
131. Besson, J., Guillemer-Neel,C. *An extension of the Green and Gurson models to kinematic hardening*. Mechanics of Materials, 2003. 35: p. 1-18.
132. Shima, S., Oyane,M. *Plasticity theory for porous metals*. International Journal of Mechanical Sciences, 1976. 18: p. 285-91.
133. Pardoen, T., Dumont, D., Deschamps, A., Brechet,Y. *Grain boundary versus transgranular ductile failure*. Journal of the Mechanics and Physics of Solids, 2003. 51: p. 637-665.
134. Schevaerts, F., Onck, P.R., Brechet, Y., Pardoen,T. *A multiscaler model for the cracking resistance of 7000 Al*. Conference proceedings EMMC9, 2006: p. 447-452.

135. Tvergaard, V., Hutchinson,J.W. *Two mechanisms of ductile fracture: void by void growth versus multiple void interaction*. International Journal of Solids and Structures, 2002. 39: p. 3581-3597.
136. Steglich, D., Brocks, W., Heerens, J., Pardoen,T. *Anisotropic ductile fracture of Al 2024 alloys*. Engineering Fracture Mechanics, 2008. In Press, Corrected Proof.
137. Khor, K.H., Buffiere, J.-Y., Ludwig, W., Toda, H., Ubhi, H.S., Gregson, P.J., Sinclair,I. *In situ high resolution synchrotron x-ray tomography of fatigue crack closure micromechanisms*. Synchroton Radiation for Advanced Materials Analysis and Processing Journal of Physics Condensed Matter, 2004. 16: p. 3511-3515.
138. Yamamoto S., Toda H., Qian L., Ohgaki T., Kobayashi M., Kobayashi T.,Uesugi K. *Assessment of Damage and Fracture Behaviors in a Cast Aluminum Alloy via In-situ Synchrotron Microtomography*. Materials Science Forum, 2006. 519-521: p. 1005-1010.
139. Buffiere, J.-Y, Ferrie, E., Ludwig, W., Gravouil,A. *Characterisation and modelling of the three dimensional propagation of short fatigue cracks*. Materials Science Forum, 2006. 519-521: p. 997-1004.
140. Qian, L., Toda, H., Uesugi, K., Kobayashi, T., Ohgaki, T., Kobayashi,M. *Application of synchrotron x-ray microtomography to investigate ductile fracture in Al alloys*. Applied Physics Letters, 2005. 87: p. 241907-241910.
141. Maire, E., Grenier, J.C. , Babout,L. *Damage investigation in aluminum alloys by X ray tomography*. Materials Science Forum, 2006. 519-521: p. 821-827.
142. Maire, E., Buffiere, J.-Y., Salvo, L., Blandin, J.J., Ludwig, W., Letang,J.M. *On the application of X-ray microtomography in the field of materials science*. Advanced Engineering Materials, 2001. 3: p. 539-46.
143. Ludwig,W. *Development and Applications of Synchrotron Radiation Microtomography*. Dissertation, LMU München, 2001.
144. www.esrf.fr.
145. www.europhysicsnews.com.
146. Baruchel, J., Boller, E., Cloetens, P., Ludwig, W., Peyrin,F., *Phase contrat tomography*, in *X-Ray Tomography in Materials Science*, Baruchel, et al., Editors. 2000, Hermes Science Publications: Paris. p. 29-43.
147. Cloetens, P., Ludwig, W., Guigay, J.-P., Baruchel, J., Schlenker, M., V. Dyck,D., *Phase contrast tomography*, in *X-Ray Tomography in Materials Science*, Baruchel, et al., Editors. 2000, Hermes Science Publications: Paris. p. 29-43.
148. Ludwig, W., Bouchet, S., Bellet, D.,Buffiere, *3D observation of grain boundary penetration in Al alloys*, in *X-Ray Tomography in Materials Science*, Baruchel, et al., Editors. 2000, Hermes Science Publications: Paris. p. 155-163.
149. Ludwig, W., Bellet,D. *Penetration of liquid gallium into the grain boundaries of aluminum: A synchrotron radiation microtomographic investigation*. Materials Science and Engineering A: Structural Materials: Properties, Microstructure and Processing, 2000. 281: p. 198-203.

Chapter 3

Materials characterisation and experimental methods

This chapter presents the investigated materials and their microstructural features. Additionally, the experimental techniques used in this project are described in detail.

3.1 Materials Characterisation

Two types of heat-treatable airframe aluminium alloys have been considered in this work, designated AA6156 and AA2139. Both have been received in the T351 condition (solutionised, stress relieved by stretching, and naturally aged), and were supplied by Alcan Centre de Recherches de Voreppe (CRV).

3.1.1 Alloy AA6156

The composition ranges of the alloy AA6156 are given in Table 3-1. Optical micrographs of the grain structure after etching with Keller's etch are shown in Figure 3-1.

Si	Fe	Cu	Mn	Mg	Cr	Zn
0.7-1.3	< 0.2	0.7-1.1	0.4-0.7	0.6-1.2	< 0.25	0.1-0.7

Table 3-1: Composition limits of alloy AA6156 alloy in wt %

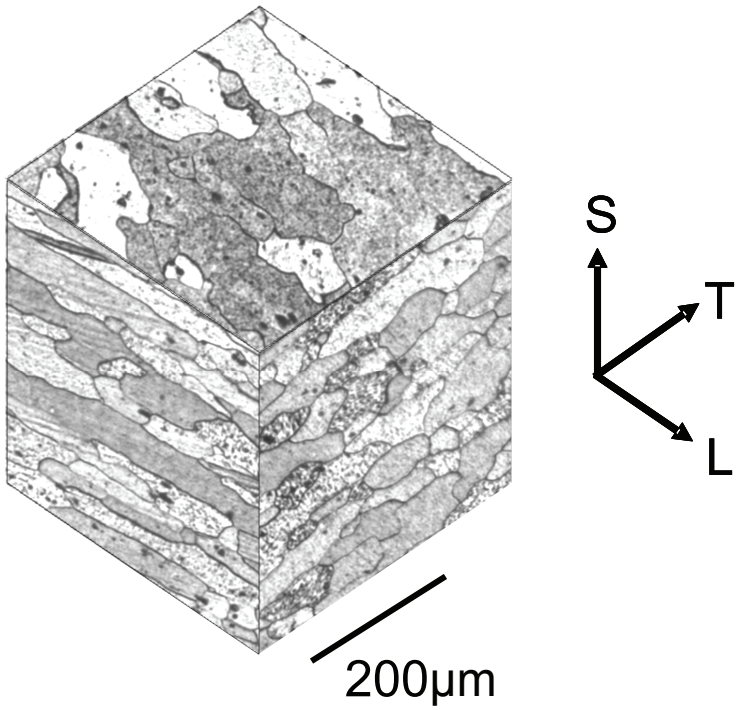

Figure 3-1: Pseudo three-dimensional optical micrograph in T3 condition for the AA6156 alloy

The sheet material has been received in 5.0mm gauge and was subsequently symmetrically machined to 3.2mm thickness. Samples of 3.2mm thickness were solutionised at 550°C for 30 min. Quenching was then carried out into: (a) water at 20°C, (b) water at 60°C, or (c) still lab air. The delay between solutionising and quenching was very short (less than 1s). Estimated cooling rates in plates of 3mm thickness for the 3 relevant cooling procedures are identified in Table 3-2 (after Hatch [1]): the values shown refer to the average rate from 400°C to 290°C. All three types of sample were subsequently subjected to a heating ramp of 20°C/h up to 190°C where they were held for 4h, reaching a peak age (T6) condition.

Quenching	to water at room temperature (RT):	to water at 60°C	in still air
Quench rate	1000°C/s	205°C/s	0.94°C/s

Table 3-2: Quench rates of plate of 3mm thickness (after [1])

3.1.2 AA2139

AA2139 sheet was supplied with a thickness of 3.2mm. The composition ranges are given in Table 3-3.

Si	Fe	Cu	Mn	Mg	Ag	Ti	Zn
<= 0.1	<= 0.15	4.5 - 5.5	0.20 - 0.6	0.20 - 0.8	0.15 - 0.6	<= 0.15	<=0.25

Table 3-3: Composition limits of alloy AA2139 in weight %

After solution treatment, the plate was stretched by 2% in the rolling direction (L). The material has been assessed in two different conditions (see Table 3-4), T351 and a treatment approximating a standard T8. For brevity, In the following T351 will be referred to as 'T3'.

T351	"T8"
As received	The as-received material is aged at 175 °C for 16 hours

Table 3-4: Tested heat treatment conditions AA2139

Optical micrographs of the grain structure after etching with Keller's etch are shown in Figure 3-2(a). The grain size was obtained from optical microscopy on etched sections using a mean linear intercept method as 60 μm in the rolling direction (L), 52 μm in the long transverse direction (T) and 24 μm in the short transverse direction (S). Figure 3-2(b) shows a typical 2D section from the synchrotron radiation computed tomography (SRCT) scan of the as received material. Detailed information on the imaging techniques and testing conditions is given in subsequent sections. The aluminium matrix (grey), intermetallics (white) and pores (black) are clearly delineated, with phase contrast fringes highlighting the associated edges/interfaces. Mean micro pore dimensions (3D Feret measurements) are given in Table 3-5. Pore content determination variation of the non-deformed material was governed by the choice of the grey scale threshold (see Table 3-5) and will be discussed in more detail later. 3D Voronoi tesellation [2] of the void distribution revealed average cell dimensions of 45μm, 48μm and 50μm in the L, T and S direction respectively, i.e. indicative of near-neighbour separation distances in these directions; *i.e.* the Voronoi cell aspect ratios for cells around pores are found to be about 1.

The particles were strongly aligned as stringers in the rolling direction (L) with stringer dimensions of the order of 15-30μm (*cf.* 1-10μm in the long transverse direction (T) and 1-6μm in the short-transverse direction (S)). The intermetallic content has been measured via grey value thresholding of field emission gun scanning electron microscope (FEG-SEM) images (backscattered electron mode). EDS analysis revealed two populations of intermetallic particles: $Al_7Cu_2(Fe,Mn)$ and Al_2Cu. The volume fraction of coarse intermetallic particles, and the Feret dimensions of Voronoi cells around pores *and* intermetallic particles obtained from SRCT data is given in Table 3-5. Pores were seen to be closely linked with the intermetallic distribution, with a large proportion being associated with one or more intermetallic particles. The alignment of pores into local chains in the L-direction is also evident in Figure 3-2(b).However, no significant distribution anisotropy for pores and particles can be detected between T and L direction using average Voronoi cell dimensions around pores and particles (see Table 3-5). Measurement of 3D void Feret dimensions and 3D Voronoi tessellation have been determined using a Matlab code developed at Centre des Matériaux at Ecole des Mines de Paris.

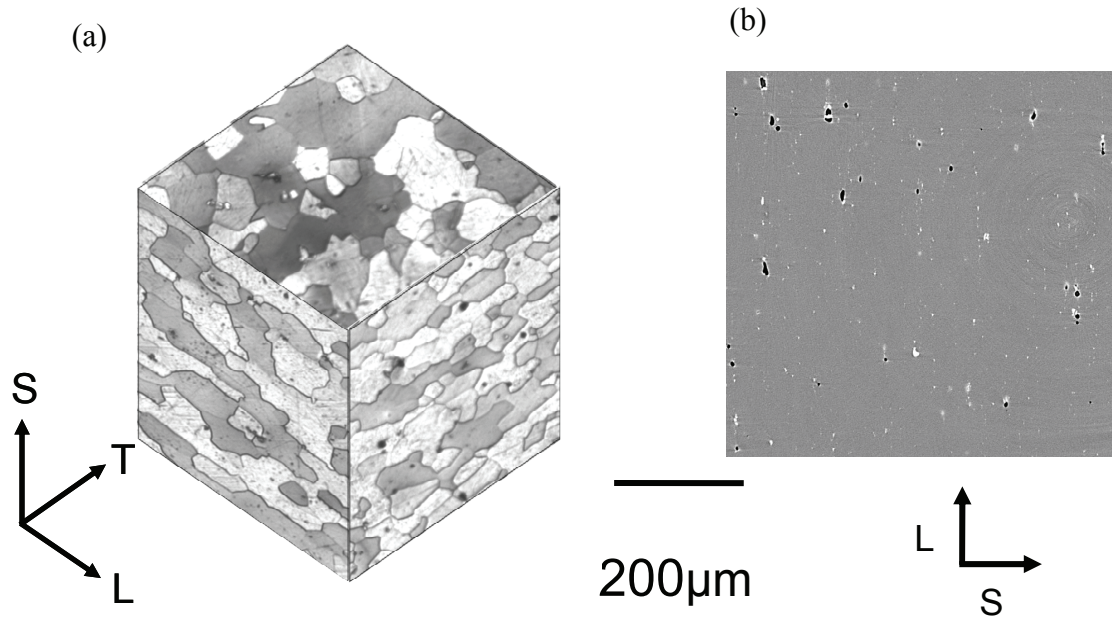

Figure 3-2: (a) Pseudo three-dimensional optical micrograph of AA2139 in the T3 condition (b) 2D SRCT section of the as-received AA2139 material in the L-S plane

	Porosity			Intermetallic particles		
f_v in %	0.33 with a variation of ±10% when setting extreme grey values.			0.45 ±15% (standard error based on repeat measurements at different magnifications).		
	Mean Feret dimensions of pores in µm			Mean Feret dimensions of Voronoi cells around 2nd phase particles and pores in µm		
	L	T	S	L	T	S
	7.6	5.4	4.5	23	24	25

Table 3-5: Porosity and intermetallic particle content, dimensions and distribution measured for AA2139

3.2 Mechanical testing

In this study 4 types of specimen have been utilised (see Figure 3-3): (a) smooth tensile bars, (b) notched tensile flat plates (EU2), (c) Kahn tear test specimen and (d) large M(T) panels. All tested material had a thickness of 3.2 mm.

For the AA6156 material only Kahn tear tests have been performed. Specimens were loaded in the T direction, cracks then propagate in the L direction; *i.e.* a T-L configuration.

For the AA2139 material two orientations of loading in the sheet plane have been investigated for all samples: L and T. At least 2 tests have been performed in each direction, except for the M(T) sample where only one test has been performed per condition and testing direction. M(T) tests for the AA2139 material in the T3 condition were only performed for T-L loading. Tensile testing has been carried out on smooth tensile samples. The displacement rate for tensile testing was 0.4mm/min and 0.34mm/min for EU2 tests. For the EU2 samples the opening displacement at both notches has been recorded to guarantee the symmetric opening displacement. Tests on notched EU2 specimens allow to investigate fracture properties at increased stress triaxialities. Kahn tear tests under displacement control have been carried out in general accord with [3] at a testing speed of 0.085 mm/min.

M(T) testing has been carried out as described in [4] at Alcan CRV. The original crack length of large M(T) specimens was 253 mm. The first 249mm were made by electrical-

discharge machining and the last millimetres were obtained by fatigue precracking. The applied maximum load during precracking was 20% of the yield strength applied to the net section. The stress ratio was 0.1 and the frequency is 3 Hz. To prevent buckling, two rigid face plates were affixed to the central portion of the specimen. Lubrication was provided between the face plates and the specimens. A displacement gauge is used to measure the crack-opening displacement across the crack mouth. The gauge length was 60 mm. A 1000 kN load cell was used and the cross head speed is 0.1 mm/min.

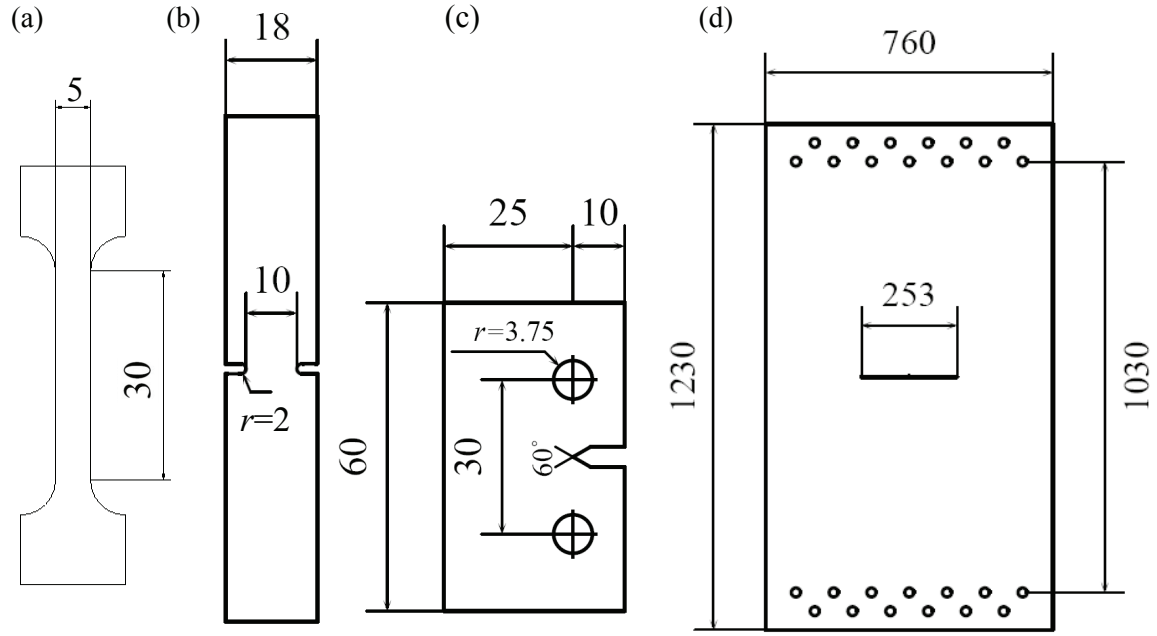

Figure 3-3: Specimen geometries for: a) tensile samples b) EU2 samples c)Kahn tear test samples d) M(T) samples (all dimensions in mm)

3.2.1 Kahn tear testing

A general view of the loading cells and measurement equipment is shown in Figure 3-4. For the use of the clip gauges for the crack tip opening displacement (COD) measurements, knife edges have been glued to the notch mouth with Araldite two component glue (see Figure 3-5). The initial distance of the knife edges was 3mm. The travel of the available clip gauge in this configuration is 4.4mm. This arrangement is considered superior to the original machined in knife edges as greater COD measurement range is achieved.

Fracture tests have been performed under displacement control in general accord with [3] in several displacement steps. The cross head displacement speed varied between 0.5mm/min and 0.085 mm/min depending on the crack length progression speed. Negligible influence of cross head speed on loads has been found in these tests. Crack length measurements have been performed via a Wild Macroscope 420 and an attached DVC 1310 camera. Lines in a distance of 1mm have been drawn on the sample via a height gage to facilitate tracking of the crack length (see Figure 3-4).

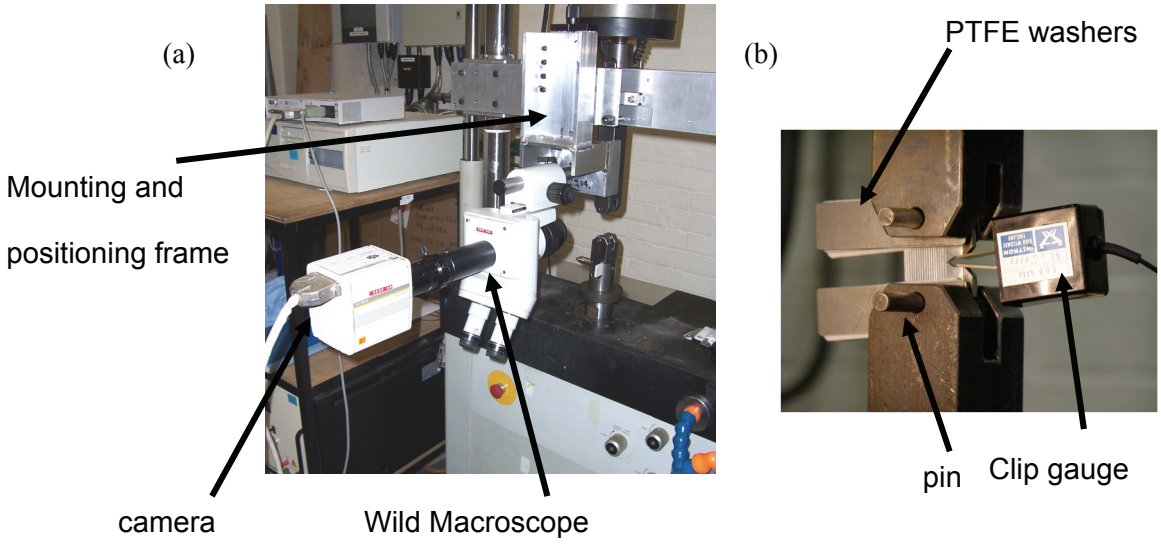

Figure 3-4: (a) photo of the Kahn tear test rig (b) photo of a mounted Kahn tear test sample

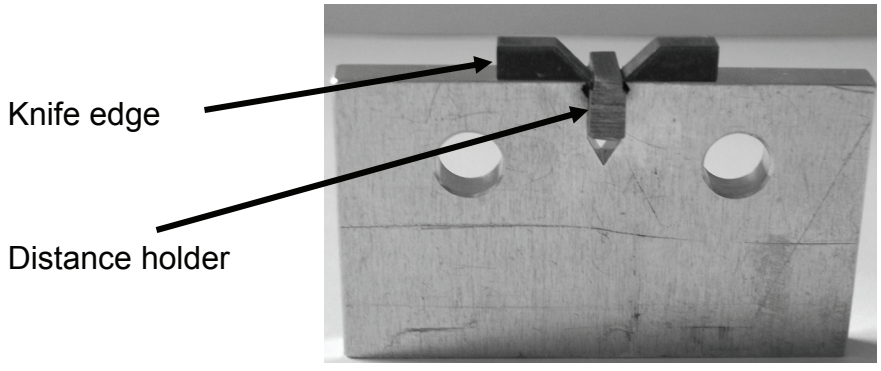

Figure 3-5: Kahn tear test specimen with distance holder and glued knife edges

3.3 Tomography sample preparation

For SRCT scanning, cracks were grown in Kahn tear test pieces (dimensions: 35mm x 60mm x 3.2mm) in general accord with [3]. Tests were arrested before final failure of the coupon either in the initiation region (loads under maximum load) or the propagation region (at a crack length of 10mm).

To facilitate high resolution SRCT imaging of the arrested crack tip region, a small 'stick' of material (dimensions 1mm x 1mm x 10mm) was extracted around the tip at the specimen mid-plane (long dimension parallel to the direction of crack extension) using a slow speed diamond saw. Different cuts have been made to obtain the 'stick' shown in Figure 3-6. The consecutive cuts are labelled 1 to 6. After cuts 3 and 4, a 1mm thin plate is obtained (see Figure 3-7). In order to guarantee the integrity of the sample, and avoid introduction of damage through the cutting process, the 1mm thick plate has been reinforced by putting an additional aluminium plate of 3.2mm thickness under it.

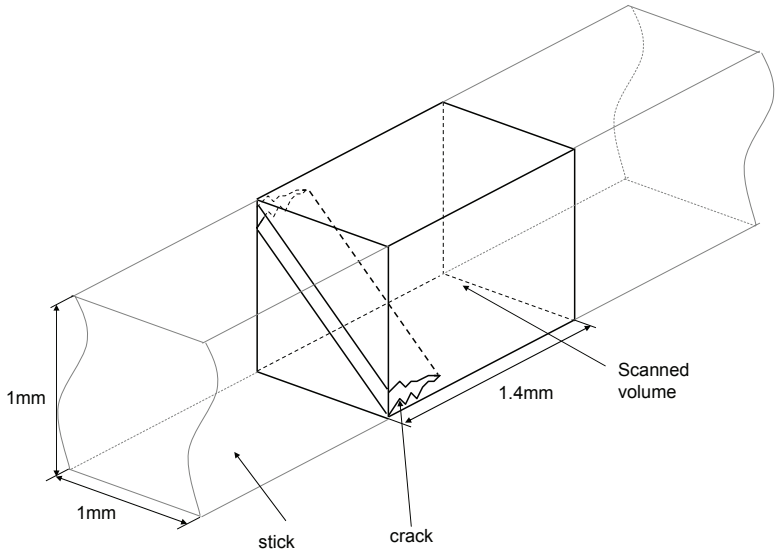

Figure 3-6: Schematic drawing of the investigated volume at the arrested crack tips.

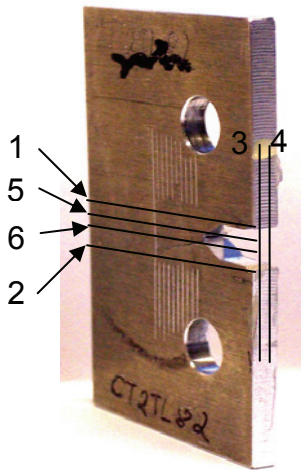

Figure 3-7: Kahn tear test samples with lines and numbers for the different diamond saw cuts

3.4 Gallium wetting

Liquid Gallium (Ga) grain boundary wetting technique has been applied in conjunction with SRCT to visualise the 3D grain structures of polycrystalline materials [5,6]. This technique is based on rapid penetration of the liquid phase along grain boundaries.

For the AA6156 material of the present study scans were carried out for both the 'as tested' crack tip samples for the 3 quench rates, and after subsequent liquid gallium (Ga) grain boundary wetting, allowing the observation of grain boundaries and their relationship to the fracture process. To ensure close contact between the sample and the liquid Ga the aluminium surface oxide was scratched during the application of heated, liquid Ga. The liquid Ga wetting makes the samples extremely brittle, and unfortunately one sample of room temperature quenched AA6156 (see Chapter 4) broke during the Ga wetting process and could not be scanned.

3.5 Synchrotron Radiation Computed Tomography (SRCT)

Tomography was performed at beamline ID 19 of the European Synchrotron Radiation Facility (ESRF), Grenoble, France, at 20.5kV. The facility provides a highly coherent, spatially and spectrally homogeneous beam with a high photon flux. For one volume 1500 radiographs were taken using a high performance CCD camera whilst the sample was turned through 180° (parallel beam conditions) in steps of 0.12°; the typical imaging time

per radiograph was 0.7s. Flat-field and dark current corrections were performed and reconstruction was carried out using a conventional filtered back projection algorithm [7]. In the reconstructed slices an isotropic voxel size of 0.7µm was obtained. Phase contrast imaging has been performed to enhance the detection of edges [8]. At ID19 this is a straightforward technique as advantage is taken of the radiation coherence by adjusting the sample-detector distance (13mm in the present work) to obtain near-field Fresnel diffraction effects. Detailed information on the imaging techniques is given in [9].

3.6 SRCT Analysis

3.6.1 Segmentation

2D and 3D imaging and analysis was carried out using the commercial software package 'VG Studio Max v1.2' [10]. For determination of the void content and pore dimensions from tomography data, a suitable segmentation method is needed.

Figure 3-8 shows (a) a typical SRCT 2D section of an imaged pore. In

Figure 3-8 (b) the grey value distribution along the red line in (a) is shown. The two grey value maxima are a result of the phase contrast.

(a) (b)

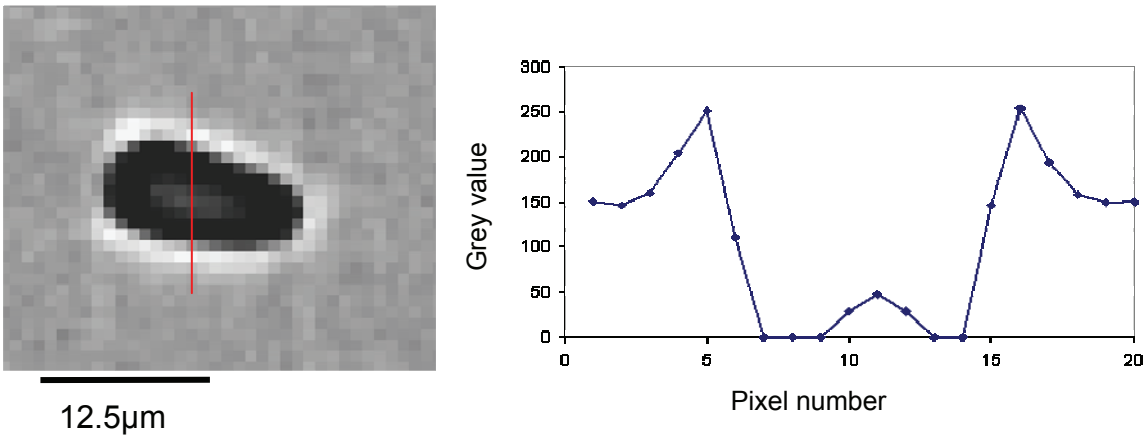

Figure 3-8: (a) Pore imaged through SRCT (b) grey value distribution along line indicated in (a)

Figure 3-9 shows the void area fraction as a function of the grey value tolerance using the so called "seed growth method". In this method every single void needs to be chosen

individually. Via clicking into the void a grey value is chosen from which a 'seed' is then growing until pixels with a grey value difference from the fist chosen pixel larger than the chosen tolerance are reached. In Figure 3-9 it can be seen that a plateau is reached for a threshold around 50-60. From a grey value of ~100 onwards the seed growth method does not allow to pick up single voids anymore as the whole matrix is chosen. For values smaller than 20 it can be seen the interior of the voids is not included. In conclusion a suitable grey value would be for example 60. The overall investigated area was ~300µm by 400µm.

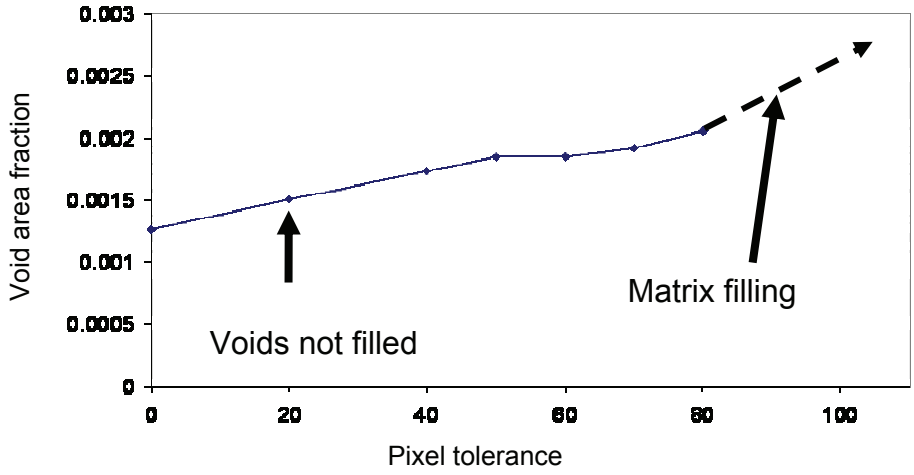

Figure 3-9: Void volume fraction measure from SRCT data for the AA2139 alloy as a function of the chosen grey value threshold in the seed growth method

Figure 3-10 shows a comparison of the void area fraction for a sequence of 13 layers (again 300 µm by 400 µm) of a given SRCT volume for the seed growth method at a grey value of 60 and the comparison to a simple thresholding method at a grey value of 77. It can be seen that very similar results are obtained. For this reason the void volume fraction has been obtained in the present study using a simple grey value thresholding method. Every layer is expected to have some deviation from the true volume average due to the heterogeneity of the microstructure. Using a larger SRCT volume (see next section) for the determination of the average void volume fraction will help to obtain a more accurate estimate of the real average void volume fraction.

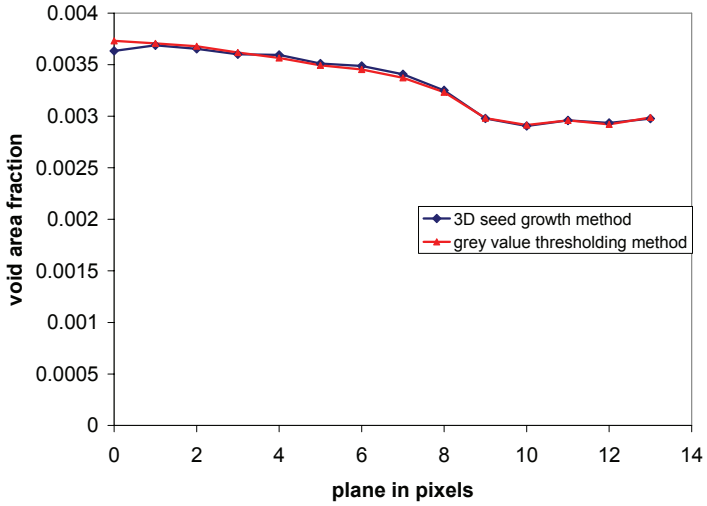

Figure 3-10: Comparison of 2D void area fraction between seed growth method (grey value 60) and grey value thresholding method (grey value77) from SRCT data for the AA2139 alloy

3.6.2 Void quantifications

Determination of void volume fractions have been performed using ImageJ [11] using a grey value threshold method such as described in the previous section. Detailed void by void inspection using a range of grey value thresholds on a range of voids showed that at grey value threshold of 90 the voids were properly segmented without neglecting interior parts of voids, and hence this value was used throughout SRCT measurements of the pore content in the AA2139 material before loading were carried out (sampling volume of 980 µm x 490 µm x 490µm). For the arrested cracks, the evolution of damage/voids ahead of the growing crack tip has been characterised in a similar sampling volume at a distance of some 70µm ahead of the overall crack tip location (representing a region of reasonably uniform damage evolution, ahead of local fluctuations in the main crack tip location and coalescence).

3.6.3 VG Studio/sum along ray analysis

Use was made of a "sum along ray" visualisation [12] available in 'VG Studio Max v1.2'[10]. Specifically, the imaged volumes containing the crack tip and associated microstructural features have been segmented (in 3D) and shown in isolation from the surrounding aluminium matrix. A 'box-car' transformation is used to fill the crack/defects

with voxels of equal grayscale, which are then viewed perpendicular to the nominal crack plane. The "sum along ray" method (see Figure 3-11) then generates a projection of the crack plane, where the grey level is directly proportional to the crack thickness, *i.e.* a crack opening displacement (COD) map is obtained.

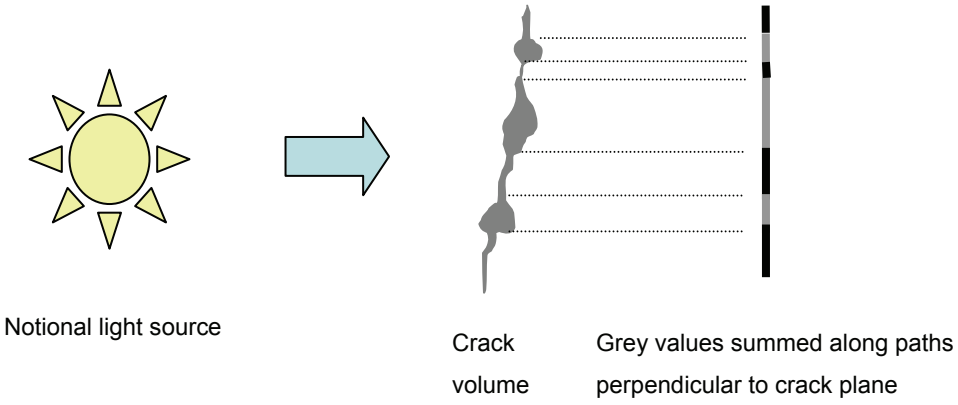

Figure 3-11: Schematic 2D illustration of the "sum along ray" algorithm: in the final projection of the crack thicker areas, in this instance associated with void growth, appear bright/white.

For the analysis of arrested cracks in the initiation region of the AA2139 alloy use was made of analysis software developed at Centre des Matériaux at Ecole des Mines de Paris. The aim was to show the local crack opening such as in the 'sum along ray algorithm' available in 'VG Studio Max v1.2' [10] and additionally provide a colour scale to quantify the local opening. Additionally, a crack height map has been produced, where the average height of the crack with respect to the loading direction is shown.

A critical step of this analysis is the segmentation of the crack volume. This step requires some care especially in the case of ductile fracture cracks, since cracks are typically very open which results in a grey level gradient within the crack. Narrow regions usually appear in black due to phase contrast fringes on the crack lips whereas highly opened regions display a combination of black close to the crack lips and grey within the voids. The fact that the grey level within the voids is very close to the grey level value within the aluminium matrix makes the analysis more complicated and could require extensive, time consuming human intervention in the segmentation process. To make the process more time efficient and avoid possible inconsistencies from the human intervention, a

completely automated procedure has been used here to produce binary images of the cracks. First an edge preserving smoothing algorithm (sometimes called 'surface blur algorithm') is applied to the whole volume. This was successful to separate the grey level dynamics of both the aluminium matrix and the inner part of the voids, without modifying the shape of the voids. The volume can then be binarized with a single thresholding operation. At this stage the binary volume contains the crack plus all the other voids in the volume. A morphologic reconstruction is done to keep only the connected voids. The local opening in loading direction and mean height position can then be computed for each location.

3.7 Differential Scanning Calorimetry (DSC)

3.7.1 Principles

Differential Scanning Calorimetry (DSC) is a thermal analysis method. With respect to aluminium alloys, solid state reactions can be detected such as precipitation, homogenisation and recystallization [13]. In DSC the difference of heat flow between a sample and a reference, in which no reactions occur, is measured as a function of temperature. A sketch of the DSC measurement device is shown in Figure 3-12 below:

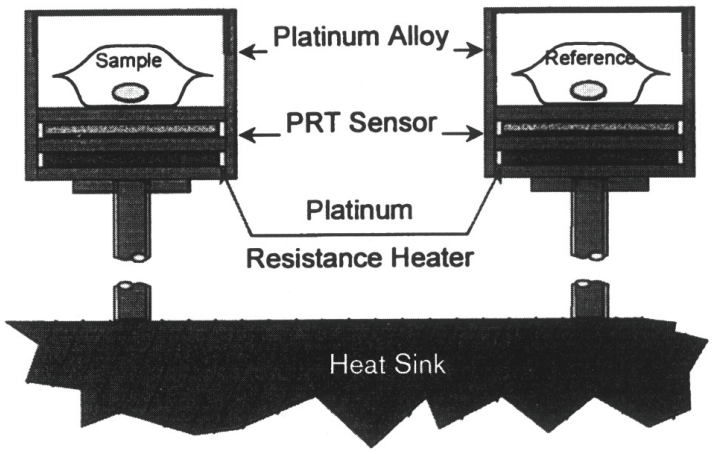

Figure 3-12: Schematic cross-section of a power compensation DSC figure (after Ref.[14])

It is common practice that the obtained curves undergo a baseline correction. The following equation can be applied for a two parameter baseline correction [15]:

$$Q_{real} = Q_{mes} + a + bT \qquad \textbf{(3-1)}$$

a and *b* can be obtained knowing certain features of the curves. For instance when 2 or more points where the heat flow is zero are known, the two parameter of the curve can be determined.

During endothermic reactions (negative heat flow) heat is added to a system to maintain a given temperature. Generally, dissolution of phases into the Al rich phase is an endothermic reaction. During exothermic reactions (positive heat flow) heat is released from the sample. The formation of new precipitate phases is an endothermic reaction.

In order to assess the precipitation reactions occurring in an aluminium alloy in a DSC it can be heated at a constant rate. It is then instructive to link the temperature of the DSC experiment to the ageing time in a conventional isothermal heat treatment. The following equation gives an estimation of the time corresponding to a temperature at which the material is in the same state [13]:

$$t_{eq} \cong \frac{T_f}{\beta}\frac{RT_f}{E}\exp\left(-\frac{E}{RT_f}\right)\left[\exp\left(\frac{E}{RT_{iso}}\right)\right]^{-1} \qquad \textbf{(3-2)}$$

Where t_{eq} is the corresponding time of an isothermal ageing, T_{iso} is the isothermal ageing temperature, T_f is the temperature attained during a constant heating rate, β is the constant heating rate, *E* is the activation energy of the reaction of interest and *R* the gas constant.

3.7.2 DSC: Experimental Method

The used DSC device was a Perkin-Elmer Pyris. Disks of 5mm diameter and 1mm thickness have been ground from the alloy of interest. In order to minimise surface plastic deformation [16], final grinding was performed on 400 Grit SiC paper.

Before the experiment, three samples of each alloy of the size of a Kahn tear test piece have been solutionised and quenched as follows:

- 20°C water quench

- 60°C water quench
- Air cool

In order to have samples with known fixed cooling rates three further samples were solutionised and quenched inside the DSC, whilst the temperature during cooling was controlled and recorded.

The corresponding cooling rates were:

- -200°C/min
- -50°C/min
- -10°C/min

All samples were subsequently aged at room temperature for 3 days. Additionally, samples were assessed in the as received condition. The heating rate for the DSC experiments was 10°C/min (from 20°C to 540°C) for all the samples.

DSC curves are shown after correction for baseline and heat capacity effects [13], i.e. they represent the heat flow due to reactions in the sample.

3.8 Scanning electron microscopy

A Jeol 6500F FEG-SEM was used for general fractography and microstructure observations at Southampton University. The beam orientation was in the test loading direction. Additional fractography on the AA2139 T3 samples has been carried out with a field emission gun scanning electron microscope (Zeiss Gemini DSM 982) at Ecole des Mines. EDX studies on the Jeol 6500F FEG-SEM have been carried out using an Oxford instruments ISIS system on ground and polished surfaces (ground with 120, 600, 1200 SiC paper and polished with 6μm, 1μm, ¼ μm diamond polishing paste) and on fracture surfaces. EBSD studies have been performed on ground and electro-polished samples (ground with 120, 600, 1200 and 4000 SiC paper) using an "HKL System" on the Jeol 6500F FEG-SEM and Channel 5 analysis software.

3.9 Transmission electron microscopy

Transmission electron microscopy (JEOL 3010) was carried out on samples of the AA6156 alloy that had been quenched at different rates. Samples were prepared by cutting thin slices (~0.3 mm) from the quenched and subsequently artificially aged samples, punched into 3 mm diameter discs and ground to a thickness of ~0.2 mm in the T-S plane. Subsequent electropolishing was performed with a twin jet electropolisher using a solution of 30% HNO_3 and 70% methanol maintained between -20˚C and -30°C.

3.10 References

[1] Hatch JE. Aluminum: properties and physical metallurgy. Metals Park, OH: ASM; 1984.

[2] Yang N., Boselli J., Sinclair, I. J. Microsc. 2001;201: 189-200

[3] ASTM-international, Standard Designation B 871 - 01. 2001: West Conshohocken, USA

[4] Bron F, Besson J, Pineau A. Mater Sci Eng A 2004 ;A 380 : 356-364

[5] Khor KH, Buffiere J-Y, Ludwig W, Sinclair I. Scripta Mater. 2006;55:47-50

[6] Ludwig W, Bellet D. Mater Sci Eng A 2000; 281: 198-203

[7]Maire E, Buffière J-Y, Salvo L, Blandin JJ, Ludwig W, Letang JM.
Adv Eng Mater 2001;3:539–46.

[8] Kocsis M, Snirgirev A. Nucl Instrum Methods Phys Res Sect A 2004;525A:79-84

[9] Ludwig W. Development and Applications of Synchrotron Radiation Microtomography, Dissertation der LMU München, München, 2001

[10] VGStudio Max 1.2, Volume Graphics GmbH

[11]Abramoff, M.D., Magelhaes, P.J., Ram, S.J. Biophoton Int, 2004;11:36-42

[12] Toda H, Sinclair I, Buffière J-Y *et al*. Philos Mag 2003;83:2429-2440

[13] M.J. Starink: Int. Mater. Rev., Vol. 49 (2004), p. 191-226

[14] www.perkinelmer.com

[15] Kamp N. Toughness-strength relationships in high strength 7XXX aluminium alloys. Ph.D. thesis, University of Southampton, 2002.

[16] Birol Y, The effect of sample preparation on the DSC analysis of 6061 alloy. Materials Institute, Marmara Research Center, 2005

Chapter 4

Quench sensitivity of toughness in an Al alloy: direct observation and analysis of failure initiation at the precipitate free zone

In this chapter the results on the toughness quench sensitivity study of the 6156 alloy is given in the form of a paper. It is mostly identical to a paper that has been published in Acta Materialia, but some additional data on DSC experiments is added.

Abstract

Analysis of toughness in 6156 Al-Mg-Si-Cu sheet has been performed using enhanced Kahn tear tests on samples quenched at different rates. Crack initiation energies were hardly affected by changing water quench temperature from 20°C to 60°C; however a significant reduction was evident on air cooling. Crack propagation energy was reduced for both 60°C water quenched and air cooled materials. Observation of failure initiation through synchrotron radiation computed tomography (SRCT), for the 60°C water quenched material revealed failure ahead of the crack tip of grain boundaries oriented at 45° to the main loading axis and crack "tongues" extending into the material ahead of the main crack. Failure was predominantly intergranular. Fractographic assessment revealed predominantly voiding and shear decohesion in the 20°C water quenched material. With the aid of the new findings past models on the influence of precipitate free zone parameters on toughness have been revised.

4.1 Introduction

The toughness reduction caused by the presence of a precipitate free zone (PFZ) adjacent to the grain boundaries is a limiting factor for application of a range of heat treatable Al based alloys. Whilst past work has investigated the process through post failure analysis of toughness test samples and some basic ideas of the influence of precipitate zone width, grain boundary coverage and local strength have been proposed [1,2,3], a full analysis that is able to encompass all the main aspects including deformation geometry, stress partitioning and failure initiation has proved elusive, and no details on failure initiation sites have been reported. Current synchrotron radiation computed tomography (SRCT) resolution capabilities (resolution better than 1μm) allows for direct visualisation of microstructure and fracture micromechanisms within a material bulk in three dimensions (3D) [4]. As such it now allows detailed assessment of fracture mechanisms and the evolution of damage. In order to gain a novel insight into the changes of fracture mechanisms of materials with a PFZ, this paper reports the application of the technique to arrested cracks, allowing the evolution of damage and coalescence of damage at the crack tip to be imaged in 3D. Additionally, via the application and diffusion of gallium into the samples, it is possible to delineate grain boundaries in SRCT [5]: the facility to image samples with and without treatment allows for detailed correlation of fracture processes to the underlying grain structure.

The material to be studied is an AA6156 Al-Si-Mg-Cu alloy, which has recently been developed for its combination of high strength aluminium and weldability, which makes it suitable for airframe applications [6]. AA6X56 Al-Si-Mg-Cu alloys display good weldability, low density, good corrosion resistance and equivalent mechanical properties to established damage tolerant alloys such AA2024, and hence may be considered as potential replacements. Such AA6X56 alloys contain relatively high solute levels which can contribute to quench sensitivity [7], and, in common with a range of other 6XXX alloys, PFZs develop at grain boundaries of quenched and aged alloys. In damage tolerant applications, toughness will be a critical factor in design, and therefore accurate understanding of the mechanisms causing quench sensitivity with respect to toughness are of interest [8].

It is well established that different quench rates affect mechanical properties such as yield strength, ultimate tensile strength and fracture toughness in age hardened Al-alloys. However, fracture toughness may be substantially more quench sensitive than yield strength [9]. The mechanisms for changes in mechanical properties due to quench sensitivity in Al-Mg-Si alloys have been attributed to the precipitation of coarse phases on grain boundaries [10,11] and dispersoids [12,13], and to solute and/or vacancy depletion in zones around those nucleation sites forming soft precipitate free zones after ageing. It has been reported that the precipitation of coarse phases on grain boundaries along with the formation of a PFZ may result in a change of fracture mode from transgranular to intergranular fracture decreasing the fracture toughness of the material [10,11]. Attempts have been made to model and predict quench effects on hardness involving quench factor analysis [13].

The microstructural changes responsible for changes in toughness are characterised here by transmission electron microscopy (TEM) and SRCT. With the aid of the new findings past models on the influence of precipitate free zone parameters on toughness will be revised.

4.2 Experimental

AA6156 sheet was supplied by Alcan CRV. The AA composition ranges are given in Table 4-1. Optical micrographs of the grain structure after etching with Keller's etch are shown in Figure 4-1.

Si	Fe	Cu	Mn	Mg	Cr	Zn
0.7-1.3	< 0.2	0.7-1.1	0.4-0.7	0.6-1.2	< 0.25	0.1-0.7

Table 4-1: Composition limits of alloy AA6156 alloy in wt %

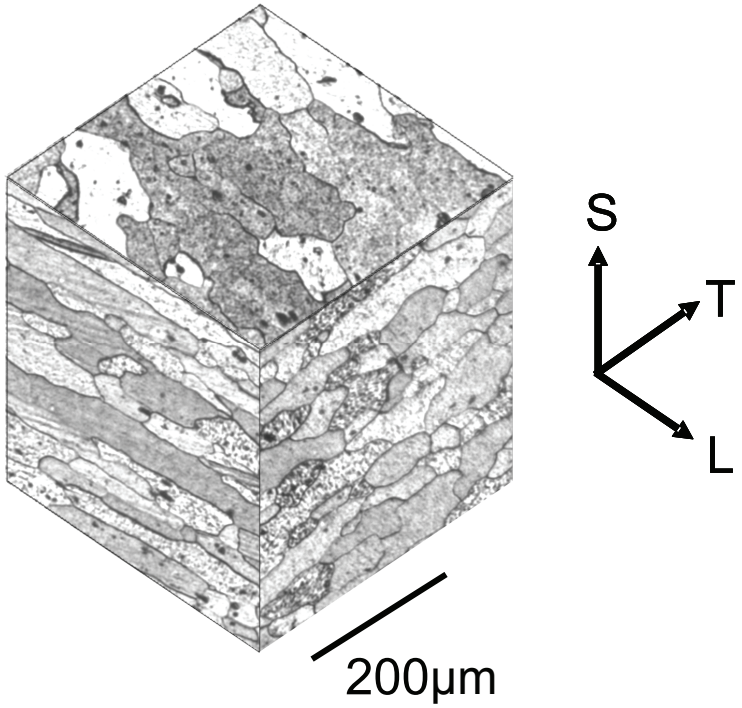

Figure 4-1: (AA6156) Pseudo three-dimensional optical micrograph in T3 condition

Samples of 3.2mm thickness were solutionized at 550°C for 30 min. Quenching was then carried out into: (a) water at 20°C, (b) water at 60°C, or (c) still lab air. The delay between solutionizing and quenching was very short (less than 1s). Cooling rates in plates of 3mm thickness for the 3 relevant cooling procedures are given in Table 4-2 (data from Hatch [14]).

Quenching	to water at room temperature (RT):	to water at 60°C	in still air
Quench rate	1000°C/s	205°C/s	0.94°C/s

Table 4-2: Quench rates of plate of 3mm thickness (after [14])

(All rates refer to the average rate over 400°C to 290°C.) All three types of sample were subsequently subjected to a heating ramp of 20°C/h up to 190°C where they were held for 4h, reaching a peak age (T6) condition. Kahn tear tests are performed under displacement control in general accord with [15].

Field emission gun scanning electron microscope (JEOL 6500F) images were used to assess material microstructures and subsequent fracture surfaces. Transmission electron microscopy (JEOL 3010) was also carried out: samples were prepared by cutting thin

slices (~0.3 mm) from the quenched and aged samples, punched into 3 mm diameter discs and ground to a thickness of ~0.2 mm. Subsequent electropolishing was performed with a twin jet electropolisher using a solution of 30% HNO_3 and 70% methanol maintained between -20˚C and -30°C.

For the SRCT assessment cracks were grown in Kahn tear test [15] pieces to a length of 10mm (arrested before final failure of the coupon). A small block of material (dimensions 1 x 1 x 10mm^3) was then extracted at the crack tip region using a slow speed diamond saw: as such, subsequent tomographic scanning of the crack itself could be carried out, as well as the material immediately ahead of the arrested tip. SRCT was performed at 20kV at beamline ID19 of the ESRF, Grenoble, France. The facility provides a highly coherent, spatially and spectrally homogeneous beam with a high photon flux. The typical imaging time was 0.7 sec. For one volume 1500 radiographs were taken using a high performance CCD camera and simultaneously the sample was turned 180° in steps of 0.12°. Flat-field and dark current corrections were performed and reconstruction was carried out using a conventional filtered back projection algorithm [5]. In the reconstructed slices an isotropic voxel size of 0.7μm was obtained. Phase contrast imaging has been performed allowing to enhance the detection of edges [16]. At the beamline ID19 this is a straightforward technique as advantage is taken of the radiation coherence by adjusting the sample detector distance (13mm in the present work) to obtain near-field Fresnel diffraction effects. Detailed information about the imaging techniques is given in [17].

Scans were carried out for both the ‘as tested’ crack tip samples, and after subsequent liquid gallium (Ga) grain boundary wetting [18], allowing the grain boundaries and their relationship to the fracture process to be imaged in three dimensions. 2D and 3D visualisation and analysis of the SRCT data was performed via the commercial software package VG Studio Max, v1.2 (Volume Graphics Gmbh), with selected 2D sections being presented here.

4.3 Results

4.3.1 TEM:

Despite the fast quench, 20°C water-quenched samples exhibited precipitate free zones (PFZs) at the grain boundaries, along with some particle decoration of the boundaries, see

Figure 4-2(a). PFZ total width was seen to vary between 40 and 70nm in the water quenched samples. For the slower quench rate of 60°C water quench, quench-induced precipitation becomes more apparent (see Figure 4-2(b)), with a substantial increase in grain boundary particle coverage with a moderate increase in PFZ width (to ~80-100nm). In the air-cooled material, the quench induced precipitates are seen to decorate the majority of the observed grain boundary areas, with a PFZ width of ~400nm being discerned (see Figure 2(c)).

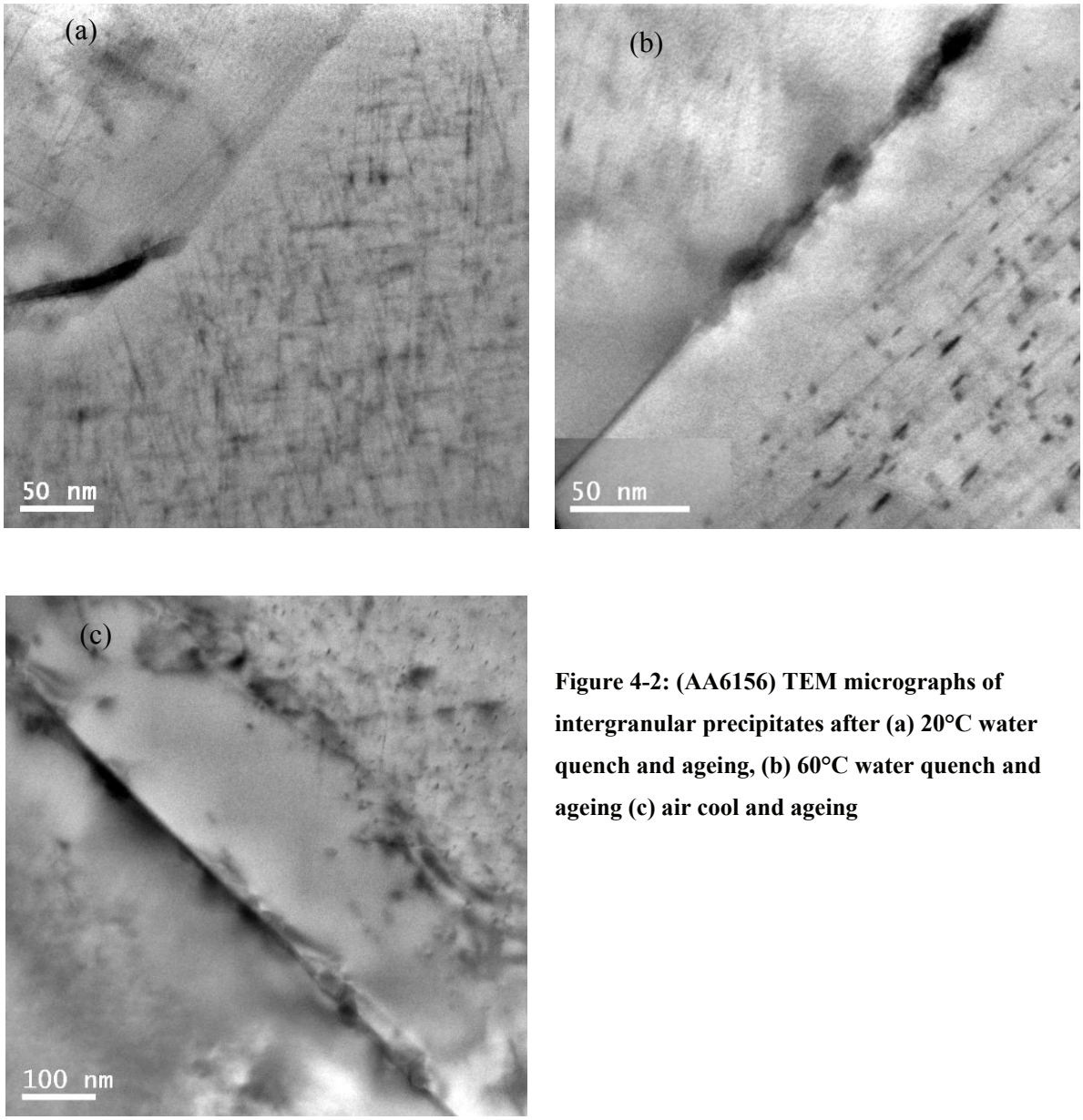

Figure 4-2: (AA6156) TEM micrographs of intergranular precipitates after (a) 20°C water quench and ageing, (b) 60°C water quench and ageing (c) air cool and ageing

Based on boundary views in thin regions of the available TEM samples, and estimating sample thickness using thickness fringes, the grain boundary coverage levels for the

quench conditions were estimated as 0.08 and 0.09 for the 20˚C quench and the 60˚C quench materials. With an estimated accuracy of about 0.02, there is not sufficient proof to determine a significant difference. The grain boundary coverage of the air-cooled material proved variable but is significantly higher. No significant quench-induced heterogeneous precipitation was identified on dispersoid particles for the 20°C and 60°C water-quenched samples. The 60°C water-quenched material showed evidence for a very limited PFZ around the dispersoid particles, however the usually curved morphology of the dispersoid particles made clear identification of a small PFZ difficult. Large elongated particles (~500nm in length) were clearly seen on the dispersoids of the air cooled material, surrounded by a substantial PFZ (see Figure 4-3).

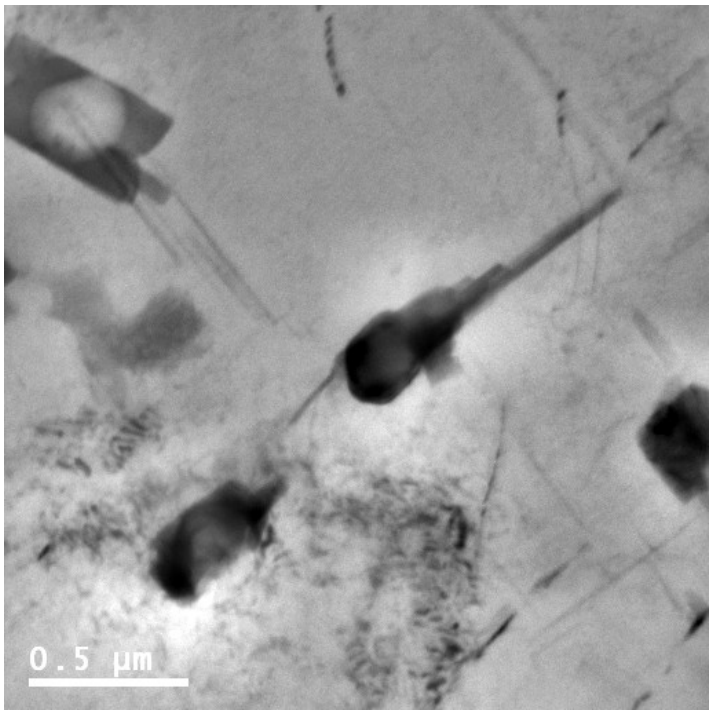

Figure 4-3: (AA6156) TEM micrograph of dispersoids (dark, equiaxed particles) after air cooling and ageing. Note the large elongated particles that nucleated on the dispersoids, with a zone devoid of the fine precipitates around them.

The diameter of hardening precipitates was of the order of several nanometres (Figure 4-2(a)). Selected area diffraction (SAD) patterns in [100] directions (not presented here) were essentially similar for the two types of water quenched samples with streaks, and local maxima on the streaks that are consistent with patterns previously reported for alloys with similar compositions [19].

4.3.2 DSC

Figure 4-4 shows DSC results for the three investigated treatments. The endothermic effect I appearing in the water quenched materials is consistent with dissolution of pre-precipitates with stability limit below about 250°C. Following recent theoretical works these pre-precipitates are considered to be co-clusters containing Mg, Si and Cu [20,21,22] which have, especially in older literature, also been indicated as GP zones [23]. The strong exothermic effect II is mainly attributable the precipitation of β″ (see Ref.[24]). The smaller exothermic effect III is possibly due to the precipitation of the Q′ [20]. The subsequent large endothermic effect IV is due to the dissolution of stable precipitate phases.

The peaks for the co-cluster dissolution (effect I) as well as for the β″ precipitate formation (effect II) are more pronounced for the 20°C water quenched material as compared to the 60°C water quenched material. In the thermogram of the air-cooled material the heat evolution during the endothermic and exothermic effects up to 300°C are much lower as compared to the water quenched materials. The co-cluster zone dissolution effect is very weak whilst the two exothermic peaks between 220 and 300°C observed for the water quenched materials appear to have merged into one broad, less intense peak. These phenomena are consistent with heterogeneous precipitation during the slower quenches and the attendant "loss" of solute, in keeping with the TEM observations of precipitation at grain boundaries and on dispersoids (Figures. 4-2 and 4-3).

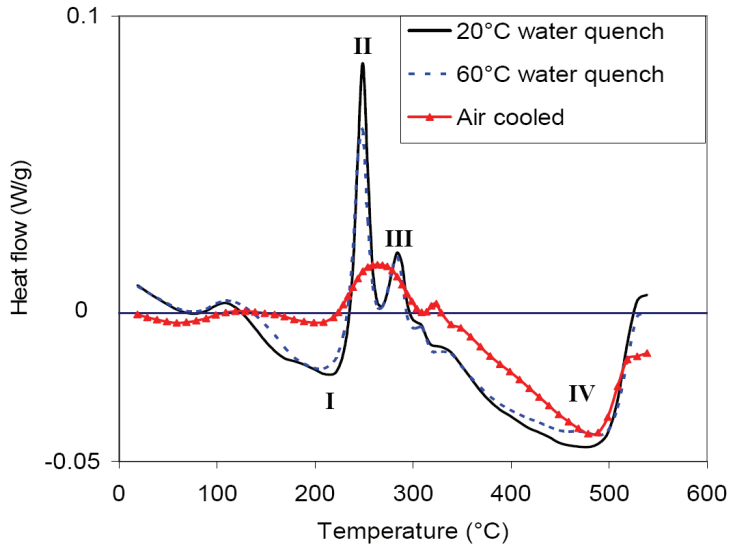

Figure 4-4 (AA6156) DSC thermograms, taken at a scan rate of 10°C/min for the samples quenched at different rates and subsequently aged at room temperature for 3 days (after [25])

Figure 4-5 shows DSC results for material that has been solutionized and subsequently quenched at different controlled cooling rates inside the DSC. For comparison the DSC curve for the air cooled material is also replotted. The main precipitation peak of the -200°C/min quenched material is stronger than for the air cooled material but in contrast to the water quenched samples the peak of β″ and Q′ formation have merged. The curve of the -50°C/min quenched material is very similar to the air cooled material, indicating that the average cooling rate in the critical temperature range during air cooling is close to -50°C/min. The precipitation peaks in the material that has been cooled at -10°C/min have almost disappeared. The general trend in these curves is as for the previously discussed results: the faster the cooling rate the stronger the reaction peaks, with the character of the air cooled material falling somewhere between the -200°C/min and -50°C/min controlled cooling materials.

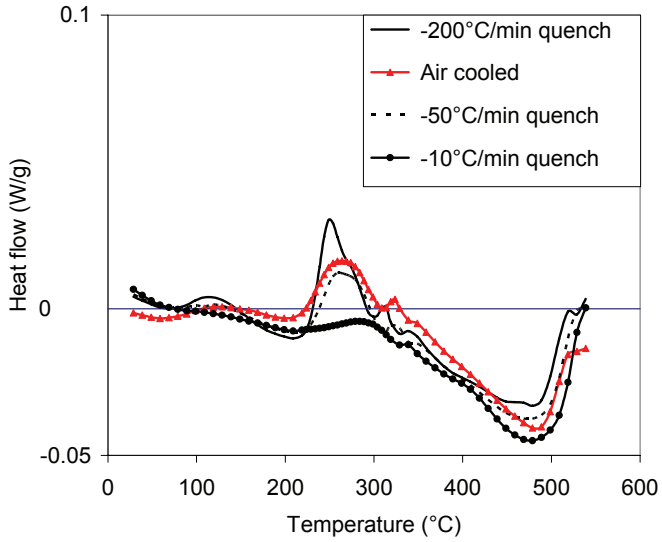

Figure 4-5 (AA6156) DSC thermograms, taken at a scan rate of 10°C/min for air-cooled material and for samples solutionized and quenched at controlled quench rates in the DSC and subsequently aged at room temperature for 3 days

4.3.3 Kahn tear testing

In the Kahn tear tests, the crack length and applied force F were measured as a function of crack tip mouth opening displacement (CMOD). Typical data are shown in Figure 4-6, showing both crack length and F/A_0 (where A_0 is the initial uncracked ligament area) as a function of CMOD.

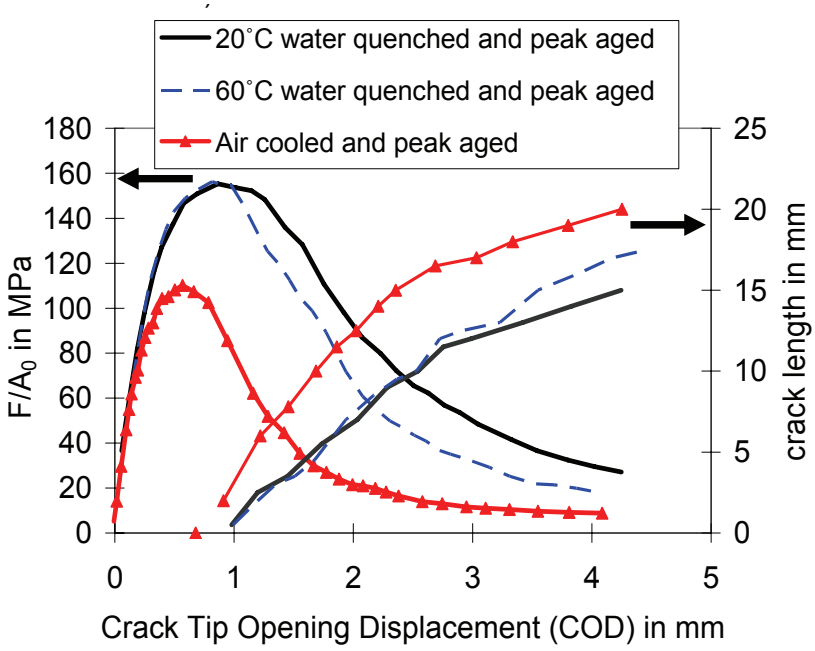

Figure 4-6: (AA6156) Kahn tear test results: nominal stress (F/A_0) and crack length versus crack mouth opening displacement for different quench rates.

The peak nominal stresses of the 20°C water quenched and the 60°C water quenched materials are very similar. The unit initiation energy (UIE, defined as the integral $\int F/A_0 \, dl_d$, where dl_d is the pin displacement, taken from the start of the test to maximum load) decreases by ~15% between the 20˚C and 60˚C water quenched materials, but drops more significantly for the air cooled material (see Table 4-3).

condition	20°C water quench + T6	60°C water quench + T6	Air-cool + T6
UIE (N/mm)	157	138	67

Table 4-3: (AA6156) Unit initiation energies for the different quench rates

After achieving the maximum nominal stress, crack propagation stresses are lower for the 60°C water quenched material as compared to the 20°C quenched materials at the same CMOD. For the air cooled material, crack propagation occurs at loads that are always lower than the water quenched materials; the initial nominal stresses as well as the nominal stresses during crack propagation are markedly reduced. The crack also grows faster for much of the test (as a function of CMOD) in the air cooled material than in the water cooled materials, indicative of substantially reduced toughness.

4.3.4 Fractography

On a macroscopic scale, the fractured tear test samples show an approximately triangular region where the crack surface is normal to the main tensile axis, followed by a transition

to a slant (~45˚) fracture mode. This is consistent with the evolution of the triaxial constraint conditions [26]: in the triangular region high stress triaxiality is encountered during crack initiation, whilst increasing plastic zone size as the crack propagates leads to a loss of constraint and hence to a decreased triaxility (see also [27]). Figure 4-7 shows SEM images of typical fracture surfaces of the three samples at the triangular region of crack growth, as indicated in Figure 4-7(d). Figure 4-7(a) shows a detailed image of a typical fracture surface region of the 20°C water quenched material; coarse voiding is the prevailing feature in this case (void diameters of the order of 10-40µm).

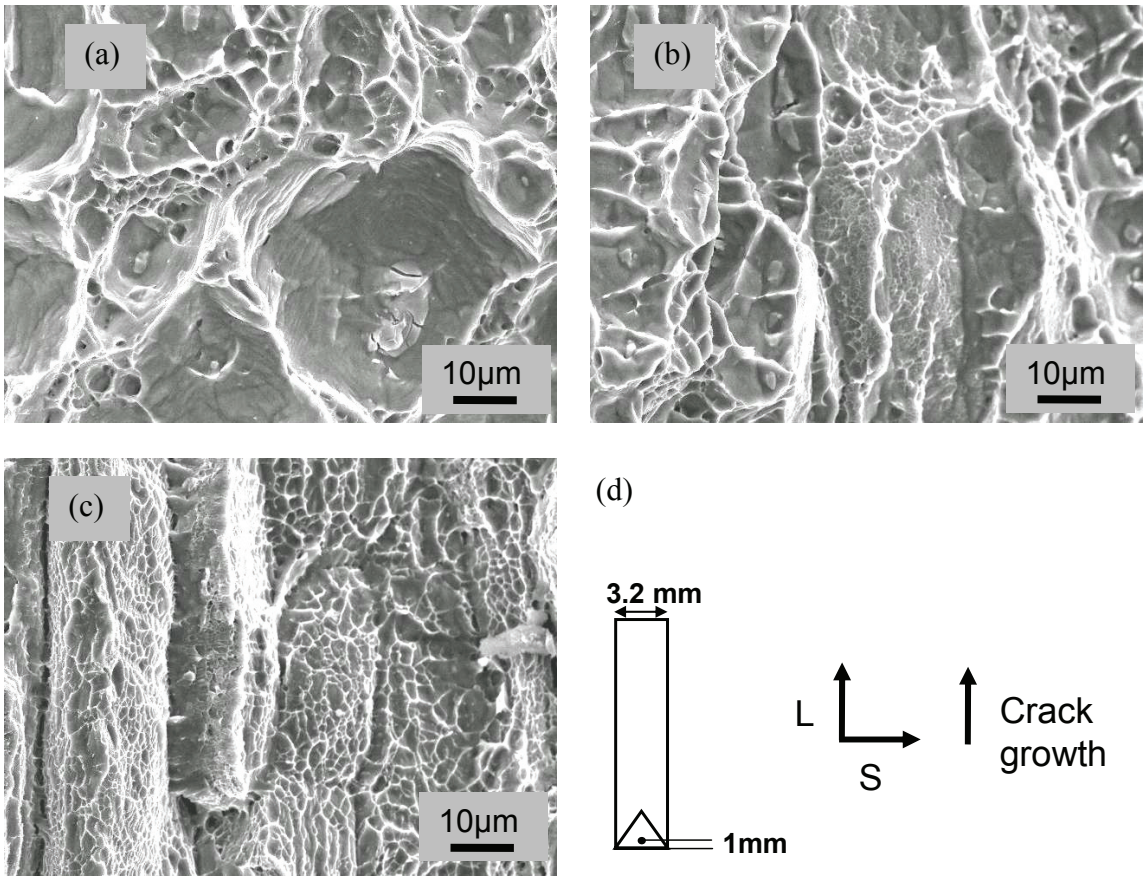

Figure 4-7: (AA6156) SEM micrographs (secondary electron mode) of the fracture surface at mid-thickness 1mm from the notch of (a) the 20°C water quenched and peak aged material, (b) the 60°C water quenched and peak aged material, (c) the air cooled and peak aged material. A schematic illustration of macroscopic fracture surface regions and position of the images is shown in (d).

The voids are evidently associated with coarse second phase particles, with a relatively small amount of final coalescence via finer, secondary void formation. Similar to the 20°C water quenched material, coarse voiding is generally prevalent in the 60°C water quenched material, see Figure 4-7(b) however, there are also aligned, finer featured regions, exhibiting small, shallow voids (diameters of the order of 1µm). With ongoing crack growth into the slant fracture regions for both water quenched conditions, an

increasing propensity for locally slant fracture was noted, with a marked reduction in the proportion of coarse voiding. In Figure 4-7(c), typical of the air cooled samples, aligned intergranular features are evident, covering the majority of the fracture surfaces. Evidence of ductile failure is seen at larger intermetallic particles on the fracture surface; however void growth is apparently limited by the onset of the intergranular failure. The failure morphology of the air cooled material is consistent with classical intergranular ductile failure and is seen to be dominant in both macroscopically flat and slant regions of the fracture surfaces [28].

Figure 4-8 shows SEM images of the fracture surface at 15mm from the notch at mid–thickness, in the macroscopically slant region. On the fracture surface of the 20˚C water quenched material (Figure 4-8(a)) there is relatively high coverage of coarse voids; however there are some additional regions which are planar, tilted and covered with fine dimples, consistent with shear decohesion. Again, the fracture surface of the 60˚C water quenched material shows similar features to the 20˚C water quenched material; however elongated apparently intergranular features are also evident (identification of intergranular failure is considered in further detail in the next section). The fracture surface of the air cooled material appears essentially similar to that in the macroscopically flat region; there are few coarse voids and a predominantly intergranular morphology is seen exhibiting fine dimples.

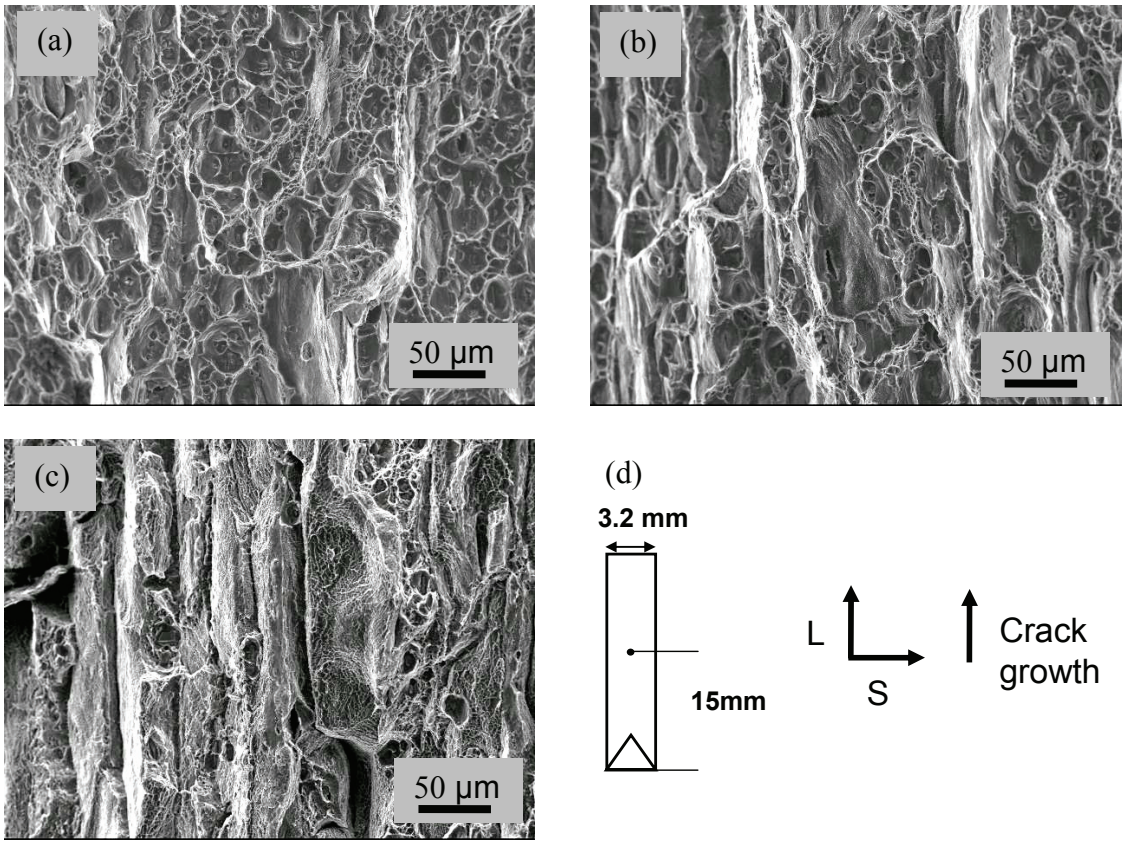

Figure 4-8: (AA6156) SEM micrographs of the fracture surface at mid-thickness at 15mm from the notch of (a) the 20°C water quenched and peak aged material, (b) 60°C water quenched and peak aged material, and (c) air cooled and peak aged material. A schematic illustration of macroscopic fracture surface regions and position of the images is shown in (d).

4.3.5 Tomography

Tomography scans of the arrested cracks offer the opportunity to observe the actual initiation of failure and the evolution of the fracture process. Figure 4-9 shows 2D tomography sections of the crack in the 60°C water quenched material before and after the gallium wetting (Figure 4-9 (a) and (b) respectively) with the crack growth direction normal to the section. The aluminium matrix (grey), intermetallics (white) and pores, as well as the crack (black), are clearly delineated, with the phase contrast fringes highlighting the associated edges/interfaces. In Figure 4-9(b) the grain boundaries can additionally be seen in white due to the local segregation of gallium. Figure 4-9(a) reveals crack areas that are oriented in the loading direction (running up and down the page in Figure 4-9) and other parts that are inclined with respect to the loading direction. There are regions of increased crack opening consistent with the presence of coarse voids along the crack. Comparing the crack in the gallium wetted sample to the sample before gallium

wetting indicates that much of the crack path follows grain boundaries. This is particularly evident for the parts of the crack that are oriented in the loading direction, but is also evident for areas that are inclined with respect to the loading direction.

An exact quantification of the fraction of crack running along the grain boundary is however difficult as both the crack surface and grain boundaries are gallium wetted and thus both appear white (scanning the grain structure of the sample before tearing is not possible by this technique as only small parts of the Kahn tear test sample can be scanned at this resolution and the Gallium wetting embrittles the sample dramatically).

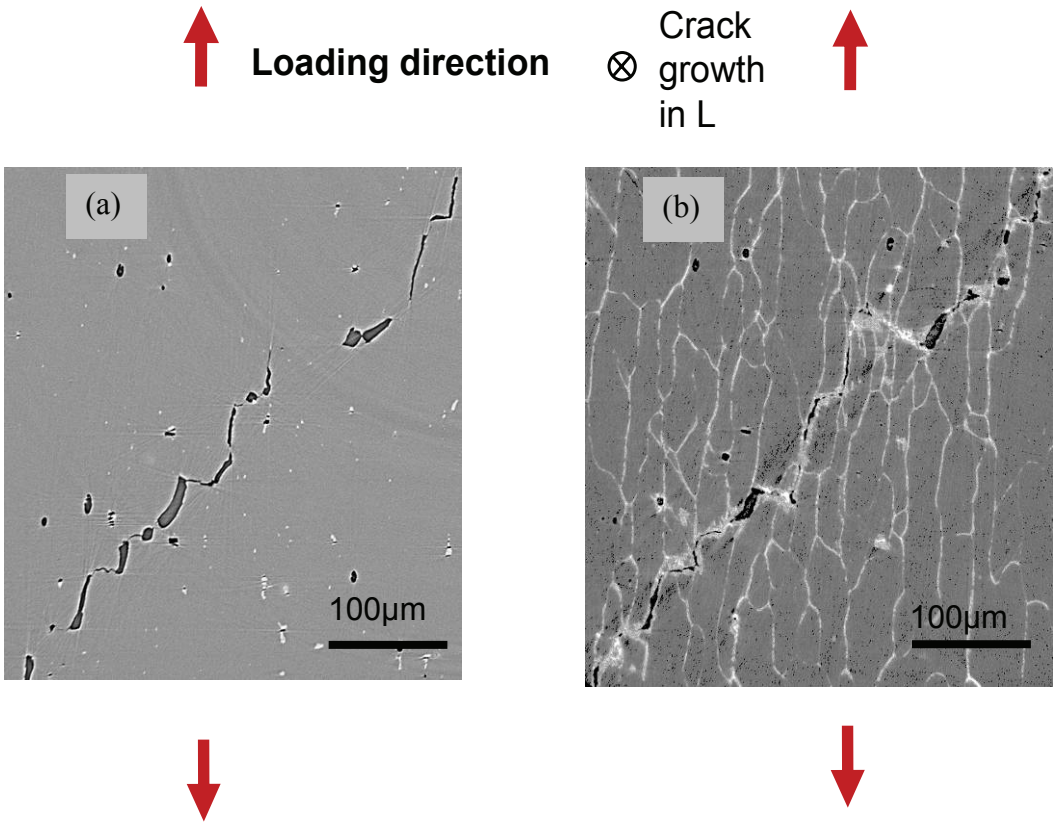

Figure 4-9: (AA6156) 2D section of tomography data showing the crack in the 60°C water quenched material (a) without gallium wetting, and (b) after gallium wetting.

Figure 4-10(a) shows damage at the very crack tip of the 60°C water quenched material before gallium wetting, whilst Figure 4-10(b) again shows the same location after the gallium treatment. Figure 4-10(a) shows a combination of coarse voids from intermetallic particles and relatively narrow cracks/voids that are inclined with respect to the loading direction. The narrow regions are seen to be disconnected with each other in the through-thickness direction, *i.e.* the crack tip is distinctly ligamented with crack "tongues" extending into the material ahead of the main crack. Considering Figure 4-10(b) it becomes clear that the narrow, tilted regions all lie on grain boundaries inclined to the loading direction.

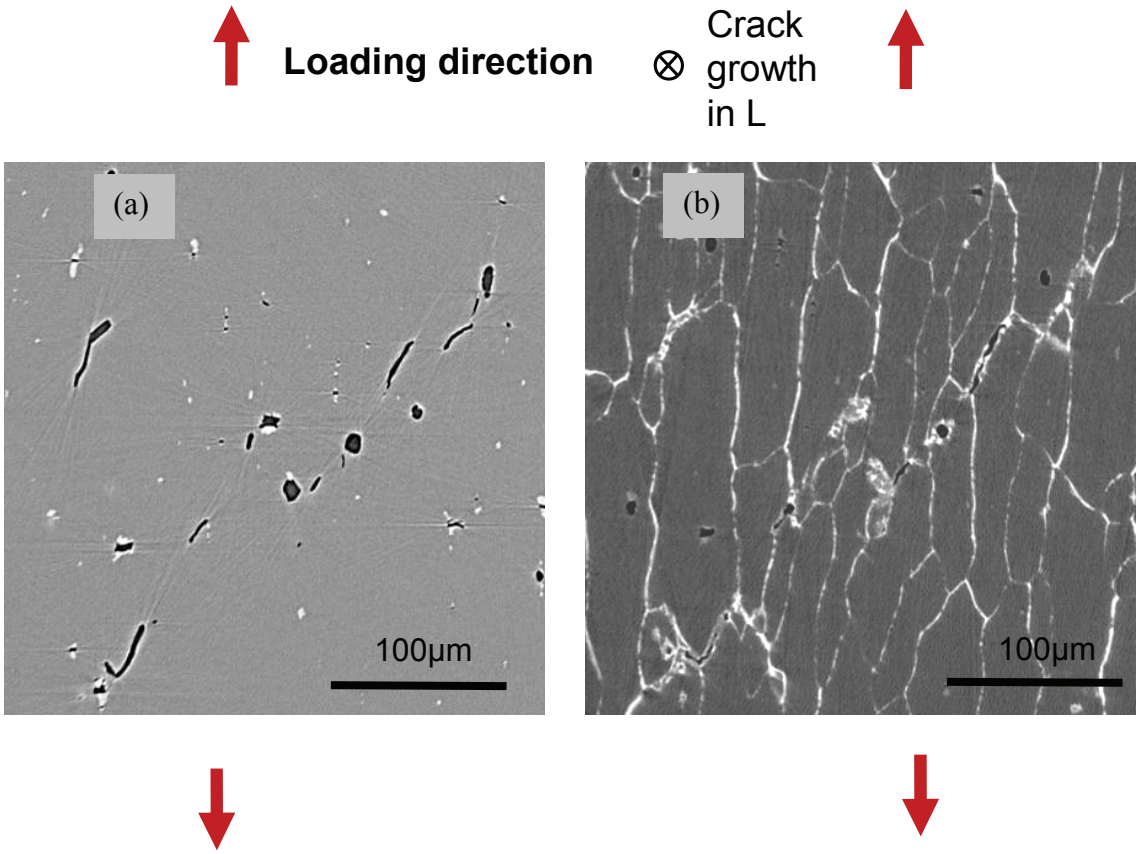

Figure 4-10: (AA6156) 2D section of tomography data showing the crack tip in the 60°C water quenched material (a) without gallium wetting, and (b) after gallium wetting.

From the observations in Figures 4-9 and 4-10, it may be seen that the initiation and coalescence of damage into a contiguous crack in the 60°C quenched material occur by a combination of coarse voiding and intergranular failure along tilted sections of the grain boundary structure. Additionally small tilted cracks that are independent from coarse voids or initial porosity and the main crack plane were identified in the material ahead of the crack tip, as exemplified by the crack in the upper left quadrant of Figure 4-10(a) seen to be at some distance (about 100µm) from the main crack plane. Figure 4-11 highlights another such independent crack exhibiting a 'V'-shape morphology; comparison of the sections obtained from scans without and without gallium wetting shows these independent cracks invariably lie on inclined grain boundaries. Many of such distinct crack initiation sites have been identified in the scanned volumes of the 60°C quenched material (50-60 per mm^3 in the region up to ~1mm from the crack tip), all of which where associated with boundaries inclined between 35 and 55° to the load direction.

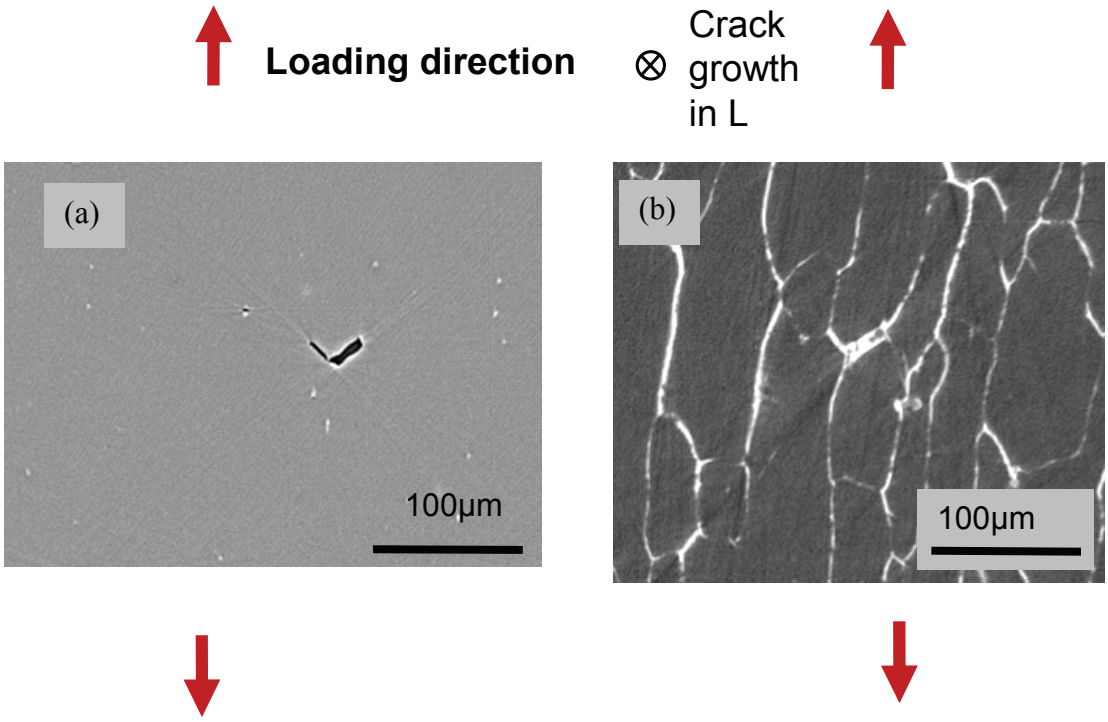

Figure 4-11: (AA6156) 2D section of v-shaped narrow crack in the 60°C water quenched material (a) without gallium, and (b) after gallium wetting.

Figure 4-12 shows sections of fracture in the 20°C water quenched material both in the main crack and the near tip region. The crack tip in this case is more dominated by regions of coarse void coalescence, with few of the inclined crack 'tongues' of the 60°C quench material. Furthermore very few independent tilted crack sections are seen ahead of the main crack.

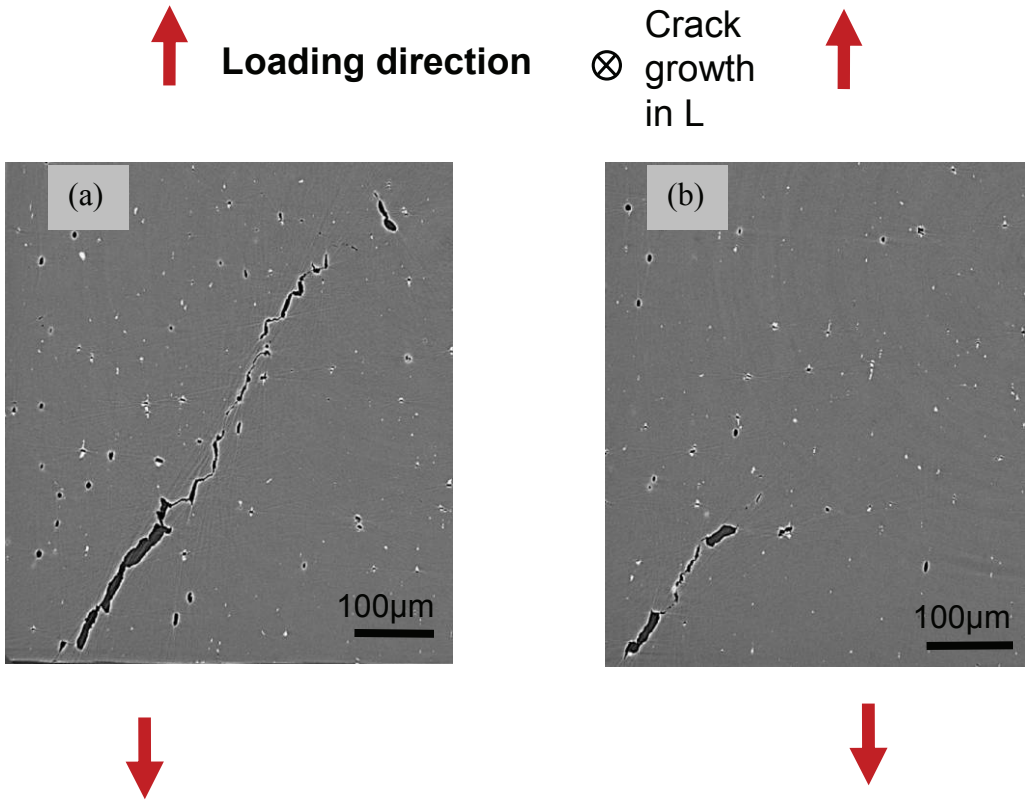

Figure 4-12: (AA6156) 20°C water quenched material: (a) 2D section of tomography data showing the main crack, and (b) 2D section of tomography data showing damage at the crack tip.

Figure 4-13 shows failure in the air cooled material before and after gallium wetting. Most of the crack opening is very narrow for this condition. There is little coarse voiding discernable, consistent with the SEM observation. Comparing the section before and after gallium wetting it appears that the fracture path is highly intergranular in nature. A significant difference with respect to the water quenched materials is the high proportion of cracking (along grain boundaries) in the loading direction (see left-hand side of Figure 4-13(a)).

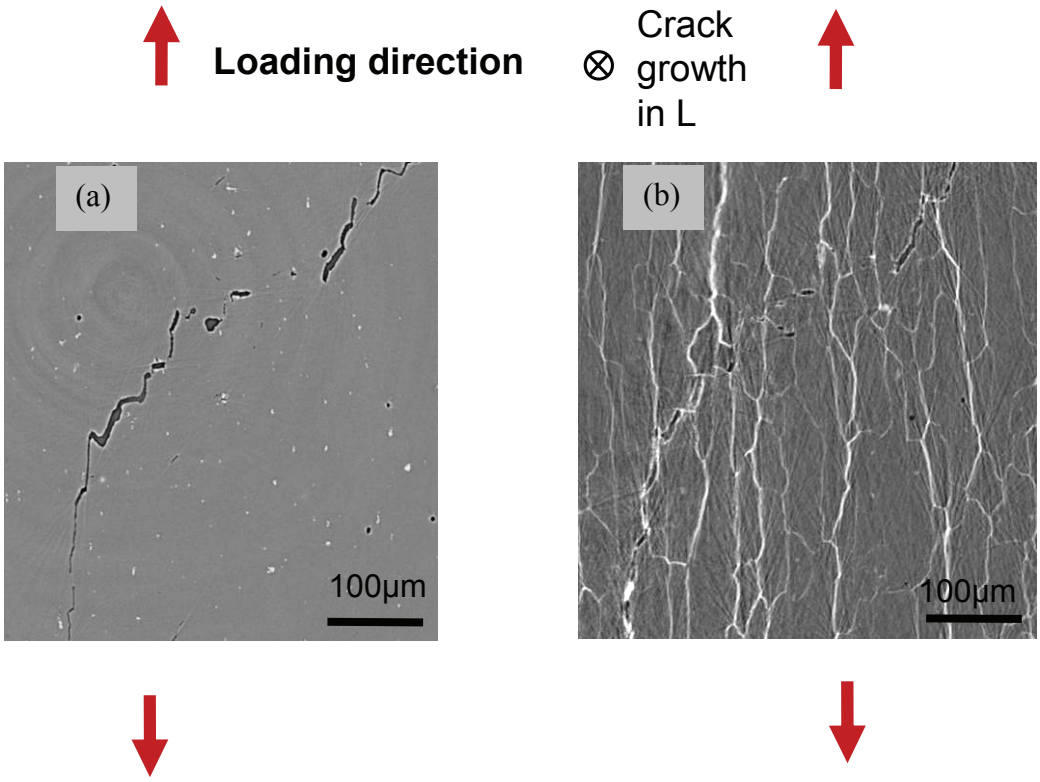

Figure 4-13: (AA6156) 2D section of tomography data of the air cooled material showing the crack (a) before the gallium wetting, and (b) after the gallium wetting.

Figure 4-14 shows a 2D section close to the crack tip in the air cooled material. The tip is narrow, and also ligamented, but to a lesser extent than in the 60°C water quenched material (~5 ligaments/mm crack width for the air cooled material compared to ~20 ligaments/mm crack width for the 60°C water cooled material). There is one independent crack visible in Figure 4-14 that lies on a grain boundary; overall however there were few independent crack sites apparent in the air cooled material (~1-10 single cracks/mm^3 within ~ 1mm of the crack tip for the air cooled material, compared to ~50-60 independent cracks/mm^3 for the 60°C water quenched material).

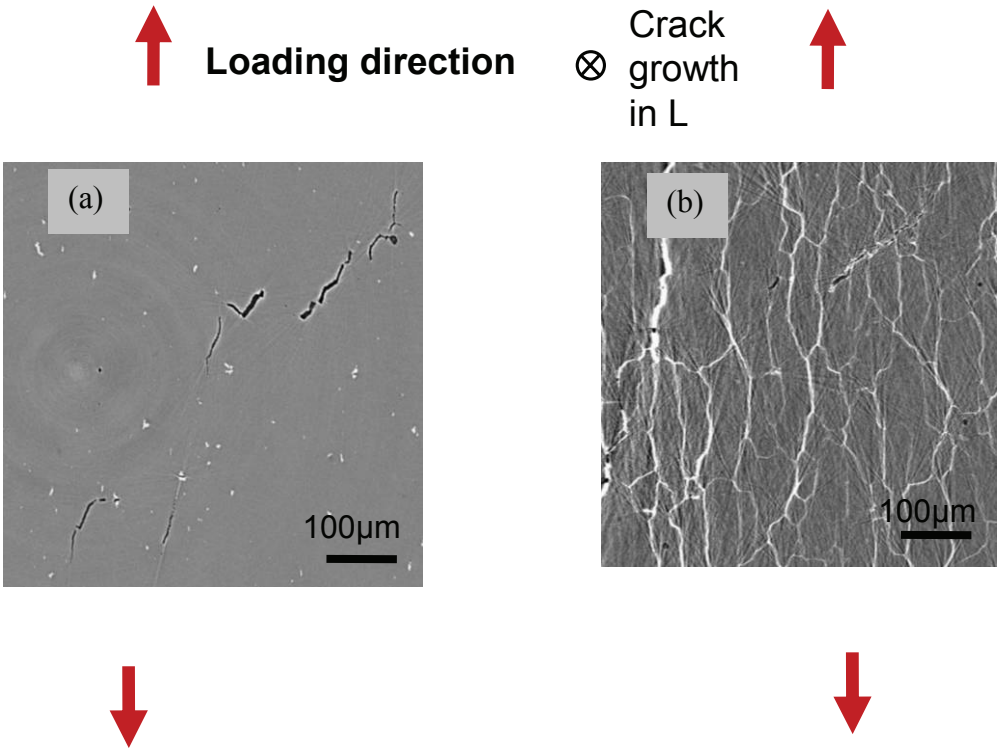

Figure 4-14: (AA6156) 2D section of tomography data of the air cooled material showing the crack tip:(a) before gallium wetting, and (b) after gallium wetting.

4.4 Discussion

4.4.1 Microstructure - strength - toughness relations

Differential Scanning Calorimetry (DSC) data on the present materials indicates that alloying elements precipitate partially during the slower cooling treatments considered here. The changes in the DSC curves between the 20°C and 60°C water quenched material are however small compared to the dramatic changes with respect to the -200°C DSC cooled material and the air cooled material. The hardness is not significantly affected by the slower water quench, whilst it is reduced by ~10% for the air cool. Similar changes in tensile behaviour between water and air quenching have been identified in Refs. [10,11] for an Al-Mg-Si-Cu alloy and been attributed to particle decoration and the formation of a wide PFZ at grain boundaries similar to that seen in this work. In addition, the significant PFZ around dispersoids with large precipitates formed on them, as evidenced in this work (Figure 4-3), is also evidence of the reduction in the amounts of solute.

Hardness and strength have been reported to be less quench sensitive than fracture toughness [9,29] which is consistent with the more volume-averaged nature of bulk plastic flow, as opposed to the localized nature of strain and damage accumulation associated with fracture. The observed combination of grain boundary particle decoration and PFZ formation has been widely discussed in relation to generation of grain boundary ductile failure (*e.g.* see [9,28,29]), consistent with the present reductions in toughness with reduced quench rates. The tomography studies of arrested cracks carried out in this work revealed clear differences in the fracture mechanisms and the evolution of damage between samples quenched at different rates. In the 60°C water quenched material the presence of inclined grain boundary failure both at the crack tip and in the material immediately ahead to the tip indicate a potentially controlling influence of shear localisation in crack initiation at boundary PFZs [30] (orientation of maximum shear stress will be close to 45º with respect to the loading direction under conditions of lower stress triaxiality of the arrested crack sections). Crack propagation in this case proceeds via intergranular areas of narrow crack opening ahead of the main crack that are inclined with respect to the loading direction, along with some opening of coarse voids, a number of which appear to develop from the intrinsic pore content of the alloy and therefore may be considered to have no real initiation stage. During crack extension those damage features then grow and ultimately link, particularly via grain boundaries that are oriented close to the loading direction. In the air cooled material it may be seen however that, given the relative absence of independent boundary failures ahead of the main crack, the initiation and coalescence of boundary failure at the crack tip is more simultaneous *(cf.* the 60°C quench material).

It is difficult to separate the potential contributions to fracture of plastic strain partitioning within the relatively soft PFZ material and local flow strains to failure associated with a high density of void nucleating particles along the grain boundaries [31]. In terms of the present results it is interesting to note that crack growth at high stress triaxiality is evidently less susceptible to quench embrittlement, i.e. crack initiation toughness is hardly reduced by the 60˚C quench (hardness testing showed no significant change in flow strength between the two water quenched materials, with the implication of essentially equivalent stress state evolution under load for these materials). Increased triaxiality is expected to favour primary void growth [27], although it may be recognised that the plane of maximum shear associated with lower stress triaxiality is more favourably inclined to

generate boundary shear in the present aligned grain structure: with the observed correlation of initial grain boundary failure (ahead of the crack) with inclined boundaries, then both factors may contribute to the change in quench sensitivity between the regions with of high and lower stress triaxiality.

4.4.2 Models for toughness in the presence of a PFZ

In order to predict the influence of microstructural changes due to the varying quench rates an appropriate micromechanical model needs to account for the identified mechanisms of crack initiation and coalescence during failure. Additionally, a distinction between the crack initiation stage (high stress triaxiality) and the crack propagation stage (lower stress triaxiality) needs to be made. In the present study, fracture of the water cooled materials in the flat/high stress triaxiality region is seen to be dominated by coarse voiding and a degree of shear decohesion and/or grain boundary failure, whilst the fracture surface of the air cooled material is dominated by intergranular features and limited coarse voiding. Thus, an appropriate micromechanical toughness model would need to take a multimechanistic approach to analyse these test conditions. Notwithstanding the need for full multimechanistic approach, several co-workers have established models for toughness based on grain boundary dominated fracture (*e.g.* in Refs. [1,3,32]). The model suggested by Embury and Nes [32] for example, considers that all strain is concentrated in the PFZ, and relates plane strain fracture toughness K_{IC} to the grain boundary particle coverage A_f:

$$K_{IC} \sim (E\sigma_R(A_f^{-\frac{1}{2}} - 1)/2)^{\frac{1}{2}} \tag{4-1}$$

where σ_R is close to the ultimate tensile strength. We will here develop a modified treatment that relaxes the assumption that all strain is concentrated in the PFZ and we will instead make the more realistic assumption of constant shear stress across the material.

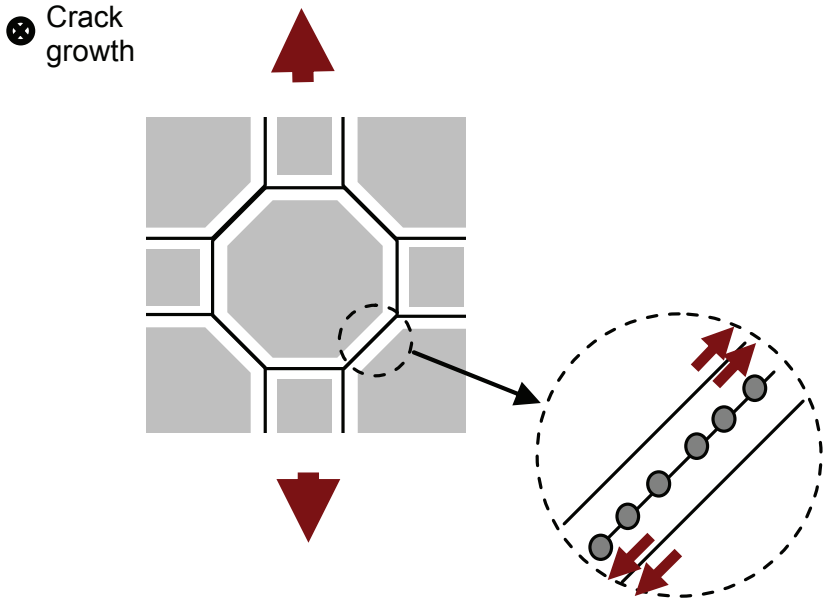

Figure 4-13: Schematic illustration of the equi-shear strain model. The grain shape depicted here has no particular meaning: the model does not assume any particular grain shape, other than that it has boundaries close to 45° with the main tensile axis

With reference to the schematic drawing in Figure 4-13, consider a material consisting of grain with typical dimension d_G, with particles on the grain boundaries covering a fraction f_{GB} and a PFZ around the grain boundary of full width d_{PFZ}. Consider that all the material is substantially plastically deformed and that the elastic part of the deformation can be neglected. Consider that the relation between shear stress, τ_G and shear strain γ_G of the grain is given by a power law hardening equation:

$$\tau_G = K_G \gamma_G^{\,p_G} + \tau_{y,G} \tag{4-2}$$

where p_G is the strain hardening exponent in the grain and K_G is the strain hardening factor in the grain. We assume that it is sufficiently accurate to describe the PFZ as a zone with homogeneous mechanical properties, and similar to the grains we take the stress-strain relationship as:

$$\tau_{PFZ} = K_{PFZ} \gamma_{PFZ}^{\,p_{PFZ}} + \tau_{c,PFZ} \tag{4-3}$$

where p_{PFZ} is the strain hardening exponent in the PFZ and K_G is the strain hardening factor in the PFZ. Following Embury and Nes, the critical shear strain at which failure occurs in the PFZ is given by:

$$\gamma_{PFZ,c} = 0.5\left(f_{GB}^{-0.5} - 1\right) \tag{4-4}$$

The total energy related to plastic deformation by shear is given by:

$$\begin{aligned} E_p &= E_{p,G} + E_{p,PFZ} \\ &\propto \frac{d_G}{d_G + d_{PFZ}}\left(\frac{1}{p_G + 1} K_G \gamma_G^{\,p_G+1} + \tau_{c,G}\gamma_G\right) + \frac{d_{PFZ}}{d_G + d_{PFZ}}\left(\frac{1}{p_{PFZ} + 1} K_{PFZ} \gamma_{PFZ}^{\,p_{PFZ}+1} + \tau_{c,PFZ}\gamma_{PFZ}\right) \end{aligned} \tag{4-5}$$

Inserting Eqs. 4-2 to 4-3 in Eq. 4-5, provides an expression for E_p at the stage where the failure process initiates in the case of a material under uniform strain. Whilst the test results here consider notched samples, i.e. with high stress concentration around the notch, we will assume that trends in measured fracture energies are related to E_p at the stage where grain boundaries ahead of the contiguous crack start to fail. We will term this $E_{p,crit}$. $E_{p,crit}$ defines a lower limit for E_p for the stage where the crack has progressed through the material. It is expected that E_p-$E_{p,crit}$ is much smaller than E_p and hence we can assume that $E_{p,crit}$ is a reasonably good measure of the total energy consumed in crack progression. Under equi-shear stress conditions, e.g. $\tau_G = \tau_{PFZ}$, and if the materials parameters (K, τ_c) and f_{GB} are known, all quantities in Eqs. 4-2 to 4-5 can be determined. These calculations have been implemented using measured and estimated parameters for 6156-T6 alloy sheet that was quenched in water at 60ºC: f_{GB}=0.09, d_{PFZ}=80nm (both from TEM data), d_G=20μm (from SEM observations), $\sigma_{y,G}$=400MPa (from proof strength of 6156-T6), $\sigma_{y,PFZ}$=160MPa (estimated form the yield strength of Al-Mg-Si alloys with Mg+Si content of about 1at% in T1 condition). We further take $\tau_{y,G}$=0.5$\sigma_{y,G}$ and $\tau_{y,PFZ}$=0.5$\sigma_{y,PFZ}$. From earlier work on Al based alloys [31] we further estimate p_G=0.5, K_G=150MPa. We have no reliable data on p_{PFZ}, and in a first approximation we will assume that any difference between p_{PFZ} and p_G is limited, i.e. $p_{PFZ} \approx p_G$.

The model reveals the underlying causes for changes in toughness and the microstructural parameters which affect these changes, with several of the results being different from hitherto published work. As anticipated, the strain in the PFZ at the grain boundary is much larger than that in the grain. For the present alloy there is about a factor 100 difference. However, for the present alloy, the total work due to plastic shear deformation is mostly stored in the grains (factor 10 difference). In fact, an analysis using estimates of the relevant parameters (f_{GB}, d_{PFZ}, d_G, $\sigma_{y,G}$, $\sigma_{y,PFZ}$, $\tau_{y,G}$, $\tau_{y,PFZ}$, p) for a range of Al based alloys which develop PFZs at grain boundaries, shows that this situation (work due to plastic deformation being mostly stored in grains), is common. Hence shear deformation of the grains contributes considerably more to toughness as compared to shear deformation of the PFZ. As a consequence, the plastic work for fracture is not proportional to $f_{GB}^{-0.5}$ as suggested by the Embury and Nes [32] approach; this proportionality is only valid if plastic work for deformation of grain is negligible compared to that in the PFZ. The influence of the different parameters on the plastic work for fracture was analysed by introducing small variations in the key model parameters. This showed that d_{PFZ} has a very limited influence: a 1% change in d_{PFZ} causes a 0.07% change in E_p; but f_{GB} has a strong influence: 1% change in f_{GB} causes a 6% change in E_p. $\sigma_{y,PFZ}$ has a very strong influence as it strongly influences the level of plastic deformation in the grain: 1% change in $\sigma_{y,PFZ}$ causes a 5% change in E_p; and also $\sigma_{y,G}$ has a very strong influence: 1% change in $\sigma_{y,G}$ causes a 18% change in E_p. As could be expected the work hardening in grain and PFZ have a significant influence on E_p: a 1% increase in both K_G and K_{PFZ} causes an increase in E_p of 6%. The effect is stronger if the work hardening behaviours of grain and PFZ change differently, and in such a manner that they will compensate yield strength differences. So if K_{PFZ} increases by 1% and K_{PFZ} remains constant, then E_p increases by 8%.

It should be noted that the present analysis provides predictions that are very different from some other published models analysing the influence of the PFZ and the grain boundary coverage on fracture energies. For instance, Li and Reynolds [33], using the approaches of Hornbogen and Gräf [1] and Kawabata and Izumi [3], indicated the following relation:

$$K_{IC} \cong \left[\frac{E_m \sigma_{PFZ} d_{PFZ} \cdot \varepsilon_{fi}}{C d_g} \right]^{1/2} \quad (4\text{-}6)$$

where E_m is the Young's modulus, σ_{PFZ} is the PFZ flow strength, C is a constant and ε_{fi} is the critical strain for the grain boundary. The latter equation assumes that the accommodation of bulk shear strain occurs within PFZs only, with local PFZ strains then decreasing with increasing PFZ width for a given grain size. This modelling approach predicts a strong increase in fracture toughness with an increase of the PFZ width, but our analysis indicates that this is not the case. Indeed apparently contradictory influences of PFZ width on fracture behaviour have been noted in the literature [26,31,34] and Unwin and Smith [31] have particularly demonstrated a negligible influence of PFZ widths between 100 and 600 nm on fracture toughness in ternary Al-Zn-Mg materials for a fixed proof stress and area fraction of boundary precipitates. (It is noted that grain boundary coverage was however quite high (~ 0.6).) The model of Dumont and co-workers [2] considers a sum of fracture energies for transgranular fracture and intergranular fracture that are weighted by the area fractions on the fracture surfaces and intergranular fracture is assumed to occur without the influence of shear. As discussed above, the latter appears to be incompatible with the SRCT observations for our samples in the lower stress triaxiality fracture region.

Whilst it is admittedly a simplified model, our new equi-shear-stress model can explain the observation that is crucial in applications: the decrease in propagation energy on reducing the severity of the quench to a quench in water at 60ºC. The TEM experiments have shown some changes in PFZ size on reducing the severity of the quench to a quench in water at 60ºC, but the model clearly shows that this should not influence the propagation energy. The grain boundary coverage, which is difficult to measure accurately, seems to increase somewhat on reducing the severity of the quench to a quench in water at 60ºC, and this can be a significant factor in the observed reduction in the propagation energy. Apart from this geometrical factor, the model also identifies the combination of yield strength and work hardening of the PFZ as important factors. Eq. 4-5 indicates that the term $\tau_{c,PFZ}\gamma_{PFZ} + K_{PFZ}\gamma_{PFZ}^{p_{PFZ}+1} / (p_{PFZ}+1)$ describes the combined effect of work hardening parameters and yield strength of the PFZ, and the sensitivity analysis above showed that for our alloy yield strength and work hardening variations both cause

significant changes in toughness. The yield strength of the PFZ can indeed vary significantly with quenching condition as the amount of co-clusters, which were identified by DSC, will depend strongly on any solute depletion in the PFZ, which in turn will have a very strong influence on local strength [22]. It is known that Cu and Mg content of the Al-rich phase can have some influence on work hardening factor K [35] and thus also changes in work hardening of the PFZ can influence the toughness significantly. (Note that the term $\tau_{c,PFZ}\gamma_{PFZ} + K_{PFZ}\gamma_{PFZ}^{\,p_{PFZ}+1}/(p_{PFZ}+1)$ indicates that if the grain boundary coverage is very high, the resulting very low γ_{PFZ} will cause any changes in work hardening to have a limited effect on toughness in comparison with changes in the yield strength of the PFZ. In such a case the yield strength of the PFZ is the determining factor, and the alloy will be extremely embrittled.)

Whilst the new model is successful in semi-quantitatively analysing the fracture at grain boundaries, it seems that in order to fully understand the fracture processes in the present materials an appropriate multimechanistic micromechanical model is required which would ideally account for the stress triaxiality influence on fracture modes and would also consider the different fracture initiation mechanisms.

4.5 Conclusions

Kahn tear tests and microstructural analysis were performed on 6156 samples which were quenched at different rates and subsequently artificially aged.

- Both the coverage of grain boundary with recipitates and PFZ width increase with changing water quench temperature from 20°C to 60°C. Heterogeneous precipitation on dispersoids and PFZ formation around the dispersoids occurred in the air cooled material.

- The crack propagation energy is substantially reduced as a result of changing water quench temperature from 20°C to 60°C. However, the crack initiation energy in high stress triaxiality condition seems less affected by the slower water quench, indicating an increased sensitivity of lower stress triaxiality failure to changes in grain boundary character.

- SEM and micro-computed tomography studies of arrested crack tips of samples before and after gallium wetting revealed the following quench effects:
    - 60°C water quenched material: comparison of the main crack before and after gallium wetting shows that much of the crack is intergranular in nature. The crack tip has a ligamented morphology and consists of coarse voids and areas of narrow opening that are inclined with respect to the loading direction. Those areas have been identified to lie on grain boundaries.

    - 20°C water quenched material: cracking of the 20°C water quenched material mainly consists of coarse voids and areas of shear decohesion. The crack tip is hardly ligamented and only very few independent crack initiation sites are seen away from the main crack.

    - Air cooled material: in the air cooled material the crack appears to be fully intergranular, few coarse voids are present and the crack opening is very narrow. Substantially fewer independent GB crack initiation sites are seen compared to the 60°C water quenched material, i.e. there is relatively little damage evolution prior crack coalescence.

- A simple model based on an equi-shear-stress assumption is derived. It shows the dominant influence of grain boundary coverage with precipitates and yield strength of the PFZ on propagation energy. For most Al based alloys PFZ width has little influence on the propagation energy.

Acknowledgements

The authors would like to acknowledge Alcan CRV for financial support and material supply, and Frederic Bron and Bernard Bes for technical discussion. We would also like to thank Jean-Yves Buffière for support in micro-computed tomography.

4.6 References

[1] Hornbogen E, Gräf M. Acta Metall 1977; 25: 877-881

[2] Dumont D, Deschamps A, Brechet Y. Acta Mater 2004; 52: 2529-2540

[3] Kawabata T, Izumi O. Acta Metall 1976: 24; 817-825

[4] Morgeneyer TF, Starink MJ, Sinclair I. Acta Mater, in press

[5] Maire E, Buffiere J-Y, Salvo L, Blandin JJ, Ludwig W, Letang JM. Adv Eng Mater 2001; 3: 539-546

[6] Dif R, Bès B, Ehrström JC, Sigli C, Warner TJ, Lassince Ph, Ribes H. Mater Sci Forum 2000; 331-337: 1613-1618

[7] Rometsch PA, Starink MJ, Gregson PJ. Mater Sci Eng A 2003; 339: 255-264

[8] Morere B, Ehrström JC, Gregson PJ, Sinclair I. Metall Trans A 2000; 31: 2503-2515

[9] Shuey RT, Tiryakioglu M, Bray GH, Staley JT. Mater Sci Forum 2006; 519-521: 1017-1022

[10] Morita S, Toda H, Takahashi A, Hoshiyama A, Kobayashi T, Nagashima H. J Jpn Inst Light Met 2001;51 : 307-312

[11] De Haas M, De Hosson JTM. J Mater Sci 2002 ; 37 : 5065-5073

[12] Bratland DH, Grong Ø, Shercliff H, Myhr OR, Tjøtta S. Acta Mater 1997;45: 1-22

[13] Rometsch PA, Wang SC, Harriss A, Gregson PJ, Starink MJ. Mater. Sci. Forum 2002; 396-402: 655-660

[14] Hatch JE. Aluminum: properties and physical metallurgy. Metals Park, OH: ASM; 1984.

[15] ASTM-international, Standard Designation B 871 - 01. 2001: West Conshohocken, USA

[16] Kocsis M, Snigirev A. Nucl Instrum Methods Phys Res Sect A 2004; 525A: 79-84

[17] Ludwig W. Dissertation der LMU München, München, 2001

[18] Ludwig W, Bellet D. Mater Sci Eng A 2000; 281: 198-203

[19] Tanaka M, Warner T. Mater Sci Forum 2000; 331-337: 983-988

[20] van Huis MA, Chen JH,. Sluiter MHF, Zandbergen HW, Acta Mater. 2007;55: 2183-2199.

[21] Sandberg N, Slabanja M, Holmestad R. Comput Mat Sci, In Press, 2007..

[22] M.J. Starink, N. Gao, L. Davin, J. Yan, A. Cerezo, Phil. Mag., Vol 85, 2005, pp. 1395-1418.

[23] Gaber A, Matsuda K, Ali AM, Zou Y, Ikeno S. Mater Sci Technol, 2004;20:1627-1631

[24]S. Esmaeili, X. Wang, D.J. Llloyd and W. J. Poole: Metall. Trans. A, Vol. 34A (2003), p.751-763

[25] Morgeneyer TF, Starink MJ, Sinclair I. Mater Sci Forum 2006; 519-521: 1023-1028

[26]Knott JF. Fundamentals of Fracture Mechanics. London: Butterworth; 1973

[27] Bron F, Besson J, Pineau A. Mater Sci Eng A 2004 ; A 380 : 356-364

[28] Vasudevan AK, Doherty RD. Acta Metall 1987; 35 : 1193-1219

[29] Dumont D, Deschamps A, Brechet Y. Mat Sci Eng A 2003; 356: 326-336

[30] G. Lutjering, A. Gysler. Proc. 1st Int. Conf. On Aluminium, Argentina (1978) published as Aluminium Transformation Technologies and Applications (edited by C. A. Pampillo, H. Biloni and J. D. Embury), p.171. Am. Soc. Metals, Ohio (1980)

[31] Unwin PT, Smith GC. J Inst Metals 1969; 97: 299-310

[32] Embury JD, Nes E. Z Metallkd 1974; 65: 45-55

[33] Li BQ, Reynolds AP. J Mater Sci 1998; 33: 5849-5853

[34] Kamp N, Sinclair I, Starink MJ. Metall Mater Trans A 2002 ;33A : 1125-1136.

[35] Zhu Z, Starink MJ, Mater. Sci. Eng A, in press.

Chapter 5

Evolution of voids during ductile crack propagation in an Al alloy sheet toughness test studied by synchrotron radiation tomography

Results of a synchrotron radiation computed tomography study of void evolution during crack propagation in Kahn tear tests of an AA2139 Al-alloy in T8 condition are presented here in the form of a paper, as has been published in Acta Materialia. It gives an illustration of the insights that can be obtained using this technique and provides data for model formulation and validation. A full assessment of the mechanical properties of the AA2139 material, further tomography results, and a model describing toughness anisotropy are given in Chapter 6.

Abstract

The anisotropy of fracture toughness in AA2139 (Al-Cu-Mg) alloy sheet has been investigated via synchrotron radiation computed tomography of arrested cracks in Kahn tear test pieces for different loading cases. The three dimensional distribution and morphology of pores and defects in the as-received state are seen to be anisotropic, with chains of voids and void elongation in the L (longitudinal) direction. For toughness testing in L-T orientation (T is long transverse), voids ahead of the crack grow and link in the L direction. In T-L tests, voids ahead of the crack tip also grow in the loading direction, although a high degree of alignment is retained in the L direction. The present work provides quantitative microstructural data that can be used as input for and validation of recent idealised model formulations and it is shown that the measured void dimensions and evolution are consistent with measured toughness anisotropy.

5.1 Introduction

Fracture toughness is a crucial material design criterion for many high strength materials applications [1,2]. Historically, two dimensional (2D) surface imaging techniques, such as optical and electron microscopy, have been used to reveal fracture micromechanisms [3,4]. With recent developments in synchrotron radiation computed tomography (SRCT) it has become possible to visualise fracture mechanisms within materials at a sub-micron scale in three dimensions (3D) [5]. Classical treatments of ductile crack growth have highlighted the geometrical aspects of damage evolution, particularly in relation to the later stages of void coalescence. The work of Hahn and Rosenfield [6] for example simply identifies the critical condition for fracture toughness with inter-void separation distance and degree of crack tip opening ('void-by-void' growth [7]). More recent works [8,9,10,11,12,13] have recognised the inevitable complications of failure in 'real' engineering materials, where defect/void distributions associated with fracture are often subject to complex patterns of spatial clustering and/or anisotropy, along with wide/multi-modal distributions in size and morphology. To date, even the most complex contemporary treatments of ductile failure [7-13] involve a variety of microstructural and micromechanical simplifications. In this respect, detailed 3D micromechanical observations of fracture/damage evolution in real microstructures may provide an important basis for parametric initialisation and validation of such models.

The present study focuses on tomographic observation of fracture in an Al-Cu-Mg alloy sheet. The primary application is for airframe manufacture, where toughness and fatigue resistance are critical. With recent progress in SRCT, several studies on the micromechanisms of failure in Al alloys have been reported. Using *in-situ* tests Qian *et al.* [14] highlight the growth of voids and their coalescence during ductile fracture of a notched specimen geometry via SRCT. Fatigue crack closure phenomena have also been observed and quantified by various researchers [15,16,17,18]. Maire *et al.* [19] have quantitatively assessed the monotonic growth of voids in a model aluminium matrix composite containing spherical ceramic particles; through careful matching of experimental conditions and parallel model formulation (*e.g.* in terms of damage volume fraction and triaxiality levels), good accord was obtained between experimental and predicted void growth behaviour.

The present work reports on the novel SRCT observation of ductile crack extension in an anisotropic high strength Al-alloy sheet, going from parent (unstrained) material to the point of coalescence with a propagating crack tip, via the analysis of arrested crack growth specimens. In particular, the relationship between prior defect geometry, spatial distribution and the micromechanisms of failure has been observed for two test orientations.

5.2 Experimental

AA2139 sheet was supplied by Alcan CRV with a thickness of 3.2mm. The nominal composition is given in Table 5-1. After solution treatment, the plate was stretched by 2%, then aged at 175 °C for 16 hours. The tensile properties of the material such as tensile yield strength (TYS) and ultimate tensile strength (UTS) are given in Table 5-2. The plastic anisotropy of the material is very small.

Si	Fe	Cu	Mn	Mg	Ag	Ti	Zn
<= 0.1	<= 0.15	4.5 - 5.5	0.20 - 0.6	0.20 - 0.8	0.15 - 0.6	<= 0.15	<=0.25

Table 5-1 Composition Limits of Alloy AA2139 in weight %

direction	L	T
TYS in MPa	440	430
UTS in MPa	478	475

Table 5-2: Tensile properties of alloy AA2139 in T8 condition for testing directions L and T

The grain size obtained by EBSD and calculated by mean linear intercept has been determined to be 42 μm in L and 20 μm in S direction.

A field emission gun scanning electron microscope (JEOL 6500F) equipped with an electron dispersive spectroscopy (EDS) analyser was used to assess material microstructures. EDS analysis revealed two populations of intermetallic particles: $Al_7Cu_2(Fe,Mn)$ and Al_2Cu. The particles were strongly aligned as stringers in the rolling direction (L) with stringer dimensions of the order of 15-30μm (cf. 1-10μm in the long transverse direction (T) and 1-6μm in the short-transverse direction (S)). The intermetallic

content has been measured via grey value thresholding of field emission gun scanning electon microscope (FEG-SEM) images (backscattered electron mode) to be ~0.004 ±15% (standard error based on repeat measurements at different magnifications).

Cracks were grown to a length of 10mm in Kahn tear test [20] pieces (dimensions: 35mm x 60mm x 3.2mm) in general accord with ASTM B 871 - 01: *i.e.* tests were arrested before final failure of the coupon. At 10mm from the notch the crack is slanted. To facilitate high resolution SRCT imaging of the arrested crack tip region, a small 'stick' of material (dimensions 1mm x 1mm x 10mm) was extracted around the tip at the specimen mid-plane (long dimension parallel to the direction of crack extension) using a slow speed diamond saw, see Figure 5-1.

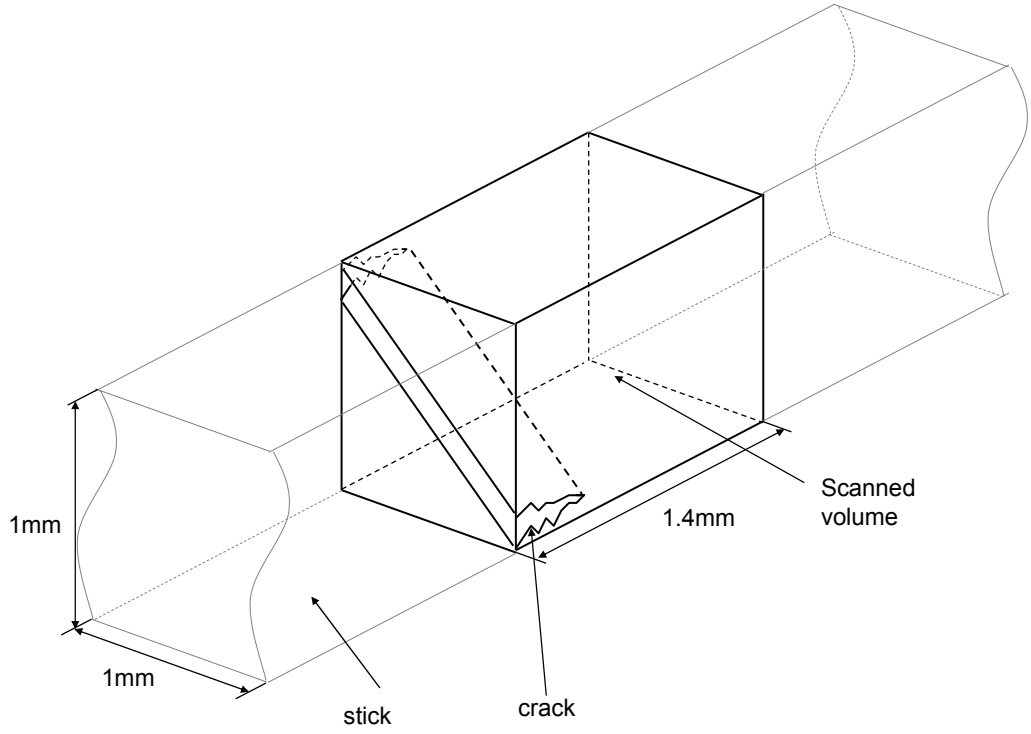

Figure 5-1: Schematic drawing of the investigated volume at the arrested crack tips

Mechanical testing and subsequent SRCT crack tip imaging has been performed in both the L-T and T-L configurations, *i.e.* in-plane testing, with loading applied in the rolling and long transverse directions respectively, see Figure 5-2. Unit initiation energies (UIE) have been calculated using the crosshead displacement and accounting for machine stiffness.

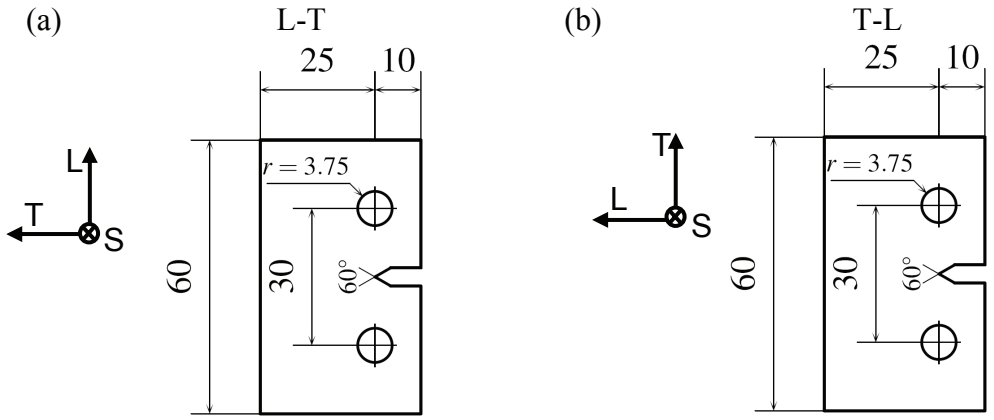

Figure 5-2: Sample and loading geometries: (a) L-T and (b) T-L; all dimensions in mm

Tomography was performed at beamline ID 19 of the European Synchrotron Radiation Facility (ESRF), Grenoble, France, at 20.5kV. The facility provides a highly coherent, spatially and spectrally homogeneous beam with a high photon flux. For one volume 1500 radiographs were taken using a high performance CCD camera whilst the sample was turned through 180° (parallel beam conditions) in steps of 0.12°; the typical imaging time per radiograph was 0.7s. Flat-field and dark current corrections were performed and reconstruction was carried out using a conventional filtered back projection algorithm [5]. In the reconstructed slices an isotropic voxel size of 0.7μm was obtained. Phase contrast imaging has been performed to enhance the detection of edges [21]. At ID19 this is a straightforward technique as advantage is taken of the radiation coherence by adjusting the sample-detector distance (13mm in the present work) to obtain near-field Fresnel diffraction effects. Detailed information on the imaging techniques is given in [22].

Subsequent 2D and 3D imaging and analysis was carried out using the commercial software package 'VG Studio Max v1.2' [23]. Use was made of a "sum along ray" visualisation [24]. Specifically, the imaged volumes containing the crack tip and associated microstructural features have been segmented (in 3D) and shown in isolation from the surrounding aluminium matrix. A 'box-car' transformation is used to fill the crack/defects with voxels of equal grayscale, which are then viewed perpendicular to the nominal crack plane. The "sum along ray" method (see Figure 3) then generates a projection of the crack plane, where the grey level is directly proportional to the crack thickness, *i.e.* a crack opening displacement (COD) map is obtained.

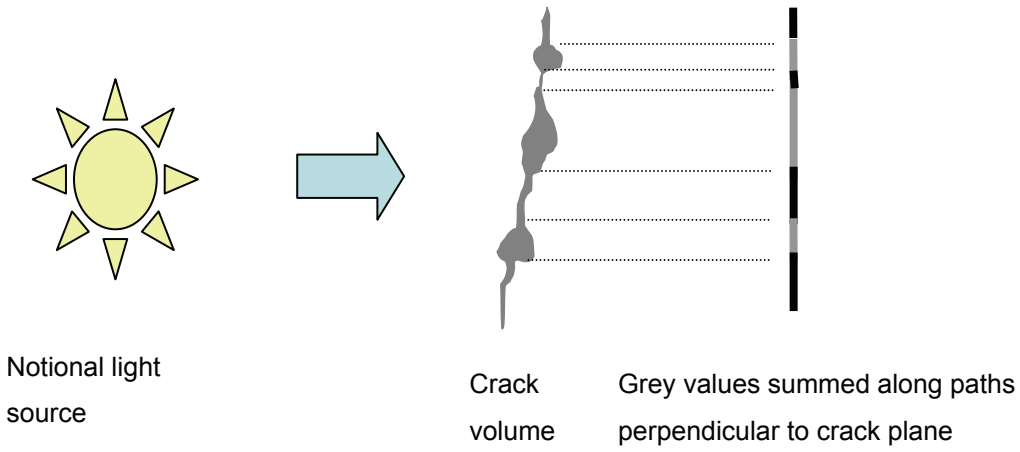

Figure 5-3: Schematic 2D illustration of the "sum along ray" algorithm: in the final projection of the crack thicker areas, in this instance associated with void growth, appear bright/white.

SRCT measurements of the prior pore content of the material (i.e. before loading) were carried out (sampling volume of 980μm x 490μm x 490μm). For the arrested cracks, the evolution of damage/voids ahead of the growing crack tip has been characterised in a similar sampling volume at a distance of some 70μm ahead of the overall crack tip location (representing a region of reasonably uniform damage evolution, ahead of local fluctuations in the main crack tip location and coalescence).

5.3 Results

5.3.1 Kahn tear test results

Figure 5-4 shows the results of Kahn tear tests in terms of force divided by the initial ligament area A_0 as a function of the crack mouth opening displacement (CMOD) and the crack length as a function of the CMOD. It can be seen that the T-L sample is less tough than the L-T sample, as for the T-L sample the nominal stress in the propagation region is lower and the crack growth is faster than for the L-T sample (particularly up to ~15mm of crack extension). Average unit initiation energies (UIE) were measured to be ~30% higher in the L-T orientation compared to the T-L (UIE values corresponding to ~ 79N/mm for T-L loading and 104N/mm for L-T loading respectively).

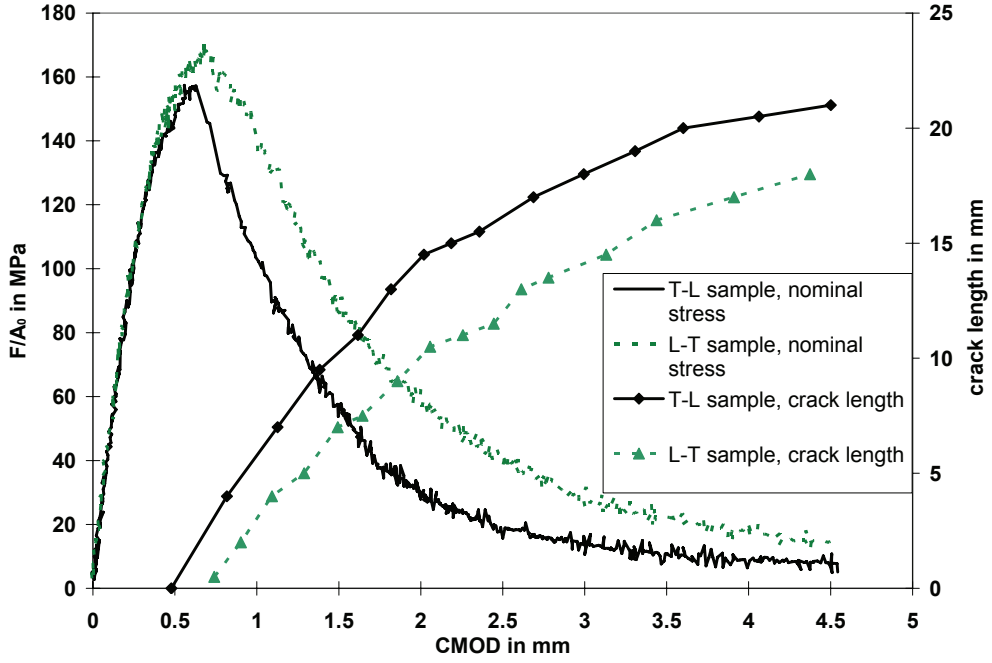

Figure 5-4: Results of the Kahn tear tests for the T-L and L-T sample for the AA2139 in T8 condition.

5.3.2 SRCT of the as-received material

Figure 5-5 shows typical 2D sections from the SRCT data taken in the as received, undeformed material. The aluminium matrix (grey), intermetallics (white) and pores (black) are clearly delineated, with phase contrast fringes highlighting the associated edges/interfaces. Pore content determination variation of the non-deformed material was governed by the choice of the grey scale threshold. Pore content is expected to be 0.0034 with a variation of ±10% when setting extreme grey values. Mean pore dimensions (3D Feret measurements) are 7.6, 5.4 and 4.5 µm in the L, T and S directions respectively. 3D Voronoi tessellation [25] of the void distribution revealed average cell dimensions of 45 and 48µm in the L and T direction respectively, i.e. indicative of near-neighbour separation distances in these directions. Pores were seen to be closely linked with the intermetallic distribution, with a large proportion being associated with one or more intermetallic particles. The alignment of pores into local chains in the L-direction is also evident in Figure 5-5(a).

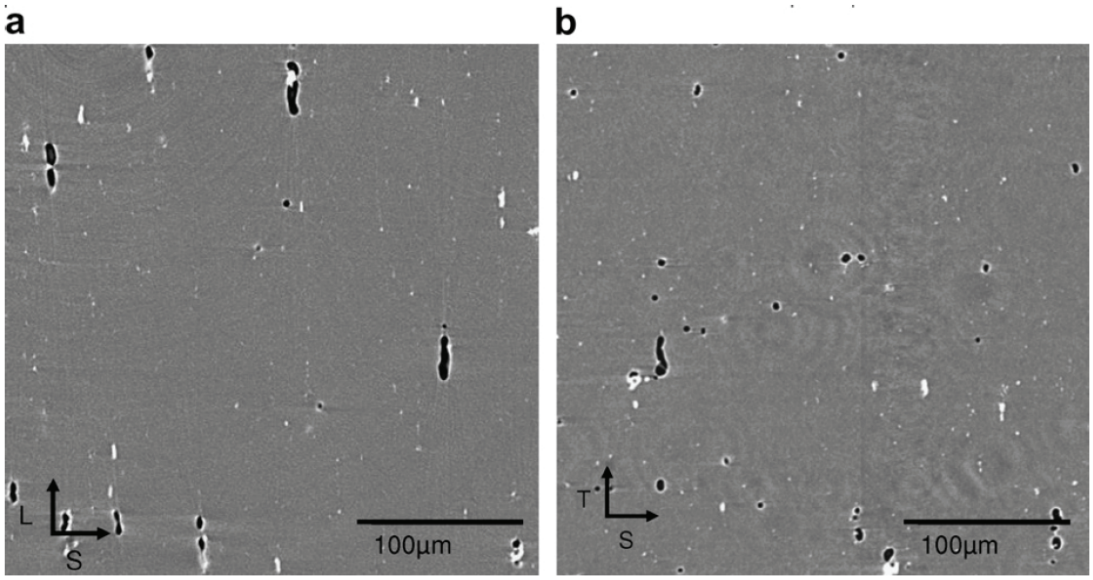

Figure 5-5: (a) 2D image of the as received AA2139 material in the L-S plane (b) 2D image of the as received AA2139 material in the T-S plane

Figure 5-6 further shows a 3D rendering of the void distribution of the as received material (*i.e.* with the aluminium matrix and secondary phase particles being rendered transparent). It should be noted that the intrinsic void content of the parent material is of course 'exaggerated' by the 3D nature of Figure 5-6, representing the void content of a thick slice of material (350µm x 350µm x 180µm) rather than a 2D section in traditional metallographic imaging. The more marked elongation in the L direction is again evident, with mean 3D Feret dimension aspect ratios of every pore in Figure 5-6 (*i.e.* for whole pores, as opposed to section planes) being measured as ~ 1.6, 1.2 and 1.5 in the L-S, T-S and L-T planes respectively.

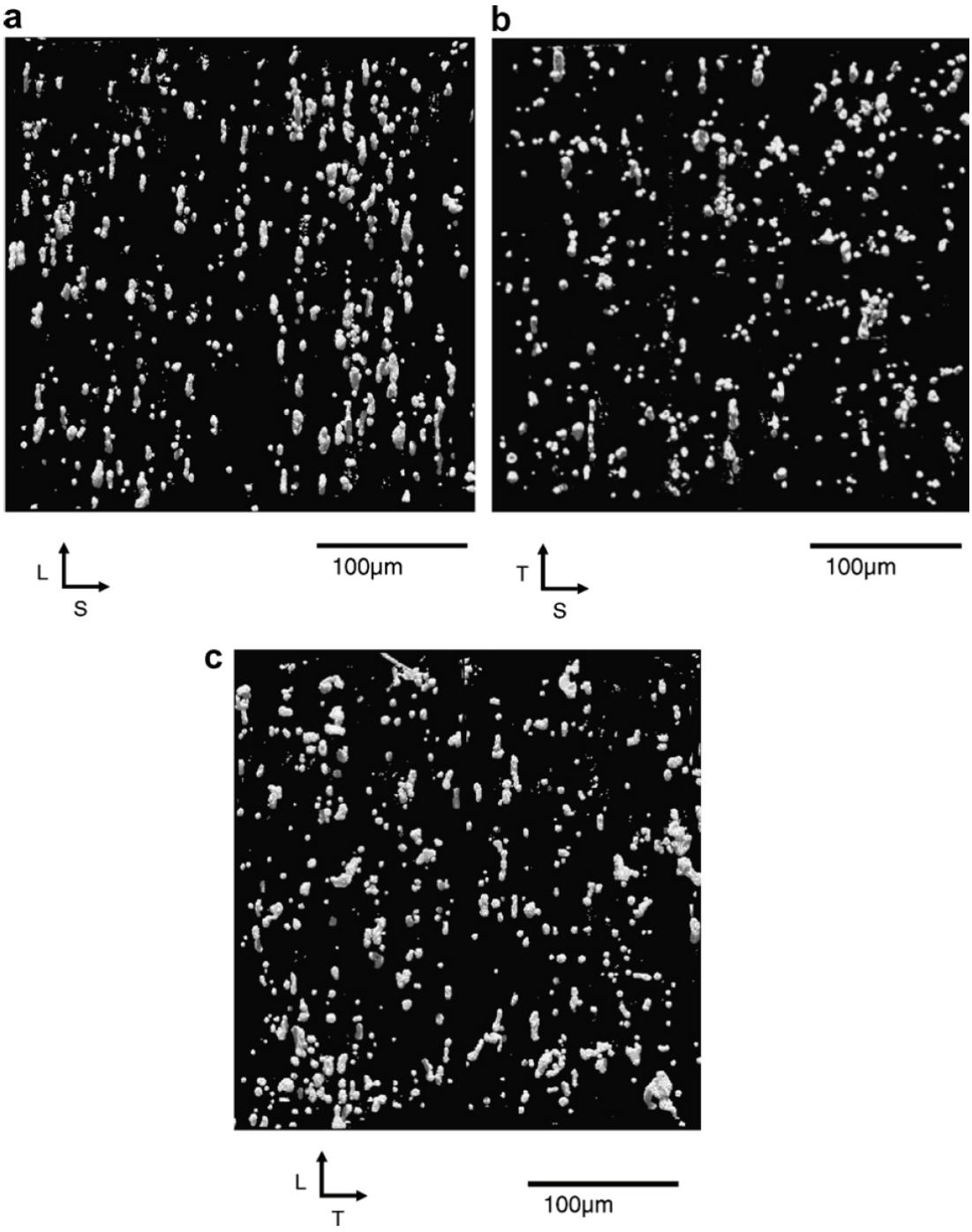

Figure 5-6: 3D rendering of pores in a volume of 350µm x 350µm x 180µm of the as received AA2139 material in: (a) the L-S plane, (b) the T-S plane and (c) the L-T plane. (As a projection of voids in a volume of material is shown, the void content appears significantly higher than the actual volume fraction).

5.3.3 SRCT of the arrested cracks

Figure 5-7 shows 2D sections of the material undergoing slant fracture at the crack tip. In Figure 5-7(a) results for the L-T test orientation are shown, i.e. corresponding to crack growth in the T direction, with elongated voids being discernable in the loading direction,

L. Figure 5-7(b) shows the T-L case, where voids are again elongated in the loading direction (the T direction in this case) but to a lesser extent than in Figure 5-7(a). In conjunction with SEM fracture surface assessment, the crack itself is seen to be made up of both coarse voids (of the order of 20µm diameter) and regions of shear decohesion. Coarse voids arise from both intermetallic particle cracking and decohesion, although with the prior presence of pores in the parent material and the observed correlation of intrinsic pores with intermetallics it is clearly difficult to discern the exact origin of each crack tip void (i.e. distinguishing growth of pores that where already present from intermetallic decohesion). It is discernable from Figure 5-7 however that a significant proportion of the intermetallics (particularly smaller ones) do not exhibit pores in the immediate vicinity of the crack.

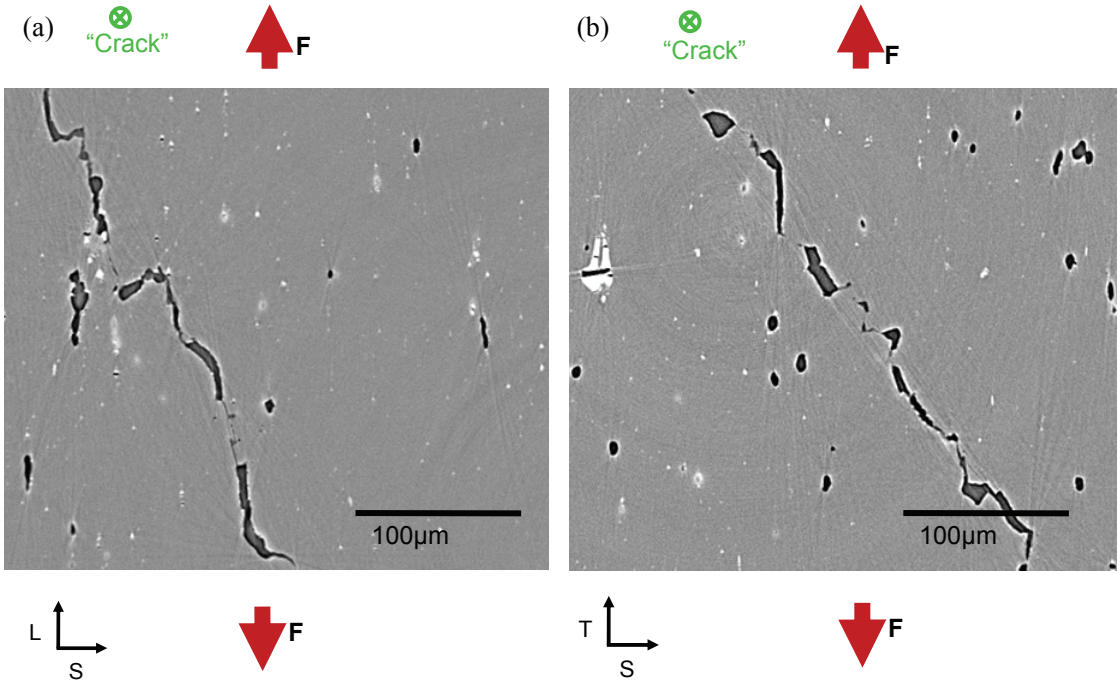

Figure 5-7: 2D SRCT sections normal to the crack growth of the AA2139 material in T8 condition: (a) L-T test orientation and (b) T-L test orientation.

Figure 5-8 and 5-9 show 3D images of the distribution of voids immediately ahead of the crack tip (~50µm ahead of the main crack tip). Similar to Figure 5-6 the Al matrix is transparent in this case and only the voids can be seen. The elongation of voids in the loading direction is particularly apparent in Figure 5-8(a); void aspect ratios for loading in rolling direction (L) are clearly higher than those for the T-direction loading (Figure 5-8(b)): the mean Feret dimension aspect ratio of every void for the L-T load cases in the L-

S plane is ~2.0 and for the T-L load cases in the T-S plane it is ~1.6, whilst in the L-T plane the mean Feret dimension aspect ratios for the L-T and T-L load cases are ~1.6 and ~1.1 respectively. A number of extremely elongated voids are seen in the L-T load case (see Figure 5-10), with the morphology of these implying that just ahead of the crack tip pore chains which existed in the L direction prior to testing have coalesced into highly elongated single bodies ("void columns"). Such behaviour has been noted in theoretical models [13], however the present results may be identified with a plane stress state (low lateral stresses) as compared to the high lateral stress condition considered in [13].

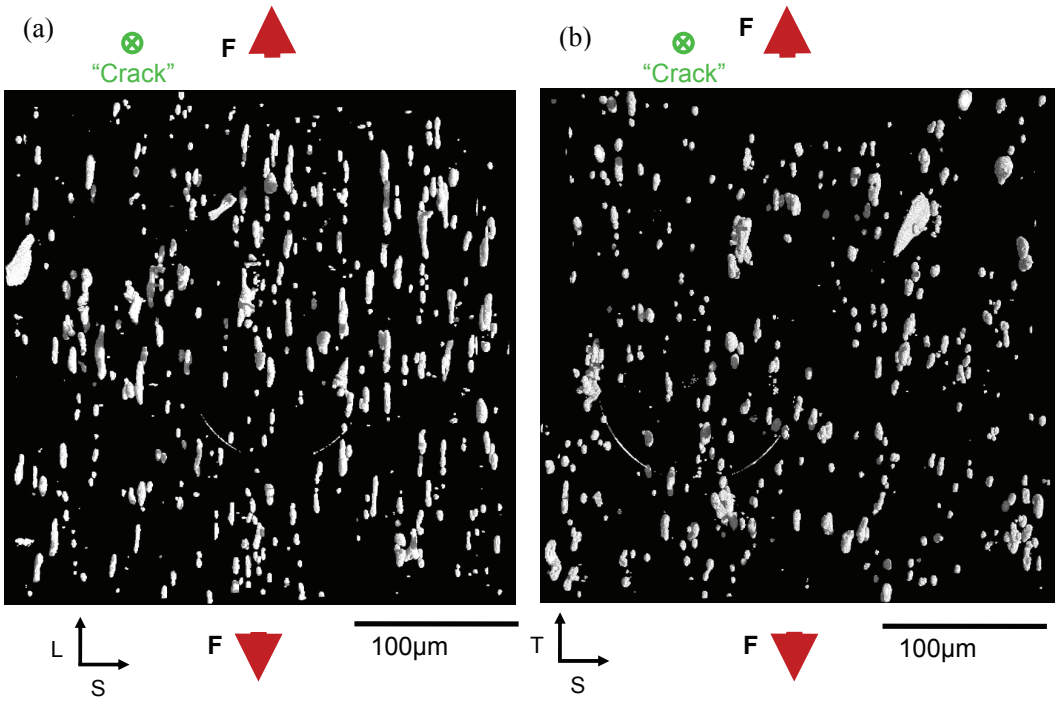

Figure 5-8: 3D void distribution and morphology for the AA2139 material in T8 condition: (a) in the L-S plane for L-T loading, and (b) in the T-S plane for T-L loading. (As a projection of voids in a volume of material is shown, the void content appears significantly higher than the actual volume fraction).

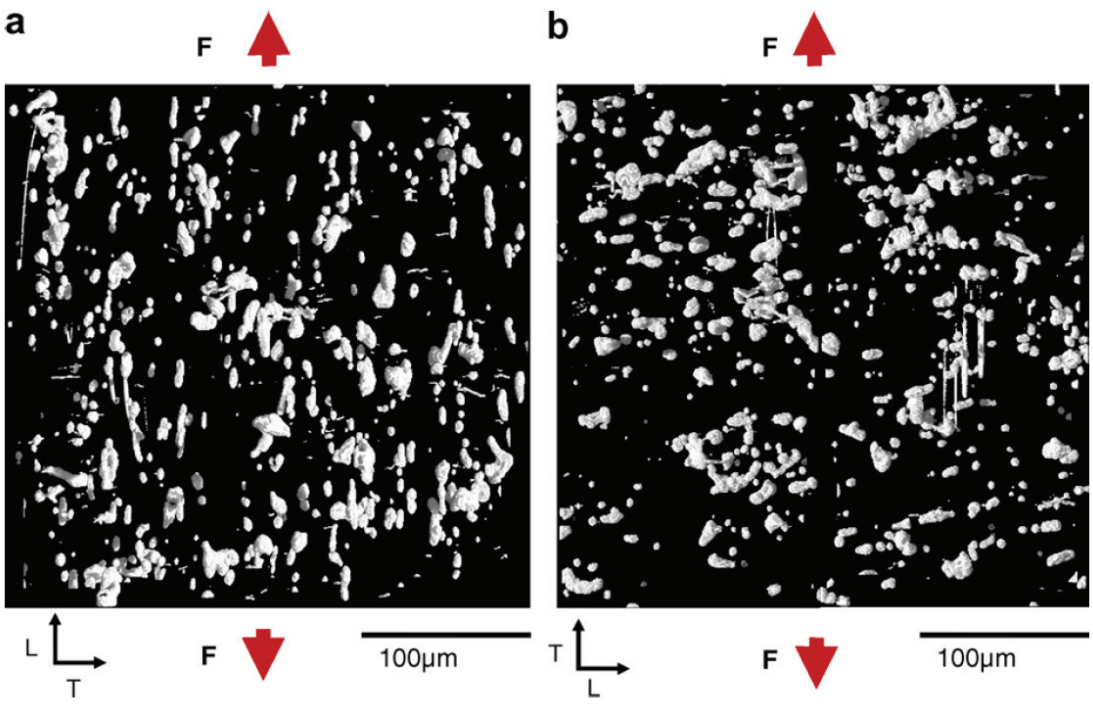

Figure 5-9: 3D void distribution and morphology in a volume of 350µm x 350µm x 180µm in the L-T plane for the AA2139 material in T8 condition for: (a) L-T loading, and (b) T-L loading. (As a projection of voids in a volume of material is shown, the void content appears significantly higher than the actual volume fraction).

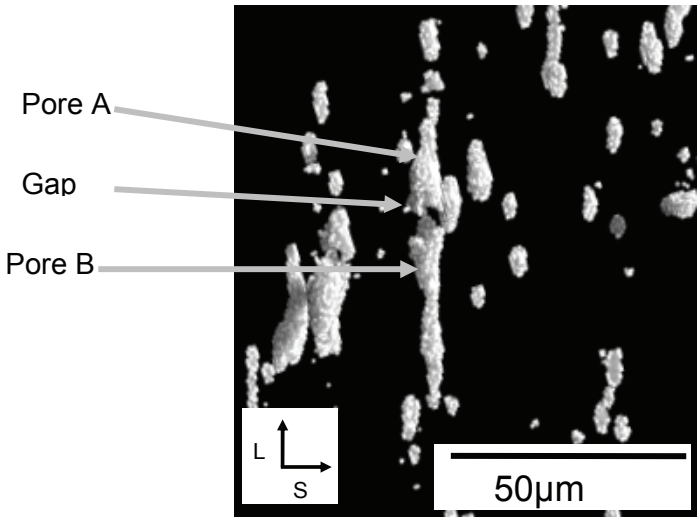

Figure 5-10: 3D Close-up image of coalescing elongated voids in the L-T sample in one column for the AA2139 material in T8 condition

Figure 5-11 shows a comparison of the crack tip regions for the L-T and T-L loading cases distinguishable from narrower shear coalescence regions as the thick regions appear brighter than the thin ones. Comparison of void position in Figure 5-11(a) and (b) shows that in the region of coalescence at the crack tip the spacing between large/primary voids

is larger for the L-T testing case (the tougher direction). This is further reflected in the number density of voids in this region in the L-T sample, measured as ~230/mm^2, whilst for the T-L sample it was approximately 20% higher (~270/mm^2). Coalesced void chains are also evident in the crack growth direction in the T-L case, see Figure 5-11(b). In this figure one void chain is magnified, and several other brighter chains are also evident (see dashed boxes indicating examples of void chains). It may be seen that at the crack front such chains extend some 50-100μm ahead of the surrounding crack front location: such local extensions of the crack are not seen in the tougher, L-T oriented test. In the L-T loading case the coalescing voids in the L direction have a final strongly elongated form (aspect ratios of up to ~ 4), *cf.* the T direction loading where an essentially penny-shaped void morphology is attained immediately before crack coalescence (void shape extended in the loading and crack growth direction). On the fracture surface for the L-T loading case the average apparent void length in the crack growth direction (T in this case) is 35μm whilst for the T-L loading case the average apparent void length on the fracture surface in the crack direction (L in this case) is 45μm.

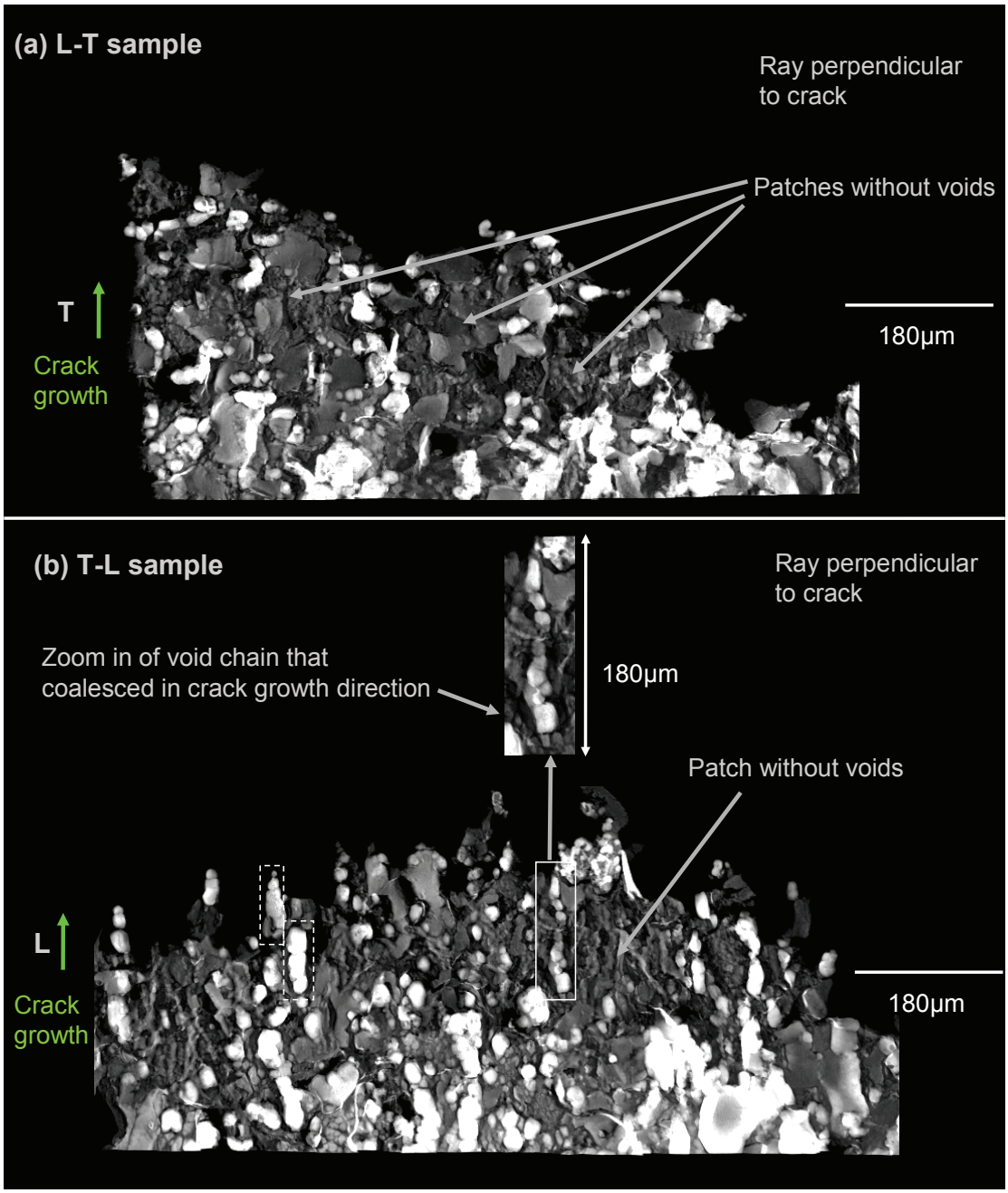

Figure 5-11: Representation of the crack tip via the "sum along ray" algorithm for the AA2139 material in T8 condition for: (a) L-T loading, and (b) T-L loading. Two coalescing void chains at the crack tip are highlighted by dashed boxes.

5.4 Discussion

From the tomography observations, the sequence of events during fracture of the present Al-Cu-Mg alloy sheet may be discerned as follows: initially the material displays a classically anisotropic intermetallic and pore distribution for a rolled material, both appearing as aligned chains elongated in the rolling direction (L). Subsequent loading in

the L direction leads to the coalescence of chains of voids in the loading direction so that large voids that are highly elongated in the rolling direction are created prior to coalescence at the crack tip (see figure 5-8), i.e. coalescence occurs heterogeneously and is a multi-stage process. Concerning the T-L case, voids are seen to grow in the loading direction, but remain primarily elongated in the rolling direction, reflecting the prior pore distribution of the parent material. Inter-void separation distances at coalescence are reduced *cf.* the L-T case, and the incidence of void coalescence in chains is seen parallel to the growth direction just ahead of the crack tip.

In the present analysis it is useful to recall the model by Tvergaard and Hutchinson [7] which provides a formulation and numerical analysis of a two-dimensional plane strain model with multiple discrete voids located ahead of a pre-existing crack tip. At initial void volume fractions that are sufficiently low, initiation and growth is approximately represented by the void by void mechanism [7]. At somewhat higher initial void volume fractions, a transition in behavior occurs whereby many voids ahead of the tip grow at comparable rates and their interaction determines initiation toughness and crack growth resistance [7]. For intermediate void volume fractions a 'hybrid' condition of void-by-void and multiple void coalescence may be encountered. Given the heterogeneous distribution of prior pores/intermetallics in our material, the void coalescence observed in the T-L case may be identified with this 'hybrid' condition. Detailed comparison of current void distributions and Tvergaard and Hutchinson's [7] prediction are difficult (contingent on various modelling parameters and assumptions), however, it may be seen that a consequence of Tvergaard and Hutchinson's [7] prediction of prior void volume fractions for void coalescence mode transitions falling close to the effective initial void content of the present material does imply that a hybrid failure mode may easily arise when voids are heterogeneously dispersed and significant local fluctuations in volume fraction are produced.

Given the elongated prior pore and intermetallic content of the present sheet material, fracture modelling results for prolate and oblate initial void shapes, as described in Refs. [8-11], are of some interest, although the present voids do not exactly present such axisymmetric morphologies. In the work of Pardoen and Hutchinson [10], toughness effects of pore shape and spatial alignment are presented [10], at least for regular (non-clustered) distributions of pores, with predictions being made in terms of plane strain J_{IC}

values. The Finite Element analysis of Pardoen and Hutchinson [10] has been carried out considering plane strain, small scale yielding conditions and only one value for the strain hardening exponent (n=0.1). Following from the known correlation of UIE and K_{IC} values [26], it is possible to at least compare the magnitude of predicted and experimental changes in toughness value with test orientation. Interpolation of results provided by Pardoen and Hutchinson [10] show that for uniformly dispersed prolate and oblate voids of aspect ratio 1.5 and 0.67 respectively at an initial pore fraction in the order of 0.5 to 0.8%, i.e. aspect ratios equivalent to those presented by the L-T and T-L tests and volume fraction of the order of the initial defect content of the alloy (pores plus intermetallics), J_{IC} should decrease by 20-30% between L-T and T-L tests. As such, the shapes of voids and volume fraction of defects are reasonably consistent with the measured difference in UIE between L-T and T-L Kahn tests of our alloy, which was about 30%. Pardoen and Hutchinson [10] further consider the influence of directional alignment of spherical voids on toughness, as illustrated in Figure 5-12, it is difficult to identify appropriate values for the regular spacings X_0^A and X_0^B in the model from the real 3D microstructure, which has substantial statistical variations.

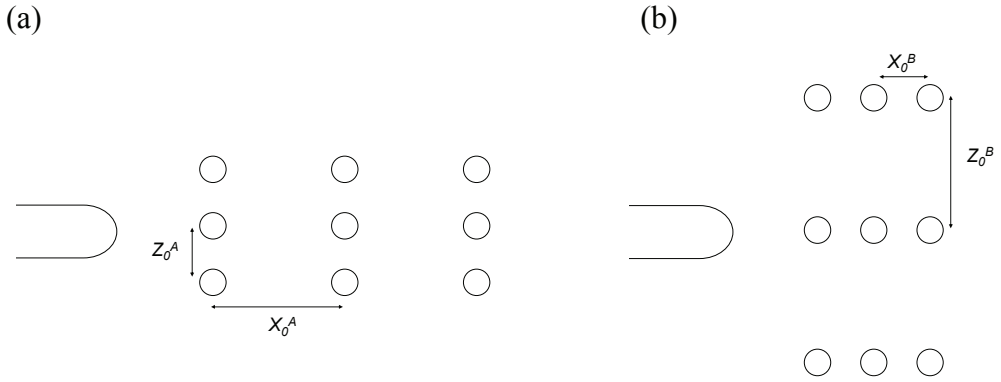

Figure 5-12: Two different crack plane orientations in a material exhibiting initially anisotropic spacing (after [10])

However, their ratio may in the first instance be anticipated to scale with the aspect ratio of Voronoi cells generated for the microstructure in the L-T plane. From tessellation analysis on the tomography data of as received samples we obtained a value of ~1.0 for the ratio of 3D Feret dimensions in L and T of the Voronoi cells, suggesting that the particle spacing may not be a primary contribution to fracture anisotropy. Thus the present analyses suggest that it is the shape of the voids rather than their distribution that causes the difference in toughness between the two orientation. It should be noted however that

comparison of experimental and modelled toughness values are subject to many simplifications in this instance (*e.g.* simplified void shapes, spatial arrangement, matrix work hardening and plastic isotropy), and the significance of average particle spacing parameters when alignment occurs within local clusters is not known.

5.5 Conclusions

- Kahn tear test on an Al-Cu-Mg sheet has shown toughness anisotropy: T-L samples are less tough than L-T samples.
- The evolution of voiding/damage during ductile crack growth has been observed via high resolution tomography in a high strength Al-alloy, showing the evolution of void growth and coalescence processes.
- The undeformed, as-received material has been investigated showing anisotropic distribution of pores: elongated aligned pores are prevalent in rolling direction
- In the case of loading in L direction (crack growth in T) voids ahead of the crack may link in the loading direction (L) and form large strongly prolate voids prior to crack coalescence
- In the case of loading in the T direction (crack growth in L), voids ahead of the crack tip have grown in the loading direction (T) but retain significant elongation in the L direction, i.e. are close to penny-shaped as coalescence occurs.
- The “sum along ray” representation of the crack in both samples elucidates that separation distances between coarse voids are shorter for crack growth in L direction than for crack growth in T direction , consistent with the measured toughness anisotropy.
- Toughness trends are in semi-quantitative accord with recent local approach finite element models of idealised void shape, distribution and alignment effects, notwithstanding the simplifications required to make these comparisons.

Acknowledgements

The authors would like to acknowledge Alcan CRV for financial support and material supply, Frédéric Bron and Bernard Bès for technical discussion Jean-Yves Buffière for

support in SRCT imaging and the assistance of Elodie Boller in the use of the beamline at the ESRF.

5.6 References

[1] Cho A, Bes B. Mater Sci Forum 2006 ; 519-521 : 603-608
[2] Warner T. Mater Sci Forum 2006 ; 519-521 : 1271-1278
[3] Haynes MJ, Gangloff RP. Metall Mater Trans A 1998; 29A, 1599-1613
[4] Ludtka GM, Laughlin DE. Metall Trans A 1982; 13A, 411-425
[5] Maire E, Buffière J-Y, Salvo L, Blandin JJ, Ludwig W, Letang J M. Adv Eng Mat 2001; 3:539-546
[6] Hahn GT, Rosenfield AR. Metall Trans A 1975;6A:653-668
[7] Tvergaard V, Hutchinson J H. Int J Solids Struct 2002;89:3581-3597
[8] Gologanu M, Leblond JB, Devaux J. J Mech Phys Solids 1993;41:1723-1784
[9] Gologanu M, Leblond JB, Devaux J. Trans ASME, J Eng Mater Technol 1994;116:290-297
[10] Pardoen T, Hutchinson JW. Acta Mater 2003;51:133-148
[11] Lassance D, Scheyvaerts F, Pardoen T. Eng Fract Mech 2006;73:1009-1034
[12] Decamp K, Bauvineau L, Besson J, Pineau A. Int J Fract 1997 ;88 :1-18
[13] Gologanu M, Leblond JB, Devaux J. Int J Solids Struct 2001;38:5595-5604
[14] Qian L, Toda H, Uesugi K, *et al.* Appl Phys Lett 2005;87:241907-241910
[15] Khor KH, Buffière J-Y, Ludwig W, *et al.* J Phys Condens Matter 2004;16:3511-3515
[16] Toda H, Sinclair I, Buffière J-Y, *et al.* Acta Mat 2004 ;52 :1305-1317
[17] Guvenilir A, Stock S R, Fatigue Fract Eng Mater Struct 1998;21:439-450
[18] Guvenilir A, Breunig, T M, Kinney J H, Stock S R. Acta Mater 1997;45:1977-1987
[19] Maire E, Bordreuil C, Babout L, *et al.* J. Mech Phys Solids 2005;53:2411-2434
[20] ASTM-international, Standard B 871 - 01. 2001.
[21] Kocsis M, Snirgirev A. Nucl Instrum Methods Phys Res Sect A 2004;525A:79-84
[22] Ludwig W. *Development and Applications of Synchrotron Radiation Microtomography*, Dissertation der LMU München, München, 2001
[23] VGStudio Max 1.2, Volume Graphics GmbH
[24] Toda H, Sinclair I, Buffière J-Y *et al*. Philos Mag 2003;83:2429-2440
[25] Yang N., Boselli J., Sinclair, I. J Microsc 2001;201: 189-200
[26] Dumont D, Deschamps A, Brechet Y. Mat Sci Eng A 2003;A356:326-336

Chapter 6

Analysis of toughness anisotropy in AA2139 Al-alloy sheet

In this Chapter an analysis of toughness anisotropy in AA2139 Al- alloy sheet is given for two heat treatment conditions (T8 and T351). It is divided into two sections. In the first section experimental results are given in form of a draft paper that includes results of microstructure analysis, mechanical testing and analysis of fracture mechanisms. In the second section a corresponding model and simulations based on the Gurson-Tvergaard-Needleman approach is given in form of a draft paper. The results and conclusions obtained on this material in Chapter 5 (in the T8 condition) are accounted for in this Chapter.

6.1 Analysis of toughness anisotropy in AA2139 Al-alloy sheet; part I: experiments

Abstract

Fracture toughness anisotropy of AA2139 (Al-Cu-Mg) in T351 and T8 conditions has been investigated via mechanical testing of smooth and notched specimens of different geometries, loaded in either the rolling direction (L) or the transverse direction (T). Fracture mechanisms have been investigated using scanning electron microscopy and through synchrotron radiation computed tomography (SRCT). For theT351 material some plastic anisotropy could be found, attributable to the pre-strain associated with the material production. The T8 material can be considered as plastically isotropic. Fracture toughness is anisotropic for both conditions whilst thoughness is substantially reduced for the T8 condition compared to the T351. Fractography and SRCT assessment have shown anisotropic initial void shapes. Alignment of voids in the direction of crack growth results in shorter inter-void ligaments during longitudinal propagation than for propagation in the transverse direction. SRCT revealed coalescence through shear decohesion in the fracture initiation region indicating the necessity to investigate and account for this mechanism.

6.1.1 Introduction

Aluminium sheet is widely used for lightweight high performance structures particularly within the transport sector. For the design of structures, it is crucial to control mechanical material properties such as fracture toughness [1,2]. In practice, the transferability of toughness trends between small test pieces (such as Kahn tear tests [3]) to large panel M(T) specimens [4] is an important aspect in optimising materials performance for components. One materials issue that is particularly difficult to take account for in predicting toughness performance of large panels is the anisotropy of toughness of sheet, which is introduced during material processing, notably the rolling and post rolling stretch.

Possible sources of toughness anisotropy are numerous. One possible cause is crystallographic textures developed during rolling which will cause the energy dissipated during fracture to depend on the local load level and consequently on the loading direction for anisotropic materials [5,6,7,8,9]. The second cause of toughness anisotropy is related to the anisotropic shape and distribution of defects introduced by the material processing [10,11,12,13]. Processing may create elongated or flat micro-voids which can either slow down or accelerate damage growth as demonstrated by recent models for ductile damage including the effect of cavity shape [14,15,16,17]. Mean void spacing, which can also depend on the direction, was also shown to affect toughness as it strongly influences the onset of void coalescence [18,19,16,10,20,21]. The third cause of possible toughness anisotropy is initial deformation as sheet materials are often prestrained. Prestrain may cause initial damage, decrease hardening capacity, increase yield stresses and generate internal back stresses (i.e. kinematic pre-hardening), all of which can be anisotropic in nature. Such effects can occur for instance in pipeline steels as sheets are deformed to form tubes or in rolled aluminium alloy sheet. This final point has been less investigated than the others but recent results show that prestrain may affect ductility and toughness [8, 22,23,24]. All factors linked to prestrain may either decrease or increase toughness but the generation of back stresses appears to have the strongest influence on toughness anisotropy as prestrain induces very little damage and as changes in isotropic hardening will affect all directions in the same way. In most engineering alloys, all three main causes for toughness anisotropy are present.

With recent developments in synchrotron radiation computed tomography (SRCT) it has become possible to observe the evolution of ductile fracture in three dimensions (3D) at sub-micron level [25]. Preliminary SRCT studies of Kahn tear test pieces of the AA2139 alloy in T8 condition ([26, Chapter 5 in this thesis]) showed that for loading in rolling direction (L) highly elongated (prolate) voids are formed whilst for loading in transverse direction penny shaped voids are formed. These observations indicated that SRCT can shed new light on the causes of toughness anisotropy in these kinds of materials, which can then support improved micromechanical models.

Hence, the aim of the present study is to provide a detailed investigation of the toughness anisotropy of the AA2139 alloy, quantifying both the mechanical response and the relevant microstructure (notably pores and their evolution) and post failure high resolution fractography. The material is studied in two different heat treatment conditions (T351 and T8). This data will be used as input and verification of a micromechanical model that is described in the companion paper (next section 6.2 in this thesis), the ultimate aim being the prediction of large panel M(T) specimen anisotropic toughness from the micromechanical model. Various specimen types are used for characterization of toughness anisotropy, whilst micromechanical damage processes for different loading directions at high levels of stress triaxiality are investigated via SRCT.

6.1.2 Experimental

6.1.2.1 Material

AA2139 sheet was supplied by Alcan CRV with a thickness of 3.2mm in a commercial T351 condition, *i.e.* solution treated, stretched and naturally aged. The composition ranges are given in Table 6.1-1.

Si	Fe	Cu	Mn	Mg	Ag	Ti	Zn
<= 0.1	<= 0.15	4.5 - 5.5	0.20 - 0.6	0.20 - 0.8	0.15 - 0.6	<= 0.15	<=0.25

Table 6.1-1: Composition limits of alloy AA2139 in weight %

The material has subsequently been tested in two different conditions (see Table 6.1-2), T351 (i.e. as-received) and after a further ageing treatment approximating a standard T8 for this alloy. In the interest of brevity, we will refer to the T351 condition as simply 'T3' for the purpose of this paper.

T351 (as received)	T8
Solutionise, quench, 2% stretch in rolling direction, naturally age	The as-received material, additionally aged at 175 °C for 16 hours

Table 6.1-2: Conditions tested for AA2139 sheet

6.1.2.2 Microscopy

Optical micrographs of the grain structure have been obtained after etching with Keller's reagent. A field emission gun scanning electron microscope (FEG-SEM, JEOL 6500F) equipped with an energy dispersive spectroscopy (EDS) X-ray analyser was used to assess material microstructures and fracture surfaces with the beam being set parallel to the loading direction (*i.e.* perpendicular to notional Mode I fracture). Fractography on the T3 samples has been carried out with a Zeiss Gemini DSM 982 FEG-SEM. The intermetallic content has been measured via grey value thresholding of FEG-SEM images obtained in backscattered electron mode.

6.1.2.3 Mechanical testing

In this study 4 types of specimen have been utilised (see Figure 6.1-1): smooth tensile bars, notched tensile bars (EU2), Kahn tear test specimen and large M(T) panels. Tests on notched EU2 specimens particularly allow fracture properties to be investigated at increased stress triaxiality. Two orientations of loading in the sheet plane have been investigated for all samples: L and T. In Kahn and M(T) specimens loaded in the L direction, cracks will propagate in the T direction; these tests are referred to as L-T, and vice versa for T-L designated tests. At least 2 Kahn tests have been performed in each condition/direction combination, whilst for the M(T) sample only one test has been performed per condition/direction. For technical reasons, M(T) tests for the T3 condition have only been carried out for T-L loading. Tensile testing has been carried out on smooth tensile samples (Figure 6.1-1 (a)). The displacement speed for tensile testing was 0.4mm/min and 0.34mm/min for EU2 tests. For the EU2 samples the opening displacement at both notches has been recorded to ensure the symmetric opening occurred. Kahn tear tests under displacement control have been carried out in general accord with [3] at testing speed of 0.085 mm/min.

M(T) testing has been carried out as described in [4] at Alcan CRV. The original crack length of large M(T) specimens is 253 mm. The first 249mm was made by electrical-discharge machining with the last millimetres then being achieved by fatigue precracking. The applied maximum load during precracking is 20% of the yield strength of the net section. The stress ratio is 0.1 and the frequency is 3 Hz. To prevent buckling, two rigid face plates are affixed to the central portion of the specimen. Lubrication is provided between the face plates and the specimens. A displacement gauge was used to measure the crack-opening displacement across the crack mouth. The gage length is 60 mm. A 1000 kN load cell was used and the cross head speed was 0.1 mm/min.

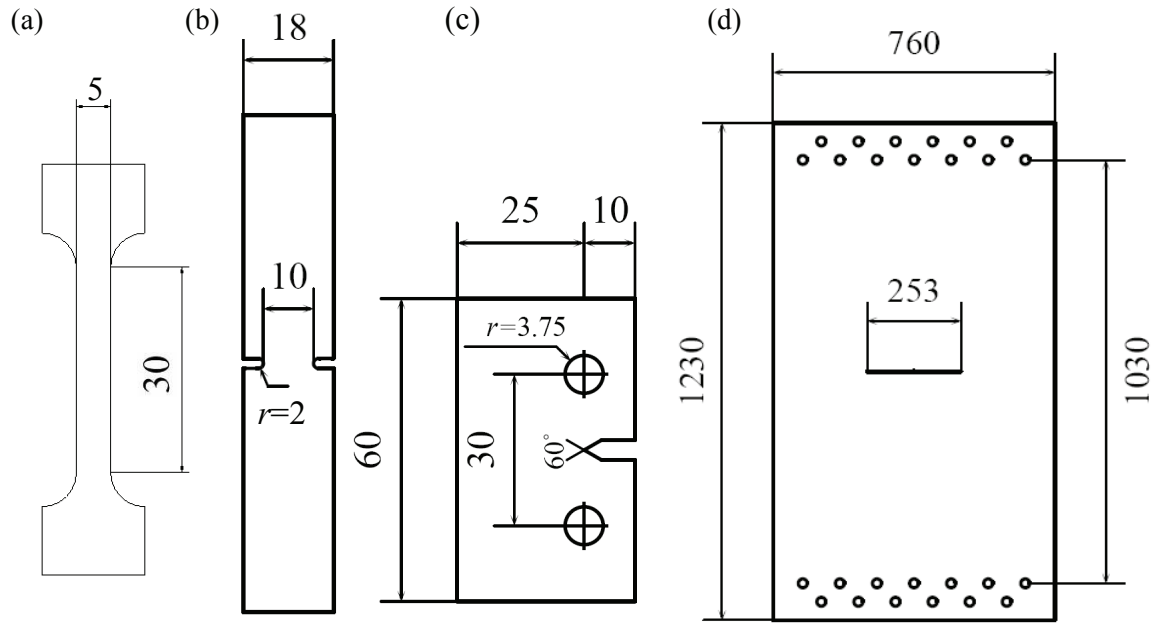

Figure 6.1-1: Specimen geometries for: (a) tensile samples (b) EU2 samples (c)Kahn tear test samples (d) M(T) samples (all dimensions in mm)

6.1.2.4 SRCT studies

For SRCT studies tests on crack growth, Kahn tear tests have been arrested at points as shown in Figure 6.1-5. The subsequent sample preparation and scanning has been carried out as described previously [26, Chapter 5 in this thesis]. For the analysis of arrested cracks in the initiation region use was made of analysis routine developed by Henry Proudhon. The aim was to show the local crack opening using a 'sum along ray algorithm' [27] and additionally provide a scale to quantify the local opening. Additionally, a crack height map has been produced, where the average height of the crack with respect to the loading direction is shown.

6.1.3 Results and analysis

6.1.3.1 Material microstructure

Optical micrographs of the grain structure after etching with Keller's reagent are shown in Figure 6.1-2(a). The grain size was obtained from optical microscopy on etched sections using a mean linear intercept method as 60 μm in the rolling direction (L), 52 μm in the long transverse direction (T) and 24 μm in the short transverse direction (S).

Figure 6.1-2(b) shows a typical 2D section from the synchrotron radiation computed tomography (SRCT) scan of the as-received material. Detailed information on the imaging techniques and testing conditions is given in [26, Chapter 5 in this thesis]. The aluminium matrix (grey), intermetallics (white) and pores (black) are clearly delineated, with phase contrast fringes highlighting the associated edges/interfaces. Mean pore dimensions (3D Feret measurements) are given in Table 6.1-3. Pore content determination variation of the non-deformed material was governed by the choice of the grey scale threshold. 3D Voronoi tessellation [28] of the void distribution revealed average cell dimensions of 45µm, 48µm and 50µm in the L, T and S direction respectively, i.e. indicative of near-neighbour separation distances in these directions [26, Chapter 5 in this thesis]. Consistent with these figures the Voronoi cell aspect ratios for cells around the pores are found to be close to 1.

	Porosity			**Intermetallic particles**		
f_v in %	0.34 with a variation of ±10% when setting extreme grey values.			0.45 ±15% (standard error based on repeat measurements at different locations and magnifications).		
	Mean Feret dimensions of pores in µm			Mean Feret dimensions of Voronoi cells around 2nd phase particles and pores in µm		
	L	T	S	L	T	S
	7.6	5.4	4.5	23	24	25

Table 6.1-3: Porosity and intermetallic particle content, dimensions and distribution of the AA2139 alloy. (Pore content and pore Feret dimension and was reported previously [26, Chapter 5 in this thesis].)

The particles were strongly aligned as stringers in the rolling direction (L) with stringer dimensions of the order of 15-30µm (*cf.* 1-10µm in the long transverse direction (T) and 1-6µm in the short-transverse direction (S)). X-ray analysis revealed two populations of intermetallic particles: $Al_7Cu_2(Fe,Mn)$ and Al_2Cu [26, Chapter 5 in this thesis]. The volume fraction of coarse intermetallic particles, and the Feret dimensions of Voronoi cells around pores and intermetallic particles obtained from SRCT data is given in Table 6.1-3. Pores were seen to be closely linked with the intermetallic distribution, with a large proportion being associated with one or more intermetallic particles. The alignment of pores into local chains in the L-direction is also evident in Figure 6.1-2(b). However, no

significant distribution anisotropy for pores and particles can be detected between T and L direction using average Voronoi cell dimensions around pores and particles (see Table 6.1-3)

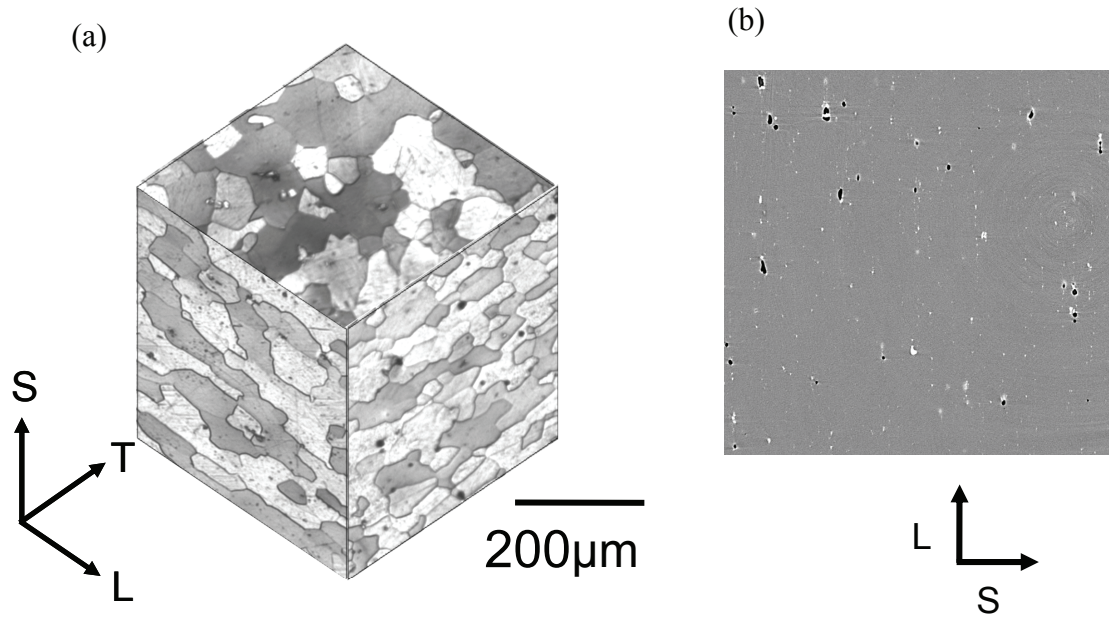

Figure 6.1-2: (a) Pseudo three-dimensional optical micrograph of the AA2139 alloy in T3 condition (b) 2D SRCT section of the as-received material in the L-S plane

6.1.3.2 Tensile testing on smooth bars

Figure 6.1-3 shows the results of tensile tests on smooth specimens tests in terms of force F divided by the initial ligament area A_0 versus engineering strain $\Delta l/l_0$ for testing in L and T directions for material in T3 and T8 conditions. In T3 condition (Figure 6.1-3a) tensile behaviour is anisotropic: For testing in L direction yield strength as well as loads for the same elongation are higher than for testing in the T direction, with a yield strength difference ~80 MPa, average flow stress difference ~15 MPa and a small difference in ultimate tensile strength. The shape of the curves especially up to 5% strain is different for the two loading directions: the transition between the elastic and plastic part of the deformation curve is smooth for T testing but relatively sharp for L testing. The through-thickness deformation is essentially the same for the two testing directions; the slope of the through-thickness variation *vs.* applied strain is close to 0.5 as for isotropic behaviour. The slight difference in initial tensile curve shape is likely to be mostly due to the prestraining by ~2% that the material has undergone.

For the material in the T8 condition (Figure 6.1-3(b)) tensile deformation curves in the different loading directions, as well as the corresponding through-thickness deformation curves, are essentially identical. Overall it is seen that the ageing treatment has lead to higher yield strength and reduced ductility compared to the T3 condition.

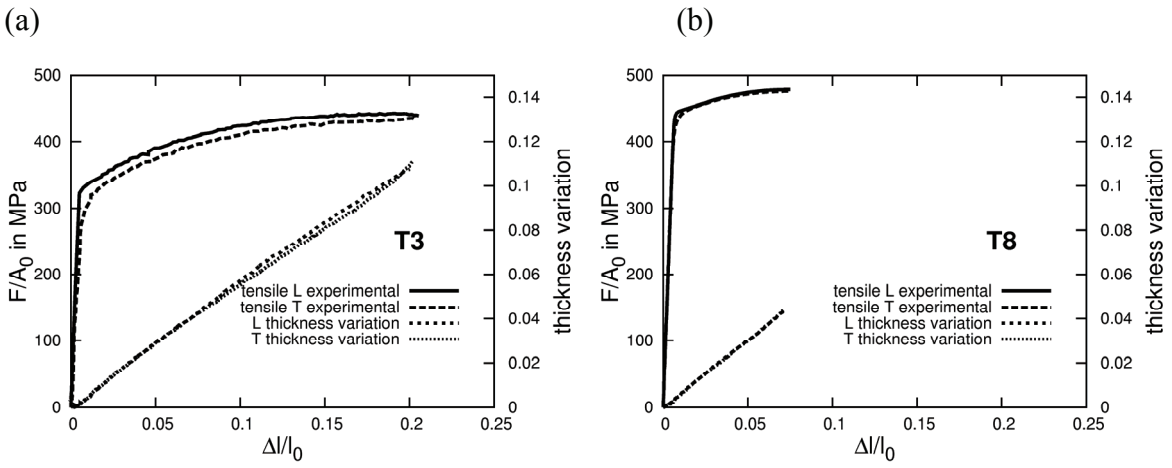

Figure 6.1-3: Tensile test results for testing up to ultimate tensile stress (UTS) in L and T direction for the AA2139 alloy in: (a) the T3 condition (b) the T8 condition

6.1.3.3 EU2 sample testing

Figure 6.1-4 shows the nominal stress vs. crack mouth opening displacement (CMOD) curves for EU2 tests in the L and T directions for material in the T3 and the T8 condition. Figure 6.1-4(a) shows anisotropy in the load curve for the T3 material only, whilst final failure occurs at similar opening displacements.

Consistent with the tensile tests the L and T loading of EU2 samples in the T8 condition (Figure 6.1-4(b)) do not show significant different plastic behaviour. However, final failure in the L direction occurs at ~0.1mm higher opening displacement than the T direction.

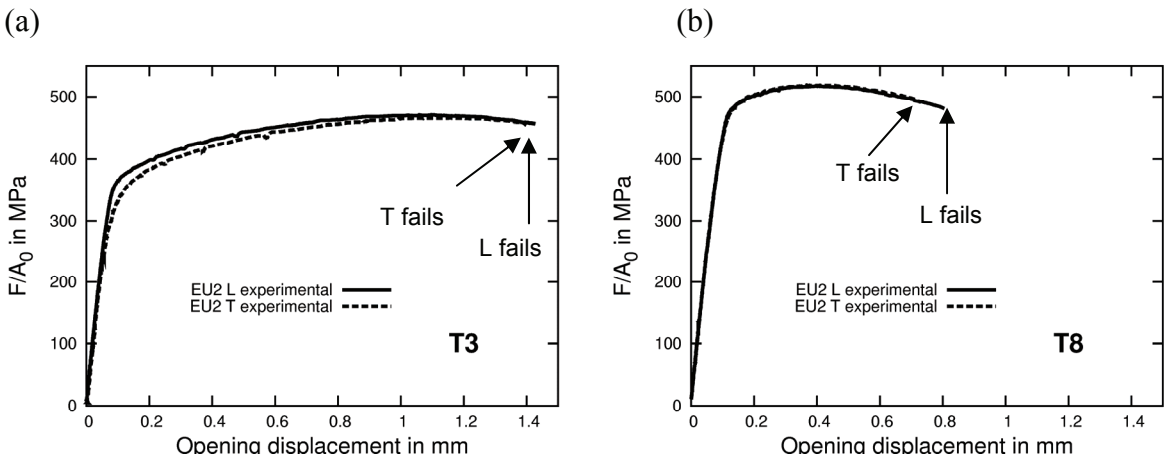

Figure 6.1-4: EU2 (notched specimen) results for L and T testing direction for the AA2139 alloy in: (a) the T3 condition (b) the T8 condition

6.1.3.4 Kahn tear testing

Figure 6.1-5 shows the results of the Kahn tear tests in terms of force F divided by the initial ligament area A_0 as a function of the CMOD along with the crack length as a function of the CMOD for L-T and T-L testing for the T3 and T8 conditions. For the T3 material (Figure 6.1-5(a)) the nominal load is smaller for the T-L testing than for the L-T up to maximum loads from ~100MPa onwards (*i.e.* indicating a lower initiation toughness). The load differences between the T-L and L-T sample are even higher in the propagation region and crack growth is faster in the T-L test orientation than in the L-T. The unit initiation energy (UIE, defined as the integral $\int F/A_0 \, \mathrm{d}l_d$, where $\mathrm{d}l_d$ is the pin displacement, taken from the start of the test to maximum load [29]) for the tests are shown in Table 6.1-4. For the T3 condition the UIE for the T-L sample is ~15% lower than for the L-T sample. For the T8 material (Figure 6.1-5(b)) the nominal load is very similar for both sample orientations up to the maximum load of the T-L sample. However, as the maximum load of the L-T sample is higher and is reached at increased pin displacement, and the UIE is 30% higher for the L-T sample than for the T-L. Nominal stresses in the propagation region are substantially lower for the T-L sample than for the L-T sample and crack growth is faster for the T-L test compared to the L-T.

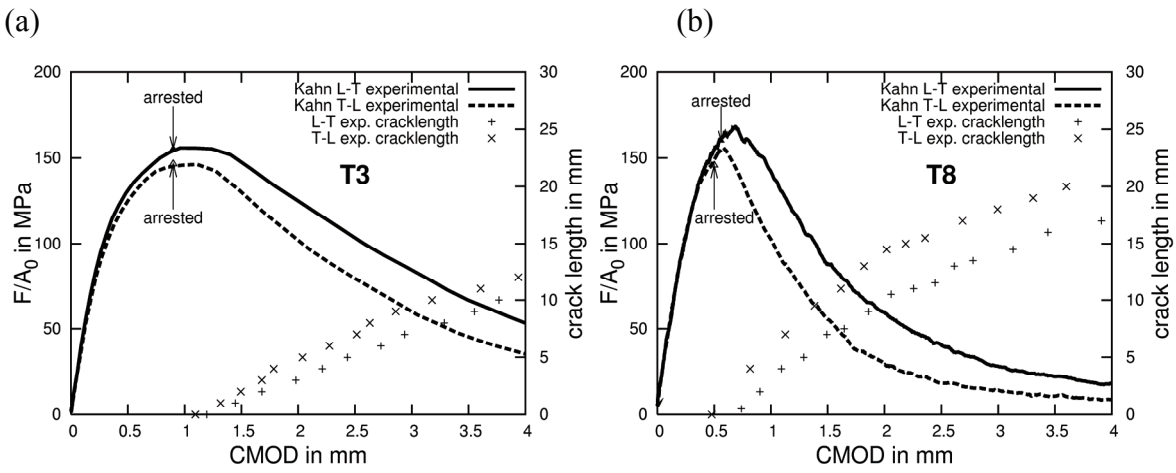

Figure 6.1-5: Kahn tear test results for L-T and T-L testing direction for the AA2139 alloy in (a) in T3 condition (b) in T8 condition and arrows indicating the test stop for tomography analysis samples

	T3	**T8**
L-T	171 N/mm	104 N/mm
T-L	148 N/mm	79 N/mm

Table 6.1-4: Unit initiation energy (UIE) for Kahn tear tests on AA2139 for the loading directions L-T and T-L and T3 and T8 conditions

6.1.3.5 M(T) testing

Figure 6.1-6 shows the results of M(T) tests for (a) the T3 condition (T-L loading only) and (b) the T8 condition and both loading directions. Strong toughness anisotropy can be identified for the T8 material. The maximum load of the L-T sample is ~24% higher than for the T-L sample, which is clearly higher than the corresponding anisotropy measured for the Kahn tear tests (8%, see Figure 6.1-5).

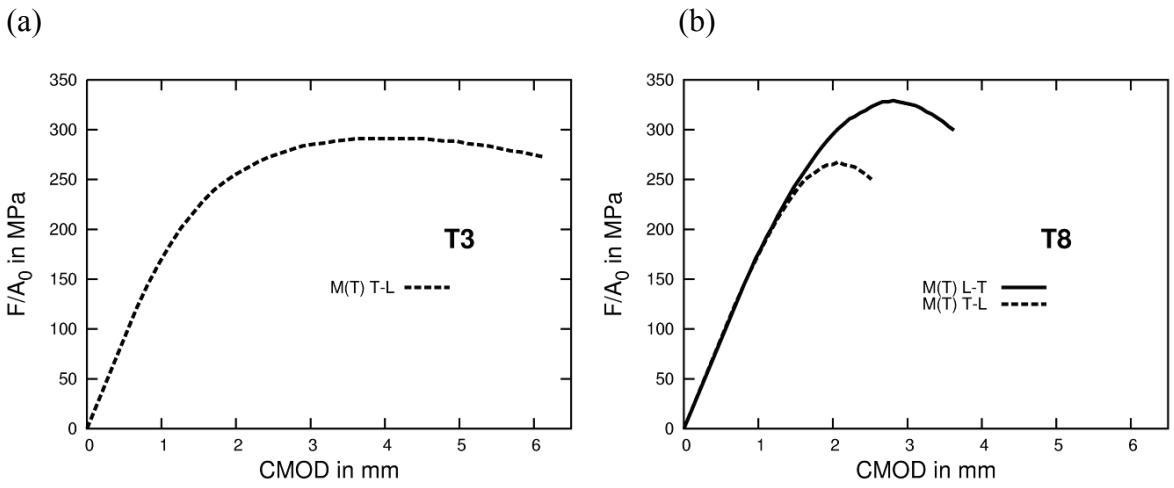

Figure 6.1-6: Results of M(T) tests for the AA2139 alloy in: a) the T3 condition b) the T8 condition

6.1.4 Fractography

6.1.4.1 Fractography of Kahn samples

The fracture of Kahn tear test samples typically starts with a macroscopically flat triangular region oriented normal to the loading direction [30], with the crack subsequently turning into a slanted crack with an angle of ~ 45º with respect to the loading direction, this is then maintained during further crack propagation (also see [30]). In Figure 6.1-7 SEM micrographs of the fracture surface of specimens for the different loading cases and T3 /T8 conditions are particularly shown for the triangular region, at mid-thickness, at 1mm from the notch root. For all cases the fracture surface is covered by dimples that can be associated either with coarse particles or initial porosity. In these images, the voids appear to have mainly coalesced via impingement. The dimples are coarser for the T3 condition than for the T8. For the T-L samples the surface morphology is more obviously directional, with void chains (see dashed boxes) apparent on the fracture surface parallel to the material rolling direction.

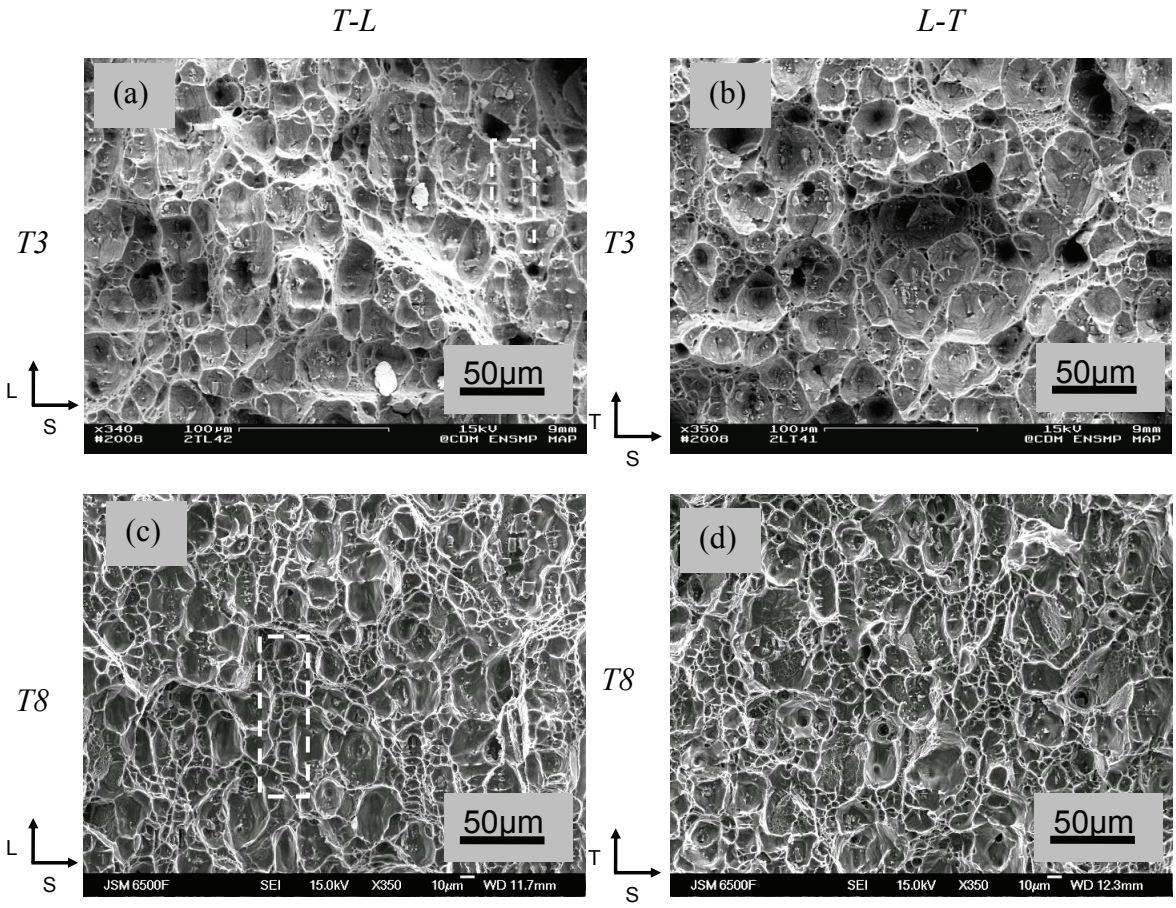

(e)

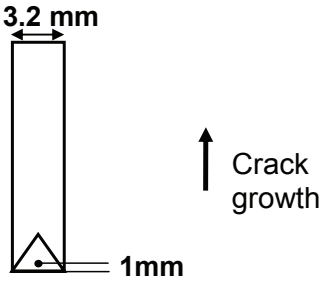

Figure 6.1-7:. SEM micrographs (secondary electron mode) of the fracture surface at mid-thickness 1mm from the notch for the AA2139 alloy of (a) T3 T-L sample, (b) T3 L-T sample, (c) T8 T-L sample, and (d) T8 L-T sample. A schematic illustration of macroscopic fracture surface regions and position of the images is shown in (e)

In the propagation region (the slanted crack growth) fracture at mid-thickness still seems to be dominated by coarse voiding (see Figure 6.1-8 corresponding to 15 mm from the

notch root). However, areas containing fine dimples can also be observed which appear consistent with shear decohesion or also called void sheeting [31]. The features on the fracture surfaces of the T-L and L-T samples appear quite similar but aligned stringers are again more apparent in the T-L sample, and less so in the L-T sample. Voids are again coarser for the material in the T3 condition than in the T8 condition.

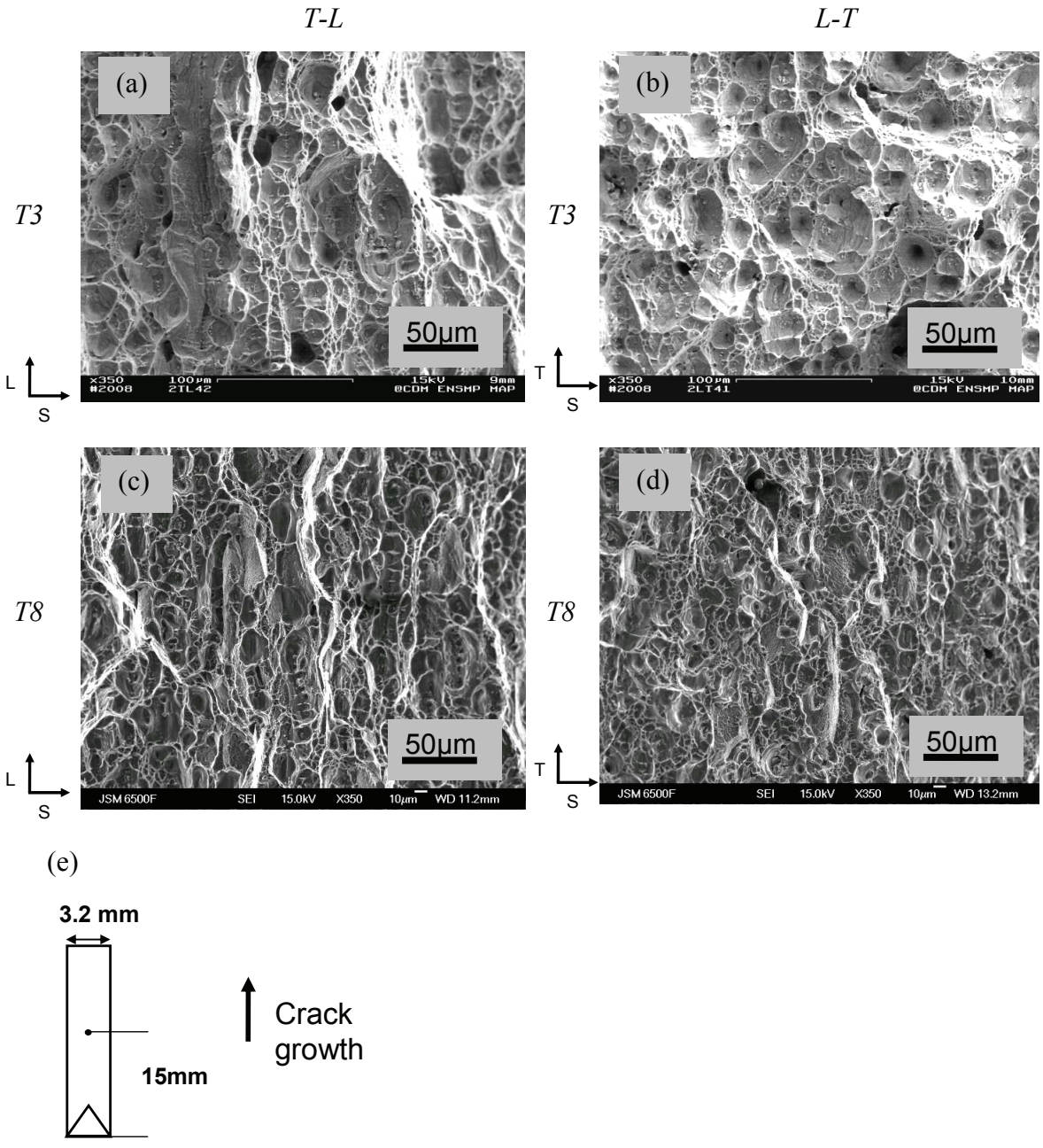

Figure 6.1-8: SEM micrographs (secondary electron mode) of the fracture surface at mid-thickness 15mm from the notch for the AA2139 alloy in (a) T3 T-L sample, (b) T3 L-T sample, (c) T8 T-L sample and (d) T8 L-T sample. A schematic illustration of macroscopic fracture surface regions and position of the images is shown in (e)

At the edge of the specimen, the area coverage of microscopically flat regions is higher than at mid-thickness (see Figure 6.1-9). The fracture surfaces of the EU2 samples (not

presented here) are similarly dominated by shear decohesion features as the Kahn samples close to the sample edge. Fractographic assessment of M(T) sample fracture surfaces has not been carried out here: it has been identified previously that for similar strength Al-alloy sheet, stress states and fracture mechanisms are very similar for Kahn tear test samples and M(T) samples [8].

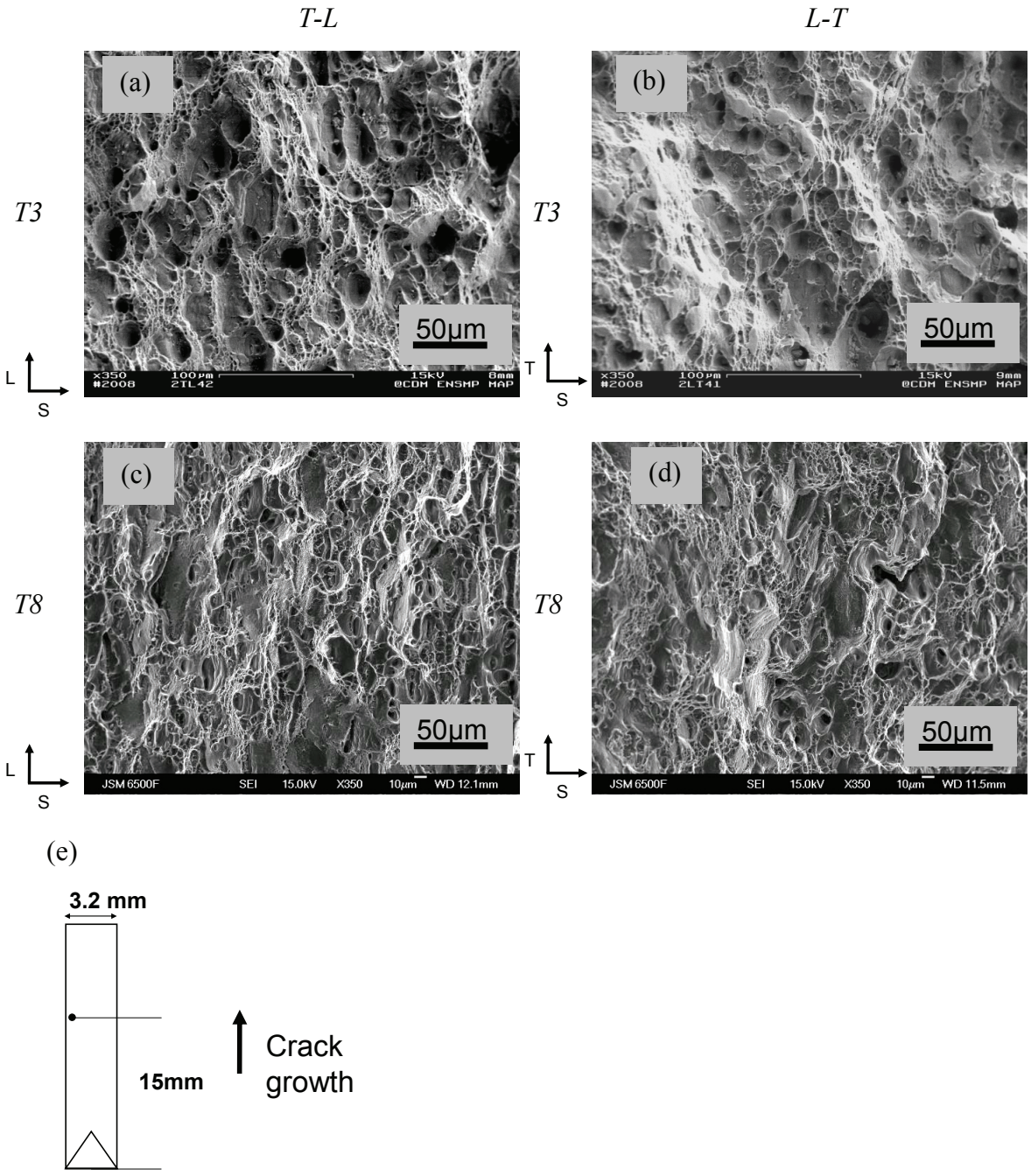

Figure 6.1-9: SEM micrographs (secondary electron mode) of AA2139 the fracture surface at the edge (near the sample free surface) 15mm from the notch of: (a) a T3 T-L sample, (b) a T3 L-T sample and (c) a T8 T-L sample, (d) T8 L-T sample. A schematic illustration of macroscopic fracture surface regions and position of the images is shown in (e)

6.1.4.2 SRCT study of fracture initiation in Kahn tear test samples

Tomography scans of arrested cracks allow observation of the initial stages of failure and the subsequent evolution of the fracture process immediately ahead of the crack tip. In the present study the fracture evolution during crack initiation at high levels of stress triaxiality around the machined notches has been captured in arrested cracks via tomography. Marks on the Kahn test curves in Figure 6.1-5 show the points at which tests have been arrested for SRCT study, Tests have been interrupted at or before reaching maximum load, which allows investigation of the damage evolution in the macroscopically flat triangular region.

Figure 6.1-10 shows a local crack opening map of those cracks for the different loading directions and heat treatments, as obtained via the sum along ray method. Even though the CMOD at which testing was interrupted in the T3 T-L sample was similar to the others investigated, the T3 L-T sample did not contain a crack (discussed further below). The opening with respect to the loading direction can be seen for each location of the crack (it should be noted that the lower image edges are not the root of the machined notch but the limits of the scanned volumes). The triangular shape of the cracks can clearly be seen. The cracks in the T8 condition have a smaller opening angle, *i.e.* are "sharper", than the cracks in the T3 T-L sample. It is also evident that the voids in the T3 T-L crack have a larger diameter and are more open than in the T8 samples, *i.e.* have grown more. This observation is consistent with the SEM fractography results (see Figure 6.1-7). In all cases there are voids reaching out ahead of the main body of the crack that are often linked to the main crack through narrow (in terms of opening) coalescence regions. These narrow coalescence regions may result from nucleation of voids at a 2^{nd} population of small 2^{nd} phase particles [30]. An especially long void chain reaching ahead the main crack can be seen for the T8 T-L image (see dashed box). Narrow coalescence regions can clearly be distinguished from coarse voids in all of the images. Even at this stage of fracture, which is governed by high stress triaxiality that is expected to favour void growth and subsequent coalescence via void impingement [30], clear evidence of coalescence through narrow flat regions is provided in Figure 6.1-10 at the respective crack fronts. Comparison of Figure 6.1-10(c) with (d) shows that the T8 T-L sample is more open in general than the T8 L-T sample, especially at the very crack front there are large areas of limited/narrow opening that link coarse voids. The crack is still macroscopically flat in this region.

Comparison of Figure 6.1-10(c) with (d) further shows that coarse voids are larger and more aligned/elongated in crack growth direction in the T8 T-L sample than in the T8 L-T sample, which is consistent with the observation made in T8 T-L and L-T samples of the same material in the propagation region [26, Chapter 5 in this thesis]. This results in shorter intervoid ligament distances between for the T-L T8 sample than for the T8 L-T sample.

Differently from the previously discussed figures, Figure 6.1-10(b) shows the distribution of voids in the T3 L-T sample that have grown ahead of the machined notch in a 420 µm thick volume. It is interesting to note that at nearly identical CMOD in the T-L sample a crack had formed but not for the L-T case: this is an additional form of anisotropy, one that is not observable in load-CMOD curves. Additionally it is interesting to compare void sizes with respect to their extension in the crack growth direction: at similar CMOD the voids contained in the crack of the T-L sample are typically extended by ~70 µm in the crack growth direction and 30-40 µm in the through-thickness direction, whilst the biggest single voids in the L-T sample are only extended by 30-40 µm in the crack growth direction and about 20-30 µm in the through-thickness direction. However, it is difficult to identify from the observed void dimensions if voids are close to coalescence or not, as coalescence may occur abruptly (this sudden void impingement can also be found in void cell calculations where coalescence occurs abruptly at a critical void volume fraction [32]).

Figure 6.1-11 shows height maps of the 3 cracks. It shows the position of the mid-crack plane with respect to the loading direction (normal to the image). In other words it can be seen if the crack is flat or rough. It can be seen that the mid-crack plane varies over about 300 µm for the 3 cracks. Abrupt jumps of 100-200 µm are discernable in the cracks. The different crack heights are seen to be linked via narrow regions that lie in the sheet plane, see below. In the first instance they are thought to lie on grain boundaries as has been identified for an AA6156 alloy [33], but this has not been explicitly confirmed.

Figure 6.1-12 shows 2D sections normal to the crack propagation direction of cracked and uncracked scanned volumes. The locations where the sections are taken from are indicated with lines on the respective figures in Figure 6.1-10 and Figure 6.1-11. In Figure 6.1-12(a), section 1 a 2D section in the T3 T-L sample ~400 µm from the crack tip is shown. The figure clearly shows large voids that have coalesced via impingement and the

height changes of the crack are also visible. Narrow crack regions are present in the sheet plane. Section 2 of Figure 6.1-12(a) shows a section at ~150 µm from the crack tip. At this location, the opening is smaller than in Section 1. These images reveal impinged voids as well as narrow crack regions normal to the loading direction, whereas SEM fractography of the regions was apparently dominated by large dimples (see Figure 6.1-7). However, the crack front of the observed arrested cracks may be further away from the notch root than the location observed via SEM.

Figure 6.1-12 (b), section 1, shows the voids grown in the previously loaded but uncracked T3 L-T sample ahead of the machined notch. Void growth is localised in a band ~400 µm wide ahead of the machined notch tip (see dashed lines). Voids that have impinged in the "future" crack plane direction can be seen, but coalescence has also occurred in columns parallel to the sheet plane. The distances between the voids seen in this section that have not coalesced yet are typically in the order of 100 µm.

The crack in the T8 T-L sample seen in section 1 of Figure 6.1-12(c) at ~550 µm from the crack tip is less open than the T3 T-L crack. Void impingement has occurred and at the left of the image, large narrow shear decohesion regions can be seen which may be the start of slant fracture. Section 2 of Figure 6.1-12 (c) shows the T8 T-L failure at ~200 µm from the crack tip where, as in the T3 material, narrow crack regions linking coarse voids at different levels have formed in the plane of the sheet.

Figure 6.1-12 (d), section 1, shows the T8 L-T crack at ~700 µm from the crack tip. Void impingement in columns and shear decohesion that may be the start of slant fracture are discernable. Section 2 of Figure 6.1-12 (d) shows the crack at ~300 µm from the notch tip: at the right part of the crack a narrow region links two coarse voids.

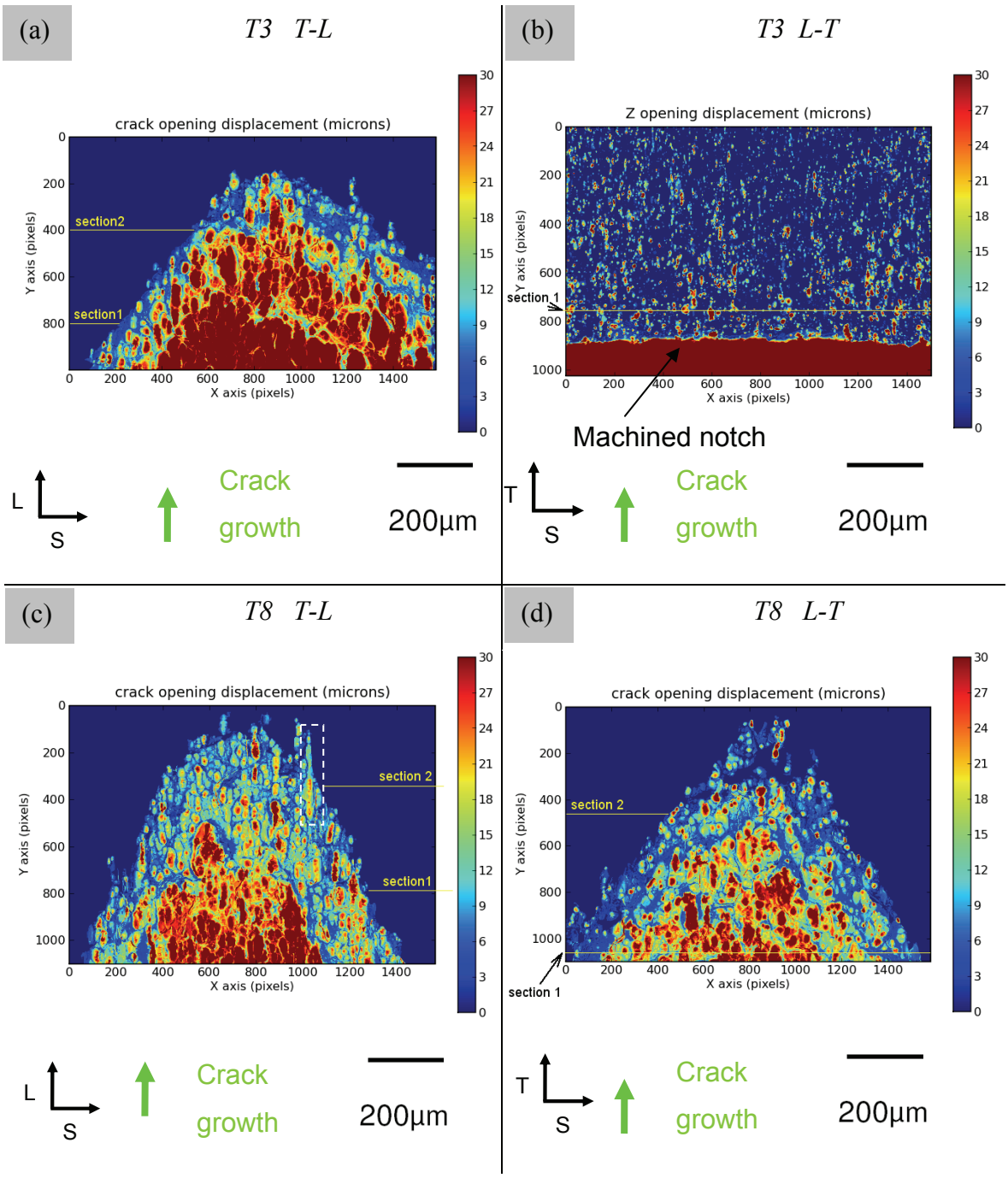

Figure 6.1-10: Representation of the cack tip opening in AA2139 via a "sum along ray method" for: (a) T-L loading in the T3 condition (b) L-T loading in the T3 condition (c) T-L loading in the T8 condition (d) L-T loading in the T8 condition; Note that in (b) the opening of all encountered voids in a volume of a thickness of 420 µm is shown: no crack had been formed yet. Section lines indicate the location of the 2D sections in Figure 6.1-12.

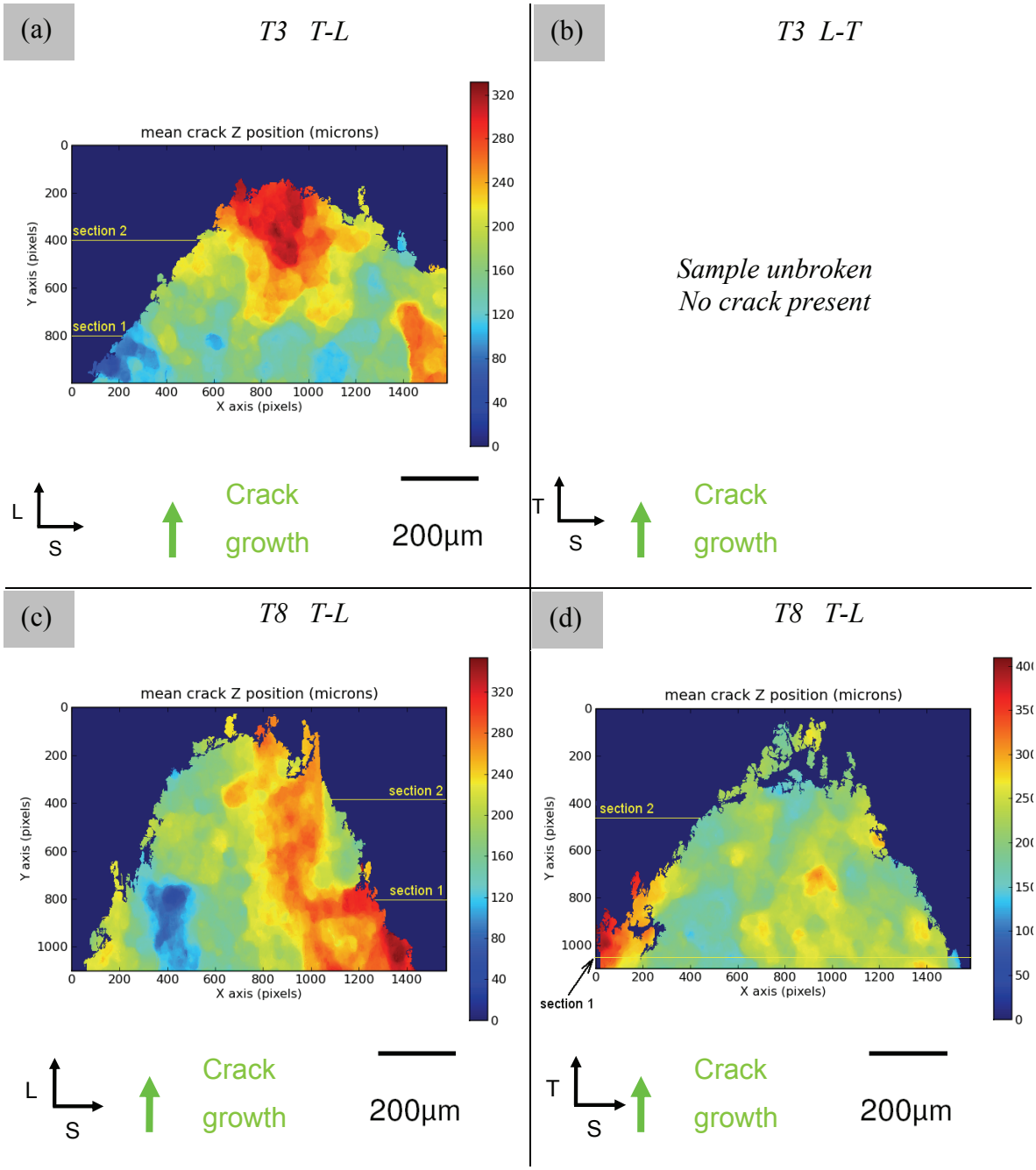

Figure 6.1-11: Representation of a crack mid-plane height map from SRCT data for the AA2139 alloy for: (a) T-L loading in T3 condition (c) T-L loading in T8 condition (d) L-T loading in T8 condition; section lines indicate the location of the 2D sections of Figure 6.1-12. For ease of visual consistency and ease of comparison with other diagrams, part (b) notionally represents the T3/L-T test, although no crack was seen in this case.

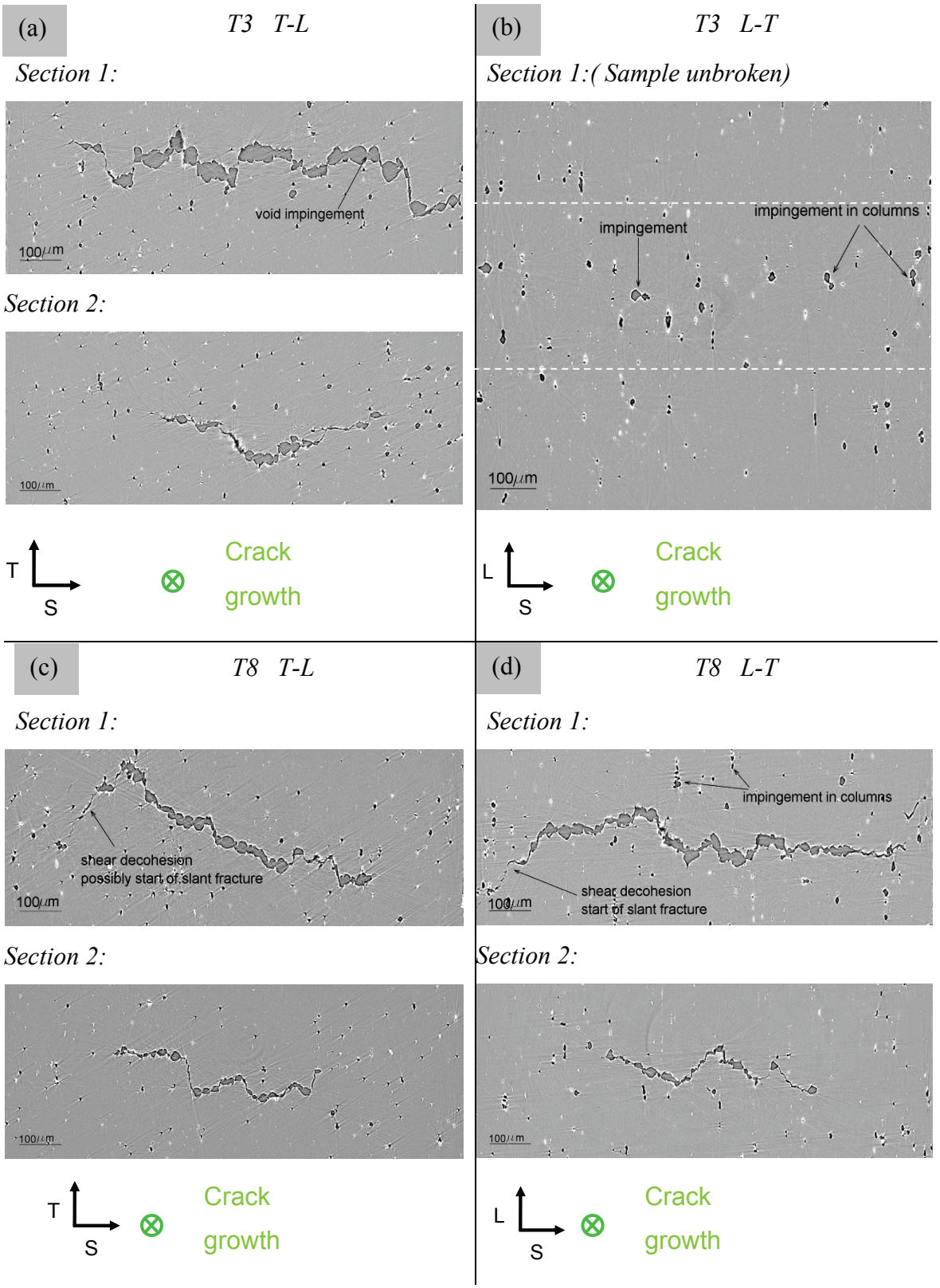

Figure 6.1-12: 2D sections of the SRCT data normal to the crack growth direction for the AA2139 alloy for: (a) T3 T-L sample, (b) T3 L-T sample, (c) T8 T-L sample, (d) T8 L-T sample. Locations where the sections are taken from are indicated with lines on Figure 6.1-10 and Figure 6.1-11

6.1.5 Discussion

6.1.5.1 Plastic behaviour

For the T3 material, tensile testing and EU2 testing both show anisotropy in the plastic deformation behaviour. The loads are higher for the L sample than for the T sample for the T3 condition indicating that there is some effect of prestraining/kinematic hardening for this material. This effect is also evident in the Kahn tear tests for the curves up to maximum load. Kinematic hardening can however only explain load differences for strains up to about 5% [34]. For the T8 material, tensile and EU2 testing show nearly no plastic anisotropy. Thus, the ageing treatment seems to have substantially decreased the effect of prestraining for the T8 material. A similar effect has been found in [35] for a 7000 series alloy: At peak age the yield stress anisotropy as an effect of prestrain had almost disappeared. Several reasons may be at the origin of anisotropy evolution during ageing such as for example the formation of precipitates with a preferred orientation but it was identified that the processes leading to these effects may be very complicated and cannot be accounted for by any one theory [35].

The curves for tensile testing indicate some load differences in ultimate tensile strength for the T3 material which indicates that there is some weak plastic anisotropy in this material which cannot be explained by the effect of prestraining. The T8 material can be considered to be plastically isotropic.

6.1.5.2 Damage mechanisms

The evolution of damage and fracture is not only influenced by microstructural features like shape and distribution of imperfections but also by continuum mechanics variables such as the stress state and in particular stress triaxiality. It has been identified that during the formation of the flat triangular region near to the notch root stress triaxiality is higher than when the crack propagates [30,36,37]. In the propagation region cracks tend to be slanted for ductile thin sheet material (such as for the material studied here). In this propagation region a plane strain state may be found with respect to the crack propagation direction [8] (although this form of crack growth is commonly identified with plane stress

conditions within the literature). High stress triaxiality has been identified to favour void growth [38].

6.1.5.3 Effect of heat treatment on toughness

Kahn tear toughness in terms of UIE is reduced by ~40% for the T8 material compared to the T3 material. The toughness anisotropy is more pronounced for the T8 than for the T3 material: *viz*. a 30% difference for the T8 material compared to 15% for the T3 material. The T8 material displays a less pronounced hardening capacity than the T3 material. The lower hardening capacity is known to lead to a faster void growth [39]. Voids are seen to have grown more at coalescence in the T3 material than in the T8 material. Localisation is known to occur at lower strains for materials exhibiting low hardening capacity than for material displaying higher hardening capacity. A competition of plastic hardening and damage softening is found in these situations [40]: increased stresses tend to increase plastic energy dissipation whereas strain localisation and in particular the formation of slanted shear bands, tend to reduce macroscopic strain to failure and consequently dissipation.

6.1.5.4 Toughness anisotropy

The toughness anisotropy of the T3 material can not be explained by the effect of kinematic hardening or plastic anisotropy as these effects are relatively weak. Kinematic hardening is only effective up to fairly low deformation levels (about 5%), whereas crack tip strains are much higher. This conclusion is corroborated by results on T8 material for which fracture anisotropy is observed even though neither kinematic hardening nor plastic anisotropy is evidenced.

The as-received material exhibits anisotropic pore shapes with an elongation in rolling direction (L). Voronoi cell calculations of cells around 2nd phase particles and pores did not show an anisotropic distribution of defects. However, stringers of aligned particles can be seen on 2D sections of the as-received material. On the crack surface of the T-L cracks in the initiation region voids are elongated in the propagation (L) direction leading to smaller separation distances than for the L-T loading (see Figure 6.1-10). For the L-T cracks and the unbroken volume, the formation of void columns in loading direction (L) can be seen (Figure 6.1-12(b)). For the T3 material it is especially interesting to see that for tests interrupted at a similar CMOD for the T-L and L-T orientation, the L-T sample

had not yet fractured. Crack propagation in the T3 L-T sample may be retarded by the larger separation distances between the coarse voids.

These findings are consistent with the investigations of fracture in the propagation region for the two loading directions in the T8 material [26, Chapter 5 in this thesis]. The present study shows that prolate voids (as opposed to oblate voids) correlate with higher toughness, which is, at least in a qualitative sense, consistent with a numerical study by Pardoen and Hutchinson [21], which compared the influence of void shape on fracture. At this point, it is particularly interesting to question if void shape anisotropy is likely to be the only reason for toughness anisotropy, as discussed in earlier work [26, Chapter 5 in this thesis]. Fractography via SEM has shown that the crack is mainly made up of coarse voids in the flat initiation region whilst, in the propagation region, there are additionally regions of shear decohesion for the T3 and T8 material. Shear decohesion is recognised to be linked to void nucleation at a 2^{nd} population of small 2^{nd} phase particles. The SEM observations as well as micro-tomography results clearly show the alignment of coarse voids and void chains that are present in the cracks within the T-L samples for T3 and T8 material that are less prevalent for the L-T sample. An alignment of pores/particles has however not been detected via Voronoi cell calculations around coarse 2^{nd} phase particles and pores. This may be linked to the heterogeneous distribution of the pores and particles that may compensate the effect of the presence of stringers on the average cell sizes. From the SEM observations alone one is inclined to deduce that during crack initiation in the flat fracture region, voids have mainly linked through void impingement especially in the T3 material. This observation would be consistent with the notion that at high levels of stress triaxiality voids will substantially grow (especially as the T3 material has a high hardening capacity) and subsequently link through void impingement. However, the novel SRCT observations of the T3 T-L specimen show that already in the stage of void growth at high stress triaxiality coalescence through narrow crack regions and nucleation at very small 2^{nd} phase particles apparently plays a significant role in the fracture process. This implies that toughness anisotropy may depend to a certain degree on the mechanisms of nucleation linked to shape and/or the spatial distribution of small 2^{nd} phase particles. Step features of the crack are revealed via height maps (see Figure 6.1-11) and 2D sections (see Figure 6.1-12) indicate that coalescence also occurs between voids that are distributed at different heights. It would even be possible that fracture occurs at grain boundaries oriented in loading direction such as observed in [33].

6.1.6 Conclusions

- Mechanical tests on smooth and notched specimen have been carried out in 2 loading directions for T351 and T8 heat treated material.

- For the T3 material the curve shapes for tensile testing and EU2 testing are slightly different for loading in the L and T directions with higher loads being observed in the L case. This difference is also reflected in the Kahn tear test for the load-displacement curves up to maximum load. The loads are higher for the L samples than for the T samples. This effect is believed to be mostly due to the prestraining/ kinematic hardening. The T8 material is less ductile than the T3 material and does not show this effect. The subsequent ageing treatment of the T8 material seems to have decreased the effect of prestraining. The T8 material can be considered as plastically isotropic.

- Some weak plastic anisotropy, that cannot be explained by the effect of prestraining, can be discerned for the T3 material as the ultimate tensile strength is slightly different. The T8 material can be considered as plastically isotropic.

- Kahn tear tests and M(T) tests show substantial toughness differences for the 2 different testing directions: The L-T samples are tougher than the T-L samples. Furthermore, the material in T3 condition is tougher than that in the T8.

- SEM fractography on Kahn tear test samples shows that void growth and shear decohesion are the dominant fracture mechanisms. Alignment of secondary phase stringers and corresponding voids in the crack propagation region is particularly visible for T-L samples.

- Novel SRCT observation of arrested cracks at high stress triaxiality close to the notch root have been carried out for the two testing orientations and heat treatment conditions. The T3 L-T sample does not contain a crack even though the CMOD at test interruption was similar to the T3 T-L sample. Void impingement in the crack plane as well as in columns in loading direction has been observed for the unbroken sample. It could be identified that voids associated with failure are still elongated in the L direction for T-L loading for the T3 and T8 material, maintaining their original

anisotropy. Inter-void ligaments are shorter for T-L samples than for L-T samples for the T8 material.

- SRCT results indicate that at the fracture initiation stage (at high levels of stress triaxiality), void coalescence at the very crack tip of the observed cracks does not only occur by impingement, but involves regions of inclined narrow opening, consistent nucleation of voids on small 2nd phase particles. Some void linking is also seen via narrow steps oriented in loading direction, which is morphologically consistent with the incidence of grain boundary failure (see [33, Chapter 4 in this thesis]).

- As discussed in previous work ([26, Chapter 5 in this thesis]), the toughness anisotropy may be linked to anisotropy of the original void shapes, although it is evident that detailed understanding of failure is likely to require a proper assessment of shear coalescence.

- The present findings indicate that a model aiming at describing and interpreting fracture toughness anisotropy needs to account for the following observed material characteristics:

    i. Plastic behaviour including kinematic/isotropic hardening and plastic anisotropy,

    ii. Anisotropic initial void shape and growth and

    iii. (Potentially anisotropic) void nucleation at a 2nd population of small 2nd phase particles leading to coalescence through narrow crack regions

Acknowledgements

The authors would like to acknowledge Alcan CRV for financial support and material supply, Frédéric Bron and Bernard Bès for technical discussion Jean-Yves Buffière for support in SRCT imaging and the assistance of Elodie Boller in the use of the beamline at the ESRF.

6.1.7 References

[1] Cho A, Bes B. Mater Sci Forum 2006;519-521:603-608
[2] Warner T. Mater Sci Forum 2006;519-520:1272-1278
[3] ASTM-international, Standard B 871 - 01. 2001.
[4] ASTM-international, Standard E 561 - 98. 1999
[5] Grange M, Besson J, Andrieu E. Int. Int J Fract. 2000;105:273-293
[6] Rivalin F, Besson, J, Di Fant M, Pineau A.Engng Fract Mech 2000;68:347-364
[7]Brunet M, Morestin F, J. Mater. Processing Technol. 2001 ;112 :214-226
[8]Bron, F., Besson, J., Engng Fract. Mech. 2006;73:1531-1552.
[9] Tanguy B, Luu TT, Perrin G, Pineau A, Besson J. (2008) Int J Press Vessels Pip, in Press
[10] Benzerga A, Besson J, Pineau A. J. Engng Mater. Technol. 1999;121: 121-229
[11] Benzerga AA, Besson J, Pineau A, Acta Mater 2004;52: 4623-4638
[12] Mir AA, Barton DC, Andrews TD, Church P. Int J Fract 2005;133:289-302
[13] Lassance, D.; Fabregue, D.; Delannay, F.; Pardoen, T. Prog Mater Sci. 2007;52:62-129
[14] Gologanu M, Leblond, JB, Devaux J. J Mech Phys of Solids, 1993;41:1723-1754.
[15] Gologanu M, Leblond, JB, Devaux, J. Trans ASME J Eng Mater Technol, 1994 ;116:290-297.
[16] Pardoen T, Hutchinson JW, J Mech Phys Solids. 2000;48:2467-2512
[17] Benzerga AA, Besson J, Pineau A, Acta Mater 2004;52: 4639-4650
[18] Thomason PF. Acta Metal 1985;33:1087-1095
[19] Thomason PF. Acta Metal 1985;33:1079-1085
[20] Gologanu, M. Leblond, J.B. Perrin, G. and Devaux, J. Int. J. Solids Structures 2001 ;38 :, 5581-5594
[21] Pardoen T, Hutchinson JW. Acta Met 2003;51:133-148
[22] Enami K, Engng Fract. Mech. 2005;72:1089-1105
[23] Enami K, J. Mat Sci. Technol., 2005 ;10 :10-41
[24] Bao Y, Treitler R. Mater Sci Engng A. 2004;384:385-394
[25]Maire E, Buffiere J-Y, Salvo L, Blandin JJ, Ludwig W, Letang J M. Adv Eng Mat, 2001, 3:539-546
[26] Morgeneyer TF, Starink MJ, Sinclair I, Acta Mater, 2008;56: 1671-1679
[27] Toda H, Sinclair I, Buffière J-Y *et al*. Philos Mag 2003;83:2429-2440
[28] Yang N., Boselli J., Sinclair, I. J. Microsc. 2001;201: 189-200
[29] Dumont D, Deschamps A, Brechet Y. Mater Sci Eng A 2003 ; A 356 :326-36
[30] Bron F, Besson J, Pineau A. Mater. Sci Eng A 2004;A 380:356-364
[31] Garrison Jr, W. M., Moody,N. R. J. Phys. Chem. Solids 1987;48:1035-1074
[32] Zhang ZL, Thaulow C, Odegard J. Engng Fract. Mech, 2000;6:155-168.
[33] Morgeneyer TF, Starink MJ, Wang SC, Sinclair I, Acta Mater, article in press doi:10.1016/j.actamat.2008.02.021
[34]Lemaitre J, Chaboche JL. Mechanics of Solid Materials, 1990, Cambridge University Press, Cambridge, U.K.
[35] Poole WJ, Shercliff HR. Mater Sci Forum 1996;217-222:1287-1292
[36] Mahgoub E, Deng X, Sutton MA. Engng Fract. Mech. 2003; 70: 2527-2542

[37] Lan W, Deng X, Sutton MA, Cheng CS, Int J Fract. 2006;141:469-496
[38]Rice J, Tracey D. J Mech Phys Sol, 1969;17: 201-217.
[39] Faleskog J, Gao X, Shih C. Int J Fract 1998;89: 355-373.
[40]Rice JR. The localisation of plastic deformation. In: Koiter WT, Editor, Proc. 14th Int. Conf. Theoretical and Applied Mechanics, Delft, North-Holland, Amsterdam 1976:207-220

6.2 Analysis of toughness anisotropy in AA2139 Al-alloy sheet; part II: model and simulations

Abstract

A model based in part on the Gurson-Tvergaard-Needleman model is constructed to describe and predict deformation behaviour, crack propagation and, in particular, toughness anisotropy in an Al alloy for aerospace application. It incorporates (i) anisotropic initial void shape and growth (ii) plastic behaviour including: isotropic/kinematic hardening and plastic anisotropy and (iii) nucleation at a 2^{nd} population of 2^{nd} phase particles leading to void sheeting; to the best of our knowledge it is the first model to include these three components. Model parameters are fitted using microstructural data and data on deformation and crack propagation for a range of small test samples. The model transferability has been shown by simulating tests of large M(T) samples showing strong fracture toughness anisotropy. A parametric study shows that nucleation of small voids at different strains for different loading directions is crucial for a correct model of toughness anisotropy; the combined effects of kinematic hardening and void growth anisotropy can not fully describe fracture toughness anisotropy

6.2.1 Introduction

Anisotropic mechanical properties are common in plastically deformed or thermomechanically processed metallic materials, e.g. in rolled sheet. One particularly important issue in design is toughness anisotropy of these materials. Furthermore, the transferability of toughness trends between small test pieces and larger structures is an important aspect in optimising materials performance in practice. Thus, a validated model linking the microstructure and fracture micromechanics to full scale component behaviour (*e.g.* full scale toughness) will be of great value in optimising materials performance and in providing predictions of full scale component behaviour.

Anisotropic plastic behaviour has been the subject of many studies and models have been proposed at both the microscopic level using a polycrystalline description for the material (see *e.g.* [1]) and at the macroscopic level (see *e.g.* [2]). Studies dealing with anisotropic rupture properties are less numerous although there are many examples for cases where the fracture resistance of structures made of sheet materials must be qualified, for instance steel pipelines, aluminium alloys for aircraft fuselage, zirconium alloys for nuclear fuel cladding. Several causes may be at the origin of anisotropic rupture properties:

(i) anisotropic plastic properties, usually related to the development of specific crystallographic textures, lead to different mechanical responses in different directions so that the plastic energy dissipated during fracture may be anisotropic [3,4]. In addition, local crack tip stresses and strains may be affected by plasticity and in particular by the shape of the yield function. Depending on the loading direction, local parameters controlling damage growth (such as stress triaxiality ratio) may depend on the loading direction [5].

(ii) processing conditions (*e.g.* hot rolling) may create initially anisotropic defects such as elongated voids and/or inclusions and anisotropic defect distribution which will lead to anisotropic fracture properties as experimentally shown in [6,7,8,9,10 Chapter 5 in this thesis],

(iii) Sheet materials are often prestrained so that they can exhibit anisotropic properties due to kinematic hardening. Recent experimental results have shown that prestrain can affect ductility [11].

Several models incorporating the above mentioned possible mechanisms for fracture anisotropy have been proposed in the literature. Models are either based on the micromechanical Gurson model [12] and its "standard" extension proposed by Tvergaard and Needleman (so called GTN model) [13] or the phenomenological Lemaitre model [14,15]. In the present study, extensions based on the GTN model will be used. Introducing plastic anisotropy can be easily done by replacing the von Mises stress in the expression of yield surface given by the GTN model by any anisotropic stress measure. The Hill [16] equivalent stress approach was first used as in [3,17,18] but more advanced recently proposed macroscopic models [2,19, 20] can also be used as shown in [21,4]. Models accounting for initial void shape and void shape evolution have been developed for prolate and oblate voids by Gologanu and co-workers [22,23]. The model was further extended to account for void coalescence [8,24,25,26] based on the initial developments of Thomason [27]. These works have shown that ductility and toughness are increased in the case of elongated cavities with the principal loading direction corresponding to the axis of symmetry due to both the cavity shape which slows down void growth and the increased inter-void ligament which delayed void coalescence. The opposite effect is obtained for flat cavities. The model has however a main limitation: cavities are assumed to be and remain axisymmetric so that the model must be adapted in case of non-axisymmetric mechanical loadings (in practice as soon as the model must be used in a finite element code) [28]. The model was coupled with Hill anisotropy in [28] to study ductility of an X52 pipeline steel. Models based on the GTN approach that simultaneously account for ductile damage and kinematic hardening have been proposed in the literature but hardly verified or tested in comparisons with actual experiments [29,30,31]. Up to now, these models have not been coupled either with plastic anisotropy nor with void shape effects. These models account for void growth leading to final failure by internal necking [27] but do not account for coalescence by void sheeting [32]. This phenomenon can however be observed in thin sheet materials [33, Section 6.1 in this thesis, 34] and should be accounted for.

In this work, a new model that incorporates (i) anisotropic initial void shape and growth (ii) plastic behaviour including: isotropic/kinematic hardening and plastic anisotropy and (iii) nucleation at a 2nd population of 2nd phase particles leading to coalescence is suggested (Section 6.2.2). These material features have been identified in an experimental study of an AA2139 aluminium alloy for aerospace application in naturally aged (T3) and artificially aged condition (T8) presented in the companion paper [33, Section 6.1 in this thesis]. The model combines ductile damage with kinematic hardening [31] and with plastic anisotropy [21]. Effect of void shape is accounted for using a novel simplified description which has the advantage of not being restricted to axisymmetric cases. The model proposes for the first time a complete framework for the description of ductile rupture in sheet metals. In Section 6.2.3, the model parameters are determined using the experimentally obtained microstructural parameters and through fitting on deformation and crack propagation data for a range of small samples; this data was presented in the accompanying article [33, Section 6.1 in this thesis]. The model incorporates simple representations of coalescence by internal necking and void sheeting. The model is validated by comparing simulated and experimental load-displacement curves obtained on large M(T) panels [35]. An identification procedure using both experimental results and unit cell calculations [36] is proposed. The model is then used (Section 6.2.4) in a parametric study to evaluate, in the case of the AA2139 aluminium alloy of this study, the role of the different parameters on toughness anisotropy.

6.2.2 Model

6.2.2.1 Constitutive equations for the undamaged materials

The constitutive model for the undamaged material is based on an additive decomposition of the elastic and plastic strain rates so that:

$$\underline{\dot{\varepsilon}} = \underline{\dot{\varepsilon}}_e + \underline{\dot{\varepsilon}}_p \qquad \textbf{(6.2-1)}$$

where $\underline{\dot{\varepsilon}}$ is the strain rate tensor and $\underline{\dot{\varepsilon}}_e$ and $\underline{\dot{\varepsilon}}_p$ are the elastic and plastic strain rate tensors respectively. The Cauchy stress, $\underline{\sigma}$, is computed from the elastic strain tensor using Hooke's law as:

$$\underline{\sigma} = \underline{\underline{E}} : \underline{\varepsilon}_e \qquad \textbf{(6.2-2)}$$

where $\underline{\underline{E}}$ is the fourth order stiffness tensor.

Constitutive equations describing the plastic behavior of the materials must include both isotropic and kinematic hardening together with plastic anisotropy. The model, which follows the formulation proposed by Lemaitre and Chaboche [37], is outlined as follows. Kinematic hardening is represented by an internal back stress tensor $\underline{X}$. The yield surface is expressed as a function of $\underline{B}$ where $\underline{B} = \underline{\sigma} - \underline{X}$. Plastic anisotropy is described using the model proposed in [38,2]. The model was initially developed without kinematic hardening and it is therefore extended to account for this effect. An effective stress B_E is defined as:

$$B_E = \left(\frac{1}{2} \left(\left| \tilde{B}_2 - \tilde{B}_3 \right|^b + \left| \tilde{B}_3 - \tilde{B}_1 \right|^b + \left| \tilde{B}_1 - \tilde{B}_2 \right|^b \right) \right)^{\frac{1}{b}} \qquad \textbf{(6.2-3)}$$

Where $\tilde{B}_1 \geq \tilde{B}_2 \geq \tilde{B}_3$ are the eigenvalues of a modified stress deviator:

$$\underline{\tilde{B}} = \underline{\underline{L}} : \left(\underline{\sigma} - \underline{X} \right) \qquad \textbf{(6.2-4)}$$

where the fourth order tensor $\underline{\underline{L}}$ is expressed as:

$$\underline{\underline{L}} = \begin{pmatrix} \left(c^2 + c^3\right)/3 & -c^3/3 & -c^2/3 & 0 & 0 & 0 \\ -c^3/3 & \left(c^3 + c^1\right)/3 & -c^1/3 & 0 & 0 & 0 \\ -c^2/3 & -c^1/3 & \left(c^1 + c^2\right)/3 & 0 & 0 & 0 \\ 0 & 0 & 0 & c^4 & 0 & 0 \\ 0 & 0 & 0 & 0 & c^5 & 0 \\ 0 & 0 & 0 & 0 & 0 & c^6 \end{pmatrix} \qquad \textbf{(6.2-5)}$$

$c^{i=1\ldots6}$ are material coeffcients representing plastic anisotropy. Coefficient *b* represents the shape of the yield function. An isotropic material corresponds to $c^{i=1\ldots6} = 1$. The usual von Mises yield criterion is then obtained for *b* = 2 or 4. Tresca yield criterion corresponds to *b* = 1 or *b* = +∞.

The yield function is then expressed as:

$$\Phi = B_E - R(p) \qquad \textbf{(6.2-6)}$$

where the function $R(p)$ represents isotropic hardening. Then the normality rule is applied so that the plastic strain rate tensor is given by:

$$\underline{\dot{\varepsilon}}_p = \dot{p}\frac{\partial \Phi}{\partial \underline{\sigma}} = \dot{p}\frac{\partial B_E}{\partial \underline{\sigma}} = \dot{p}\underline{n} \qquad \textbf{(6.2-7)}$$

The evolution of p is given by the consistency equation $\Phi = 0$, $\dot{\Phi} = 0$. The evolution of the kinematic hardening variable is assumed to obey a nonlinear rule; it is described by a second order tensor state variable, $\underline{\alpha}$, whose evolution is given by:

$$\underline{\dot{\alpha}} = \underline{\dot{\varepsilon}}_p - \frac{3}{2}\frac{D}{C}\dot{p}\,\underline{X} = \dot{p}(\underline{n} - \frac{3}{2}\frac{D}{C}\underline{X}) \qquad \textbf{(6.2-8)}$$

D and C are two material parameters. Finally, the back stress $\underline{X}$ is related to $\underline{\alpha}$ by:

$$\underline{X} = \frac{2}{3}C\underline{\alpha} \qquad \textbf{(6.2-9)}$$

A more general form could be used in the case of anisotropic materials using fourth order tensors for D and C [39,40].

6.2.2.2 Constitutive equations including damage growth

The model described above must be extended to account for ductile damage while preserving the description of plastic anisotropy and kinematic hardening. The proposed extension is based on the Gurson-Tvergaard-Needleman (GTN) model [13,41]. The GTN model was extended to include Hill anisotropy [3, 42] and, more recently, to account for above described plastic anisotropy [21]. Several extensions of the GTN model to kinematic hardening have been proposed in the literature [29,43,44,45,31] but were limited to isotropic plasticity.

The model developed here is based on the work of Besson and Guillemer-Neel [31]. Damage is represented by a single scalar variable representing the void volume fraction, f. The model is based on the definition of an effective scalar stress, σ_* [46], which depends on the macroscopic stress tensor and f. σ_* is assumed to be a

homogeneous function of degree 1 of $\underline{\sigma}$ so that: $\partial\sigma_* / \partial\underline{\sigma} : \underline{\sigma} = \sigma_*$. In the case of the "standard" GTN model, σ_* is an implicit function of $\underline{\sigma}$ which is obtained by solving the following equation:

$$\Psi\left(\sigma_*, \sigma_{eq}, \sigma_{kk}, f\right) = \frac{\sigma_{eq}^2}{\sigma_*^2} + 2q_1 f_* \cosh\left(\frac{q_2}{2}\frac{\sigma_{kk}}{\sigma_*}\right) - 1 - q_1 f_*^2 = 0 \qquad \textbf{(6.2-10)}$$

where σ_{eq} is the von Mises stress and σ_{kk} the trace of the stress tensor. q_1 and q_2 are model parameters representing void interaction and f_* is an *ad hoc* function of f introduced to model void coalescence [13]. Accounting for plastic anisotropy is done by replacing the von Mises stress by any anisotropic scalar stress measure in Eq.(6.2-10). It is proposed to phenomenologically describe anisotropic damage growth by replacing the trace of the stress tensor by a modified value expressed as:

$$\sigma_K = \alpha_L \sigma_{LL} + \alpha_T \sigma_{TT} + \alpha_S \sigma_{SS} \qquad \textbf{(6.2-11)}$$

where $\alpha_{i=L,T,S}$ are parameters to be determined. Directions L, T and S are assumed to be material directions. This approximate solution is indeed easier to implement and computationally more efficient than the anisotropic models proposed in [22,23,25,28] which explicitly account for cavity shape effects. Note that these models are limited to axisymmetric cavities subjected to axisymmetric loading conditions (although they are extended to deal which generic 3D loadings) whereas the extension proposed here is always valid. If kinematic hardening is to be accounted for it becomes necessary to introduce the $\underline{B} = \underline{\sigma} - \underline{X}$ tensor to define an effective scalar stress B_*. Taking into account plastic and damage anisotropy, B_* is implicitly defined by:

$$\Psi\left(B_*, B_E, B_K, f\right) = 0 \qquad \textbf{(6.2-12)}$$

The yield function can then be expressed as:

$$\Phi = B_* - R(p) \qquad \textbf{(6.2-13)}$$

where the function $R(p)$ still represents isotropic hardening. The plastic strain rate tensor is still given by the normality rule as:

$$\underline{\dot{\varepsilon}}_p = (1-f)\dot{p}\frac{\partial \Phi}{\partial \underline{\sigma}} = (1-f)\dot{p}\frac{\partial \underline{B}_E}{\partial \underline{\sigma}} \qquad \textbf{(6.2-14)}$$

The (*1 - f*) factor is introduced in the previous equation so that:

$$\underline{\dot{\varepsilon}}_p : \underline{B} = (1-f)\dot{p}B_* \qquad \textbf{(6.2-15)}$$

which represents the equality between the macroscopic plastic dissipation (left hand-side) and the microscopic dissipation (right hand-side) [47]. $\dot{p}$ can be calculated for rate independent materials using the consistency condition: for a rate dependent material, $\dot{p}$ is expressed as a function of B_* (e.g. Norton flow). Finally it is necessary to derive equations to obtain the back stress $\underline{X}$. Eq. (6.2-8) is kept to describe the evolution of the kinematic hardening state variable $\underline{\alpha}$.

Note that as the trace of the plastic strain tensor is not equal to zero, the trace of $\underline{\alpha}$ will also be not zero. However Eq. (6.2-9) cannot be used directly to compute the back stress $\underline{X}$ as the macroscopic back stress would not vanish as the material breaks (i.e. for $f_* = 1/q_1$). To solve this problem, one defines an intermediate back stress, $\underline{\chi}$, which can be interpreted as the back stress at the microscopic level. $\underline{\chi}$ is related to $\underline{\alpha}$ using Eq. (6.2-9): $\underline{\chi} = \frac{2}{3}C\underline{\alpha}$

Following Besson and Guillemer-Neel [31], the actual back stress, $\underline{X}$, is computed such that:

$$\underline{\chi} = \frac{2}{3}X_*\frac{\partial X_*}{\partial \underline{X}} \qquad \textbf{(6.2-16)}$$

In practice, this equation must be iteratively solved with respect to $\underline{X}$. Computing as the solution of $\Psi(X_*, X_E, X_K, f) = 0$ would not give expressions equivalent to Eq. (6.2-9) in the limit case $f = 0$ as plastic anisotropy would be taken into account. For that reason, it is preferable to use isotropic definition of the effective stress to apply the previous equation. In that case, X_* is defined as the solution of $\Psi(X_*, X_{eq}, X_{kk}, f) = 0$.

6.2.2.3 Damage growth and failure

In the experimental study of the companion paper [33, Section 6.1 in this thesis] it was found that void coalescence through both void impingement and void sheeting plays an important role in failure. In particular, in the crack propagation regime coalescence is dominated by nucleation at a 2nd population of small 2nd phase particles. The evolution of the porosity is controlled by void growth and strain controlled nucleation of new voids and is expressed as [48]:

$$\dot{f} = (1-f)\,trace(\underline{\dot{\varepsilon}}_p) + \left(A_n^1 + A_n^2\right)\dot{p} \qquad \textbf{(6.2-17)}$$

where the first term on the right-hand side corresponds to void growth (and mass conservation) and the second term corresponds to void nucleation. Material parameter A_n^1 controls nucleation rate for void nucleation at coarse intermetallic particles. A_n^2 controls nucleation at a 2nd population of smaller 2nd phase particles observed in slanted areas, which appears to control fracture in low stress triaxiality regions as evidenced in [33, Section 6.1 in this thesis].

In the case of void impingement failure, the f^* function introduced by Tvergaard and Needleman [13] is used to represent the increased damaging effect of voids during coalescence. It is expressed as follows:

$$f^* = \begin{cases} f_g + f_n & \text{for} \quad f_g < f_c \\ f_c + f_n + \delta(f_g - f_c) & \text{for} \quad f_g > f_c \end{cases} \qquad \textbf{(6.2-18)}$$

where f_c represents the critical growth void volume fraction for which coalescence via impingement starts. It is determined by unit cell calculations here. δ is an ‘‘accelerating’’ factor which represents the increased softening effect of voids once coalescence has started. Note that nucleated damage is not taken into account in the acceleration ($\delta(f_g - f_c)$) as coalescence by void impingement is essentially controlled by growth. In the case of void sheeting, failure occurs due to rapid nucleation on secondary particles: as such, A_n^2 needs to be large enough to promote rapid failure.

When standard finite element techniques are used, models including damage lead to material softening and mesh size dependence. In that case, it is necessary to fix the mesh size in order to obtain results transferable from one sample to another [49,50,21,51] (although improved, so called ‘‘non-local’’ models can be used to obtain mesh independent results [52,53]). Consequently, the mesh size and in particular the mesh height in the direction perpendicular to the crack plane, $h_\perp$ [54] should be considered as an adjustable parameter tuned to represent crack growth. It needs to be tuned on specimens containing cracks.

6.2.2.4 Finite strain formulation

Ductile rupture is always accompanied by large deformations so that a finite strain formalism must be used when implementing constitutive equations. Specific implementations using the finite strain formalism proposed by Simo[55] and Simo and Miehe [56], have been used by Mahnken [57], and Reusch et al. [58]. A computationally more efficient treatment of finite strain may be obtained using generic formulations based on reference frames which facilitate keeping the standard small strain formulation, *i.e.* using an additive strain decomposition as in Eq.(6.2-1), [59]. Invariant stress and strain rate measures $\underline{s}$ and $\underline{\dot{e}}$ are defined by transport of the Cauchy stress $\underline{\sigma}$ and strain rate $\underline{\dot{D}}$ into the co-rotational reference frame which is characterized by the rotation $\underline{Q_c}$: $\underline{s} = \underline{Q_c}.\underline{\sigma}.\underline{Q_c^T}$ and $\underline{\dot{e}} = \underline{Q_c}.\underline{D}.\underline{Q_c^T}$. The evolution law for $\underline{Q_c}$ is expressed as:

$$\underline{\dot{Q}_c} = \underline{\Omega}.\underline{Q_c} \text{ with } \underline{Q_c}(t=0) = \underline{1} \qquad \textbf{(6.2-19)}$$

$\underline{D}$ and $\underline{\Omega}$ are respectively the symmetric and the skew-symmetric parts of the velocity field gradient. The corresponding objective stress rate is the Jaumann rate.

6.2.2.5 Simulation technique

The modified GTN model was implemented in the FE software Zebulon, developed at Ecole des Mines de Paris [46,60]. An implicit scheme is used to integrate the constitutive equations. The consistent tangent matrix is computed using the method proposed in [45]. The material is considered as broken when f_* reaches $1/q_1$. In that case, the material behaviour is replaced by an elastic behaviour with a very low

stiffness (Young's modulus: E_b = 1 MPa). A similar technique was used in [46] showing convergence of the results for sufficiently low values of the Young modulus E_b. Gauss points where these conditions are met are referred to as ''broken Gauss points''. Calculations were done using linear elements with full integration using a B-bar method to control volume change in each element [61]. 3D elements were used. When all Gauss points in an element are "broken", the element is removed from the calculation. In regions where the crack propagates, eight nodes (3D) elements were used. Convergence in terms of macroscopic load and local damage growth was checked as proposed in [56]. Usual symmetry conditions are accounted for in order to reduce the size of the calculations.

Experiments show that the crack initiates with a flat triangle and propagates in a slant mode of ductile tearing. Simulation of flat to slant transition was performed in [62] in the case of dynamic crack growth but no attempt was made to compare results with actual tests. The transition was also modelled in [63] but matching simultaneously crack paths and load–displacement curves was not possible. More recently the flat to slant transition was obtained in [64,65] but comparison with experiments was also missing. Due to the difficulties encountered to model the transition, the crack is also modelled here as being flat. Material parameters were adjusted to match both load levels and crack lengths. The same solution was adopted in [21] using the Rousselier model [66] and in [67] using a 3D cohesive zone model.

6.2.3 Parameter identification

In this Section the different parameters for the AA2139 alloy in the two conditions (T351/T8) are fitted. For the naturally aged material (T351) the following material characteristics have been found relevant: (i) anisotropic initial void shape and growth (ii) plastic behaviour including: isotropic/kinematic hardening and plastic anisotropy and (iii) nucleation at a 2nd population of 2nd phase particles leading to void sheeting are relevant. The plastic behaviour of the artificially aged material (T8) is limited to isotropic hardening. The naturally aged material displays lower yield strength and higher hardening capacity than the artificially aged material.

6.2.3.1 Procedure for the naturally aged T351 material

The main material characteristics that are accounted for in the model are:

(i) Plastic behaviour consisting of:
- Isotropic hardening
- Kinematic hardening
- Plastic anisotropy

(ii) Void growth

(iii) Nucleation of voids

For the description of the plastic behaviour the material defects such as initial porosity and void nucleation at coarse 2nd phase particles cannot be neglected as volume fractions are high enough for the present material to influence the overall structural behaviour. For this reason void growth effects need to be accounted for during the fitting of plastic behaviour parameters. The fitting of the parameters associated with each of these components is conducted in stages. To fit void growth parameters unit cell calculations will be used as this has the advantage of providing physical justification to the fitting parameters [68]. In the present identification method the void growth parameters will be fitted before fitting the plastic behaviour using a simplified plastic behaviour not accounting for plastic anisotropy and kinematic hardening. This is justified by the fact that plastic anisotropy is fairly weak and kinematic hardening only influences the material behaviour for strains that are substantially lower than at coalescence. The parameters for void sheeting and nucleation of voids on a smaller population of 2nd phase particles will be identified for tests on Kahn specimens. An overview over the different steps and parameters of the identification procedure is given in Table 6.2-1. The procedure is explained in more detail in the following Sections.

Step 1)	Void growth parameter: fitting the model to unit cell calculations using an automatic optimization procedure				
	Identification of :	Tvergaard Fitting parameter :	q_1		
		Anisotropic void growth parameters:	α_T (T-direction)	α_L (L-direction)	α_S (S-direction)
Step 2)	Parameters to fit isotropic/kinematic hardening and plastic anisotropy: a) Numerical simulation of prestraining by 2% in rolling direction; b) Simulation of tensile and EU2 tests with initialized parameters and parameter fitting using an automatic optimization procedure				
	Identification of :	Isotropic hardening:	R_0	K_1	k_1
		Kinematic hardening:	C	D	
		Plastic anisotropy:	$c^{i=1,\ldots,6}$	b	
Step 3)	Parameters for nucleation of 2nd population of 2nd phase particles: Trial and error simulation of Kahn tear tests with the aim to fit the nominal stress CMOD curves				
	Identification of :	Critical strains for nucleation at 2nd population of 2nd phase particles	$p_{crit\,L}$	$p_{crit\,T}$	
		Mesh size	$h_\perp$		

Table 6.2-1:Parameter identification procedure for the AA2139 alloy in the T3 condition

Step 1: 2D unit cell calculations for different stress triaxialities (0.85, 1.00, 1.25, 1.50) have been carried out. The stress triaxialities correspond to values found in finite element analyses of crack propagation in Kahn tear test specimens. The unit cell is a cylinder with a height of $2H_0$ (oriented in the loading direction) and radius R_0. Periodic boundary conditions are used. The initial porosity is set at 0.34% (determined via micro-computed tomography [33, Section 6.1 in this thesis]) and the initial cell aspect ratio H_0/R_0 is set equal to the measured mean Feret dimensions ratios for Voronoi cells around pores and particles, which provides H_0/R_0 =1 [33, Section 6.1 in this thesis]. To enhance speed of calculations, cell calculations were carried out on 2D meshes. Here for every loading direction (L,T,S) different 2D meshes are used to account for the average initial pore Feret dimensions in loading direction obtained from the tomography data of the as-received material. The cavity is

assumed to be a different ellipsoid for each loading direction (L, T, S): only the cavity dimension in the direction in which the loads are applied corresponds to the measured average dimension. The other void dimensions are given by the geometrical average of the two other Feret dimensions. For instance for the case of L-direction loading the void size is given by (see also Figure 6.2-1):

$$R_z = l/2$$
$$R_x = \sqrt{t\,s}/2 \qquad \textbf{(6.2-20)}$$

Where *l, t, s* are the measured initial average pore Feret dimensions of the material and R_z and R_x are major and minor axis of the pore ellipse. The initial void volume fraction is kept constant in the calculation for all directions and is equal to the measured average initial porosity (0.34%). Figure 6.2-2(a) shows the results of a unit cell calculation in terms of deformation and evolution of void volume fraction for a stress triaxiality of 1.25 for the three loading directions and for different values of *b* which is the exponent influencing the yield surface shape as described in Section 6.2.2 (*b*=4 corresponds to the von Mises criterion and *b*=8 is closer to the Tresca criterion). An initial identification of the parameter *b* via simulations of EU2 samples and tensile tests on smooth samples neglecting material softening through voids and comparison to experiments lead to *b*=8. Values higher than 4 are consistent with values given in the literature for Al alloys [38,2]. It can be seen that void growth and coalescence (abrupt slope change corresponds to coalescence) occurs later for loading in the L direction than for loading in the T and S directions. This trend is consistent with the anisotropic void growth prediction made by the Gologanu-Leblond-Devaux model [22,23]. It can also be seen that the fracture criterion influences the results substantially: void growth and coalescence occurs faster for the *b*=8 setting than for the von Mises criterion. The parameter identification is performed using an optimisation algorithm and using an elastic-plastic material fitted on L direction tensile test data. Figure 6.2-2(b) shows the results of a calculation with a GTN material element using fitted anisotropy parameters for the three different directions. The critical strains at coalescence are shown as squares in the figure. Comparison is made for void volume fraction and force evolution. For all calculations the critical void volume fraction f_c is set to 4.5% which represents an average of the values found in unit cell calculations for different directions and stress triaxilities. The weighting

factor δ is set to 3.0. The results of the fitting of the parameters q_1, α_L, α_T, α_S (also see Eq. (6.2-11))are shown in Table 6.2-2.

Figure 6.2-3 shows the critical strains at coalescence obtained from unit cell calculations at different stress triaxalities for L and T loading direction. The difference between critical strain for L and T loading are the higher the lower the stress triaxiality. The higher the stress triaxiality the lower the strain at coalescence.

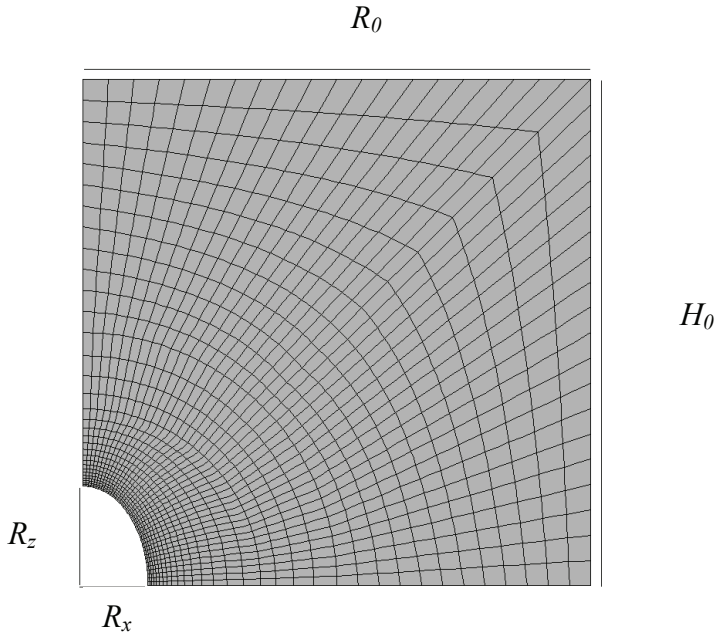

Figure 6.2-1: Example of a 2D unit cell mesh for loading in L (vertical) direction. The anisotropic void shape / pore elongation in L can be seen.

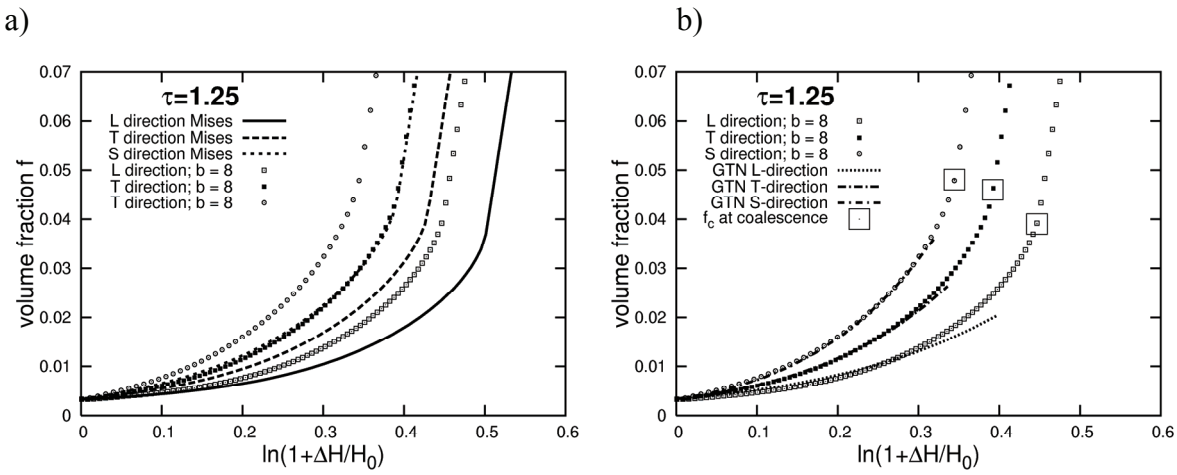

Figure 6.2-2: Results of unit cell calculations for rotation symmetric void cells for different directions at a stress triaxiality of τ=1.25 and (a) Mises criterion (*b*=4) and (b) *b*=8 ; in (b) also the fit of calculations with Gurson elements is shown (for theAA2139 alloy in the T3 condition)

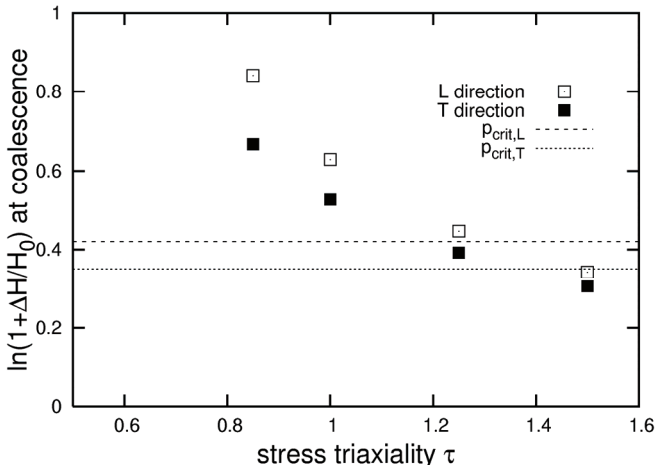

Figure 6.2-3: Results of unit cell calculations rotation symmetric void cells, critical strains at coalescence for different stress triaxialities and loading in L and T direction (AA2139 alloy in T3 condition; *b*=8)

Step 2: For the simulation of prestraining an "imaginary" material, whose properties are supposedly close to the real non-prestrained material, is used which is prestrained in the simulation through loading on a volume element by 2% in rolling direction L. Subsequently, the prestrained material, whose parameters are initialized during the prestraining, is used to simulate tensile and EU2 tests in L and T direction. The simulation results are fitted to the experimental results using a simplex optimisation algorithm. Parameters for isotropic hardening, kinematic hardening, and plastic anisotropy are identified simultaneously in this optimization process. Coefficients $c^{4\ldots6}$ play a limited role and are assumed to be equal to 1 as shear stresses remain small.

The following law for the isotropic hardening is used.

$$R(p) = R_0\left[1 + K_1(1 - e^{-k_1 p})\right] \qquad \textbf{(6.2-21)}$$

The values for void growth parameters (q_1, α_L, α_T, α_S) obtained in Step 1 are used. The nucleation of voids on a 1st population of coarse 2nd phase particles is taken into account for parameter fitting. Micro-tomography studies on the material have shown that a certain strain is needed until all coarser 2nd phase particles are fractured [43]. To represent this effect A_n^1 is expressed as:

$$A_n^1 = \begin{cases} A_n^{01} & for\ p_s \le p \le p_e \\ 0 & \text{otherwise} \end{cases} \qquad \textbf{(6.2-22)}$$

where A_n^{01} is a constant. Nucleation starts at the beginning of the deformation (p_s=0) and ends at p_e =10% strain. This means that the entire volume fraction of coarse 2nd phase particles (0.4%) is considered to have "transformed" into voids at 10% strain.

Step 3: Figure 6.2-4 shows the results of a calculation of Kahn tear tests using the parameters obtained from the first two optimization processes.

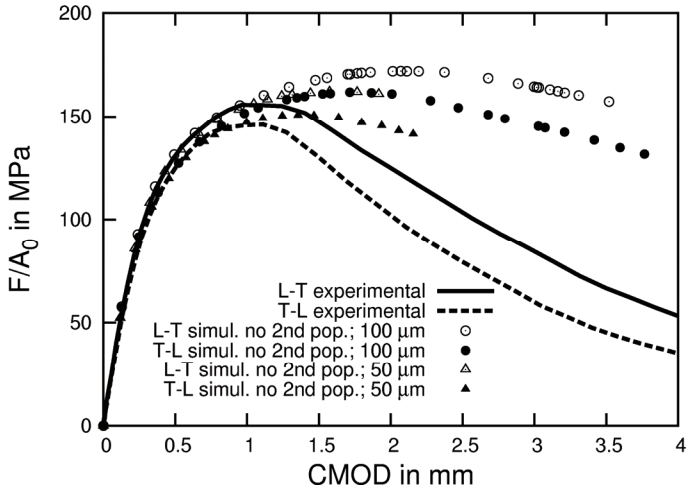

Figure 6.2-4: Simulation of the Kahn tear tests (for AA2139 alloy in T3 condition) without 2nd nucleation for different mesh sizes (100 and 50 µm element height)

It can be seen that the anisotropic void growth parameters (α_L, α_T, α_S) do cause a toughness anisotropy in this calculation. It shows that the use of the anisotropic void growth parameters (α_L, α_T, α_S) may be an alternative to the Gologanu-Leblond-Devaux model [22,23]. However, the maximum loads as well as the propagation loads are overestimated for a mesh height of 100 µm. As it is shown in Figure 6.2-4 with an element height of 50µm the propagation loads are reduced but still higher than the experimentally found loads. It has been suggested in [50] to use the height of the localization band as element height. In Figure 6.1-12(b) in [33, Section 6.1 in this thesis] it can be seen that the used mesh height (100 µm) may be a reasonable localization band height. The simulation carried out here does however not account for shear decohesion or void sheeting that have been observed in experimental investigations [33, Section 6.1 in this thesis].

In order to be able to fit the descending curve part of the Kahn tear tests it is therefore suggested here to use different critical strains for each loading direction at which the nucleation at a small population of 2nd phase particles starts.

A_n^2 controls nucleation of voids at a 2nd population of smaller 2nd phase particles leading to coalescence. For L and T direction different critical strains ($p_{crit\,L}$, $p_{crit\,T}$) are used.

$$A_n^2 = \begin{cases} A_n^{02} \;\; for\; p_{ci} \le p \\ 0 \quad \text{otherwise} \end{cases} \qquad \textbf{(6.2-23)}$$

A_n^{02} has got high values so that the material is almost immediately breaking when the critical strains are reached. This simplified method to represent damage and coalescence anisotropy may be justified by tomography studies [33, Section 6.1 in this thesis] where already in the crack initiation region it could be seen that the Kahn tear test sample for L-T did not contain a crack whilst the T-L sample did contain a crack at similar strains. Additionally it could be seen that coalescence distances between voids were smaller for T-L samples than for L-T samples that may lead to higher deformation between voids till coalescence.

The final parameters found in the optimisation and other measured parameters are given in Table 6.2-2. They provide mostly excellent fits to the data (see the next sub-section).

Elastic-plastic behavior					
E *in GPa*	v	R_0 in MPa	K_1	k_1	
70	0.3	237	1.43	6.90	
Kinematic hardening					
C in MPa	D				
14947	261				
Plastic anisotropy					
c^1	c^2	c^3	$c^{i=4,5,6}$	b	
1.1	1.14	0.904	1.0	8	
Void anisotropy					
α_T (T direction)	α_L (L direction)	α_S (S direction)	q_1	f_c	δ
0.967	0.322	1.46	1.81	4.5%	3.0
Damage					
f_0 *in %*	f_n *in %*	$p_{crit\,L}$ *in %*	$p_{crit\,T}$ *in %*	A_n^{02}	A_n^{02}
0.34	0.45	35	42	30	30
Element sizes					
Height:	Width:	Through-thickness:			
100µm	100 µm	533 µm			

Table 6.2-2: Parameters for the naturally aged T351 material (AA2139) simulations

6.2.3.2 Procedure for the artificially aged (T8) material

The parameter identification for the artificially aged T8 material has been carried out similarly to the naturally aged material (see Table 6.2-3). However, as the artificially aged material hardly exhibited any effect of kinematic hardening and plastic anisotropy, these features will not be accounted for in the model. For this reason no prestraining is simulated. It has been found that a good EU2 curve fit can only be obtained for b=12 (close to Tresca criterion). For b=4 (von Mises criterion) the loads were too high.

The following equation is used for isotropic hardening:

$$R(p) = R_0\left[1 + K_0 p + K_1(1 - e^{-k_1 p}) + K_2(1 - e^{-k_2 p})\right] \qquad \textbf{(6.2-24)}$$

The parameters used for the artificially aged material simulations are shown in Table 6.2-3.

Elastic-plastic behavior							
E in GPa	ν	R_0 in MPa	K_0	K_1	k_1	K_2	k_2
70	0.3	400	0.00832	0.261	16.8	0.115	704
	b=12						
Void anisotropy							
α_T	α_L	α_S	q_1	f_c	δ		
1.015	0.518	1.317	2.2	4.5%	3.0		
Damage							
f_0	f_n	$P_{crit\,L}$	$P_{crit\,T}$	A_n^{02}	A_n^{02}		
0.34%	0.45%	23%	29%	14.0	14.0		
Element sizes							
Height:	Width:	Through-thickness					
100µm	100 µm	533 µm					

Table 6.2-3: Parameters for simulations of the artificially aged (T8) material (AA2139)

6.2.4 Model predictions

The simulation results for tests on small samples with the fitted parameters are shown here. Using these parameters simulations for tests on large M(T) samples were subsequently performed. The role of the different material parameters is investigated in a parametric study. The findings made using the present model are then compared to results found using models from the literature.

6.2.4.1 Comparison with data for small specimens and M(T) specimens.

Figure 6.2-5, Figure 6.2-6 and Figure 6.2-7 show the simulation and experimental results for tensile, EU2 and Kahn tear testing for the two testing directions and the different heat treatment condition. A good fit is achieved for the tensile curves (see Figure 6.2-5). The initial part of the EU2 curves is also very well fitted (see Figure 6.2-6). However, the opening at which the samples fail are not predicted correctly via the simulations. The samples break earlier in the simulations than in experiments which may be due to the fitting of fracture parameters at higher stress triaxility. The Kahn tear test curves (Figure 6.2-7) are well fitted for the T-L naturally aged and T-L artificially aged material. The maximum load for the naturally aged L-T sample is

slightly underestimated by the simulation. The T-L artificially aged material curves underestimated the loads slightly in the propagation region.

Figure 6.2-8 shows results of M(T) experiments and simulations for (a) the naturally aged material and (b) the artificially aged material. The simulation of the naturally aged T-L sample the loads obtained from simulations are only slightly above the experimental results. The overall prediction is good. Whilst the artificially aged T-L sample loads are slightly overestimated in the simulation, the maximum load ratio between L-T and T-L testing is well represented. The good results of the simulations carried out for M(T) samples (see Figure 6.2-8) provide an independent validation of the model's predictive capabilities (this data is unseen data), and thus shows that this method of accounting for toughness anisotropy may represent toughness anisotropy on samples of very different sizes. The active plastic zone size, when the end of the finely meshed zone is reached, is shown in Figure 6.2-9. It can be seen that for the naturally aged material the test standard requirement of small scale yielding is no longer met [35] which is also consistent with the validity calculations made according to the standard. For the artificially aged material the yielding conditions are still met which is also found in the calculations according to the test standard.

In [21] it has been shown that for very thin sheet material local buckling may occur during M(T) tests despite the use of an anti-buckling device. As the sheet material investigated in the present study is relatively thick local buckling should be negligible and is hence not considered.

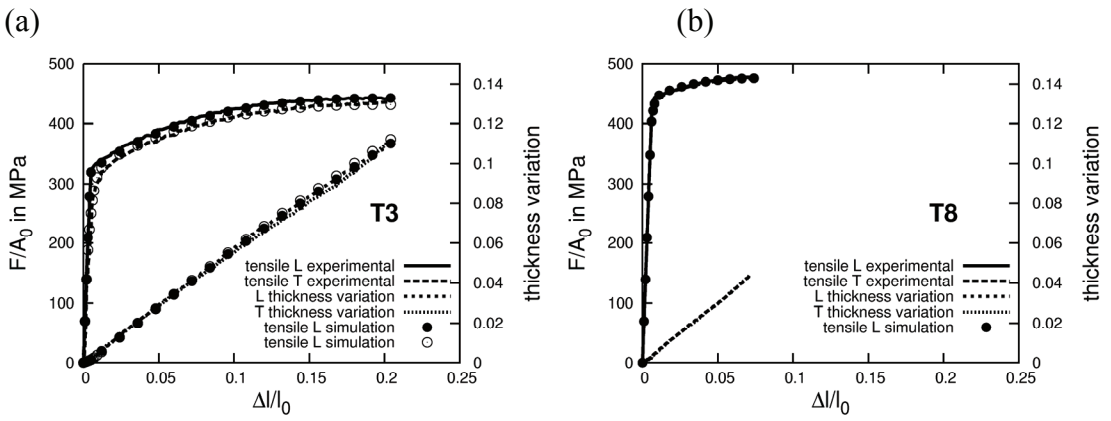

Figure 6.2-5: Tensile tests experimental and simulation for naturally aged and artificially aged (T3 and T8) material (AA2139)

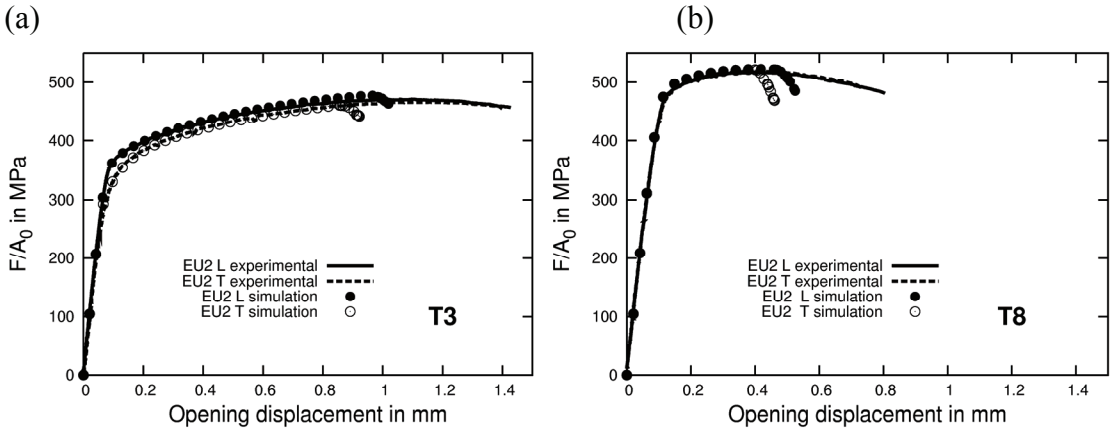

Figure 6.2-6: EU2 tests experimental and simulation for naturally aged and artificially aged (T3 and T8) materials (AA2139)

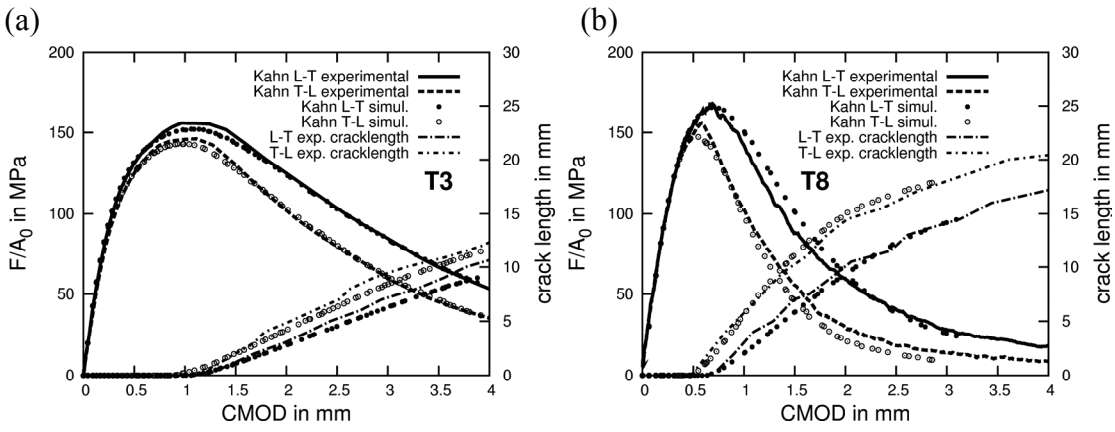

Figure 6.2-7: Kahn tear test tests experimental and simulation for naturally aged and artificially aged (T3 and T8) materials (AA2139)

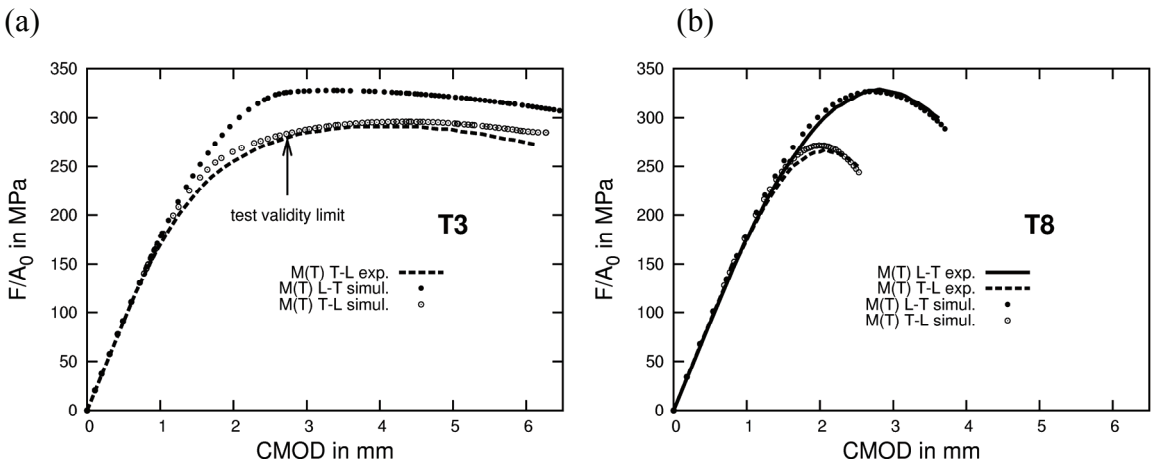

Figure 6.2-8: M(T) test results for simulation and experiment for naturally aged and artificially aged (T3 and T8) materials (AA2139)

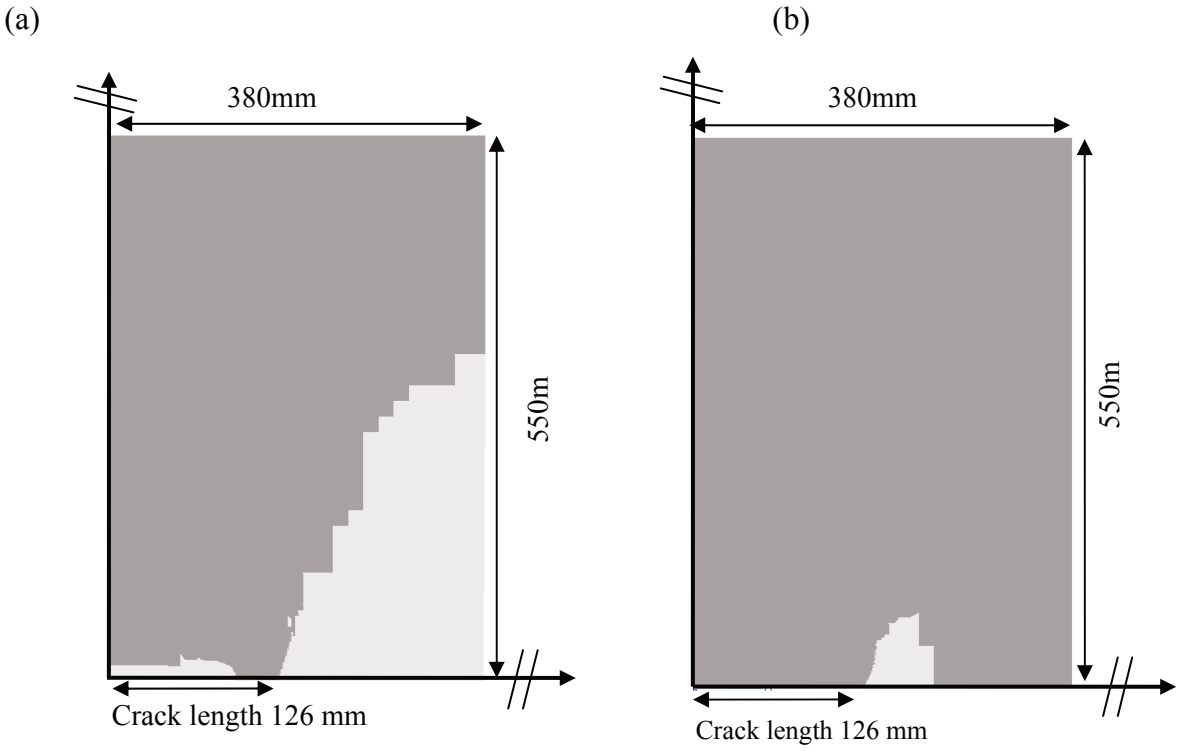

Figure 6.2-9: A quarter of an M(T) sample with active plastic zone (in bright) at 126mm crack extension for (a) a naturally aged (T3) sample and (b) an artificially aged (T8) sample (AA2139)

6.2.4.2 Parametric study on the naturally aged (T3) material

Study with the same critical strain (for $p_{crit\,L} = p_{crit\,T}$) for both loading configurations

Figure 6.2-10 shows a simulation for the naturally aged material where the same critical strains for T-L and L-T direction are applied for the 2nd nucleation at small particles. It can be seen that only the 1st part of the curves are slightly different due to the kinematic hardening and plastic anisotropy. This is consistent with the idea that in this part of the loading the material behaviour is mainly governed by plastic properties. It can be seen that from maximum load onwards the two curves almost superpose. This implies that neither kinematic hardening nor plastic anisotropy may describe the toughness anisotropy. This simulation also shows that the anisotropic growth parameters (α_L, α_T, α_S) have a minor effect in this simulation, and that they cannot explain the toughness anisotropy. Unit cell calculations show that coalescence through impingement occurs at substantially higher strains than the strains (p_c) at which the 2nd nucleations starts here, especially at lower stress triaxialities, so that the influence of the anisotropic void growth parameters (α_L, α_T, α_S) is reduced through the 2nd nucleation (also see Figure 6.2-3).

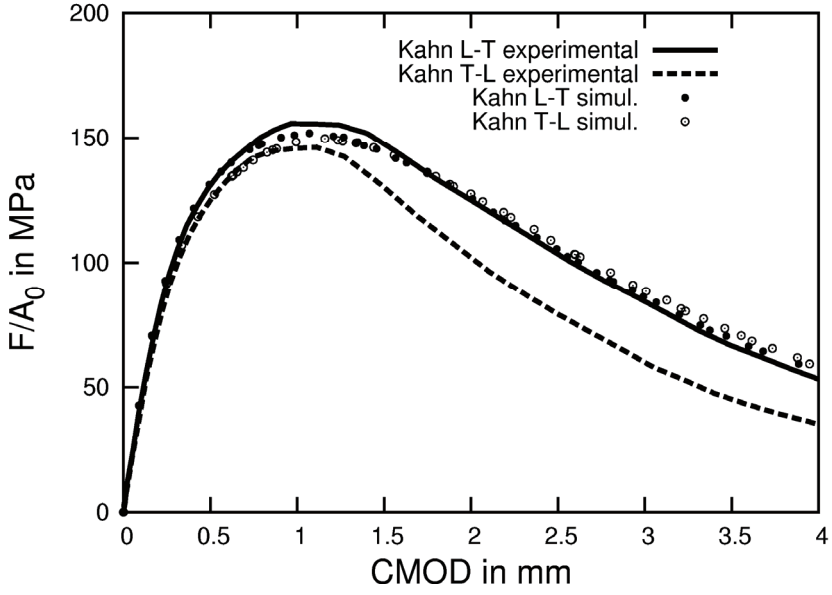

Figure 6.2-10: Simulation of the Kahn tear tests for $p_{crit\,L} = p_{crit\,T}$ =42% (AA2139 T3 condition)

Study for *b*=4 and *b*=8 and plastic isotropy (c^i=1.0)

Figure 6.2-11 shows the results of a simulation for L-T loading for material using the full model and material without plastic anisotropy (c^i=1.0) for different yield surface shapes (*b*=8 ;*b*=4). In the case of isotropic plastic behaviour coefficients R_0 and C are slightly modified so that the same uniaxial response in the L direction (which in that case is the main loading direction of the Kahn specimen) is obtained as for the "full" model. It can be seen that the change from plastic anisotropy to plastic isotropy has only little effect on overall curve shape. The nominal stress up to the maximum load is slightly increased for plastic isotropy at *b*=8 compared to plastic anisotropy at *b*=8. For isotropic plasticity and *b*=4 which is the Mises criterion the nominal stress is increased. This is consistent with the idea that at multiaxial stress states the yielding occurs at higher stresses for *b*=4 than for *b*=8.

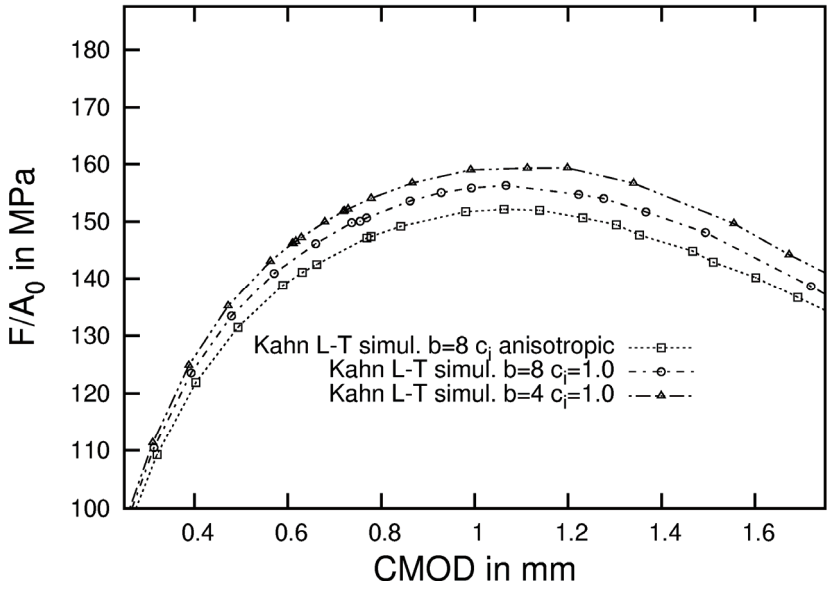

Figure 6.2-11 :Simulation for *b*=4 and *b*=8 and plastic isotropy (c_i=1.0) (AA2139 T3 condition)

Study without kinematic hardening

Figure 6.2-12(a) shows simulation for both loading configurations for material without kinematic hardening but which is prestrained (*i.e.* material behaviour that corresponds to an elastic plastic material that has been identified in an L tensile test). Pre-kinematic hardening in the L direction was replaced by an additional isotropic

hardening. The material without kinematic hardening is less tough than the material using the full model. In an analysis of the calculations higher equivalent strains have been found at the same prescribed displacement for the calculation without kinematic hardening than for the "full" calculation using kinematic hardening. Thus the critical strains at which the nucleation at small particles starts are attained at smaller prescribed displacements for the material without kinematic hardening than for the "full" calculation. It is believed that this is a structural effect. This accounts for a slight decrease of the force for the L-T configuration. For the T-L configuration the load is initially higher than for the "full" model as the T direction is also hardened. The same structural effect leads to faster load decrease in the propagation regime.

Study without prestraining

In Figure 6.2-12(b) it can be seen that the non prestrained material is softer than the prestrained material. Maximum loads are attained for higher opening displacements for the non prestrained material then for the prestrained material. It has been found that the plastic zone size for the non-prestrained material is larger than for the prestrained material which leads to a larger sample deformation and a larger CMOD at similar loads. The shift of the load maximum may be interpreted as the main reason why loads are increased in the propagation region for the non-prestrained material.

The curves of the non –prestrained material reach lower loads than the prestrained material. The beginning of the curves is very similar as no anisotropy has been introduced through prestraining. The material with elastic-plastic behaviour corresponding to the L material shows little anisotropy to maximum load of the T-L sample as the effect of prestraining is no longer there in terms of anisotropy.

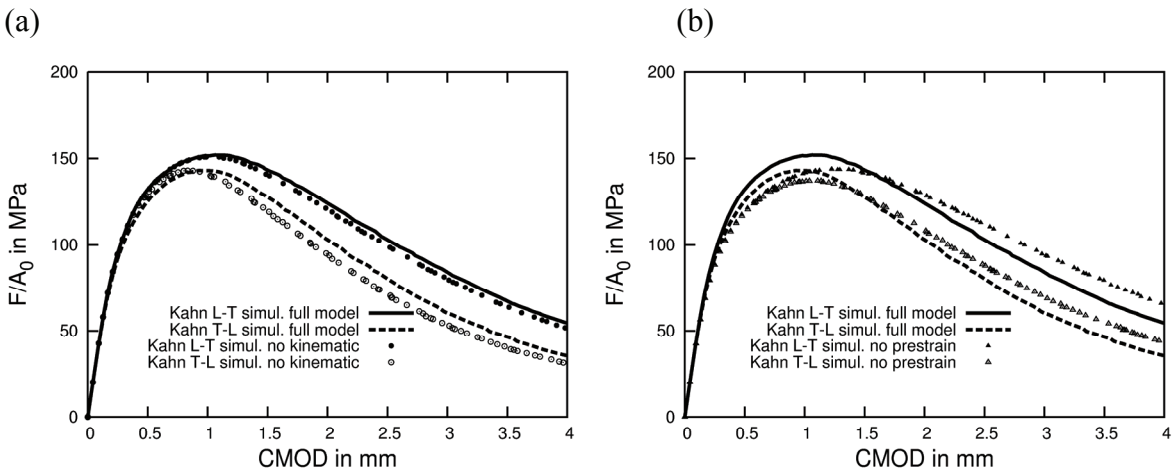

Figure 6.2-12: Simulation (a) without kinematic hardening (b) without prestraining (AA2139 T3 condition)

6.2.4.3 Comparison with models from the Literature

In a previous finite element study Pardoen and Hutchison [26] have linked anisotropic shape of initial voids to fracture toughness anisotropy (J_{IC}). In [10, Chapter 5 in this thesis] a comparison between these results and the results on the AA2139 alloy in T8 condition has been made in terms of initial void aspect ratio and toughness anisotropy, in terms of unit initiation energies, at high level of stress triaxiality. Despite the model simplifications a similar *trend* in toughness anisotropy has been found at similar initial void volume fractions suggesting that initial anisotropic void shape may be a reason for fracture toughness anisotropy.

In the first part of this Chapter subsequently obtained SRCT results provide new insights into fracture mechanisms in the fracture initiation region at high stress triaxiality indicating that coalescence mechanisms involving nucleation at a 2nd population of small 2nd phase particles may play a major role in fracture. The model presented here can reproduce a similar influence of anisotropic initial void shape on fracture toughness anisotropy as the model of Pardoen and Hutchinson [26] when neglecting nucleation at small particles. However, to reproduce actual absolute toughness values and the load evolution at lower levels of stress triaxiality an anisotropic nucleation at a population of small 2nd phase particles needs to be included in the model. Thus the present modelling indicates that initial void shape anisotropy may not be the only reason for toughness anisotropy and that anisotropic coalescence

mechanisms involving a small population of 2nd phase could substantially contribute to toughness anisotropy.

6.2.5 Conclusions

In this work a model to describe and predict toughness anisotropy during ductile fracture of an Al-alloy in two conditions for aerospace application based on the Gurson-Tvegaard-Needleman model has been proposed. It incorporates (i) simplified 3D anisotropic void growth, (ii) plastic behavior consisting of: isotropic/kinematic hardening, plastic anisotropy and (iii) nucleation at small 2nd phase particles at anisotropic critical strains to account for void sheeting. For the first time a model for kinematic hardening accounting for ductile damage has been successfully applied to structures. A new simple method to account for initially anisotropic void shape and growth is suggested that is easier to implement than other approaches and is not restricted to axisymmetric cavities. The model parameters have been fitted on several kinds of samples: smooth tensile bars, notched tensile samples and Kahn tear test pieces. Model ingredients are based on a thorough experimental basis including microstructure characterization and observation of fracture via classical fractography and micro-tomography studies of arrested cracks presented in the companion papers (Section 6.1 and Chapter 5 of this thesis). It has been found that neither kinematic hardening nor plastic anisotropy can describe toughness anisotropy. Also accounting for void growth anisotropy is not sufficient to describe toughness anisotropy at realistic loads. It has also been found in the experimental study of the companion paper [33, Section 6.1 in this thesis] that void coalescence though nucleation at small 2nd phase particles plays an important role, in particular in the crack propagation regime. It is proposed to account for coalescence and nucleation at a 2nd population of small 2nd phase particles via nucleation at different critical strains for the different material directions which may be linked to potential anisotropic shape and/or distribution of small 2nd phase particles. Application of the found parameters to large M(T) samples shows that this method is suitable to predict fracture toughness anisotropy fitted on small samples. The effect of prestrain and plastic anisotropy is relatively weak for the present material. However, it may be important to use these model features to describe the behaviour of other materials (for example steel X100).

Slant fracture has not been reproduced in the present study and the use of the Lode parameter as suggested in [69,64] should be considered to address this issue.

6.2.6 References

[1]Cailletaud G. Int. J. Plasticity 1992;8:55-73
[2]Bron F, Besson J. Int. J. Plasticity 2004;20:937-963
[3]Rivalin F, Besson J, Pineau A, Di Fant M. Eng. Fract Mech 2000;68:347-364
[4]Tanguy B, Luu TT, Perrin G, Pineau A, Besson J. Int. J. of Pressure Vessels and Piping in press, 2008
[5]Benzerga A, Besson J, Batisse R, Pineau A. Modelling Simul. Mater. Sci. Eng. 2002;10:73-102
[6]Steglich D, Brocks W, Heerens J, Pardoen T. Eng Fract Mech 2008 in press
[7] Dumont D, Deschamps A, Brechet Y. Mater Sci Eng A. 2003 ;A356 :326-336
[8]Benzerga, A, Besson, J, Pineau, A. J. Eng. Mater. Technol. 1999;121:221-229
[9] Benzerga AA, Besson J, Pineau A, Acta Mater 2004;52: 4623-4638
[10]Morgeneyer TF, Starink MJ, Sinclair I, Acta Mater, 2008;56: 1671-1679
[11]Enami K. Eng. Fract. Mech. 2005;72:1089-1105
[12]Gurson AL. J. Eng. Mater. Technol. 1977;99:2-15
[13]Tvergaard V, Needleman A. Acta Metall. 1984;32:157-169
[14]Lemaitre, J, Desmorat R.,Sauzay M. Eur. J. Mech. 2000;19A:187-208
[15]Hammi Y, Horstemeyer MF. Int. J. Plasticity 2007,23:1641-1678
[16] Hill, R. 1950, The mathematical theory of plasticity. Clarendon Press, Oxford.
[17]Benzerga AA, Besson J. Eur. J. Mech. 2001;20A:397-434
[18]Brunet M, Morestin F, Walter-Leberre H. J Mat. Proc. Technology 2005;170:457-470
[19]Karafillis, AP, Boyce MC. J. Mech. Phys. Solids 1993;41:1859-1886
[20]Barlat F, Aretz H, Yoon JW, Karabin ME, Brem JC, Dick RE. Int. J. of Plasticity 2005;21:1009-1039
[21]Bron F, Besson J. Eng. Fract. Mech. 2006;73:1531-1552
[22]Gologanu M, Leblond J, Devaux J. J. Mech. Phys. Solids 1993;41(11):1723-1754
[23]Gologanu M, Leblond JB, Devaux J. J. Eng. Mater. Technol. 1994;116:290-297
[24]Gologanu M, Leblond JB, Perrin G, Devaux J. Int. J. Solids Structures 2001;38:5581-5594
[25]Pardoen T, Hutchinson JW. J. Mech. Phys. Solids 2000;48(12):2467-2512
[26]Pardoen T, Hutchinson JW. Acta Met 2003;51:133-148
[27]Thomason PF. Acta metal 1985;33:1079-1085
[28]Benzerga A, Besson J, Pineau A, Acta Mater. 2004; 52:4639-4650
[29]Mear ME, Hutchinson JW. Mechanics of Materials 1985;4:395-407
[30]Ristinmaa, M. Mechanics of Materials 1997;26:227-245
[31]Besson J, Guillemer-Neel C. Mechanics of Materials 2003;35:1-18
[32]Garrison WM, Moody NR. J. Phys. Chem. Solids 1987;48:1035-1074
[33]Morgeneyer T.F., Besson J., Proudhon H., Starink M.J. and Sinclair I., article under preparation, Chapter 6.1 in this thesis
[34] Bron F, Besson J, Pineau A. Mater Sci Eng A 2004 ;A 380 : 356-364
[35]ASTM E561-98, 1999
[36]Koplik J, Needleman A. Int. J. Solids Structures 1988;24:835-853

[37]Lemaitre J, Chaboche JL. Mechanics of Solid Materials, 1990, Cambridge University Press, Cambridge, U.K.
[38]Barlat F, Lege DJ, Brem JC. Int. J. Plasticity 1991;7:693-712
[39]Chaboche JL. in : Unified constitutive laws of plastic deformation, Academic Press, 1996, 1-68
[40]Chow CL, Yang XJ. J. Mater. Processing Technol. 2003;133:304-310
[41]Tvergaard V. Advances in Applied Mechanics 1989;27:83-151
[42]Brunet M, Morestin F. J. Mater. Processing Technol. 2001;112: 214-226
[43]Becker R, Needleman A. J. Applied Mech. 1986;53: 491-499
[44]Leblond JB, Perrin G, Devaux J. Eur. J. Mech. 1995;14A(4): 499-527
[45]Arndt S, Svendsen B, Klingbeil D. Technische Mechanik 1997;17(4):323-332
[46]Besson J, Steglich D, Brocks W. Int. J. Solids Structures 2001;38(46-47):8259-8284
[47]Shima S, Oyane M. Int. J. Mech. Sci. 1976;18:285-291
[48] Chu C, Needleman A. Engng Mater. Technology 1980;102:249-256
[49]Rousselier G. Nucl Eng Des 1987;105:97-111
[50]Gullerud AS, Gao X, Dodds RH, Haj-Ali R. Eng. Fract. Mech. 2000;66:65-92
[51]Ruggieri C, Panontin T, Dodds R. Int J Fract 1996;82:67-95
[52]Enakoutsa K, Leblond JB, Perrin G. Comput Methods Appl Mech Eng 2007;196(13-16):1946-1957
[53]Mediavilla J, Peerlings RHJ, Geers MGD. Int J Numer Methods Eng 2006;66(4):661-688
[54]Siegmund T, Brocks W. Int J Fract 1999;99:97-116
[55]Simo JC. Comp. Meth. Appl. Mech. Engng 1992;99(1):61-112
[56]Simo, JC, Miehe C. Comp. Meth. Appl. Mech. Engng 1992;98(1),41-104
[57]Mahnken, R. Int. J. Plasticity 1999;15:1111-1137
[58]Reusch F, Svendsen B, Klingbeil D. Eur. J. Mech. 2003;22A:779-792
[59]Sidoroff F, Dogui A. Int. J. Solids Structures 2001;38: 9569-9578
[60]Besson J, Foerch R, Comput Methods Appl Mech Eng 1997;142:165-187
[61]Hughes TJR. Int J Numer Meth Engng 1980;15:1413-1418
[62]Mathur KK, Needleman A, Tvergaard V. J. Mech. Phys. Solids, 1996;44:439-459.
[63]Besson J, Brocks W, Chabanet O, Steglich D. Eur. J. Finite Elements, 2001:10:401-415
[64]Xue L. Int. J. Solids Struct 2007;44:5163-5181
[65]Xue L, Wierzbicki T. Eng. Fract. Mech., in press 2008
[66]Rousselier G. in : Continuous damage and fracture, 2000, p. 293-303
[67].Roychowdhury S, Roy YDA, Dodds RH. Eng. Fract. Mech., 2002;69:983-1002
[68]Faleskog J, Gao X, Shih CF. Int J Fract 1998;89:355-373
[69]Nahshon K, Hutchinson JW. Eur. J. Mech. 2008;27A:1-17

Chapter 7

Conclusions

In this thesis the influence of microstructural features on fracture toughness has been assessed for two Al-alloys. A thorough experimental investigation of microstructure, mechanical behaviour and fracture mechanisms has been carried out. Additionally, based on these observations models to describe and predict microstructure-toughness relationships have been developed. The use of Synchrotron Radiation Computed Tomography was shown to be a useful tool to obtain novel qualitative and quantitative information on fracture mechanisms and their influence on toughness. The opportunity to investigate the evolution of damage via arrested cracks has proved to be particularly valuable.

Analysis of toughness quench sensitivity in 6156 Al-Mg-Si-Cu sheet has been performed via enhanced Kahn tear tests and a microstructural analysis on material which was quenched at different rates and subsequently artificially aged. Both the coverage of grain boundary decoration and PFZ width increase with changing water quench temperature from 20°C to 60°C. Heterogeneous precipitation on dispersoids and PFZ formation around the dispersoids occurred in the air cooled material. The crack propagation energy is substantially reduced as a result of changing water quench temperature from 20°C to 60°C. However, the crack initiation energy in high stress triaxiality condition seems less affected by the slower water quench, indicating an increased sensitivity to changes in grain boundary character in low stress triaxiality conditions. SRCT of arrested crack tips of samples before and after gallium wetting revealed that in the 60°C water quenched material much of the crack is intergranular in nature. The crack tip has a ligamented morphology and consists of coarse voids and areas of narrow opening that are inclined with respect to the loading direction. Those areas have mostly been identified to lie on grain boundaries. A population of independent grain boundary secondary crack initiation sites is also seen ahead of the

main crack tip. Cracking of the 20°C water quenched material mainly consists of coarse voids and areas of apparent shear decohesion: the crack tip is hardly ligamented and few independent crack initiation sites are seen away from the main crack. In the air cooled material cracking appears to be fully intergranular; few coarse voids are present and the crack opening is narrow. Substantially fewer independent GB crack initiation sites are seen compared to the 60°C water quenched material, *i.e.* there is relatively little damage evolution prior crack coalescence. A simple model based on an equi-shear-stress assumption is derived, suggesting a dominant influence of grain boundary coverage and yield strength of the PFZ on propagation energy. The model also indicates that for most Al based alloys PFZ width has little influence on the propagation energy.

Fracture toughness anisotropy of AA2139 (Al-Cu-Mg) in T351 and T8 conditions has been investigated via mechanical testing of smooth and notched specimens of different geometries and sizes, loaded in the rolling direction (L) or the transverse direction (T). It was found that plastic behaviour of the T351 treated material involved of isotropic/kinematic hardening and weak plastic anisotropy. The artificially aged material (T8) exhibited isotropic hardening and no plastic anisotropy could be discerned. Kahn tear tests and M(T) tests showed substantial toughness differences for the 2 different testing directions: the L-T samples are tougher than the T-L samples. The material in the T351 condition is tougher than the T8. SEM fractography of Kahn tear test samples showed that void growth and shear decohesion are the dominant fracture mechanisms. Some alignment of dimple stringers in the crack propagation region is visible for T-L samples; this is less pronounced for the L-T samples. SRCT results of the undeformed, as-received material has shown anisotropic features of pores: elongated aligned pores are particularly prevalent in the rolling direction. SRCT analysis of arrested cracks at high stress triaxiality close to the notch root has been carried out for the two testing orientations and heat treatment conditions. Void impingement in both the crack plane and in columns in the loading direction has been observed for the L-T T351 sample. It could be identified that even close to the crack tip voids remain elongated in the L direction for T-L loading of the T351 and T8 material. Inter-void ligaments are smaller in the crack in T-L samples than for L-T samples for the T8 material. The occurrence of void coalescence via bands of narrow crack opening (as opposed to impingement) is visible in the SRCT

data at the fracture initiation stage at high levels of stress triaxiality. Step-wise height changes in the crack are observed, where coarse voids are linked via narrow coalescence regions parallel to the sheet plane. These findings reveal the necessity to investigate and account for coalescence mechanisms involving void nucleation at small 2^{nd} phase particles. The evolution of voiding/damage for the material in T8 condition during crack propagation at lower levels of stress triaxiality has also been observed via high resolution tomography. In the case of loading in the T direction (crack growth in L), voids ahead of the crack tip have grown in the loading direction (T) but retain significant elongation in the L direction, *i.e.* are close to penny-shaped as coalescence occurs. The representation of crack propagation in both samples indicates that, consistent with the crack initiation region close to the notch tip, separation distances between coarse voids are shorter for growth in the L direction than the T, consistent with the measured toughness anisotropy.

Initial comparison of the present experimental results for AA2139 toughness was made with a recent numerical study of the literature of the influence of initial void shape anisotropy on fracture toughness anisotropy at high levels of stress triaxiality: this revealed similar trends to those determined experimentally. A more detailed numerical model to describe and predict experimentally determined toughness anisotropy of the investigated material based on the Gurson-Tvergaard-Needleman model has been further proposed in the present thesis. It incorporates the observed material characteristics such as: (i) anisotropic void growth, (ii) plastic behaviour involving isotropic/kinematic hardening and plastic anisotropy, and (iii) nucleation at small 2^{nd} phase particles at anisotropic critical strains to account for void sheeting. A new simple method to account for initially anisotropic void shape and growth is suggested that is easier to implement than other approaches and is not restricted to axisymmetric cavities. The model parameters have been fitted on experimental data for several kinds of small samples. Model parameters are based on a thorough experimental basis including microstructure characterization and observation of fracture mechanisms. It has been found that neither kinematic hardening nor plastic anisotropy can describe toughness anisotropy. Also accounting for void growth anisotropy is not sufficient to describe toughness anisotropy at realistic loads. It is proposed to account for coalescence and nucleation at a 2^{nd} population of small 2^{nd} phase particles via nucleation at different critical strains for the different material

directions. Application of the found parameters to large M(T) samples shows that this method is suitable to predict fracture toughness anisotropy fitted on small samples. These findings suggest that the effect of anisotropic initial void shape may not be the only origin of fracture toughness anisotropy but that a anisotropic coalescence processes involving nucleation at a small population of 2^{nd} phase particles may also contribute to fracture toughness anisotropy.

Chapter 8

Further work

8.1 The main topics for further work

In this thesis the use of Synchrotron Radiation Computed Tomography (SRCT) allowed to gain new insights into mechanisms of failure. Via investigating arrested cracks it has been possible to obtain information about the evolution of damage from the damage ahead of the crack tip to the contiguous crack. The new findings revealed features such as void sheeting at fracture initiation that are difficult to detect via post failure SEM analysis. However, an arrested crack represents only a 'snapshot' of the damage evolution. The exact damage evolution during the test at defects such as initial pores and intermetallic particles could not be observed. Further insight in ductile fracture mechanisms would be gained if it was possible to perform *in situ* tests at even higher resolution on full size test samples that allow to image identical sample locations several times at different opening displacements.

FE models to describe and predict ductile fracture such as the Gurson-Tvergaard-Needleman model are limited to the representation of a heterogeneous microstructure in a simplified way using averages of heterogeneous material parameters. It can however be seen in the tomography observations of fracture of this thesis that the fracture process is of very heterogeneous nature governed by local competitions between fracture mechanisms linked to local stress states and local microstructural features. With increasing computational performance it may be possible in the future to simulate (and mesh) real heterogeneous microstructures that have been identified through high resolution tomography. With future available *in situ* tomography test data it would then be possible to directly compare the FE predictions and experimental observations which would allow to gain further insight in the

competition of fracture mechanisms and evaluate assumptions and critical fracture parameters.

The present study has also shown that it would be important to obtain quantitative information at higher resolution than at the one available at present via SRCT. For example, a reliable quantification of grain boundary particle coverage through tomography or other techniques would be very valuable in terms of the validation of models. In terms of void sheeting mechanisms observations would need to be made at the scales of small 2nd phase particles such as dispersoids to understand the nucleation mechanisms and the influence of the particle characteristics such as shape and distribution on fracture.

In a more general view of progress in micromechanical modelling, it is clear that there is significant scope for refining the models, *i.e.* by explicitly considering effects that occur on a smaller length scale. For instance modelling of failure processes on the scale of grain boundary precipitates (a few tens of nm) and the precipitate free zone around them may be valuable. Also refinement of micromechanical models down to the scale of dislocations and their interactions with the microstructure could clarify more details of relevant processes.

Another field of research in ductile fracture is the phenomenon of flat to slant fracture transition which is still not well understood. Experiments at different levels of stress triaxiality and for mixed modes are certainly needed to obtain more knowledge about the mechanisms in slant fracture. The micromechanical Gurson-Tvergaard-Needleman approach is often used in FE models for ductile fracture. This model accounts for void growth and can typically not reproduce slant fracture. However, it can be seen in experiments that void growth especially in the slant fracture region at lower stress triaxiality is very limited. Thus, it seems crucial to account for fracture mechanisms at low stress triaxiality in the FE models. In the next Section some preliminary results on the attempt to account for mechanisms at low stress traxiality in the Gurson-Tvergaard-Needleman approach framework is given.

8.2 Slant fracture: a preliminary assessment of possible further work.

Modelling of slant fracture is one of the areas of further research identified above. To assess the possibilities and to indicate the direction such studies may take in the future some additional research on the flat to slant crack transition for thin ductile materials has been performed. As the modelling of the flat to slant transition was not the main objective of the present thesis, only some preliminary, non-rigorous findings are presented.

8.2.1 Motivation

Experimental results indicate that in the slant fracture region, fracture is not dominated by void growth but by shear decohesion mechanisms [1,2]. In a finite element study [3] the crack propagation of a meshed flat and a slant crack have been investigated. The stress fields ahead of the respective cracks during crack propagation under remote mode I loading have been compared and it was identified that for a slant crack the constraint and the mean stress ahead of the crack are reduced whilst the effective stress is augmented compared to a flat crack. This promotes a shearing type of fracture. Figure 8-1 shows a 2D SRCT section of the flat to slant fracture transition in the AA2139 alloy in T8 condition. It can be seen that void growth is substantially higher for the in the flat region than in the slanted regions.

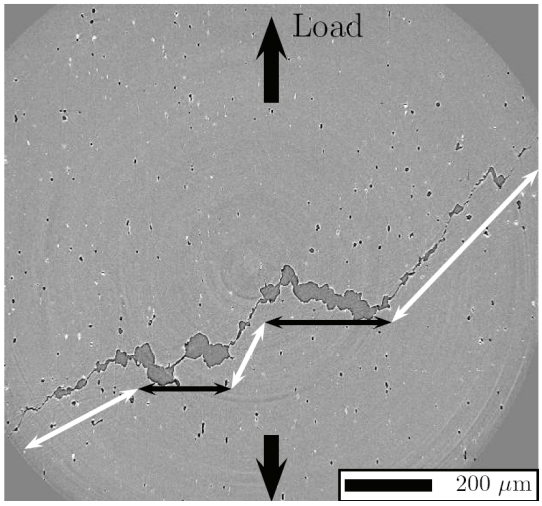

Figure 8-1: 2D SRCT section (normal to crack propagation direction) of an arrested Kahn tear test in the flat to slant transition region of the AA2139 material in T8 condition. Black arrows indicate flat and white arrows the slanted region

8.2.2 Model

In general terms, shear is thought to play a major role for the flat to slant transition and for ductile fracture. Thus a way is developed here to incorporate shear fracture in the Gurson model framework. The idea is to add nucleation of a second population of voids as a function of the encountered stress state and, particularly shear. As shown in recent models [4,5] the Lode parameter may be an adequate indicator for shear. Here the Lode parameter for strain rates, $\mu_{\dot{p}}$, is used based on the idea that it is the deformation rate in a shear configuration that may cause shear and slant fracture. $\mu_{\dot{p}}$ is defined as:

$$\mu_{\dot{p}} = \frac{\dot{p}_2}{\dot{p}_1 - \dot{p}_3} \qquad \textbf{(8-1)}$$

Where $\dot{p}_i$ are the eigenvalues of the strain rate tensor. In the framework of the Gurson model the following equation for nucleation of a 2nd population of voids is generally used:

$$\dot{f}_n = A_n \dot{p} \qquad \textbf{(8-2)}$$

Where $\dot{f}_n$ is the void nucleation rate, $\dot{p}$ the strain rate and A_n may be any positive function of the state variables.

It is suggested here to nucleate voids for a Lode parameter value close to $\mu = 0$ (corresponding to generalized shear). A similar idea has been suggested in [6] where coalescence is suggested to occur at shear fracture. However, this model has not been applied to structures.

A very narrow Gaussian function around $\mu = 0$ is used here to have a continuous function. It is also suggested to nucleate from a certain critical strain p_c onwards. The following equation shows the suggested nucleation function:

$$A_n = A_0 \cdot e^{-\left(\frac{\mu_{\dot{p}}}{\mu_{\dot{p}}^0}\right)^2} \; (p > p_c) \qquad \textbf{(8-3)}$$

Where A_0 is a constant and $\mu_{\dot{p}}^0$ is a constant to adjust the shape of the Gaussian function.

8.2.3 Results and discussion: Example for slant fracture

Here an example of a simulated flat to slant transition is presented. The model parameters are given in Table 8-1. Unlike the model in Chapter 6.2 kinematic hardening, plastic anisotropy and anisotropic void growth are neglected. The elastic-plastic behaviour has been identified on a T tensile test curve for the AA2139 T351 material.

Void growth		Damage		Nucleation for shear			
q_1	q_2	f_0	f_n	A_0	$\mu_{\dot{p}}^0$	p_c	
1.97	0.91	0.33%	0.45%	2.0	0.011	0.1	
Elastic-plastic behaviour							
E in GPa	v	R_0 in MPa	K_0	K_1	k_1	K_2	k_2
70	0.3	250	0.0544	1.121	7.148	0.273	187.9
a=b=12							
Element sizes							
x=50 μm	y= 53 μm	z= 100 μm (through -thickness)					

Table 8-1: Parameters for presented slant fracture simulation

The crack path found in the simulation is shown in Figure 8-2. The cracked elements are shown in orange. The flat triangular region close to the notch is clearly formed. It subsequently turns into a slant crack, consistent with experimental observations.

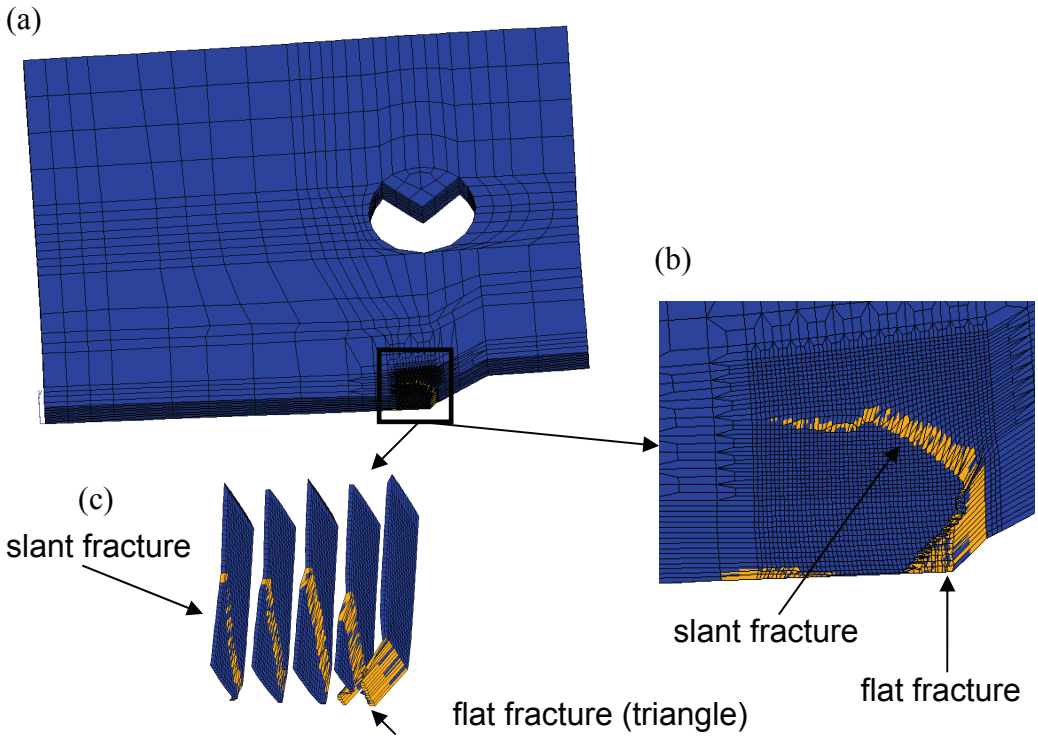

Figure 8-2: Slant fracture simulation result:(a) meshed quarter of a Kahn tear test sample (b) zoom into finely meshed initiation region (c) element "slices" in the fine region. Broken elements are shown in orange

Figure 8-3 shows the structural response in terms of Force F divided by initial ligament area A_0 versus CMOD for experiments in T-L and L-T configuration and simulation results for T-L loading. The loads up to maximum load are predicted correctly. However, the load decrease in the simulation starts at a higher COD than in the experiment, so that the simulation results for the T-L configuration are located between the experimental results for T-L and L-T loading. The descending slope is however predicted correctly. Simulated loads are in the range of the experimental results which represents an advantage compared to other attempts made to model slant fracture (*e.g.* [7,8]) that did not fit experimental results or that were not compared to them.

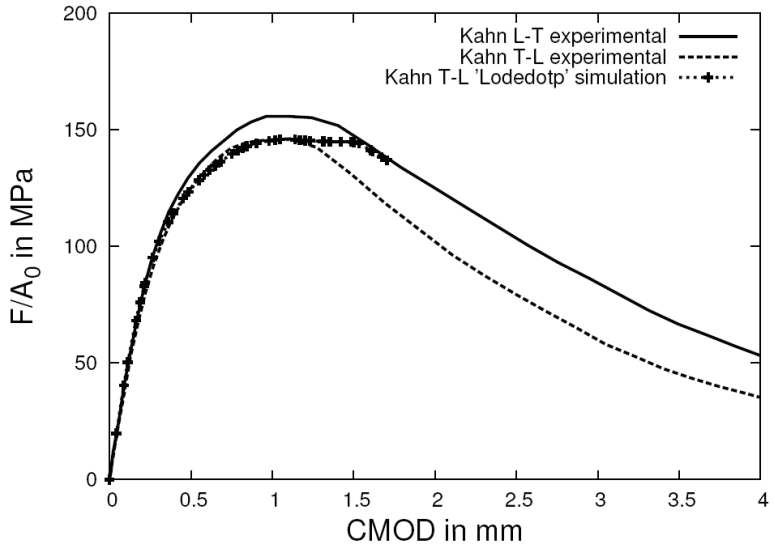

Figure 8-3: Kahn tear tests: experimental and simulated structural response for AA2139 naturally aged

These results show that accounting for shear fracture processes may lead to a better comprehension and prediction of slant fracture, the flat to slant transition and ductile fracture in general. The strong points of the model modification presented here are that predicted loads are in a reasonable range compared to simulations. The modification can easily be implemented in a Gurson model. Negative points are that 3 new parameters $\mu_{\dot{p}}^{0}$, A_0 and p_c need to be fitted which may be time consuming as computation times are long. A fine mesh needs to be used to be able to approximate the slanted fracture path.

8.1.1 References

[1] Bron F, Besson J, Pineau A. Mat Sci Eng A. 2004 ;380 :356-364
[2] Garrison WM, Moody NR, J. Phys. Chem. Solids ,1987;48: 1035-1074
[3] Mahgoub E, Deng X, Sutton MA. Engng Fract Mech. 2003;70:2527-2542
[4] Xue L. J. Int. J. Solids Struct 2006 ;44 :5163-5181
[5] Xue L, Wierzbicki T. Engng Fract Mech. 2007;75: 3276-3293
doi:10.1016/j.engfracmech.2007.08.012
[6] Nahshon K, Hutchinson JW. Eur. J. Mech. 2008;27A:1-17
[7] Mahgoub E, Needleman A, Tvergaard V. J Mech Phys Solids. 1996:44:439-459
[8] Besson J, Steglich D, Brocks WB. Int J Solids Structures 2001;38:8259-8284